



The University of
Nottingham

**DISCRETE ELEMENT MODELLING OF
GEOGRID-REINFORCED RAILWAY BALLAST
AND TRACK TRANSITION ZONES**

By

Cheng Chen

M.Sc., B.Eng.

**Thesis submitted to the University of Nottingham
for the degree of Doctor of Philosophy**

June 2013

To my parents

Abstract

Track deterioration has a serious influence on the safety and efficiency (speed restriction) of train operations. Many expensive, disruptive and frequent repair operations are often required to maintain the ballast characteristics due to the problem of settlement. Because of this, a geogrid solution that has proved to be a simple and economical method of reinforcing track ballast is widely used.

This project presents an evaluation of the behaviour of geogrid-reinforced railway ballast. Experimental large box pull-out tests were conducted to examine the key parameters influencing the interaction between ballast and the geogrid. The experimental results demonstrated that the triaxial geogrid with triangular apertures outperforms the biaxial geogrid with square apertures and the geogrid aperture size is more influential than rib profile and junction profile. The discrete element method (DEM) has then been used to model the interaction between ballast and geogrid by simulating large box pull-out tests and comparing with experimental results. The DEM simulation results have been shown to provide good predictions of the pull-out resistance and reveal the distribution of contact forces in the geogrid-reinforced ballast system.

The discrete element method has also been used to simulate cyclic loading of geogrid-reinforced ballast under confined and unconfined conditions. For the confined condition, box tests have been simulated on unreinforced samples and reinforced samples with different geogrid positions and geogrid apertures. The response of the ballast layer reinforced with geogrid under repeated loading agrees with experimental results. It was found that the optimum location of geogrid is 100 mm depth from base, and the triaxial geogrid outperforms biaxial geogrid. For the unconfined condition, cyclic loading of a trough of ballast has also been simulated, and the sample with the geogrid at 50mm from the sub-ballast layer performs best. It was also found that the used of two geogrids at both 50mm and 150mm from the sub-ballast gave a smaller settlement than using a single layer geogrid, or the unreinforced ballast. The geogrid

reinforcement limits the lateral displacement in reinforced zone, which is approximately 50mm above and below the geogrid.

Previous investigations have shown that the abrupt stiffness change in track support is often associated with accelerated rates of deterioration of track geometry, high maintenance demand, and poor ride quality. However, at present, there is no detailed understanding of the mechanisms of track geometry deterioration at transition zones. This work provides insight into the factors that can cause or accelerate track degradation at the transition zones, in order to identify and evaluate appropriate mitigation design. A simple track transition model with dimensions 2.1m x 0.3m x 0.45m was simulated by using PFC^{3D}. In order to identify and evaluate appropriate mitigation methods, two kinds of transition patterns, including a single step change and a multi step-by-step change for subgrade stiffness distribution were tested. The influence of the train direction of travel and speed on the transition were also investigated. In addition, geogrid was used in the ballast layer to examine the effects of geogrid reinforcement.



DECLARATION OF ORIGINALITY

Title of Thesis: *Discrete Element Modelling of Geogrid-reinforced Railway Ballast and Track Transition Zones*

I declare that the thesis hereby submitted for the degree of Doctor of Philosophy at the University of Nottingham is my own work except as cited in the references and has not been previously submitted for any degree.

The following publications are fully related to the research work conducted in this PhD program:

Journal papers

Chen, C., McDowell, G. R., Thom, N. H., 2012. Discrete element modelling of cyclic loads of geogrid-reinforced ballast under confined and unconfined conditions, *Geotextiles and Geomembranes* **35**, 76-86.

Chen, C., McDowell, G. R., Thom, N. H., 2013a. A study of geogrid-reinforced ballast using laboratory pull-out tests and discrete element modelling. *Geomechanics and Geoengineering: An International Journal* (Accepted for publication).

Chen, C., McDowell, G. R., Thom, N. H., 2013b. Investigating geogrid-reinforced railway ballast: experimental pullout tests and discrete element modelling. *Special issue of Soils and foundations*. August, (Accepted for publication).

Chen, C. and McDowell, G. R. 2013. An investigation of dynamic behaviour of track transition zones using discrete element modelling. *Acta Geotechnica* (under review).

Conference Papers

Chen, C., McDowell, G. R., Thom, N. H., 2012. Investigating geogrid-reinforced ballast using laboratory pull-out tests and discrete element modelling. 2nd International Conference on Transportation Geomechanics, Sapporo, Japan.

McDowell, G. R., de Bono, J., Chen, C., Cai, W. Ferellec, J-F., Li, H. and Falagush, O., 2012. Recent applications of DEM in Geomechanics. 3rd international Workshop on Modern trends in Geomechanics, Nottingham, UK.

Name : CHENG CHEN

Signature :

Date : 06/06/2013

Acknowledgements

This study would not have been completed without the help from many people. First and foremost, I would like to sincerely thank my supervisor, Professor Glenn McDowell, who had led me through all these years of hard working, given expert supervision, read my numerous revisions and made it a high quality final product. Under his guidance, not only I learnt how to do research, but also learnt from him about the attitudes to life. I would also like to express my sincere gratitude to the following people for their advice and help:

- Dr. Nicholas Thom, co-supervisor, for his inputs and advices.
- Dr. Alec Marshall for his invaluable comments and suggestions on my thesis.
- Dr. Jean-francois Ferellec for his help in the Discrete Modelling work in this project as well as the many interesting discussion on matters out of research.
- All the technicians and experimental officer in the School of Civil Engineering.
- All the colleagues and friends at NCG whom I have had many enjoyable times.
- Finally, I would like to thank my parents and my sister for their constant support, belief and encouragement.

Table of Contents

CHAPTER 1 INTRODUCTION.....	1
1.1 Background	1
1.2 Aims and objective of the project	3
CHAPTER 2 LITERATURE REVIEW: MECHANICAL BEHAVIOUR OF RAILWAY BALLAST AND GEOGRID	7
2.1 Introduction	7
2.2 Ballasted track system.....	7
2.2.1 Track components and functions	8
2.2.2 Force exerted on ballast	10
2.2.3 Ballast deformation and track settlement	13
2.3 Ballast properties	14
2.3.1 Ballast specification.....	15
2.3.2 Effect of particle shape on ballast functions	18
2.3.3 Effect of gradation	21
2.4 Mechanical behaviour of ballast under repeated loading	22
2.4.1 Resilient behaviour	22
2.4.2 Plastic behaviour	27
2.5 Geogrid reinforcement	31
2.5.1 Tensar polymer geogrids	31
2.5.2 Reinforcing principle	33
2.5.3 Behaviour of geogrid reinforced granular material	36
2.6 Pull-out mechanism	39
2.7 Summary	41
CHAPTER 3 DISCRETE ELEMENT METHOD (DEM)	43
3.1 Introduction	43

3.2 Discrete element modelling using PFC ^{3D}	44
3.2.1 The PFC ^{3D} particle-Flow Model	44
3.2.2 Distinct-Element Method	45
3.2.3 Calculation Cycle	46
3.2.4 Clump logic.....	49
3.3 Contact constitutive models.....	51
3.3.1 Linear elastic contact model.....	51
3.3.2 The Bonding Models	52
3.4 Boundary conditions	56
3.4.1 Overview of DEM boundary conditions	56
3.4.2 Rigid walls	58
3.5 Use of DEM in geogrid-reinforced ballast.....	60
3.5.1 Modelling mechanical response of railway ballast.....	60
3.5.2 Modelling ballast particle shape	62
3.5.3 DEM on interlocking behaviour of geogrid.....	65
3.6 Summary	70

CHAPTER 4 LABORATORY LARGE BOX PULL-OUT TEST... 71

4.1 Introduction	71
4.2 Test procedure	72
4.3 Results.....	76
4.4 Discussion.....	81
4.5 Conclusions	84

CHAPTER 5 GEOGRID MODELLING USING PFC^{3D} 85

5.1 Preliminary study.....	85
5.2 Biaxial geogrid	87
5.2.1 Numerical modelling procedure	87
5.2.2 Calibration tests.....	89
5.3 Triaxial geogrid	93
5.4 Conclusions	96

CHAPTER 6 DISCRETE ELEMENT MODELLING OF LARGE BOX PULL-OUT TEST..... 97

6.1 Introduction 97
6.2 Modelling ballast particle shape..... 99
6.3 Particle-pouring test simulation 101
6.4 Numerical modelling procedure..... 104
6.5 Results and discussion 109
 6.5.1 Simulation results using 2-ball clumps..... 109
 6.5.2 Effect of ballast particle shape..... 115
 6.5.3 Simulation results using 8-ball tetrahedral clumps..... 118
6.6 Conclusions 122

CHAPTER 7 DISCRETE ELEMENT MODELLING OF CYCLIC LOADING OF GEOGRID-REINFORCED BALLAST UNDER CONFINED AND UNCONFINED CONDITIONS..... 124

7.1 Introduction 124
7.2 Box test simulation 125
 7.2.1 Box test description 125
 7.2.2 Modelling procedure..... 127
 7.3.3 Results and discussions 132
7.4 Composite Element Test (CET)..... 141
 7.4.1 The test description..... 141
 7.4.2 Modelling procedure..... 143
 7.4.3 Results and discussion 144
7.5 Conclusions 149

CHAPTER 8 DISCRETE ELEMENT MODELLING OF TRACK TRANSITION ZONES 151

8.1 Introduction 151
8.2 Problem definition 152
8.3 DEM of track transition..... 154

8.3.1 Sample preparation	154
8.3.2 Determination of the subgrade stiffnesses through a plate bearing test simulation	156
8.3.3 90 degrees out of phase loading.....	158
8.4 Results and discussion.....	161
8.4.1 Influence of phase loading	161
8.4.2 Influence of different subgrade stiffness	162
8.4.3 Influence of moving direction	166
8.4.4 Influence of different frequency of cyclic load (train speed)	166
8.4.5 Influence of axle load	169
8.4.6 Influence of geogrid in transition zones	169
8.5 Conclusions	171
CHAPTER 9 CONCLUSIONS AND SUGGESTIONS FOR FURTHER RESEARCH.....	173
9.1 Conclusions	173
9.2 Suggestions for further research.....	175
REFERENCES	180

Chapter 1 Introduction

1.1 Background

The railway is an integral part of the transport network as it has a large capacity and is financially viable. However, traditional railway foundations or substructures have become increasingly overloaded in recent years, owing to the rapidly increasing number of faster and heavier trains. Two significant problems arising from increasing axle loads are track deformation and ballast degradation. The maintenance cycles are becoming more frequent and increasingly expensive as a result of these problems. To achieve optimum performance of the rail maintenance and minimize the maintenance cost, it is necessary to understand the behaviour of railway ballast and how the solutions of maintenance work.

The track substructure layers consist of the ballast layer, subballast layer and subgrade layer. The short and long term settlements due to static and dynamic loading occur in these layers. Figure 1.1 shows a typical profile of the relative contributions of substructure components to track settlement based on a good subgrade foundation (Selig and Waters, 1994). It is clear from the figure that the ballast layer accounts for most of the vertical deformation of a rail track, compared to the subgrade and subballast layer. The strain generated in ballast and the breakage of ballast particles are regarded as the main factors which increase the permanent strain progressively with running trains (Esveld, 2001). In order to reduce vertical track settlement, emphasis must be placed on the ballast material.

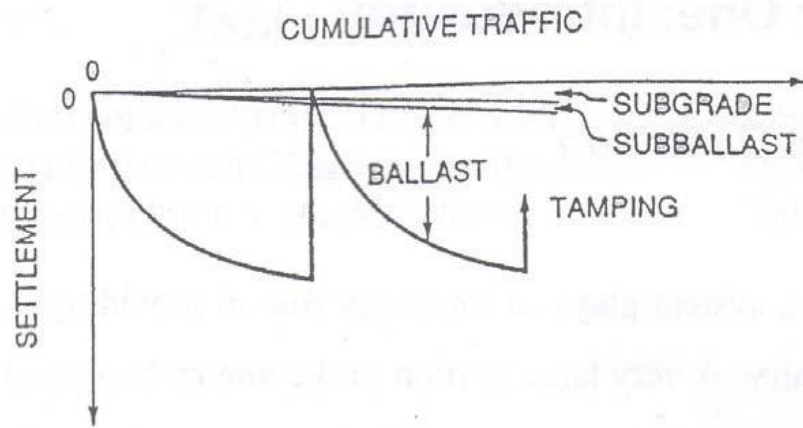


Figure 1.1 Substructure contributions to settlement (Selig and Waters, 1994)

Since the introduction of the Tensar geogrid in the early 1980s, the application of reinforcing geogrid has been proved to be a simple and economical method which can reduce the permanent settlement in the ballast layer (see Figure 1.2). However, no significant work has been done on understanding the characteristics of grid/ballast interaction. Current practice involving geogrid reinforcement is still limited to experience gathered on site based on ad hoc work. The development and optimisation of geogrid reinforcement of railway ballast has the potential to allow longer maintenance cycles translating to cost savings. To optimize the geogrid/ballast system and identify the key elements involved, five main strands of experimental work, namely Composite Element Test (CET), Railway Test Facility (RTF), Pull-out Test, Box test and Large-scale Triaxial Test, have been developed and carried out in the University of Nottingham. These experimental tests have investigated the interlocking of grid, the ratio of aperture size to ballast size, the shape of grid as well as the position of grid within the ballast layer. Work carried out in the Nottingham Railway Test Facility by Brown et al. (2007) showed that there was significant reduction in total settlement by the geogrid reinforced sample. The geogrid was placed at the bottom of the ballast layer on the silt subgrade. Milligan and Love (1985) have investigated the behaviour of reinforcing granular layer over soft clay. It was found that the mean angle of load spread increased from 38 degrees in the unreinforced sample to over 50 degrees in the geogrid-reinforced sample.



Figure 1.2 Tensar TriAx geogrid installed under the granular sub-ballast layer to increase bearing capacity in Belgium (Tensar, 2010)

Traditional analytical and numerical methods are unable to investigate the interlocking effect of ballast /geogrid system, because it is characterised by strong discontinuous behaviour. The discrete element method (DEM) (Cundall and Strack, 1979) provides a way to investigate the mechanical behaviour of granular material at both micro and macro level. This numerical modelling approach allows finite displacements and rotations of discrete bodies and recognises new contacts automatically during the calculation process. It enables investigation of the micro mechanics of the deformation of granular materials that cannot be easily studied in laboratory tests. Previous studies (see literature review) have proved that DEM can not only investigate the mechanical behaviour of granular material but also model the geogrid and ballast interaction. Thus, it provides a powerful numerical tool for modelling the micro mechanical behaviour of railway ballast and the interlocking behaviour of geogrids under static and cyclic loading conditions.

1.2 Aims and objective of the project

The ultimate aim of this project is to improve modelling of ballast and geogrids in order to optimise design of geogrid-reinforced ballast systems. Figure 1.3 shows the component parts of the project.

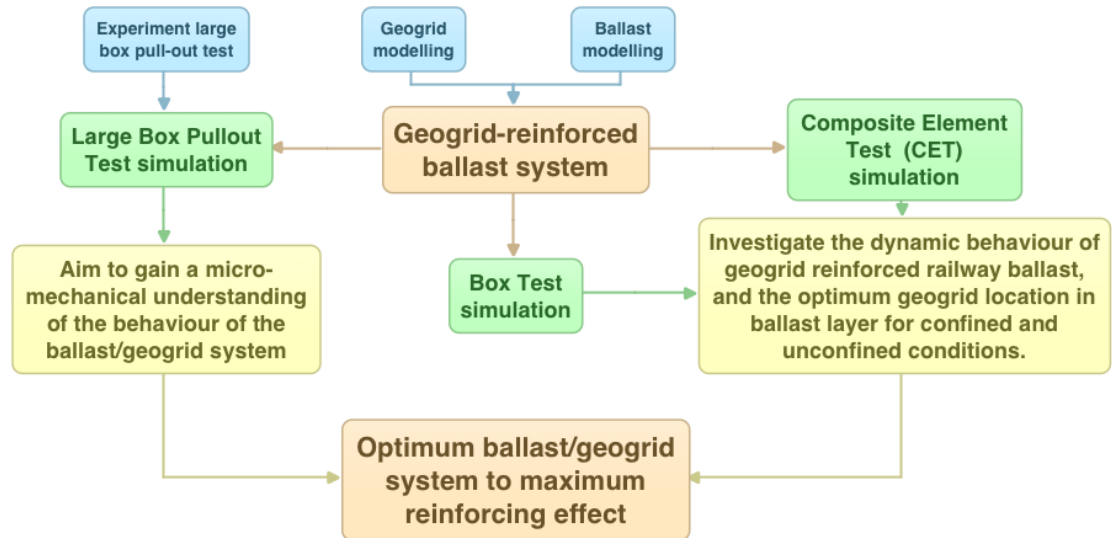


Figure 1.3 Component parts of the project

To achieve the aim, the following specific objectives are required:

1. A literature review on the behaviour of ballast and geogrid.
2. Modelling a suitable ballast particle in PFC^{3D} and investigation of the effect of particle shape on mechanical response.
3. Modelling and calibration of different kinds of geogrids including biaxial and triaxial geogrids.
4. Simulations of large box pull-out tests investigate the interlock between ballast and geogrid under static loading and study of the effect of relative size of the geogrid to the ballast.
5. Comparison of pull-out test simulation results with experimental data.
6. Simulations of box test and composite element test (CET) to investigate the interlock between ballast and geogrid under cyclic loading for confined and unconfined conditions.
7. 3-sleeper transitions model to investigate track transition zones from a micro mechanical perspective.

1.3 Thesis Outline

This thesis is structured into nine chapters. A brief outline of the thesis is given below.

Chapter 1 provides a brief background and states the objectives of the work.

Chapter 2 contains a brief introduction of ballasted track system, a literature review of ballast characteristics, a review of the mechanical behaviour of railway ballast and a review of the geogrid reinforcement in railway track. Finally, a review of the pull out mechanism is presented.

Chapter 3 generally describes the theory of the discrete element method and a basic overview of PFC^{3D}. Recent applications of DEM in modelling railway ballast and polymer geogrid are reviewed.

Chapter 4 gives details on laboratory large box pull-out test undertaken to evaluate and validate the DEM large box pull-out test simulation. The effects of geogrid aperture and rib profile on interlocking behaviour are also investigated by comparing performance of six different types of geogrids.

Chapter 5 presents a simple geogrid model which consists of parallel bonded single balls. Then a detailed calibration of the geogrid model is presented.

Chapter 6 presents the results of large box pull-out test simulations using different particle shapes under different surcharges. The effects of particle shape on the mechanical response of the ballast/geogrid system are investigated. A quantitative comparison of the experiments and DEM simulations is also presented.

Chapter 7 presents the box test and composite element test simulations. The optimum geogrid location and number of geogrid layers in the ballast layer for confined and unconfined conditions are investigated. The performance of biaxial and triaxial geogrid and the effect of subgrade stiffness are also investigated.

Chapter 8 investigates track transition zones from a micro mechanical perspective, and provides insight into the factors that can cause or accelerate track degradation at the transition zones, in order to identify and evaluate appropriate mitigation design.

Chapter 9 presents the conclusions derived from this research, and recommendations for possible future research.

Chapter 2 Literature review: mechanical behaviour of railway ballast and geogrid

2.1 Introduction

In order to research and further optimize geogrid-reinforced railway ballast, a sufficient understanding of the behaviour of ballast and geogrid is imperative. In this chapter, an introduction of track components, ballast functions, and track forces will first be presented. Then a literature review of ballast characteristics and the effect of ballast shape and degradation on ballast functions are presented. Next, a brief description of ballast specification and ballast deformation are given. The detailed mechanical behaviour of railway ballast under cyclic loading is then discussed and the reinforcing principle of the geogrid is presented. Finally, a review of the pull-out mechanism is presented.

2.2 Ballasted track system

Esveld (2001) expressed that the main advantages of ballasted track are:

- proven technology;
- relatively low construction costs;
- simple replacement of track components;
- easy to maintain;
- good drainage properties;
- good elasticity;
- good absorption of noise.

2.2.1 Track components and functions

The main components of ballasted track structures may be divided into two main categories: superstructure, and substructure. The superstructure consists of the rails, the fastening system, and the sleepers (ties). The substructure consists of the ballast, the subballast and the subgrade. The superstructure and the substructure are separated by the sleeper-ballast Interface. The traffic load is transferred from superstructure to substructure via the sleeper-ballast interface (Selig and Waters, 1994). Figure 2.1 and 2.2 show the components of a conventional ballasted track.

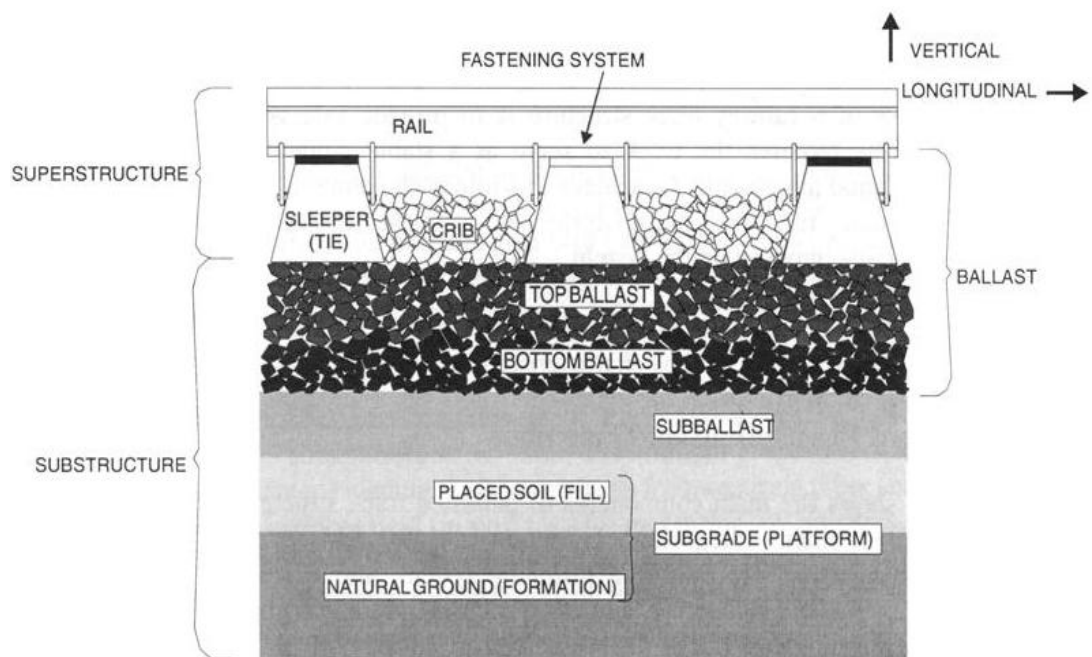


Figure 2.1 Track structure components in lateral view (Selig and Waters, 1994)

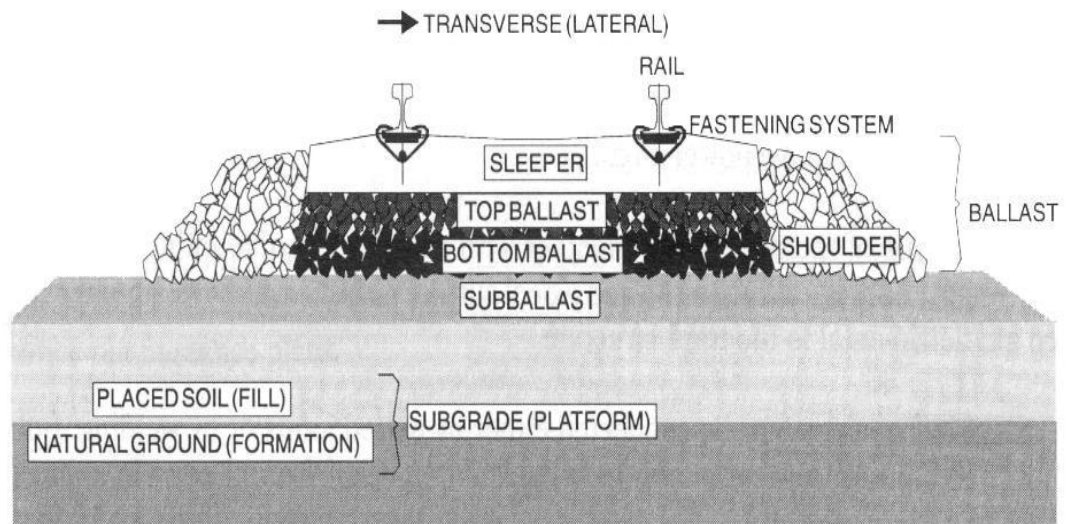


Figure 2.2 Track structure components in cross section view (Selig and Waters, 1994)

The rails are a pair of longitudinal steel members and also the only part of track component that has direct contact with the train wheels. The main function of the rails is to guide the train wheels evenly and continuously. In addition, the rails must be stiff enough to act as beams which transfer the traffic loading to the spaced sleeper supports with minimum deflection between supports. The fastening system retains the rails against the sleeper and resists vertical, lateral, longitudinal and overturning movements of the rail caused by the wheels and by temperature changes in the rails.

The functions of sleepers are to transfer the load from the rails to the ballast and also restrain the rail movement by anchorage of superstructure in the ballast (Selig and Waters, 1994). Wood and concrete sleepers are the two most common types of sleepers. With the increasing number of heavier and faster trains, concrete sleepers have become more popular recently as they are economic and stiff enough to support under heavy traffic. In modern concrete sleepers rubber pads are required between the rail seat and the concrete sleeper surface to reduce rail-sleeper contact forces, wheel-induced vibration and noise. They also provide electrical insulation for the track signal circuits.

According to the local availability, various materials have been used for ballast such as crushed granite, basalt, limestone, slag and gravel. The graded ballast is placed as the top layers of the substructure where the sleepers are embedded. The main ballast functions were summarized by Selig and Waters (1994) as follows:

1. Retain the track in a proper position by resisting forces applied to the sleepers.
2. Provide some of the resiliency and energy absorption to the track.
3. Provide sufficient voids for storage of contaminating material in the ballast, and movement of particles through the ballast.
4. Allow adjustment of track geometry by the ability to rearrange ballast particles with tamping.
5. Provide immediate drainage of water falling onto the track.
6. Relieve pressure from the sleeper bearing area to tolerable stress level for the underlying material.

Compared with ballast, subballast is a generally finer and more broadly-graded granular material. It further reduces the stress at the bottom of ballast layer to an acceptable level for the top of the subgrade. Moreover, it prevents fine material from moving up from the subgrade into the ballast (Selig and Waters, 1994). The subgrade provides a stable foundation for the ballast and subballast layers and can be natural ground or placed soil.

2.2.2 Force exerted on ballast

Understanding the various types and magnitudes of forces is fundamental to understand how ballast works in rail track. Generally the forces due to moving traffic and changing temperature are classified as vertical, lateral, and longitudinal forces. Vertical forces are the main imposed forces on ballast, and lateral forces and longitudinal forces are much harder to quantify than vertical forces (Selig and Waters, 1994).

As Figure 2.3 shows, the vertical forces have two directions: upwards and downwards. The lift force is induced by the rail to resist the downwards tendency. However, the vertical downwards force is often regarded as having a static component and a dynamic variation about the static value. The static load is equal to the vehicle weight, while the dynamic load is a function of track condition, train characteristics, operating conditions, train speed and environmental conditions. Figure 2.4 show the static and dynamic wheel loads plotted as cumulative frequency distribution curves for the Colorado test track and mainline track between New York and Washington respectively (Selig and Waters, 1994). Clearly, the dynamic increment is more noticeable for high vertical wheel loads and also is more significant for the example (b) than the example (a). This is due to the better track condition for the Colorado test track. It also can be concluded that a high dynamic load occurred at a high speed, which in turn exerts a high stress onto the ballast causing possible breakage of material.

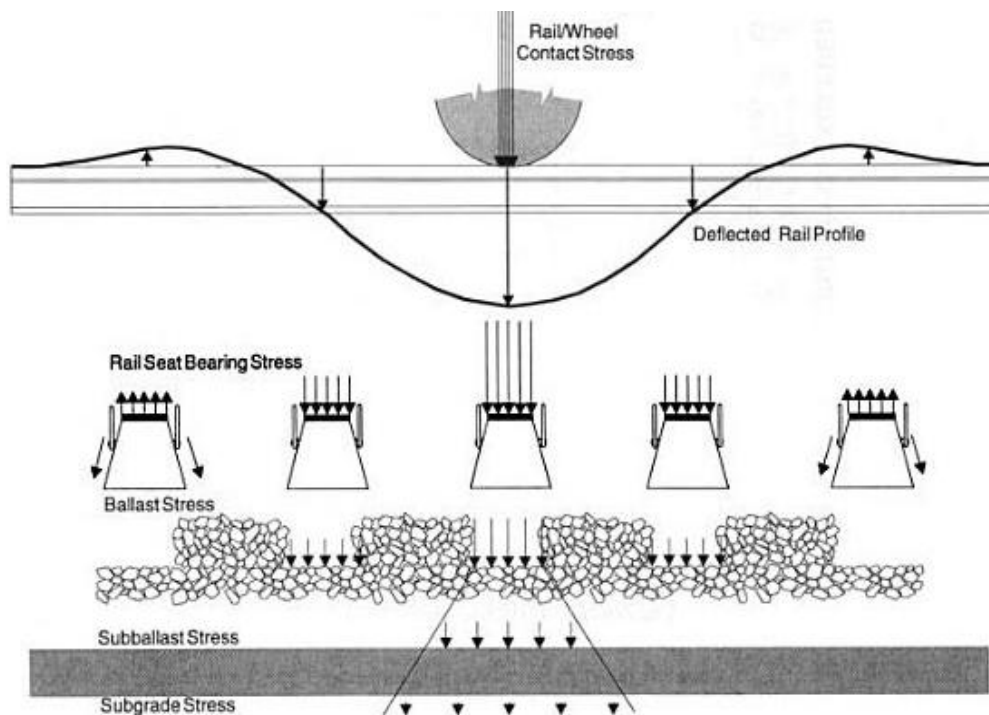


Figure 2.3 Typical wheel load distribution into the track structure (Selig and Waters, 1994)

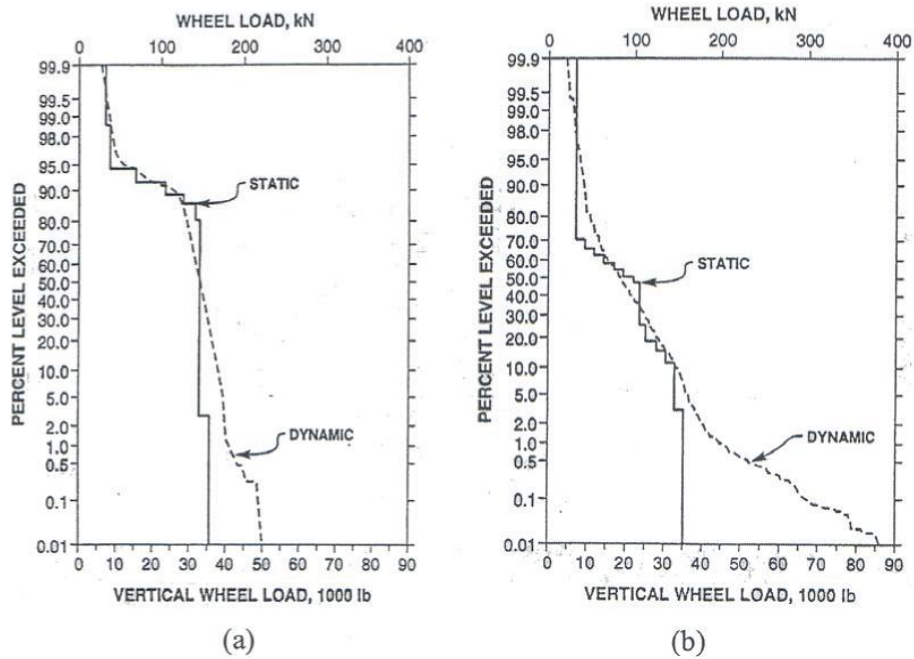


Figure 2.4 Static and dynamic wheel loads for (a) Colorado test track and (b) mainline track between New York and Washington (Selig and Waters, 1994)

The lateral forces act parallel to the long axis of the sleepers. Selig and Waters (1994) states that the lateral force mainly occurs from lateral wheel force due to the friction between the wheel and rail especially at a curved track. It also comes from the buckling reaction force which arises from buckling of rails due to the high longitudinal force. The longitudinal forces are parallel to the rail. The sources of this force consist of locomotive traction force due to acceleration and braking, thermal expansion and contraction of rails, and rail wave action (Selig and Waters, 1994).

The other very significant force applied on the ballast is achieved through ‘squeezing’ the ballast. This can be credited almost solely to the tamping procedure. Ballast tamping has been recognised as the most effective method to correct and restore track geometry. Not surprisingly, it is also the most common railway maintenance technique used today. The tamping procedure includes lifting the rail and inserting tines which will vibrate and move towards each other, ‘squeezing’ the ballast underneath the sleeper into position. The high squeezing and plunging force often causes material breakage and this is known to be the most destructive element in

railway operation in terms of ballast deterioration, even more than that due to a high speed train (Wright, 1983). Figure 2.5 illustrates the tamping procedure.

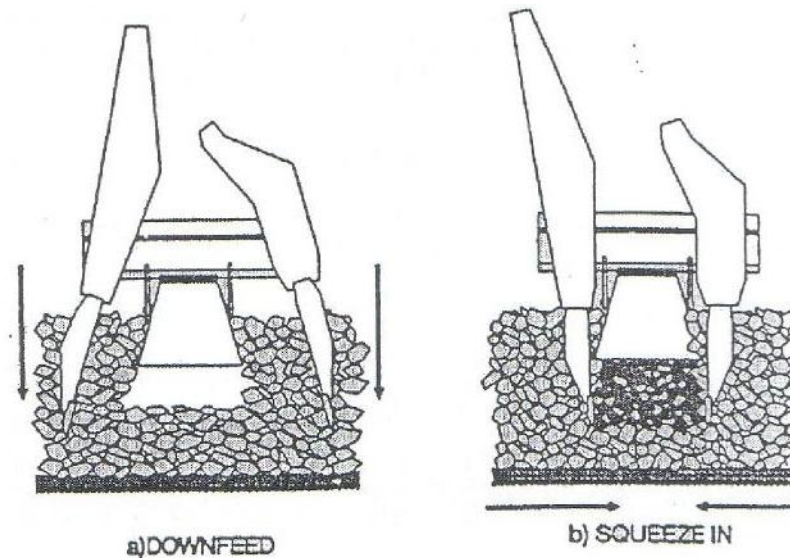


Figure 2.5 Tamping procedures (Selig and Waters, 1994)

2.2.3 Ballast deformation and track settlement

Selig and Waters (1994) expressed that all the stresses and caused settlements occur in the track substructure layers and may be due to several different causes including short and long term settlements due to static and dynamic loadings. The ballast deformation arises from ballast particles rearranging into a more compact configuration and particle breakages occur at contact points. It is a well-known fact that after tamping the ballast settles rapidly and then the rate of settlement decreases with increasing traffic. It is often assumed that the settlement of the track is proportional to the logarithm of the number of axles having passed; however examination of all available data indicates a significant underestimation can occur for large numbers of axles (Shenton, 1985).

According to Dahlberg (2001), there do not seem to be any generally accepted damage and settlement equations describing the long-term behaviour of the track.

Moreover, most descriptions of the settlement found are empirical. Besides, the track settlement is mostly considered to be a function of the magnitude of loading and/or a function of the magnitude of loading cycles. However, Dahlberg (2001) considered the properties of ballast and subgrade materials should also be added in the model.

Dahlberg (2001) classified the reasons that track settlement occurs in two phases:

- Directly after tamping, when rate of settlement is relatively fast until the ballast is consolidated.
- Settlement with time (or load) is an approximate linear relationship.

The second phase of settlement results from several main ballast and subgrade behaviour mechanisms:

- Continuation of volumetric densification caused by repeated train loading.
- Ballast fouling: for example, ballast material penetrates/sinks into the sub-ballast and subgrade.
- Ballast breakage from train loads and environmental factors causing volumetric reduction.
- Volume reduction due to abrasive wear. Particles diminish in volume caused by abrasive contact forces between the particles.
- Irreversible deformation due to micro-slip between ballast particles at loading.
- Sleeper sinking deeper into the ballast layer: this could be caused not only by lateral movement of ballast or subgrade particles but also lateral and longitudinal movement of the sleeper.

2.3 Ballast properties

Traditionally, the main factors in the choice of ballast materials are availability and economic reasons. Ideal ballast materials are angular, crushed, hard stones and rocks,

uniformly graded, free of dust and dirt, and not prone to cementing action (Selig and Waters, 1994). However, there has not been universal standard on the specification. The ability of ballast to perform its functions depends on the particle characteristics (e.g. particle size, shape, angularity, hardness, surface texture and durability) together with the in-situ physical state (e.g. grain structure and density).

2.3.1 Ballast specification

Typical ballast ranges from 20 to 50mm in diameter and its performance is governed by the physical characteristics as well as the packing assembly. No single characteristic controls ballast behaviour and many relevant characteristics are listed in Table 2.1. The United Kingdom follows the European Railway Ballast Specification BS EN 13450 (2002). This standard comprises 5 properties which define the specification of track ballast: ballast grading, Los Angeles Abrasion (LAA), micro-Deval attrition, flakiness index, and particle length. This specification requires the ballast to conform to the particle size distributions shown in Table 2.2.

The LAA test measures a material toughness or tendency to break. The test measures the particle resistance to fragmentation with the provision of a Los Angeles Abrasion (LAA) coefficient. The LAA coefficient is the percentage of material passing through the 1.6mm sieve upon completion of the test. The LAA test involves rotating 10kg of dry ballast with 12 steel balls weighing a total of 5kg in a large steel drum. The dry ballast is subjected to 1000 revolutions with a rotational speed of 31-33 rotations per minute. The shelves inside the steel drums will pick up and drop the ballast at a distance almost equivalent to the drum diameter making the LAA a crushing test. The ballast is then sieved to achieve the LAA coefficient. A high LAA value signifies a brittle material. BS EN 13450 (2002) limits the LAA value to 20 (Lim, 2004).

Table 2.1 Typical Ballast Characteristics

KEY CHARACTERISTICS	BS EN STANDARDS/ SPECIFICATIONS
DURABILITY	
Los Angeles Abrasion	BS EN 1097-2: 1998 / LAA index ≤ 20
Deval Abrasion (wet and dry)	BS EN 1097-1: 1996/ M_{DE} index ≤ 7
Crushing value	BS 812-111: 1990/ ACV $\leq 22\%$
SHAPE CHARACTERISTICS	
Flakiness/ Elongation/ Angularity or Particle Length (shape index)	BS EN 933-2/3: 1997/ Flakiness index ≤ 35 and Elongation index ≤ 50 . Particle Length ≤ 4
GRADATION	
Size distribution	BS EN 933-2: 1996/ Size to be between 31.5mm to 50mm.
UNIT WEIGHT	
Particle density/ Water adsorption	BS EN 1097-6: 2000/ Specifications of categories in BS EN still not considered appropriate for rail track use
Bulk density and voids	BS EN 1097-3: 1998/ Not available
ENVIRONMENTAL	
Freeze-thaw breakdown	BS EN 1367-1: 2000/ Refer to BS EN 13450: 2002, Annex F
Sulfate soundness	BS EN 1367-2:1998/ Refer to BS EN 13550: 2002, Annex G
COMPOSITION	
Chemical analysis	BS EN 1744-1: 1998/ Not available

Table 2.2 Particle Size Distribution Specification (British standard Institution, 2012)

Square Mesh Sieve (mm)	Cumulative % by mass passing BS sieve
80	100
63	100
50	70-99
40	30-65
31.5	1-25
22.4	0-3
31.5-50	≥50

In accordance with BS EN 13450 (2002), the Deval attrition test measures the particle resistance to wear with the provision of a Micro-Deval Attrition (MDA) coefficient. The Deval attrition test is very similar to the LAA test; however, the Deval attrition is a wet test in contrast to the dry LAA test. In the micro-Deval test, 2 specimens of dry ballast material, 5kg each, are segregated in two separate steel drums. Steel balls (9.5mm diameter) weighing a total of 5kg, smaller than those used in the LAA are also added into the steel drums together with 2 litres of water. 14,000 revolutions are then applied to the steel drums. The rotational speed is approximately 100 rotations per minute. The MDA coefficient is the percentage of material passing through the 1.6mm sieve upon completion of the test. A high MDA coefficient indicates the ballast specimen is more susceptible to wear. BS EN 13450 (2002) requires the mean value of MDA to be less than or equal to 7 (Lim, 2004).

The flakiness index test measures the ‘flatness’ of a particle. The British Standard (British Standard 812, 1983) defines a flaky particle as one where the thickness to width ratio is less than 0.6. The flakiness index test involves 2 sieving operations. The first operation involves sieving the particles into various particle size fractions. The second operation involves sieving each fraction with bar sieves which have

parallel slots of width 0.5 times that of the standard sieve. The flakiness index is defined as the percent by weight of flaky particles passing the bar sieve. BS EN 13450 (2002) indicates that the flakiness index shall be less than or equal to 35. Particle length index is defined as the percent of particles with length equal or more than 100mm for a sample size exceeding 40kg. The test involves manual measurement of each particle. BS EN 13450 (2002) states that the particle length index shall be less than or equal to 4.

2.3.2 Effect of particle shape on ballast functions

Particle shape influences not only the physical state of the assembly (grain structure and porosity) but also the particle interaction (interparticle friction, contact force and coordination number). In the past, various attempts have been made to characterise the particle shape of railway ballast. However, due to the complexity and irregularity of the shape of particle, universally accepted effective parameters on shape characteristic have not been established so far. In the railway industry, various shape characteristics (i.e. flakiness, elongation, sphericity, angularity and surface texture) are used.

Flakiness or flatness

A flat particle is defined as one in which the ratio of thickness to width of its circumscribing rectangular prism is less than a specified value. This ratio is called the flakiness ratio of a particle P and can be expressed as:

$$P = a/b \quad (0 < P \leq 1.0), \quad (2.1)$$

Where a = thickness of the particle, b = width of the particle.

After having conducted a set of triaxial ballast tests to investigate the ballast shape on ballast performance, Roner (1985) found that randomly placed flaky material had a higher mobilised friction angle than did nonflaky material at the same void ratio. However, when the flaky particles became oriented, their behaviour was highly anisotropic. When they are oriented at the angle of the shear plane they had significantly

lower deviator stress and angle of internal friction than nonflaky particles. When the flaky particles were oriented perpendicular to the direction of applied stress, they had a much higher deviator stress and angle of internal friction than nonflaky materials.

Similarly, Selig and Waters (1994) concluded that any quantity of flaky particles, either randomly oriented or oriented other than generally parallel to the failure plane, increases the shear strength of the granular specimen. Orientation parallel to the failure plane, when a significant proportion of the particles are flaky, will cause a substantial strength reduction. The disadvantage of increased flakiness appears to be increased abrasion, increased breakage, increased permanent strain accumulation under repeated load, and decreased stiffness.

From the ballast maintenance point of view, increasing the percentage of the flaky particles could increase the ballast degradation rate and the degree of fouling and thus will increase the ballast maintenance work. Furthermore, better particle interlocking due to the existence of a substantial portion of flaky particles in a ballast sample will make the ballast maintenance work more difficult. So, it is reasonable to assume that the ballast maintenance work increases with the percentage of the flaky particles in a ballast (Han, 1998).

Angularity or roundness

Angularity, or its inverse, roundness, is a measure of the sharpness of the edges and corners of an individual particle. A widely accepted definition for roundness by Pettijohn (1957) defines the roundness as the ratio of the average radius of curvature of the corners and edges of a particle to the radius of the maximum inscribed circle. According to this definition, roundness ρ can be expressed as follows:

$$\rho = \frac{1}{N} \sum_{i=1}^N \left(\frac{r_i}{R} \right) \quad (2.2)$$

where r_i = individual corner radius,

R = radius of circle inscribed about the particle, and

N = number of corners on the particle.

Holubec and Appolonia (1973) concluded that a crushed stone with angular particles has greater elastic and permanent deformations under repetitive loading conditions than does a gravel composed of rounded particles. Previous researches (Thom and Brown, 1988 and 1989) shows that increased particle angularity increased the shear strength. However, particle breakage increases and specimen stiffness decreases as well. At the same compactive effort a more angular material will tend to form a higher voids ratio which will result in less strength increase than at the same void ratio (Selig and Waters, 1994).

Ballast fouling capacity and drainage ability mainly depend on the ballast voids ratio. Because an angular ballast can produce better particle interlocking, it generally has looser initial and final particle skeletons than a rounded ballast, Therefore, an angular ballast usually has a relatively larger voids ratio than does a rounded ballast, which means that an angular ballast has a better ballast fouling resistance capacity and drainage ability. However, from the ballast maintenance point of view, angular ballast may need more ballast maintenance work because it is easily degraded and deformed under the repeated loading of trains. Moreover, better particle interlocking could make the ballast maintenance more difficult.

Surface texture

Surface texture is believed to have an important effect on ballast performance. A rough particle surface is critical to form a high inter-particle friction force, which will increase the shear strength of the ballast and the track stability. On the contrary, a smooth surface will create a low inter-particle friction force which will result in an easy rearrangement of particles and cause more ballast-related track deformation. To quantify the ballast particle surface texture, a visual estimate of particle surface roughness is recommended (Han, 1998). Particle surface roughness is divided into four group categories in the visual method. They are rough, medium rough, medium smooth and smooth. For the visual estimate of the particle surface roughness of a ballast sample, an index called the sample average roughness index I_{rough} is used. The sample average roughness index is defined using the weighted average of the group roughness as follows:

$$I_{\text{rough}} = \frac{\sum(W_i I_{ai})}{W_t} \quad (2.3)$$

where W_t = total dry weight of the ballast sample,

W_i = total dry weight of group i the ballast sample, and

I_{ai} = visually estimated roughness for group i .

The recommended values of the average roughness index (I_{rough}) are 1.0, 0.75, 0.5 and 0.25 to represent rough, medium rough, medium smooth and smooth ballast groups, respectively (Han, 1998).

2.3.3 Effect of gradation

The selection of the particle size distribution of ballast layer has a great effect on both in-situ performance and the economic evaluation of track design. It is widely accepted that a narrow gradation would best meet the requirements for railway ballast. Sufficient voids are formed within the railway ballast with a narrow gradation and, therefore, it provides efficient drainage of water from the ballast trackbed.

Based on a literature review, Han (1998) concluded that (1) broadening a ballast gradation generally increases the ballast shear strength, (2) ballast shear strength not only depends on the value of coefficient of uniformity (C_u), but also depends on the ballast mean size (D_{50}), and (3) increasing the ballast mean size (D_{50}) generally increases the ballast shear strength. Roenfeld (1980) conducted repeated load triaxial tests on limestone ballast with different gradings. He found that the cumulative plastic strain for the uniform ballast ($C_u=1.14$) was almost double that for the more broadly-graded ballast ($C_u=4.1$). Also, the particle degradation for the uniform ballast was four to five times greater than for the more broadly-graded ballast.

According to railroad field experience a narrowly-graded and medium-sized ballast is preferred for facilitating the ballast maintenance because these kinds of ballast are easily handled by the ballast maintenance machines, easily cleaned when they are fouled, and easily used for adjusting the track geometry. The relation between the ballast gradation and the ballast functions of drainage depends on the voids in the ballast. From this point of view, a large size and narrowly-graded ballast is preferred.

2.4 Mechanical behaviour of ballast under repeated loading

2.4.1 Resilient behaviour

Understanding of the behaviour of granular material under loading plays a very important role in the modern railway system. Basically, the deformation response of granular material under repeated loading consists of residual (permanent) deformation and recoverable (resilient) deformation which will be introduced in this section. As shown in Figure 2.6, the difference between the maximum strain under peak load and the permanent deformation after loading for each cycle is defined as the resilient strain.

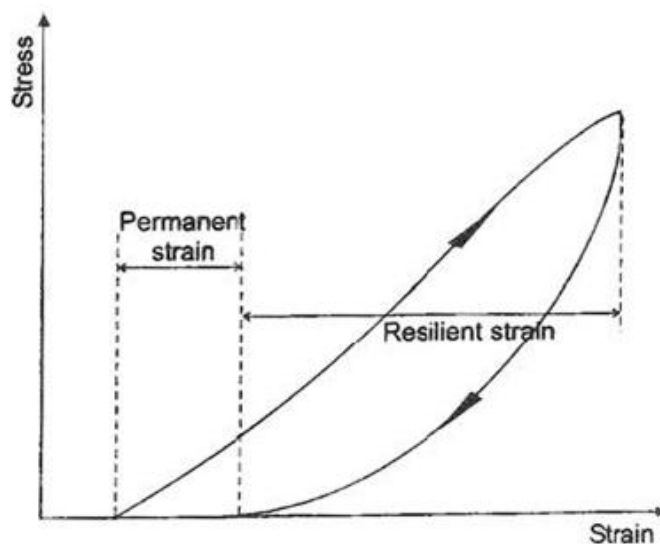


Figure 2.6 Strains in granular materials during one cycle of load application (Lekarp et al., 2000a)

The resilient behaviour of granular material is characterized by the resilient modulus (M_r) and Poisson's ratio (ν) defined in Equation 2.4 and 2.5. Seed et al. (1962) defined the resilient modulus as the repeated deviator stress by the resilient axial strain after unloading in triaxial test.

$$M_r = \frac{\Delta(\sigma_1 - \sigma_3)}{\varepsilon_{1,r}} \quad (2.4)$$

$$\nu = -\frac{\varepsilon_{3,r}}{\varepsilon_{1,r}} \quad (2.5)$$

where: σ_1 = Major principle stress (axial stress)

σ_3 = Minor principle stress (horizontal stress)

$\varepsilon_{1,r}$ = Resilient axial strain

$\varepsilon_{3,r}$ = Resilient horizontal strain

Figure 2.7 plots the axial strain response to the deviator stress applied in a triaxial cyclic test, with an initial loading path followed by a series of unload-reload loops. The resilient strain decreases as the number of unload-reload loop applications increases. In brief, the resilient modulus increases gradually at the beginning, and ultimately comes to an approximately constant value after a certain number of load cycles. Both resilient and plastic behaviour of granular material under cyclic loading are normally studied using cyclic triaxial testing. According to Lekarp et al. (2000a) and Kwan (2006), the main factors that affect the resilient response of ballast are now presented.

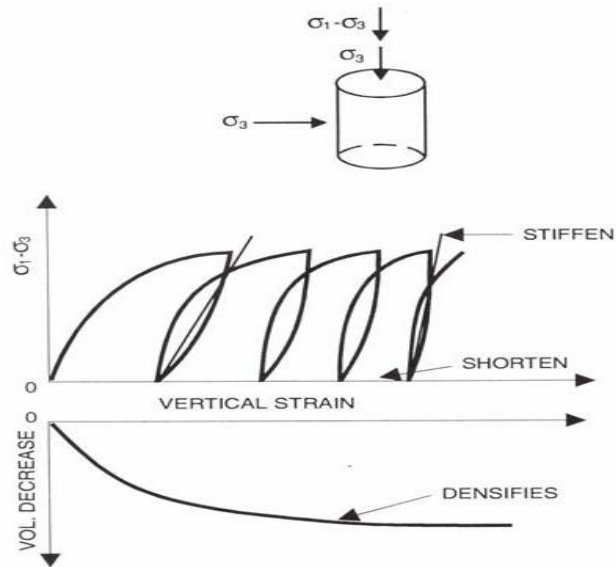


Figure 2.7 Ballast behaviour in the cyclic triaxial test (Selig and Waters, 1994)

Effect of stress level

Lekarp et al. (2000a) summarised that the resilient response of granular material is influenced mostly by stress level. Lackenby et al. (2007) conducted a series of triaxial tests on ballast and indicated that the resilient modulus increased with increasing confining pressure, as shown in Figure 2.8.

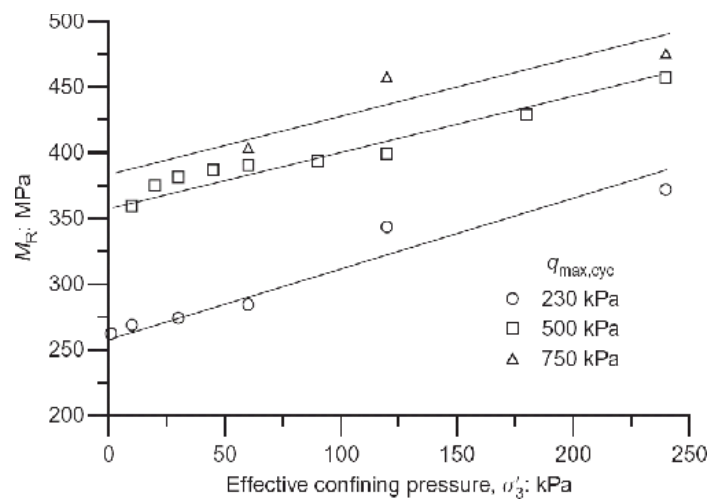


Figure 2.8 Resilient modulus M_R response under various stress states after 500,000 cycles (Lackenby et al., 2007).

Effect of initial density

Hicks and Monismith (1971) and Kolisoja (1997) found that the resilient modulus increased with increasing density. This might be because an increase in density results in an increase in the co-ordination number (the average number of contacts per particle) and a decrease in the average contact stress between particles. This then leads to a decrease in the total deformation and, hence, an increase in resilient modulus. Moreover, Hicks and Monismith (1971) concluded from their experiments that the effect of density was more significant in partially crushed gravel than crushed rock. The resilient modulus was found to increase with relatively density in partially crushed gravel. The effect of the density on the resilient modulus in fully crushed rock was negligible. This is probably because the partially crushed gravel is less angular than the crushed rock (Aursudkij, 2007). For railway ballast, Shenton (1974) indicated that the porosity has little influence on the resilient modulus. Thom and Brown (1988), and O'Reilly and Brown (1991) also reported similar observations in their studies. Unlike the behaviour of granular materials under monotonic loading where density plays an important role, it can be seen from the above findings that the effect of density on the resilient properties of granular material is still unclear. This agrees with the conclusion from Lekarp et al. (2000a). For ballast material, the data suggests that density does not affect the resilient modulus.

Effect of frequency and number of cycles

It is generally agreed that the impact of frequency and load duration on the resilient behaviour of granular materials is not significant (e.g. Seed et al., 1965; Morgan, 1966; Hicks, 1970; Boyce et al., 1976; Thom and Brown, 1988). Suiker et al. (2005) and Lackenby et al. (2007) conducted cyclic triaxial tests on ballast and showed that the application of cyclic loading can lead to a considerable increase in material stiffness. The resilient modulus generally increases gradually with the number of repeated load applications as the material stiffens (Moore et al., 1970 and Lackenby et al., 2007). Figure 2.9 shows the effect of the number of cycles on the resilient modulus. Researchers (Hicks, 1970; Shenton, 1974 and Alva-Hurtado, 1980) found that, after a certain number of repeated load applications, the material behaves in an almost purely resilient manner and the resilient modulus eventually comes to an approximately constant value.

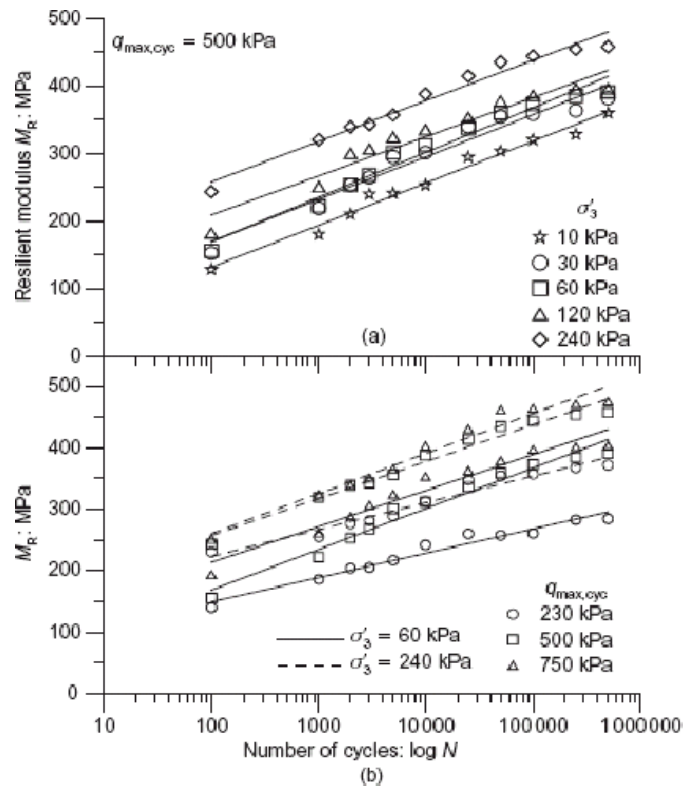


Figure 2.9 Resilient modulus M_R response under various stress states: (a) effect of confining pressure σ'_3 and number of cycles N on M_R for $q_{\max, \text{cyc}} = 500$ kPa and (b) effect of $q_{\max, \text{cyc}}$ on M_R for $\sigma'_3 = 60$ and 240 kPa (Lackenby et al., 2007).

Effect of particle characteristics

Researchers (Janardhanam and Desai, 1983; Thom and Brown, 1989; Thompson, 1989; O'Reilly and Brown, 1991; and Lekarp et al., 2000a) showed that the resilient behaviour of ballast is, to some degree, affected by the particle shape, particle size, particle strength and the gradation. Many studies (Hicks, 1970; Hicks and Monismith, 1971; Allen, 1973; Allen and Thompson, 1974; Thom, 1988; Thom and Brown, 1989) have reported that crushed aggregates which have angular to subangular shaped particles give a higher resilient modulus than uncrushed gravel with subrounded or rounded particles. A rough particle surface is also said to result in a higher resilient modulus. Thom and Brown (1988 and 1989) reported that for granular materials the resilient modulus increased with increasing particle surface friction angle (the surface friction coefficient between a particle of approximately 20 mm and concrete

surface). Kolisoja (1997) showed that the magnitude of the resilient modulus increased linearly with the equivalent or average particle size D_{ekv} .

2.4.2 Plastic behaviour

The irrecoverable strain of granular material as shown in Figure 2.6 is often a trigger for tamping maintenance on a rail track. In general, particle breakage and rearrangement are regarded as the main contributors of the accumulation of such permanent strain. Moreover, a weaker stone will result in more permanent deformation even if all other properties (shape, roughness) remain the same. In addition, although the effect of stone stiffness is small, the larger the elastic deformation at particle contacts, the easier slip becomes. This causes the acceleration of irrecoverable strain. Factors affecting the permanent strain response of granular materials are now presented.

Effect of stress level

Stress level is one of the most important factors that affect the amount of permanent deformation of granular materials. Brown and Hyde (1975) concluded that the permanent strain was directly proportional to the ratio of deviatoric stress q to confining stress σ_3 . Lackenby et al. (2007) reached a similar conclusion by conducting a series of cyclic triaxial tests on ballast under various loading conditions. They found that permanent axial strain decreased with decreasing maximum deviator stress and increasing confining pressure. Figure 2.10 shows the permanent axial strain and permanent volumetric strain response as a function of number of cycles and confining pressure.

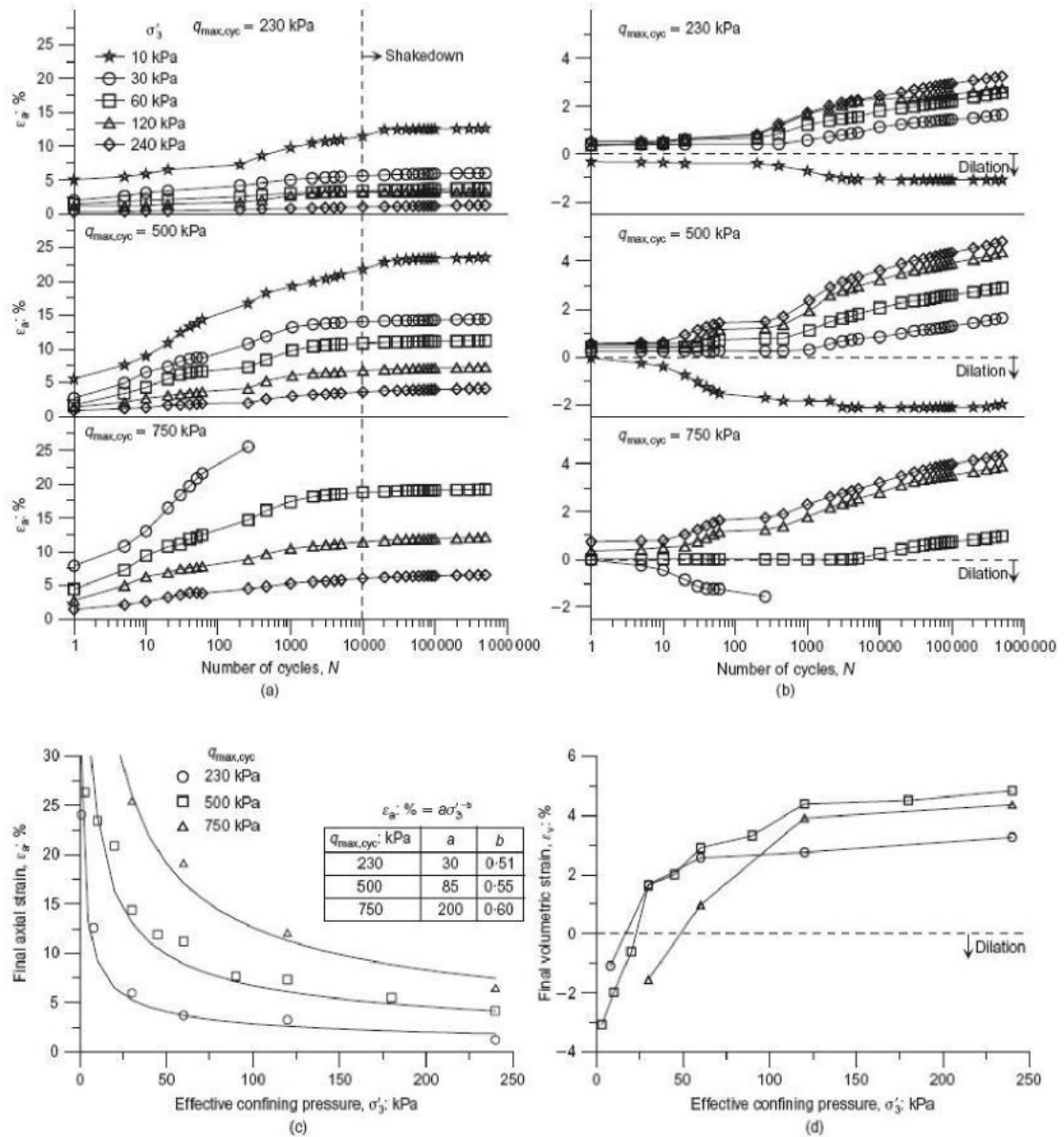


Figure 2.10 Strain response under cyclic loading: (a) axial strain ϵ_a as a function of the number of cycles N ; (b) volumetric strain ϵ_v as a function of N ; (c) final ϵ_a after 500,000 cycles and (d) final ϵ_v after 500,000 cycles (Lackenby et al., 2007).

Effect of initial density

The effect of initial density state on permanent strain accumulation is shown in Figure 2.11. Knuston (1976) indicated that in triaxial test, a lower initial density of the specimen will lead to a larger permanent strain.

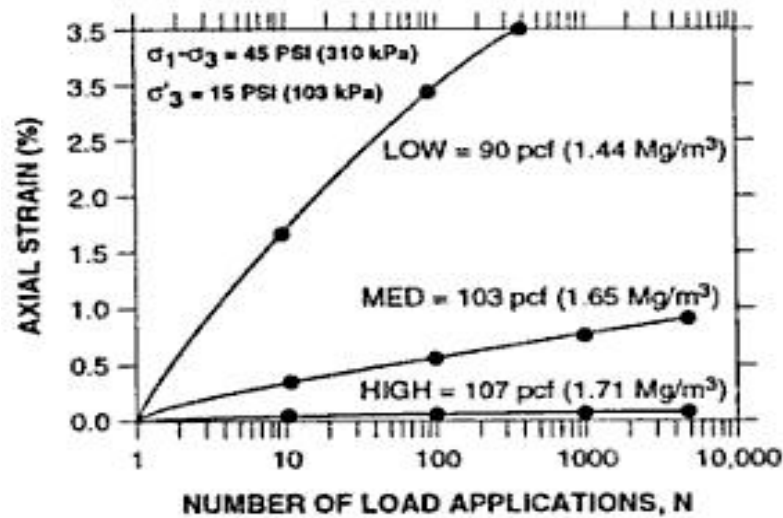


Figure 2.11 Effect of density on permanent deformation response of ballast (Knutson, 1976)

Effect of frequency, number of cycles and sequence of loading

Shenton (1974) investigated the influence of loading frequency on the accumulation of permanent strain in ballast and showed that the loading frequency did not affect the accumulation of permanent strain. Figure 2.12 shows a plot of normalised axial strain after 104 cycles against frequency for the same value of deviator and confining stress (Shenton, 1974). Recently, Eisenmann et al. (1994) demonstrated that only the higher range of frequencies specific to high-speed lines (speed > 225 km/h) would affect the settlement of ballast. Thus, in general, the response approximately is frequency independent, except that higher frequencies may cause a dynamic increment to be superimposed on the "static" load.

For railway ballast under typical wheel loads, it is widely agreed that permanent deformation is generally proportional to the logarithm of the number of loading cycles, as shown in Figure 2.13. The rate of accumulation of permanent strain has generally been found to decrease with increasing number of cycles (Morgan, 1966; Shenton, 1974 and McDowell et al., 2005). However, Lekarp (1997) and Lekarp and Dawson (1998) indicated that for low applied stress, granular material has a limiting permanent strain, while, for high applied stress, the rate of accumulation of

permanent strain will continue to increase with increasing number of cycles (i.e. the structure collapse).

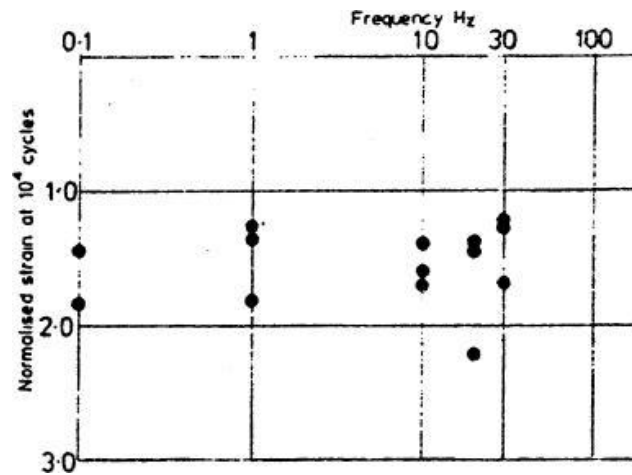


Figure 2.12 Effect of loading frequency (Shenton, 1974).

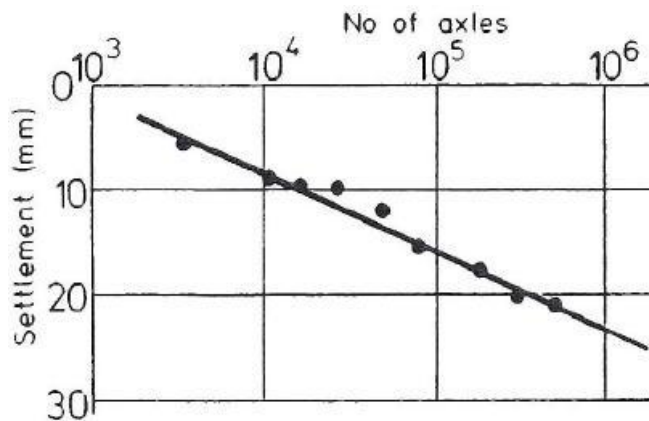


Figure 2.13 Permanent deformation as a linear function of logarithm of number of load cycles (Shenton, 1974).

The effect of the sequence of loading has been investigated by Stewart and Selig (1984) and Selig and Waters (1994). Their results showed that the sequence of loading did not affect the accumulation of permanent strain. Figure 2.14 shows typical results for strain accumulation under different loading sequences. In these experimental tests different magnitudes of deviator stress were used and the deviator stress was changed after every 1000 load applications. Clearly the final permanent strains for all the different loading sequences are approximately equal.

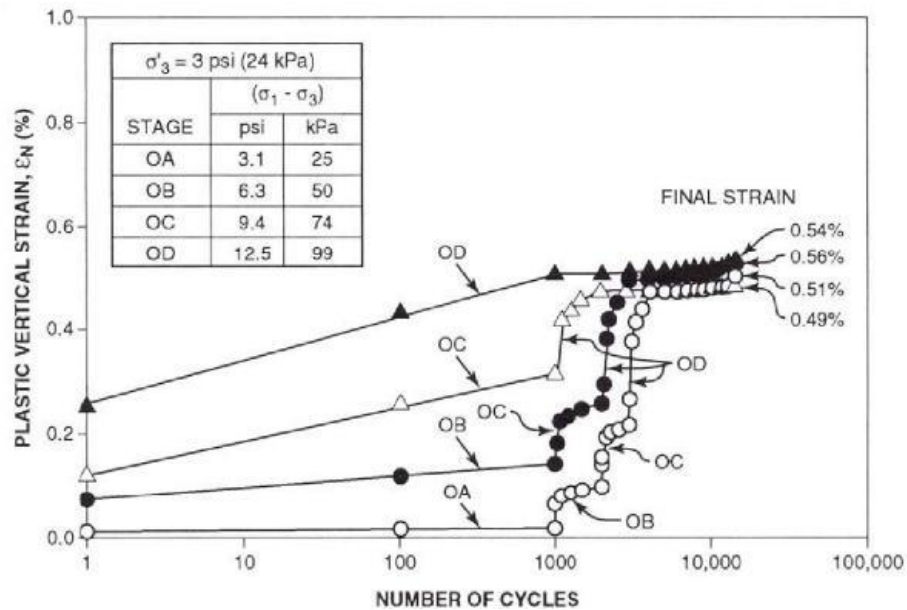


Figure 2.14 Effect of difference in sequence of loading on permanent strain (Selig and Waters, 1994).

2.5 Geogrid reinforcement

The application of geogrids to prevent the track deterioration has grown rapidly in the last few decades. The track deterioration is different from global failure of structures like landslides, because it is an accumulation of plastic deformations either in the ballast layer or in the subgrade layer. The deterioration especially in soft subgrade layer has serious influence on the safety and efficiency (speed restriction) of train operations. Many expensive, disruptive and frequent repair operations are often required to maintain the ballast characteristics due to the problem of settlement. Because of this, the use of geogrids has proved to be a simple and economical method of reinforcing track ballast. It provides an extremely cost-effective solution for the reinforcement of ballast over a soft subgrade.

2.5.1 Tensar polymer geogrids

Tensar biaxial geogrids were developed in the 1980s to reinforce unbound and bound materials. They are manufactured through precise extrusion of sheets of

polypropylene. Accurate patterns of punched holes are stretched under controlled temperature conditions. It is termed a biaxial geogrid as it is stretched in two orthogonal directions.

Tensar SS geogrids, shown in Figure 2.15, are mainly used for the reinforcement of soil and aggregates, often in road pavements and foundation reinforcement projects. The SS geogrids are stiff grids with integral junctions and are oriented in two directions with the resulting ribs having a high degree of molecular orientation and hence high strength. As seen, the SS geogrids have an approximately rectangular cross section with sharp corners. Tensar produce a range of SS grids with different strengths and aperture sizes.

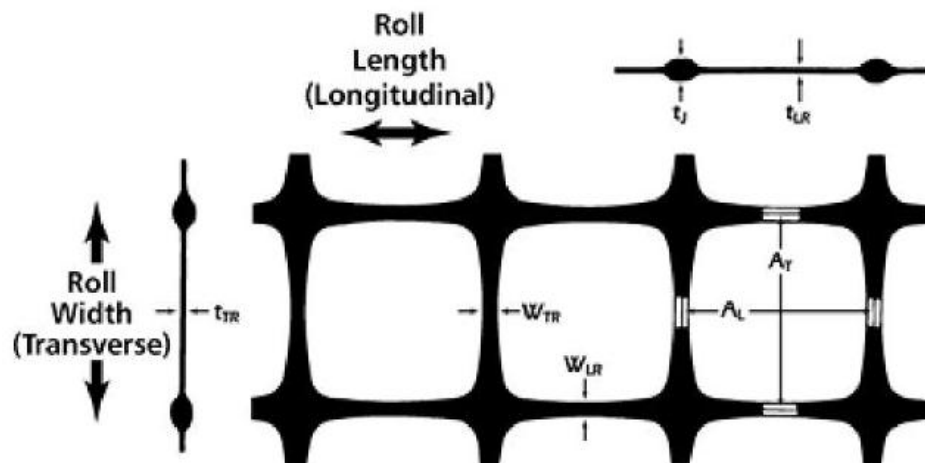


Figure 2.15 Tensar SS geogrid (Tensar, 2010)

In the recent years, Tensar has created a new product achieved by the changing from rectangular to triangular grid aperture. The new products are known as TriAx geogrids as illustrated in Figure 2.16. The TriAx geogrid is produced from an extruded sheet of polypropylene. This is then punched with an array of holes and stretched to create the unique TriAx structure. The design of the junctions providing high junction efficiency, results in a product with high junction strength and stiffness. Rigorous testing has been conducted in line with each of the three directions. In each direction tested, the TriAx geogrid was found to

have high strength junctions and stiff ribs providing effective mechanical interlock of aggregate particles into aperture.

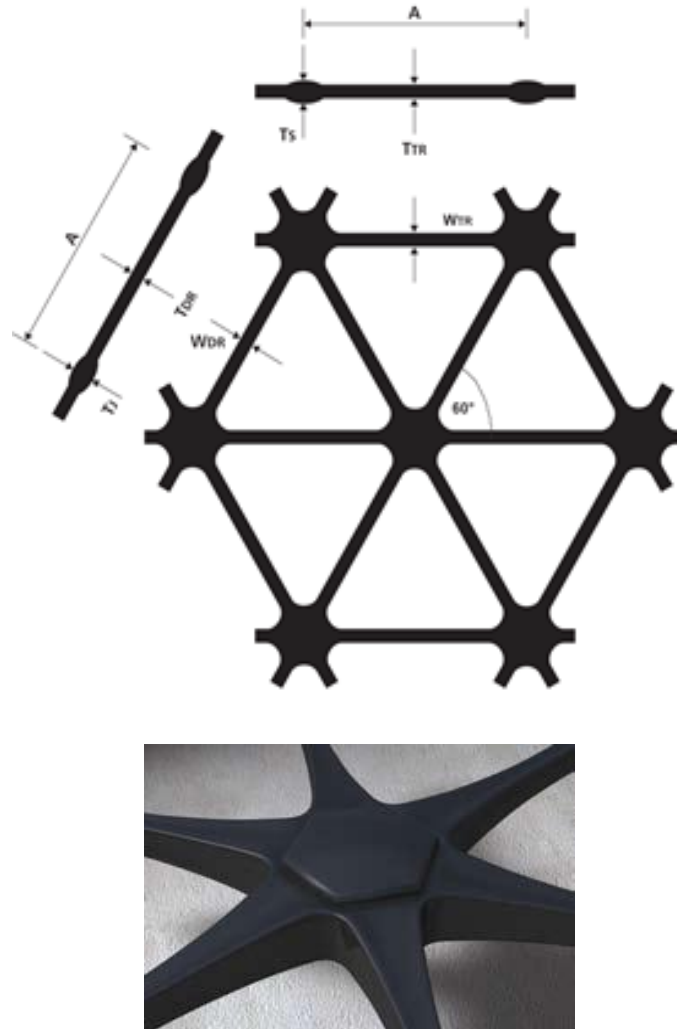


Figure 2.16 Tensar TriAx geogrid (Tensar, 2010)

2.5.2 Reinforcing principle

Selig and Waters (1994) described polymer geogrids as plastic sheets in the form of a grid with aligned long-chain polymer molecules stretched to achieve high stiffness and strength. As Figure 2.17 shows, the tensile strength of geogrid provides confinement to resist granular extension strain and hence the railway trackbed can be reinforced.

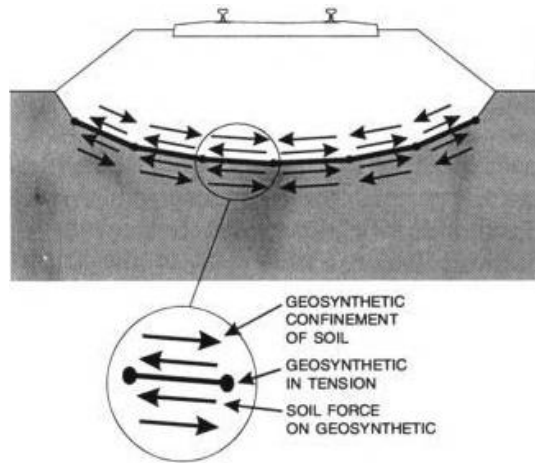


Figure 2.17 Reinforcing effect of geogrid (Selig and Waters, 1994)

It is widely agreed that an appropriate stiffness and an ability to interlock effectively with the material is vital to achieve the reinforcing effect of a polymer geogrid. The geogrid works on the premise that the ballast penetrates the apertures and interlocks with the grid. This interlock leads to a strong horizontal shear resistance and restrains the ballast from lateral movement even when dynamic loading is applied. In practice this means that the settlement rate is reduced. Figure 2.18 shows the interlock mechanism of polymer geogrid.

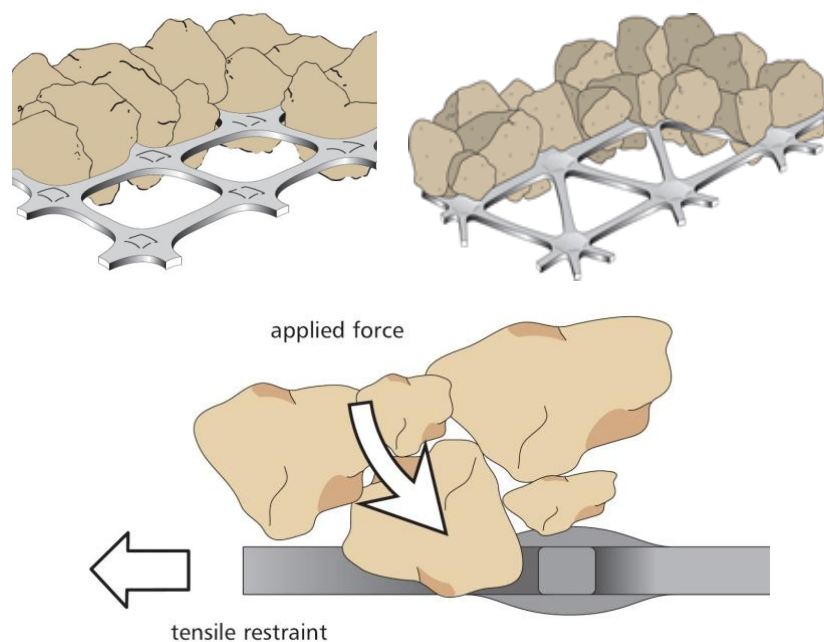


Figure 2.18 Interlock of granular material and geogrid (Tensar, 2010)

An important factor to consider is the placement and installation of the geogrid. If this is not done according to required standards it could lead to rapid initial settlement until adequate interlock is achieved. Generally, there are two major application areas for the use of Tensar geogrids within the track substructure. Geogrid can be used in the ballast layer as shown in Figure 2.19, to reduce the rate of track settlement and hence extend the maintenance cycle frequency with huge whole life cost benefits. Also Figure 2.20 shows geogrid can be used in the sub-ballast layer to increase the bearing capacity especially over soft subgrade, with significant thickness reductions and savings in both the capital and environmental costs (Tensar, 2007).

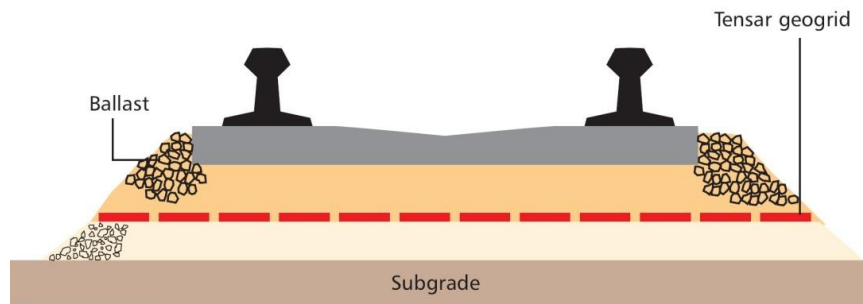


Figure 2.19 Stabilisation of the ballast layer (Tensar International, 2007)

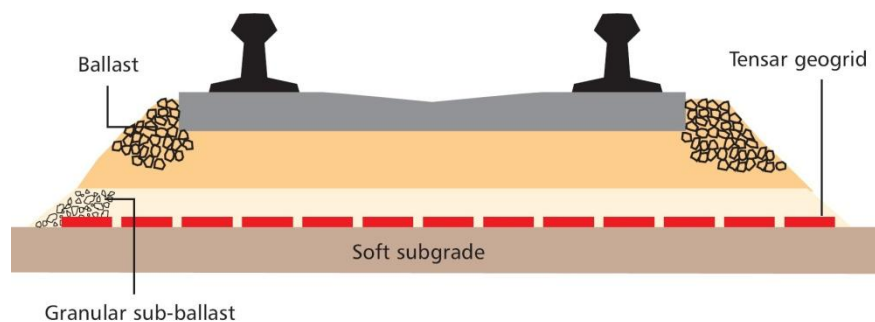


Figure 2.20 Stabilisation of the sub-ballast layer (Tensar International, 2007)

In a mechanically stabilised layer, aggregate particles interlock within the geogrid and are confined within the apertures, creating an enhanced composite material with improved performance characteristics. The structural properties of the mechanically stabilized layer are influenced by the magnitude and depth of the confined zones as

shown in Figure 2.21. The shape and thickness of the geogrid ribs and the overall structure of TriAx have a direct influence on the degree of confinement and efficiency of the stabilised layer.

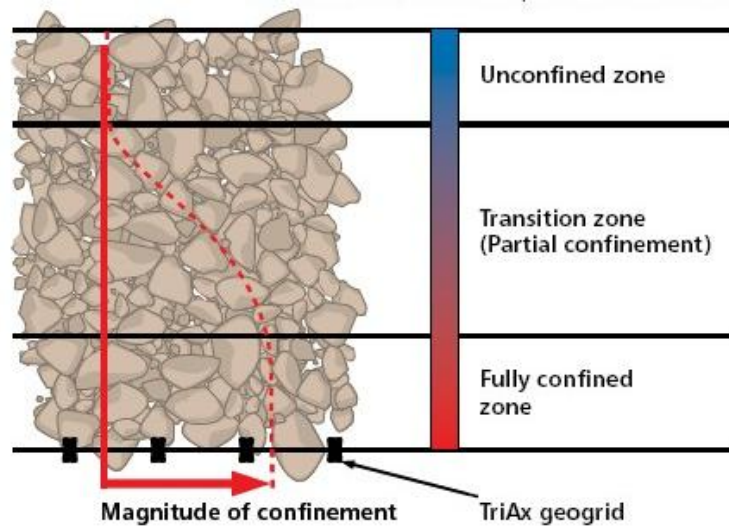


Figure 2.21 Aggregate confinements within a mechanically stabilised layer (Tensor, 2010)

2.5.3 Behaviour of geogrid reinforced granular material

Oxford University (1980) carried out model footing experiments to investigate the benefit of reinforcing a granular layer over soft clay. The test consistently demonstrated a 40% improvement in bearing capacity. It was concluded that the interlocking mechanism of the polymer grid resisted tensile strains preventing lateral movement of particles in the loaded area (Milligan and Love, 1985). Data from the test indicated that the mean angle of load spread increased from 38 degrees in the unreinforced case to more than 50 degrees with a polymer grid. It was concluded that a reinforced granular layer can reduce construction thickness by approximately 50% to achieve a similar stress on the subgrade.

Chan (1990) did a series of full-scale experiments to investigate the influence of geosynthetics on the permanent deformation characteristics of granular bases in a pavement. In his experiments, he considered different types and stiffnesses of

geosynthetics as well as varying placement level in the granular base. He concluded that:

- the permanent deformation resistance of most geosynthetic-reinforced granular bases was improved,
- the improvement level depends largely on the quality and thickness of the granular base as well as the location of the geosynthetic within the base.

For weak granular bases, e.g. low elastic stiffness, such as those constructed of sand and gravel, a significant improvement in permanent deformation resistance was achieved with the introduction of a polymer grid. The effect is most obvious with the grid installed either in the middle or at the bottom of the layer. A stiffer grid also produced better results with the large vertical deformations and high stress which Chan applied to his granular base. In Chan's (1990) account, there is minimal benefit if the geosynthetic is placed too far down in the layer. In his opinion, placing geosynthetics at the middle of a base layer not exceeding 200mm depth, gives an optimum improvement. Chan also noted that geogrid performs better than geotextile in terms of reducing permanent deformation, even where it has a lower stiffness. He attributed this to the interlocking effect of the geogrid.

Raymond (2002) carried out repeated load test on rounded ballast samples and found that settlement was reduced by at least 50% over 10000 cycles with a maximum stress of 40 kPa. McDowell & Stickley (2006) examined the performance of geogrid-reinforced ballast using a box test which simulated train loading. Conclusions of box tests have been performed on each of two ballasts: unreinforced and reinforced, with the use of geogrids. It appears that for much more crushable ballast, the use of a geogrid gives a minor improvement in performance. For ballast of much better quality, the improvement is much more marked. They also found that the grid with aperture size 65mm performed much better than with a 39mm aperture size and an increase in thickness of the grid also improved the performance slightly for the large aperture size. The use of a geogrid marginally increased the stiffness and had a marginal effect on particle breakage, but reduced permanent settlement significantly. In addition, it was found that in the box tests, the ballast only needed to be tamped

half as much as compared to when a geogrid had been installed at an appropriate position. McDowell et al. (2006) developed a discrete element model for geogrid-reinforced ballast and investigated the influence of the ratio of the geogrid aperture size to particle diameter. They found that a ratio of 1.4 gave the optimum performance in terms of smallest settlement.

Brown et al. (2006) used the Nottingham Railway Test facility (RTF) to investigate the performance of geogrid reinforced ballast. As shown in Figure 2.22, when the ballast was reinforced with a 30-65 polymer geogrid, an increase in the time between maintenance operations of a factor of about 2.5 was possible. According to the work of Brown et al. (2007), they concluded that the application of appropriate geogrid reinforcement significantly reduced the rate of settlement and the required maintenance frequency. In agreement with McDowell & Stickley (2006) they also came to the conclusion that the ratio of geogrid aperture to ballast particle size was influential. Besides, Brown et al. (2007) had drawn other conclusions that the geogrid stiffness, rib shape, subgrade strength and level of overburden pressure all influence the ballast settlement.

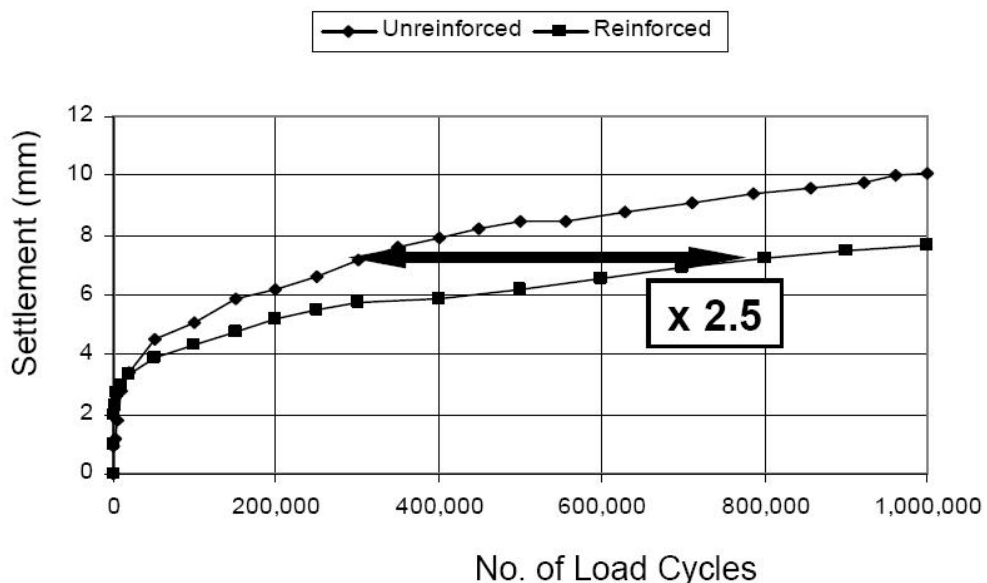


Figure 2.22 Relative performance of reinforced (30-65 polymeric geogrid) and unreinforced ballasted track (Brown et al., 2006)

2.6 Pull-out mechanism

Previous studies have reported that the total pull-out resistance depends on the geogrid geometry, particle size distribution, and particle density. Specifically, Jewell (1990) reported that the geogrid pull-out failure mechanism is a function of the ratio of transverse rib spacing (S) and the average particle size (d_{50}), the compaction moisture content and the soil stiffness.

Wilson-Fahmy et al. (1994) carried out a series of pull-out tests on one stiff and two flexible commercially available geogrids in dense sand. Their results showed that failure is usually by sheet pull-out or tension failure. They recommended that since a great portion of the pull-out force may be transmitted by the transverse ribs to the junctions, some geogrids are susceptible to junction failure during tests of short duration. Hence, the long term resistance of junctions should be considered in determining the anchorage capacity of the geogrid. Factors such as the extensibility of longitudinal and transverse ribs and the flexural rigidity of transverse ribs are shown to influence the load distribution in the geogrid structure.

Bergado et al. (1987) investigated the interaction between soil and geogrids by using both direct shear and pull-out tests, and applied the results to a case study. A polymer geogrid was used with clayey sand. They concluded that the pull-out resistance of the geogrid using cohesive backfill consists of adhesion between the soil and the reinforcement on the solid surface area (plan area) of the geogrid, as well as the bearing pressure of the soil in front of all transverse members which behaved as a strip footing embedded in the soil.

Palmeira and Milligan (1989) attempted to investigate the influence of boundary conditions on pull-out test results. They found that the internal friction angle between the soil and reinforcement could be severely overestimated because of friction on the internal front wall of the box in small scale tests. They recommended lubricating the front face and increasing the scale of the tests as well as taking into account the friction due to the wall in friction coefficient calculation.

Forsman and Slunga (1994) carried out large pull-out tests using different length geotextiles and geogrid specimens with sand, crushed rock and light expanded clay aggregate (LECA). From the test results they concluded that the average shear resistance decreases when the length of a specimen increases in a pull-out test. The reason is the process of progressive failure along the extensible reinforcement length. Furthermore, the effect of the rigid front wall and sleeve also decreased when the length of the specimen increased. The results showed that the properties of reinforcement like the modulus of deformation, the strength of the reinforcement, the strength of the junctions in the grid and the rigidity of the transverse bearing members all affect the relationship between pull-out displacement (actual displacement of the grid) and the clamp displacement.

Oostveen et al. (1994) conducted a series of large pull-out tests on steel and extensible geogrid with cohesionless soil. The results showed that the shear stress distribution along a geogrid is influenced by the proximity of the front wall, which is in agreement with the finding of Palmeira and Milligan (1989), so that even though they used a large pull-out inclusion, for more extensible inclusions, the elongation of the inclusion during the pull-out tests resulted in a non-uniform shear stress distribution along the surface of the geogrid.

Theoretically it has been accepted now that the resistance of a geogrid to pull-out is provided by three components, namely, the frictional resistance of the longitudinal and transverse ribs and the bearing resistance of the transverse ribs (Koerner et al. 1989), see Figure 2.23. The ultimate pull-out resistance, F , can be obtained as follows (Jewell et al. 1984; Koerner et al. 1989):

$$F = F_1 + F_2 + F_3 = 2 * (A_l + A_t) * \sigma_n * \tan\delta + A_b * \sigma_n * N_q \quad (2.6)$$

where, F_1 = ultimate frictional resistance of all longitudinal ribs,

F_2 = ultimate frictional resistance of all transverse ribs,

F_3 = ultimate bearing resistance of all transverse ribs,

A_l = area covered by longitudinal ribs,

A_t = area covered by transverse ribs,

A_b = bearing area of transverse ribs,

σ_n = normal stress,

N_q = bearing capacity factor,

δ = interface angle of friction (i.e., between soil and geogrid) that can be obtained from large shear box test results.

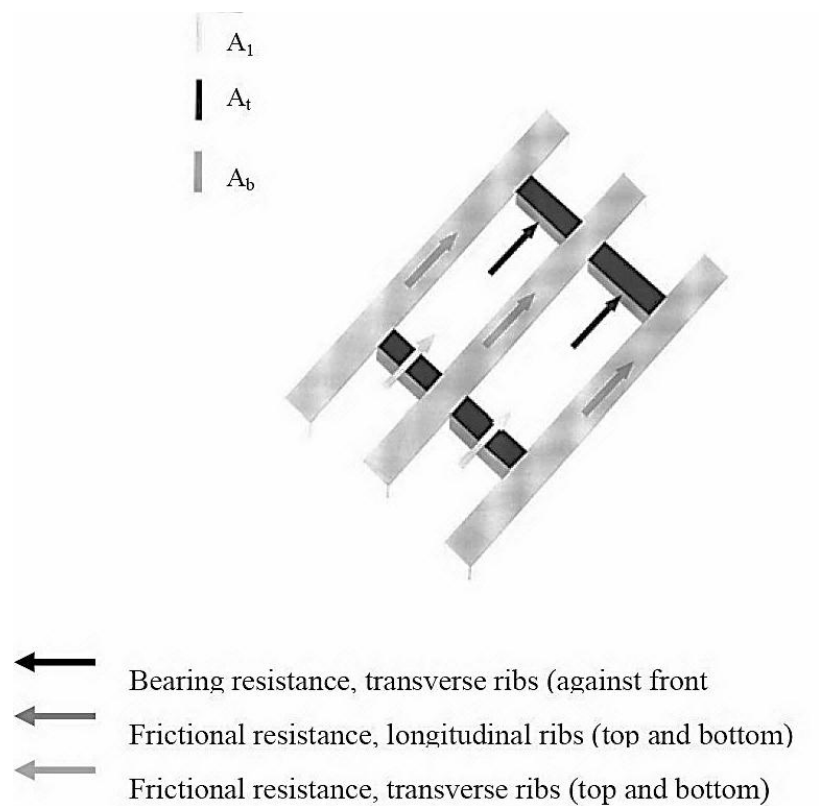


Figure 2.23 Components of pull-out force (Moghadas and Small, 2005)

2.7 Summary

The literature review presented in this chapter has described the structure of the conventional ballasted track and the loads applied to it. The ballast specifications and the effect of particle shape on ballast functions have been discussed. Under repeated

loading, the resilient and permanent behaviour of ballast are mainly affected by the confining pressure and the applied cyclic loading.

The reinforcing principles of a polymer geogrid, the behaviour of geogrid reinforcement under loading and the pull-out mechanism have been summarised. However, the fundamental characteristics of grid/aggregate interaction have not been researched at a detailed level. The understanding of how geogrid reinforcement can be designed into rail track structures for different situations is still limited. The remainder of this thesis presents the large box pull-out test simulation, box test simulation, CET simulation as well as the laboratory validation large box pull-out test to investigate the interlock mechanism between geogrids and ballast and therefore gain insight into how geogrid-ballast systems can be designed to optimise performance.

Chapter 3 Discrete element method (DEM)

3.1 Introduction

The discrete element method is a numerical model capable of describing the mechanical behaviour of assemblies of discs and spheres (Cundall and Strack, 1979). It provides a way of investigating the mechanical behaviour of granular materials both microscopically and macroscopically. Compared to laboratory tests, the discrete element method has the advantage that an identical sample can be reused for different loading conditions. Furthermore, it enables the investigation of some features which cannot be measured in laboratory tests, such as: interparticle friction, movement of particles and distribution of contact forces. Hence, the material properties and the effect of loading condition can be investigated without any influence from the initial sample preparation method.

This chapter generally presents a basic knowledge of DEM and PFC^{3D} and a review of the application of DEM in granular material. Section 3.2 presents the computer code PFC^{3D} and the conceptual model of discrete element method. The basic calculation procedure in PFC^{3D} is also described in sub-section 3.2.3. It is then followed by the description of bonding models in Section 3.3 and clump logic in Section 3.4, respectively. Finally, recent applications of DEM in modelling railway ballast and Polymer geogrid are reviewed in Sections 3.5 and 3.6, respectively.

3.2 Discrete element modelling using PFC^{3D}

3.2.1 The PFC^{3D} particle-Flow Model

A general particle flow model simulates the mechanical behaviour of a system comprised of a collection of arbitrarily-shaped particles. The model is composed of distinct particles which displace independently from one another and interact only at contacts or interfaces between the particles. Newton's laws of motion provide the fundamental relationship between particle motion and the forces causing that motion. The particles allowing to be bonded together at their contact points can model more complex behaviour. When the inter particle forces (i.e. tensile, shear or moment) acting on any bond exceeds the bond strength, that bond is broken. This allows tensile forces to develop between particles. In addition, the formation of cracks that may cause blocks to fragment into smaller blocks can model the interaction of these bonded "blocks".

PFC^{3D} provides a particle-flow model under the following assumptions:

1. The spherical particles are treated as rigid bodies.
2. The contacts occur over a vanishingly small area (i.e. at a point).
3. The behaviour of the contacts is characterized using a soft contact approach wherein the rigid particles are allowed to overlap one another at contact points.
4. The magnitude of the overlap is related to the contact force via the force displacement law, and all overlaps are small in relation to particle sizes.
5. Bonds can exist at contacts between particles.
6. All particles are spherical; however, the clump logic supports the creation of super-particles of arbitrary shape. Each clump consists of a set of overlapping spheres, and acts as a rigid body with a deformable boundary.

PFC^{3D} is suitable for modelling the stress-strain response of a granular assembly. The deformation of a granular assembly such as sand and rock as a whole is described

well by this assumption, since the deformation results primarily from the sliding and rotation of the rigid particles and the interlocking at particle interfaces and not from individual particle deformation.

The PFC^{3D} particle-flow model includes “balls” and “walls”. Walls allow the application of velocity boundary conditions to assemblies of balls for purposes of compaction and confinement. The balls and walls interact with one another via the forces that arise at contacts. However, contacts may not exist between two walls; thus, contacts are either ball-ball or ball-wall.

3.2.2 Distinct-Element Method

PFC^{3D} models the movement and interaction of stressed assemblies of rigid spherical particles using the distinct element method (DEM). The DEM was introduced by Cundall (1971) for the analysis of rock mechanics problems and then applied to soils by Cundall and Strack (1979). According to the definition in the review of Cundall and Hart (1992), PFC^{3D} is regarded as a discrete element code even though it allows finite displacements and rotations of discrete bodies, including complete detachment, and recognizes new contacts automatically as the calculation progresses.

In the DEM, the equilibrium contact forces and displacements of a stressed assembly of particles are found by tracing the movements of the individual particles. These movements are the result of the propagation through the particle system of disturbances caused by specified wall and particle motion and/or body forces: a dynamic process. The speed of propagation depends on the physical properties of the discrete system.

The above dynamic behaviour is described numerically by a timestepping algorithm in which it is assumed that the velocities and accelerations are constant within each timestep. The DEM is based on the idea that the time step chosen may be so small that, during a single time step, disturbances cannot propagate from any particle further than its immediate neighbours. Then, at all times the resultant forces on any

particle are determined exclusively by its interaction with the particles with which it is in contact. This is the key feature of the DEM which makes it possible to simulate the non-linear interaction of a large number of particles without excessive memory requirements or the need for an iterative procedure.

3.2.3 Calculation Cycle

The calculations performed in PFC^{3D} are via a timestepping algorithm that requires the repeated application of Newton's second law to each particle, a force-displacement law to each contact, and constant updating of wall positions. The calculation cycle is illustrated in Figure 3.1. The law of motion is applied to each particle to update its velocity and position based on the resultant force and moment resulting from the forces acting on it. The force-displacement law applied to each contact to update the contact forces is based on the relative motion between the two entities at the contact and the contact constitutive model. Also, the wall positions are updated based on the specified wall velocities. The force-displacement law and the law of motion are described in the following subsections.

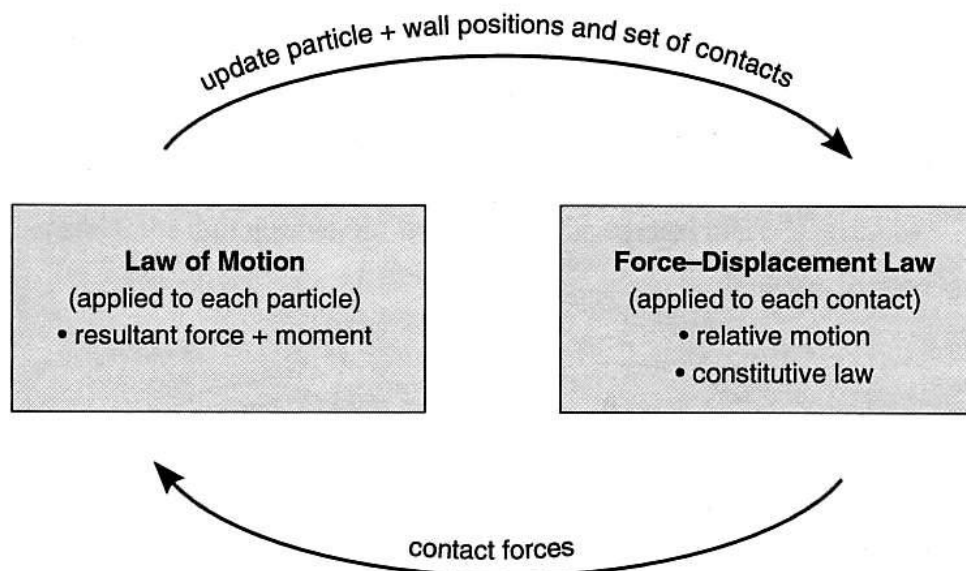


Figure 3.1 Calculation cycle use in PFC^{3D} (Itasca, 1999)

Force-Displacement Law

The force-displacement law will be presented for the cases of ball-ball contact and ball-wall contact. As mentioned before, it is applied at the start of each cycle to contacts to obtain new contact forces. The contact force vector F_i can be resolved into normal and shear components with respect to the contact plane as

$$F_i = F_i^n + F_i^s \quad (3.1)$$

where F_i^n and F_i^s denote normal and shear components respectively.

The force-displacement law relates these two components of force to the corresponding components of the relative displacement via the normal and shear stiffnesses (k_n, k_s) at the contact. The normal contact force vector is calculated by:

$$F_i^n = K^n U^n n_i \quad (3.2)$$

where K^n is the normal stiffness, U^n is the overlapping of the two entities and n_i is the unit normal vector. For ball-to-ball contact, the normal vector is directed along the line between ball centres. For ball-to-wall contact, normal vector is directed along the line defining the shortest distance between the ball centre and the wall.

The shear contact force is computed in an incremental fashion. When the contact is formed, the total shear contact force is initialized to zero. Each subsequent relative shear displacement increment results in an increment of elastic shear force that is added to the current value. The shear elastic force-increment vector is calculated by

$$\Delta F_i^s = -K^s V_i^s \Delta t \quad (3.3)$$

where K^S is the shear stiffness [force/displacement] at the contact and V_i^S is the shear component of the contact velocity and Δt is the timestep. Finally, the new shear contact force is calculated by summing the old shear force vector existing at the start of the timestep with the shear elastic force-increment vector

$$F_i^S = \{F_i^S\}^{[old]} + \Delta F_i^S \quad (3.4)$$

Law of Motion

The motion of a rigid particle is determined by the resultant force and moment vectors acting upon it. The equations of motion can be expressed as two vector equations. One of which relates the resultant force to the translational motion and the other relates the resultant moment to the rotational motion. The equation for translational motion can be written in the vector form

$$F_i = m(\ddot{x}_i - g_i) \quad (3.5)$$

where F_i = Sum of all externally applied forces acting on the particle

m = Total mass of the particle

\ddot{x}_i = Acceleration of particle

g_i = Body force acceleration vector (e.g., gravity loading)

And the equation for rotational motion is written in the vector form:

$$M_i = I\dot{\omega}_i = \left(\frac{2}{5}mR^2\right)\dot{\omega}_i \quad (3.6)$$

where M_i = Resultant moment acting on particle

I = Moment of inertia of a particle

$\dot{\omega}_i$ = Angular acceleration of a particle

R = Radius of a spherical particle whose mass is distributed uniformly throughout its volume.

The equations of motion, given by Equations 3.5 and 3.6, are integrated using a centred finite-difference procedure involving a timestep of Δt . The velocity (\dot{x}_i) and angular velocity ($\dot{\omega}_i$) are computed at the mid-intervals of $t \pm n\Delta t/2$, while the quantities x_i , \dot{x}_i , $\dot{\omega}_i$, F_i and M_i are computed at the primary intervals of $t \pm n\Delta t$. The accelerations are calculated as

$$\ddot{x}_i^{(t)} = \frac{1}{\Delta t} (\dot{x}_i^{(t+\Delta t/2)} - \dot{x}_i^{(t-\Delta t/2)}) \quad (3.7)$$

$$\ddot{\omega}_i^{(t)} = \frac{1}{\Delta t} (\dot{\omega}_i^{(t+\Delta t/2)} - \dot{\omega}_i^{(t-\Delta t/2)}) \quad (3.8)$$

Inserting these expressions into Equations 3.5 and 3.6 and solving for the velocities at time $(t + \Delta t/2)$ result in

$$\dot{x}_i^{(t+\Delta t/2)} = \dot{x}_i^{(t-\Delta t/2)} + \left(\frac{F_i^{(t)}}{m} + g_i \right) \Delta t \quad (3.9)$$

$$\dot{\omega}_i^{(t+\Delta t/2)} = \dot{\omega}_i^{(t-\Delta t/2)} + \left(\frac{M_i^{(t)}}{I} \right) \Delta t \quad (3.10)$$

Finally, the position of the particle centre is updated by the velocities in Equation (3.9) and (3.10) as

$$x_i^{(t+\Delta t)} = x_i^{(t)} + \dot{x}_i^{(t+\Delta t/2)} \Delta t \quad (3.11)$$

3.2.4 Clump logic

A clump behaves as a rigid body (i.e. the balls comprising the clump remain at fixed distances from each other). Internal overlapping contacts are ignored in calculations, resulting in a saving of computational time compared to a similar calculation in which all contacts are active. In this sense, a clump differs from a group of particles that are bonded to one another (agglomerate).

The total mass of a clump m , the location of the centre of mass of clump $x_i^{[G]}$ and the moments and products of inertia I_{ii} and I_{ij} , which are the basic mass properties of a clump, are defined by the following equations

$$m = \sum_{p=1}^{N_p} m^{[p]} \quad (3.12)$$

$$x_i^{[G]} = \frac{1}{m} \sum_{p=1}^{N_p} m^{[p]} x_i^{[p]} \quad (3.13)$$

$$I_{ii} = \sum_{p=1}^{N_p} \left\{ m^{[p]} \left(x_j^{[p]} - x_j^{[G]} \right) \left(x_j^{[p]} - x_j^{[G]} \right) + \frac{2}{5} m^{[p]} R^{[p]} R^{[p]} \right\} \quad (3.14)$$

$$I_{ij} = \sum_{p=1}^{N_p} \left\{ m^{[p]} \left(x_i^{[p]} - x_i^{[G]} \right) \left(x_j^{[p]} - x_j^{[G]} \right) \right\} ; (j \neq i) \quad (3.15)$$

where N_p is the number of balls in the clump, $m^{[p]}$ is the mass of a ball, $x^{[p]}$ is the centroid location of the ball and $R^{[p]}$ is the radius of the ball.

The motion of a clump is determined by the resultant force and moment vectors acting upon it. Because a clump is treated as a rigid body, its motion can be described in terms of the translational motion of a point in the clump and the rotational motion of the entire clump. The equation for translational motion can be written in the vector form

$$F_i = m(\ddot{x}_i - g_i) \quad (3.16)$$

where F_i is the resultant force, the sum of all externally-applied forces acting on the clump and g_i is the body force acceleration vector arising from gravity loading. The equation for rotational motion can be expressed in the matrix form as

$$\{M\} - \{W\} = [I]\{\alpha\} \quad (3.17)$$

where

$$[M] = \begin{Bmatrix} M_1 \\ M_2 \\ M_3 \end{Bmatrix}$$

$$[W] = \begin{Bmatrix} \omega_2\omega_3(I_{33} - I_{22}) + \omega_3\omega_3I_{23} - \omega_2\omega_2I_{32} - \omega_1\omega_2I_{31} + \omega_1\omega_3I_{21} \\ \omega_3\omega_1(I_{11} - I_{33}) + \omega_1\omega_1I_{31} - \omega_3\omega_3I_{13} - \omega_2\omega_3I_{12} + \omega_2\omega_1I_{32} \\ \omega_1\omega_2(I_{22} - I_{11}) + \omega_2\omega_2I_{12} - \omega_1\omega_1I_{21} - \omega_3\omega_1I_{23} + \omega_3\omega_2I_{13} \end{Bmatrix}$$

$$[I] = \begin{bmatrix} I_{11} & -I_{12} & -I_{13} \\ -I_{21} & I_{22} & -I_{23} \\ -I_{31} & -I_{32} & I_{33} \end{bmatrix}$$

$$[\alpha] = \begin{Bmatrix} \alpha_1 \\ \alpha_2 \\ \alpha_3 \end{Bmatrix} = \begin{Bmatrix} \dot{\omega}_1 \\ \dot{\omega}_2 \\ \dot{\omega}_3 \end{Bmatrix}$$

in which $[M]$ is the resultant moment about the centre of mass, ω_i is the angular velocity about the principal axis and $\dot{\omega}_i$ is the angular acceleration about the principal axes, referred to a local coordinate system that is attached to the clump at its centre of mass. The equations of motion, given by Equations (3.16) and (3.17), are integrated using a centred finite-difference procedure involving a timestep of Δt as described in section 3.2.3.

3.3 Contact constitutive models

3.3.1 Linear elastic contact model

The stiffness model provides an elastic relation between the contact force and relative displacement in the normal and shear directions via Equations (3.2) and (3.3). The linear contact-stiffness model which is defined by the normal and shear stiffness k_n and k_s of two contacting entities (ball to ball or ball to wall), assumes that the stiffness of the two contacting entities act in series. The contact stiffness for the linear contact model can be calculated by

$$K^n = \frac{k_n^{[A]} k_n^{[B]}}{k_n^{[A]} + k_n^{[B]}} \quad (3.18)$$

$$K^s = \frac{k_s^{[A]} k_s^{[B]}}{k_s^{[A]} + k_s^{[B]}} \quad (3.19)$$

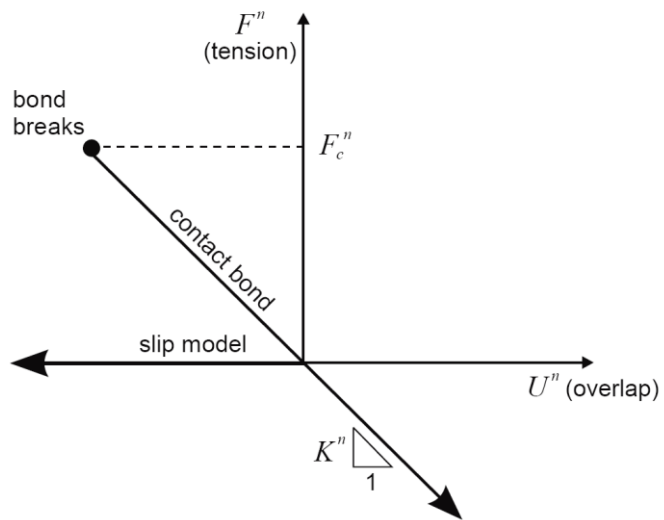
where the superscripts [A] and [B] denote the two entities in contact.

3.3.2 The Bonding Models

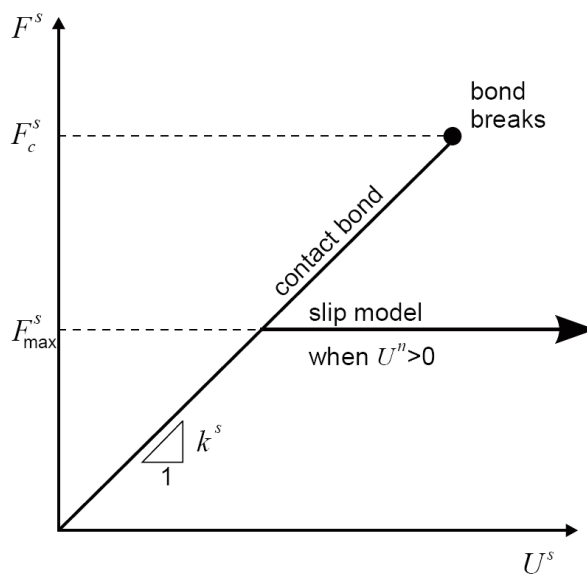
The bonding model serves to limit the total normal and shear forces that contact can carry by enforcing bond strength limits. PFC^{3D} allows particles to be bonded together at contacts. Two bonding models are supported: a contact bond model and a parallel bond model. Once a bond is formed at a contact between two particles, the contact continues to exist until the bond is broken.

The contact-bond model

A contact bond can be envisaged as a pair of elastic springs with constant normal and shear stiffnesses acting at the contact point. These two springs have specified shear and tensile normal strengths. The constitutive behaviour relating the normal and shear components of contact force and relative displacement for particle contact occurring at a point is shown in Figure 3.2. The contact bond breaks when the contact force exceeds either the normal contact bond strength or the shear contact bond strength. The particles bonded together with a contact bond cannot slip but they can roll over each other. Figure 3.3 illustrates a contact bond that allows rolling of ball A relative to ball B without slipping, thus without breaking the contact bond. It is noted that this case only occurs for balls that are free to roll.



(a)



(b)

Figure 3.2 Constitutive behaviour for contact occurring at a point : (a) normal component of contact force; (b) Shear component of contact force (Itasca, 1999)

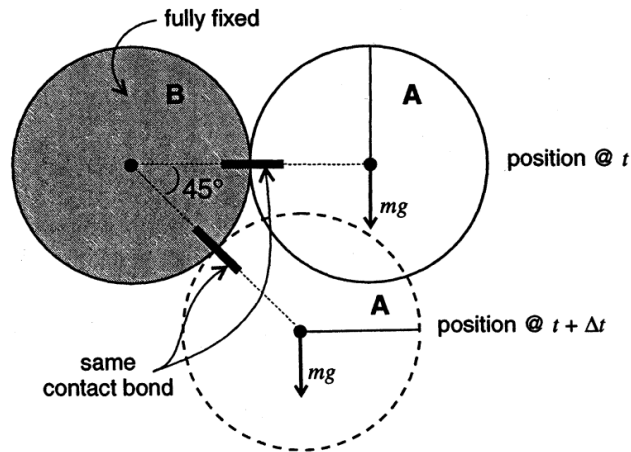


Figure 3.3 Rolling without slip at a contact bond (Itasca, 1999)

The parallel-bond model

A parallel bond can be envisaged as a disc of elastic glue lying on the contact plane (see Figure 3.4). The parallel bond can transmit both forces and moments between particles, while contact bonds can only transmit forces acting at the contact point. The behaviour of the parallel bond is similar to that of the contact bond, as shown in Figure 3.2. Relative motion at the contact causes a force and a moment to develop within the parallel bond as a result of the stiffness of the parallel bond. The parallel bond breaks when the stress in any part of the bond exceeds the parallel bond strength.

If the parallel-bond model is used in the simulation, parallel bonds are installed at all real contacts (with non-zero overlap) and virtual contacts (with a separation between two particles less than 10^{-6} times the mean radius of the two particles). The total force and moment associated with the parallel bond are denoted by \bar{F}_i and \bar{M}_i . Each of these vectors can be resolved into normal and shear components with respect to the contact plane as

$$\bar{F}_i = \bar{F}_i^n + \bar{F}_i^s \quad (3.20)$$

$$\bar{M}_i = \bar{M}_i^n + \bar{M}_i^s \quad (3.21)$$

where \bar{F}_i^n , \bar{M}_i^n and \bar{F}_i^s , \bar{M}_i^s denote the normal and shear component vectors, respectively. These vectors are shown in Figure 3.4.

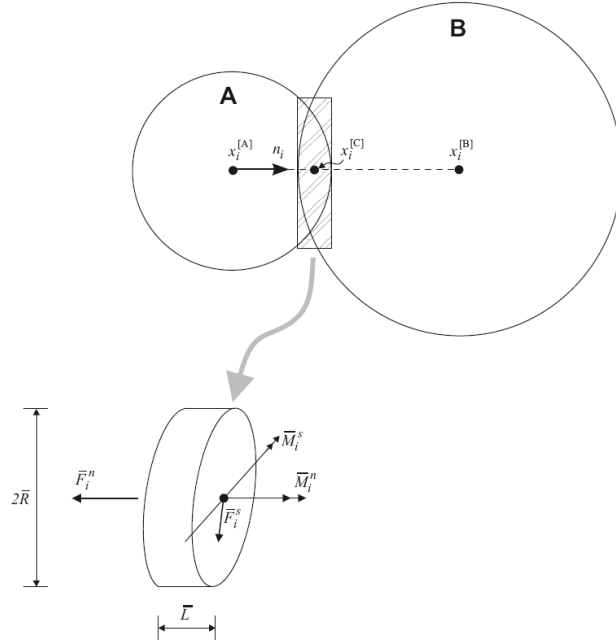


Figure 3.4 Parallel bond depicted as a cylinder of cementitious material (Itasca, 1999)

In terms of beam theory, the maximum tensile stress and the maximum shear stress on the bond periphery can be calculated by

$$\sigma_{max} = \frac{-\bar{F}^n}{A} + \frac{|\bar{M}_i^s|}{I} \bar{R} \quad (3.22)$$

$$\tau_{max} = \frac{|\bar{F}_i^s|}{A} + \frac{|\bar{M}_i^n|}{J} \bar{R} \quad (3.23)$$

where A is the area of the bond disc, J is the polar moment of inertia of the disc cross-section, I is the moment of inertia of the disc cross-section about an axis through the contact point and \bar{R} is the radius of the bond disc. These quantities are given by

$$A = \pi \bar{R}^2$$

$$J = \frac{1}{2}\pi\bar{R}^4 \quad (3.24)$$

$$I = \frac{1}{4}\pi\bar{R}^4$$

3.4 Boundary conditions

3.4.1 Overview of DEM boundary conditions

In continuum numerical modelling the choice of boundary conditions plays an important role and boundaries are equally important in DEM. A key choice in setting up a DEM simulation is to decide on the spatial domain that will be considered (O’Sullivan, 2011). The boundaries of this domain must then be numerically described in the DEM model. In continuum modelling there are displacement boundary conditions, along which the displacement is restricted or specified, and traction boundary conditions, along which stress is specified. Similarly, in a DEM simulation, displacement boundary conditions can be achieved by fixing or specifying the positions of selected particles; force boundary conditions can be achieved by applying specified forces to selected particles. If applied, an external force is added to the contact forces acting on the particle and the resultant force is then used to calculate the particle accelerations and incremental displacements.

DEM is well suited to problems involving large deformations, and forces may need to be applied to different particles as the system deforms. Consequently, algorithms to select boundary particles are needed. As shown in Figure 3.5, four types of boundary condition are considered, in order of their popularity of use; these are rigid wall, periodic boundary conditions (Thornton, 2000), membrane boundaries (McDowell et al. 2012; Cheung and O’Sullivan, 2008 and Cui et al. 2007) and axisymmetric boundaries (Weatherley, 2009 and Cui et al. 2007). In the following simulations of this project, such as the pull-out test and box test, the rigid walls are used as boundary conditions. For this reason, rigid walls are detailed in the following section.

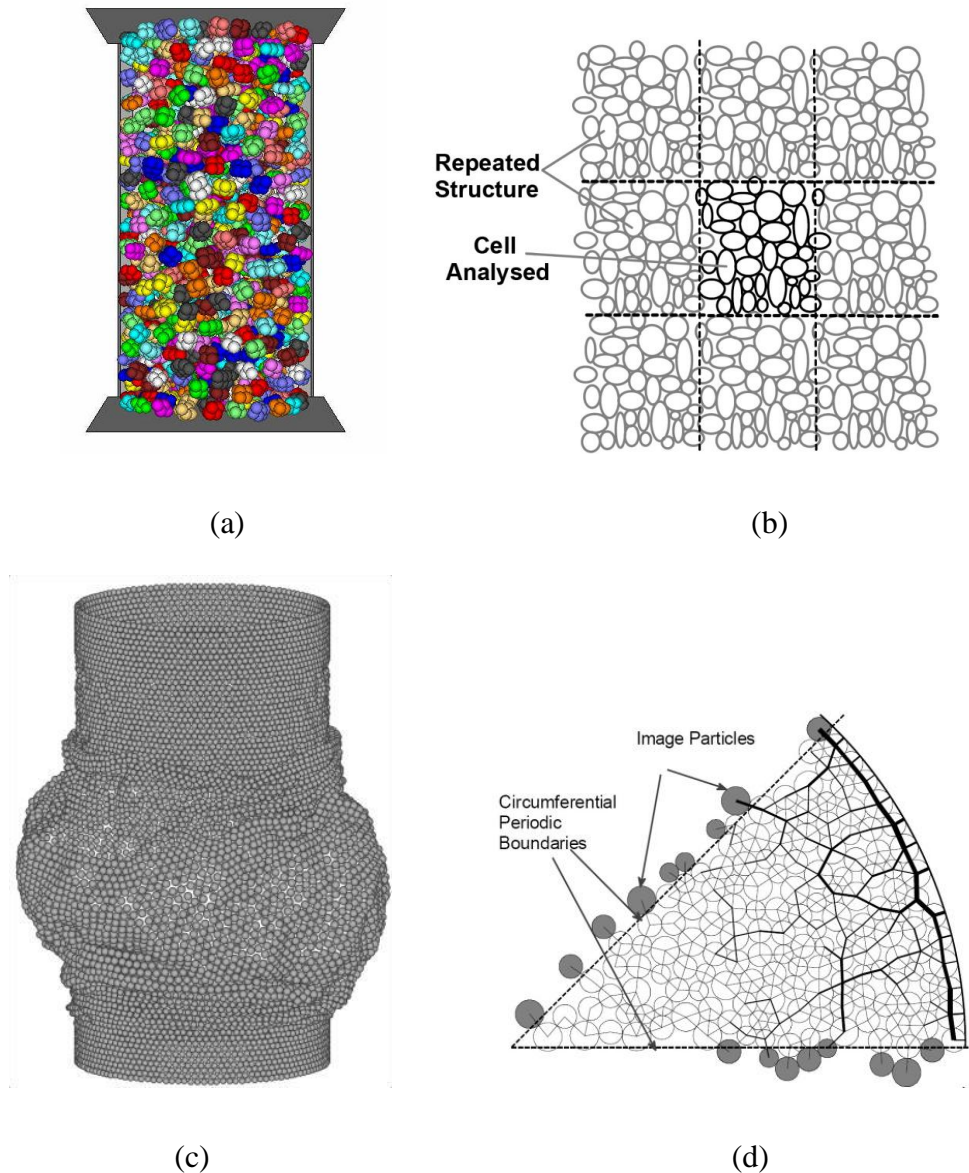


Figure 3.5 DEM boundary conditions: (a) rigid planar and cylindrical boundaries used to simulate triaxial test (McDowell et al., 2006); (b) periodic boundaries (Cheung and O’Sullivan, 2008); (c) membrane boundaries (McDowell et al., 2012); (d) axisymmetric boundaries (Cui et al. 2007)

Poschel and Schwager (2005) proposed an alternative implementation of rigid boundaries, where the boundaries are made up of particles. Their implementation has the advantage of generating “walls” with a geometrical roughness. Marketos and Bolton (2010) described a detailed study on the use of planar boundaries in DEM simulations. They highlight the difference in packing geometry that exists close to the particle boundary and the influence this has on the contact force network and the implications for calculating strain.

3.4.2 Rigid walls

Rigid boundaries are simple analytically described surfaces and they can be planar or curved. Figure 3.5a gives the example of triaxial compression test simulation using rigid wall boundary conditions. Rigid boundaries can also be used to simulate inclusions or machinery interacting with the granular material. For example rigid wall boundaries were used to represent the railway sleeper in the following chapters including the box test, composite element test and transition zone modelling. These boundaries themselves have no inertia; the contact forces determined at the particle-boundary contacts are used to update the particle coordinates only. While the forces acting on the walls do not influence motion of the walls, the user can control the wall movement by explicitly specifying a wall velocity. Users can also specify wall velocities indirectly, by developing an algorithm for the servo-control mechanism to move the walls; for example the wall velocity can be related to the current stress conditions, as considered further below. In either case, when the balls are moved, forces and deformations are applied to the assembly of particles through the walls according to the wall-particles contacts. In typical DEM simulations contacts are not generated between walls that intersect or touch.

In some DEM codes the analyst may need to specify whether the particles will contact the outside or the inside of the boundary (wall). Care must be taken as the contact normal direction will depend on the order in which the vertices are input, with the normal pointing in exactly the opposite direction if the vertices are input in a clockwise, rather than a counter-clockwise order. If a particle is located on the inactive side of a wall, no contact will develop between the particle and the wall and it can simply move, unimpeded through the wall. Besides, if the wall stiffness is too low, a particle can move from the active to inactive side of the wall and essentially “fall” through the wall.

For simulations that require constant loading throughout the test (e.g. triaxial test and constant stress creep test), the servo-control mechanism is implemented. The servo-control mechanism is a function that is integrated in PFC^{3D} to maintain a constant stress (axial and confining) throughout the simulation. This servo function is called

on every calculation cycle to determine the current wall stresses and then adjusts the wall velocities in such a way to reduce the difference between measured stress and required stress. The calculation algorithm for the servo-control mechanism is described below:

$$\dot{u}^{(w)} = G(\sigma^{measured} - \sigma^{required}) = G\Delta\sigma \quad (3.25)$$

where G is the ‘gain’ parameter estimated using the following reasoning. The maximum increment in wall force arising from wall movement in one timestep is:

$$\Delta F^{(w)} = k_n^{(w)} N_c \dot{u}^{(w)} \Delta t \quad (3.26)$$

where N_c is the number of contacts on the wall and k_n is the average stiffness of these contacts. Hence the change in mean wall stress is

$$\Delta\sigma^{(w)} = \frac{k_n^{(w)} N_c \dot{u}^{(w)} \Delta t}{A} \quad (3.27)$$

where A is the wall area. For stability reasons, the change in wall stress must be less than the difference between the measured and required wall stress. To fulfil this stability requirement, a relaxation factor α is introduced such that

$$|\Delta\sigma^{(w)}| < \alpha |\Delta\sigma| \quad (3.28)$$

Substituting Equations (3.25) and (3.27) into Equation (3.28)

$$\frac{k_n^{(w)} N_c G |\Delta\sigma| \Delta t}{A} < \alpha |\Delta\sigma|$$

$$G = \frac{\alpha A}{k_n^{(w)} N_c \Delta t} \quad (3.29)$$

where G is the ‘gain’ parameter to be substituted in Equation (3.25) for adjusting the wall velocity to achieve the required wall stress in numerical servo-control.

3.5 Use of DEM in geogrid-reinforced ballast

3.5.1 Modelling mechanical response of railway ballast

Railway ballast generally comprises large, angular particles of typical size approximately 40mm. In order to investigate the response of ballast, it is effective to simulate ballast using DEM. Previous research studies (e.g. Lim and McDowell, 2005; McDowell et al., 2006; Lu and McDowell, 2007 and 2008; Lobo-Guerrero and Vallejo, 2006; Hossain et al., 2007 and Lu and McDowell, 2010) have shown some feasibility of simulating the behaviour of railway ballast using DEM. This section will review previous studies on discrete element modelling of ballast.

Lim and McDowell (2005) used agglomerates of bonded balls to model railway ballast in the simulations of single particle crushing test. Their results showed that the distribution of strengths correctly follows the Weibull distribution, and the size effect on average strength was consistent with that measured in laboratory. Lim and McDowell (2005) also simulated oedometer tests on the crushable ballast particles using agglomerates of bonded balls (Figure 3.6b) and compared with the results from laboratory tests. They found that the yield stress for the agglomerates was less than that for the real ballast; this is most likely due to the spherical shape of agglomerates, which leads to columns of strong force in the simulated sample. Box tests which simulate traffic loading were simulated by Lim and McDowell (2005) using both spheres and 8-ball cubic clumps, as shown in Figure 3.6c. They found that the 8-ball clumps give much more realistic mechanical behaviour due to particle interlocking. A similar conclusion was drawn by McDowell et al. (2006) when they used both spheres and 8-ball cubic clumps in simulations of triaxial tests. They also pointed out that, as breakage was not considered in their simulations, comparing to the experimental results (Indraratna et al. 1998), dilatation rather than contraction was observed at high confining pressure.

Lu and McDowell (2006) used a simple two-ball clump with two additional small asperities bonded at the surface (Figure 3.6d), which represents a single ballast particle, to model particle abrasion in the box test simulations. As significant asperity breakage occurs in the early cycles of load, a realistic response is observed such that permanent settlement is approximately proportional to the logarithm of the number of cycles of load. However, after the early cycles, the settlement response is approximately linear with number of cycles: this is due to insufficient interlock given by the simplistic clumps.

Lu and McDowell (2008) investigated the stress-strain behaviour of railway ballast under monotonic loading using DEM. The results show that particle shape, interparticle friction, interlocking and asperity fracture all influence the mechanical behaviour of ballast particles. Even though more angular particles with an increased coefficient of friction were used to increase the shear strength of the assembly, the shear strength was still very low compared to that of real ballast. By adding weak parallel bonds between clumps to simulate surface texture and enhance the shear resistance of each particle contact, the correct shear strength of railway ballast can be simulated. They showed that the monotonic shearing behaviour of railway ballast can be correctly modelled under a range of confining pressures using a ten-ball triangular clump with eight asperities bonded (Figure 3.6e).

Lu and McDowell (2010) continued the foregoing research, with particular focus on modelling railway ballast under cyclic triaxial loading. The same ten-ball triangular clumps bonded with eight asperities described by Lu and McDowell (2008) were used. Monotonic tests were performed on the breakable sample under a range of confining pressures from 15 kPa to 140 kPa. Tests were also simulated using uncrushable clumps to investigate the influence of asperity abrasion. Cyclic triaxial tests were then simulated on the same breakable sample as the monotonic tests under a range of stress conditions. The results showed that the clumps are able to capture the behaviour of ballast under monotonic and cyclic loading and asperity abrasion

played an important role in governing strength and volumetric strain under monotonic loading, or permanent strain under cyclic loading.

Lobo-Guerrero and Vallejo (2006) studied the effect of crushing on railway ballast in a simulated track section by using a circular disc to represent each single ballast particle. Two hundred cycles of loading were applied to the circular disc aggregate through three simulated sleepers. The method of modelling particle crushing developed by Lobo-Guerrero and Vallejo (2005) was used in their simulations. They found that permanent deformation increased considerably when particle crushing was included and that particle crushing was concentrated underneath the simulated sleepers. However, the effects of particle shape and mass were not considered in their simulations. Hossain et al. (2007) studied the effect of angular ballast breakage on the stress-strain behaviour of railway ballast under different confining pressures using biaxial test simulations. Two dimensional angular shaped clumps were used in their simulations to model particle interlocking. Similar to the method introduced by Lobo-Guerrero and Vallejo (2005), particle crushing was simulated by releasing discs from the clump when the internal tensile stress induced by contact forces was greater than or equal to 10 MPa. Hossain et al. (2007) showed that particle breakage had a significant effect on both the axial strain and the volumetric strain.

3.5.2 Modelling ballast particle shape

As described in the previous sub-section, various particle shapes have been used to represent real ballast particles, as shown in Figure 3.6. The choice of spheres obviously makes the contact detection and the force calculation easier and also the calculation faster than any other shape. The use of spheres is also a weakness because most ballast particle shapes are irregular and angular. To model such a complex shape using PFC^{3D}, the approach which bonds spheres together as an agglomerate shown in Figure 3.6b, have been used by Lim and McDowell (2005). However, the use of such “agglomerates” proved computationally time-consuming, and produces porous particles if mono-disperse spheres are used.

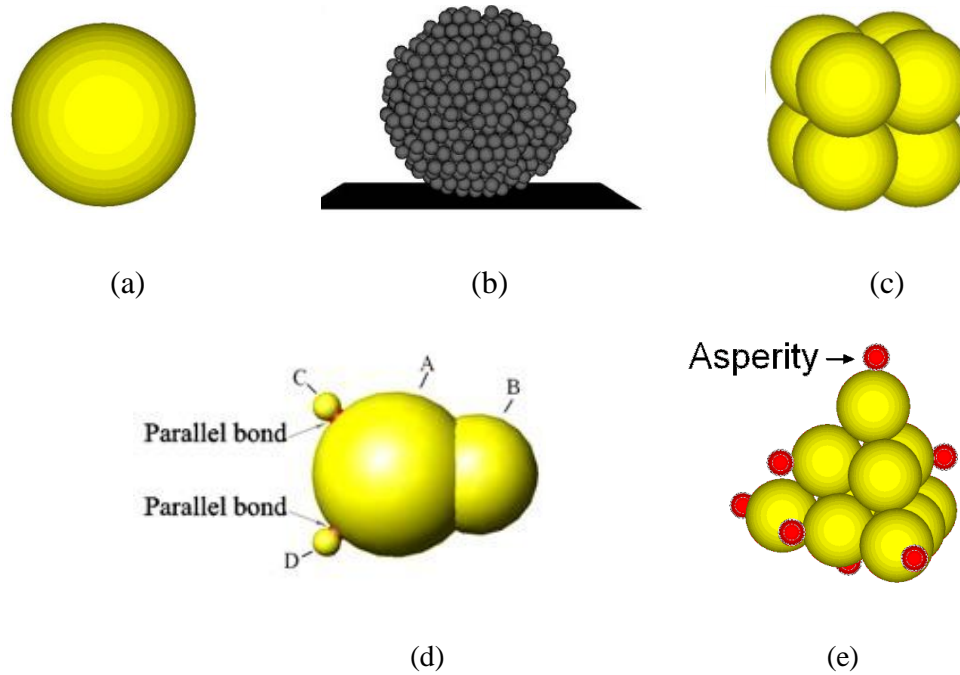


Figure 3.6 PFC^{3D} models for ballast particle: (a) single sphere; (b) 48mm agglomerate initially containing 1477 balls of diameter 3.55mm; (c) 8-ball cubic clump; (d) two-ball clump with two asperities; (e) ten-ball triangular clump with eight small balls (asperities) bonded

Lu and McDowell (2007) developed a simple method to make clumps of overlapping spheres and in which internal contacts are ignored, so that the clump behaves as a rigid body. In their clump model procedure, the balls generate along different directions, whereas Ferrellec and McDowell (2008) developed a different simple method in which balls are generated along surface normals. Different physical parameters have an impact on the resolution of the model particle and control the number of spheres inside the particle: the more spheres the better the resolution (Figure 3.7). Besides, Ferrellec and McDowell (2008) also introduced other published methods of clump generation, including clustering method (Wang et al. 2007), dynamic method (Matsushima et al. 2003) and sphere fit method (Price et al. 2007). It should be noted that the use of clumps of overlapping spheres has the problem of overlapping mass. As the density is non-uniform, the moments of inertia are incorrect. Ferrellec and McDowell (2010) addressed this issue, and offered a simple solution to reduce the error in the principal moments of inertia. The solution improves not only the behaviour of particle, but also computational time.



Figure 3.7 Real ballast particle (left) and models with decreasing number of spheres from left to right (Ferrellec and McDowell, 2008).

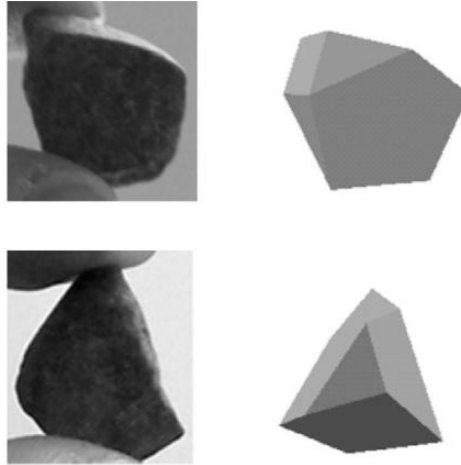


Figure 3.8 The aggregate particle shown by photos and the generated BLOCK3D element (Huang, 2010)

After realizing the limitation of spherical element shape, Barbosa (1990) developed a new program called “BLOCKS3D” which utilized arbitrarily shaped elements instead of spherical elements. Block shaped elements are more realistic than spherical elements especially in modelling crushed particles like railroad ballast aggregates. Nezami et al. (2004) proposed a fast contact detection algorithm called “Fast Common Plane” for 3D block shaped discrete elements. With this advanced algorithm, a 3D discrete element analysis code “DBLOCK3D” was developed (Hashash et al. 2005) for the simulation of granular media and soil-machine interaction. According to the ongoing research, Nezami et al. (2006) developed the “Shortest Link Method” to search the common plane. Zhao et al. (2006) implemented this algorithm to DBLOCKS3D and developed a modified DEM code “BLOKS3D”. Nezami et al. (2007) successfully utilized “BLOKS3D” to simulate a bucket-soil interaction model. Figure 3.8 shows that BLOKS3D uses user-defined 3-D “blocks” or polyhedrons as the basic elements to realistically simulate ballast

aggregate particles (Huang, 2010). Besides, Harkness (2009) has developed a typical distinct element numerical model of a triaxial test specimen made up of particles representative of real ballast, formed using the potential particle method.

3.5.3 DEM on interlocking behaviour of geogrid

DEM was used to investigate the interlocking behaviour of geogrids under static and cyclic loading conditions (Konietzky et al. 2004). Pull-out tests and calibrated triaxial tests with different load levels were simulated to investigate the interlocking effect. Pull-out tests were performed using a calibrated 4 x 4 geogrid, of mesh size 39mm, formed using approximately 31,000 balls, as shown in Figures 3.9a and 3.9b. Figure 3.9c shows a sketch of the whole model, which consists of a box 70cm x 18 cm x 18 cm. The aggregate was reproduced by approximately 50,000 balls according to a graded grain size distribution given in Figure 3.10a. Figure 3.10b shows a part of the whole model with a geogrid and a complete set of aggregate particles.

Three different loading conditions were investigated: surface surcharge of zero, 13.2 kPa and 35.4 kPa respectively. Figure 3.11 shows the total pull-out force as a function of pull-out length for the three load cases. As expected, higher vertical loads produce higher pull-out forces. Konietzky et al. (2004) found that the geogrid leads to a significant increase in contact force near the geogrid, and the zone of influence appears to extend to approximately 10cm either side of the geogrid.

Triaxial laboratory tests have shown that in the case of installed geogrids, considerably higher deviatoric stresses are necessary to produce the same deviatoric strain as for samples without geogrids. This effect cannot be explained by the apparent confining pressure caused by the stiffness of geogrid alone; the interlocking effect also causes this apparent confinement. The numerical modelling via PFC^{3D} should give deeper insight into these effects. Figure 3.12a shows the numerical model of triaxial sample, which contains three layers of geogrid at one-quarter depth, mid-depth and three-quarters depth. They explained the simulation results in terms of particle-geogrid interlock: in the immediate vicinity of the geogrid the interlocking

keeps the crushed rock material together. However, in between the geogrid layers the interlocking effect is restricted to the central part of cross-section (bridge effect between the geogrid), and near to the model boundaries the contact forces are strongly reduced. The bridging effect between geogrid layers is evident in Figure 3.12b. They also compared the results of one geogrid layer and three geogrid layers, and found that both the vertical and radial displacements using three geogrid layers were reduced by approximately 50%. The simulation results demonstrated that multiple layers of geogrid may be useful in reduction of displacement which is similar to the experimental large-scale triaxial test results.

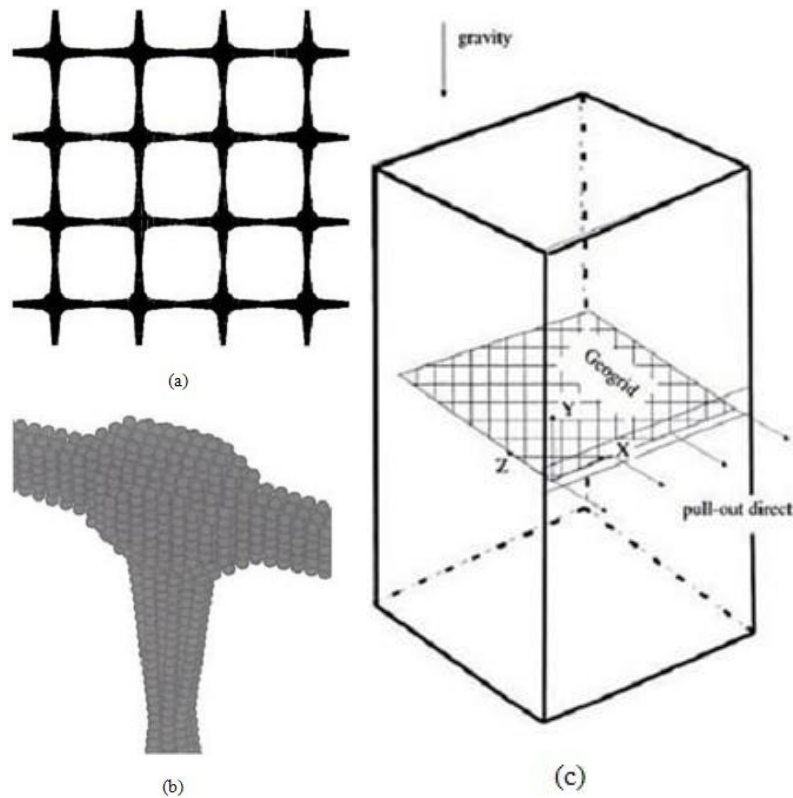
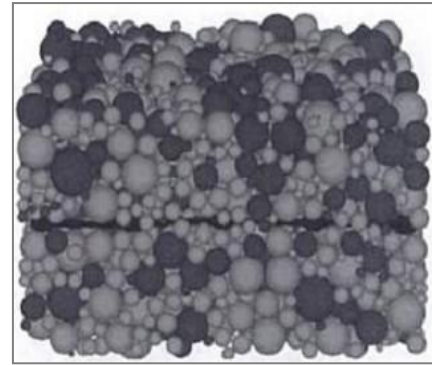
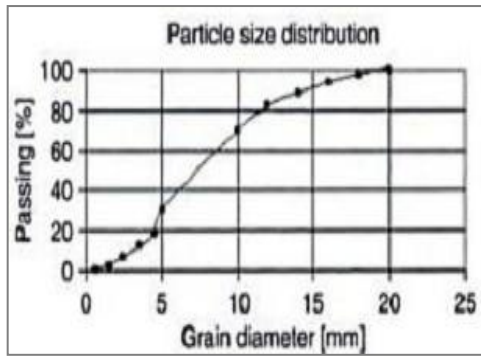


Figure 3.9 Numerical model: (a) SS-30 geogrid with 9 cells; (b) detail view of numerical SS-30 geogrid model; (c) sketch of simulation of pull-out test (Konietzky et al. 2004)



(a)

(b)

Figure 3.10 Aggregate particles: (a) particle size distribution; (b) geogrid with complete set of aggregate particles (Konietzky et al. 2004)

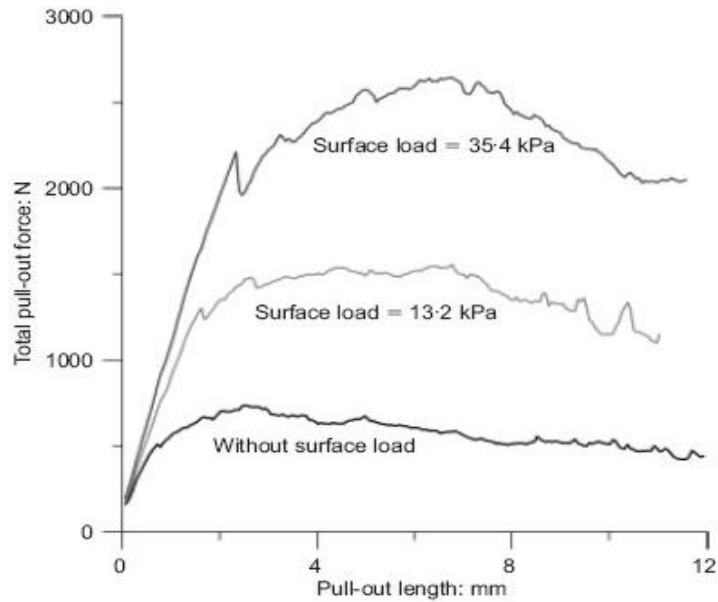


Figure 3.11 Total pull-out force as a function of pull-out length (Konietzky et al. 2004)

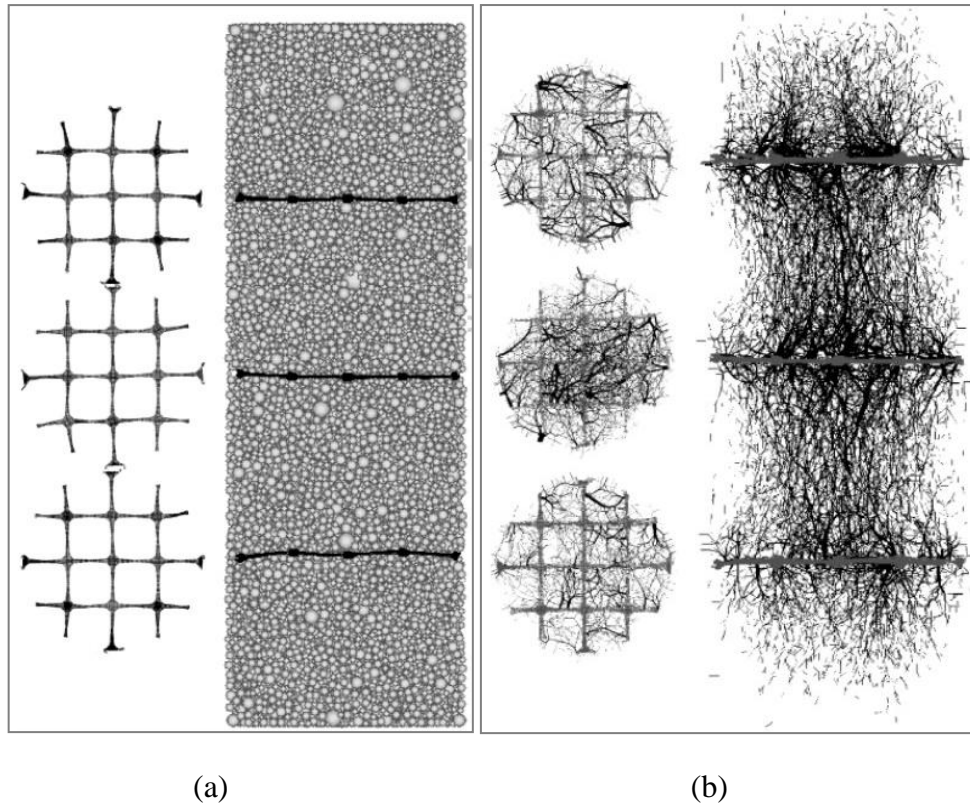


Figure 3.12 Numerical model: (a) triaxial sample with three geogrid layers; (b) Contact force distribution and geogrid after partial horizontal and vertical unloading (Konietzky et al. 2004).

Ferrellec and McDowell (2012) presented a simple test which consists of pulling apart of two apertures of a square geogrid between two rectangular rods. This kind of square geogrid typically presents buckling as illustrated by the laboratory test in Figure 3.13. Figure 3.14 shows the simulation of this test using different sections for the geogrid ribs. Figure 3.14a uses a single row of spheres to represent the rib; Figure 3.14b uses three contiguous rows of spheres and Figure 3.14c uses two layers of the spheres used in Figure 3.14b. Figures 3.14a and 3.14b show that the single layer models present only horizontal deformation. Figure 3.14c, however, shows the typical buckling behaviour expected for this kind of geogrid. This first simple test shows that it is important to reproduce accurately the geometrical shape of the geogrid to obtain the correct deformation even in the case of a simple geogrid type.

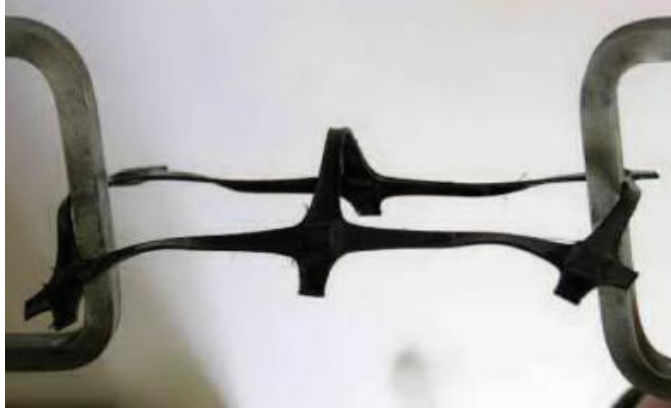


Figure 3.13 Typical deflection of geogrid under extension (Ferrellec and McDowell, 2012)

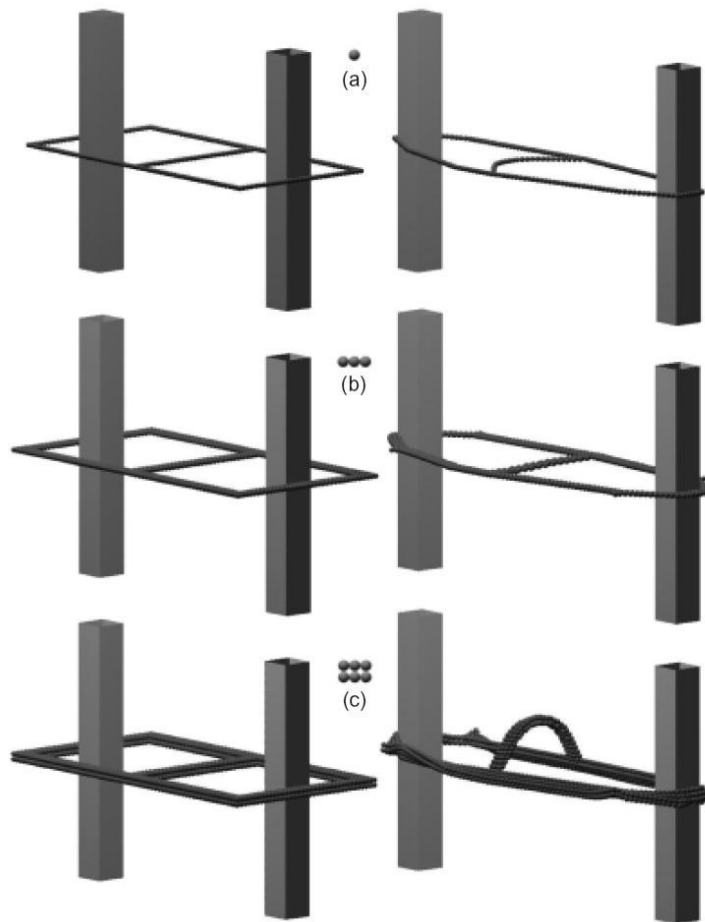


Figure 3.14 Two-aperture extension tests: (a) single-sphere row rib, (b) three-sphere row rib and (c) two layers of three sphere row rib before and after extension (Ferrellec and McDowell, 2012)

3.6 Summary

The discrete element method (DEM) has proved to be a powerful numerical tool to provide micro scale information which has been difficult to obtain through physical tests. In this chapter, the basic concept and theoretical background of both DEM and PFC^{3D} model have been described. The calculation cycle in PFC^{3D} is a time-stepping algorithm involving the repeated application of the Law of Motion and the Force-Displacement Law. PFC^{3D} allows particles to be bonded together at contacts to form an “agglomerate”. Two bonding models are supported: the contact-bond model and the parallel-bond model. In previous research, these two bonding models were applied in the modelling of granular material and geogrid. Clump logic is also provided in PFC^{3D}, so that more complicated shape particles can be modelled by using clumps which are entities of overlapping balls. Internal overlapping contacts are ignored in calculations of clumps, resulting in a reduction of computational time compared to calculations using agglomerates in which all contacts are active. According to the review of DEM studies on ballast-geogrid systems, DEM seems to hold much promise as a tool for investigating ballast-geogrid composite systems and optimising performance by choosing appropriate geometries.

Chapter 4 Laboratory large box pull-out test

4.1 Introduction

Geogrids have been successfully used as reinforcement in railway track for decades. A geogrid can be placed within the ballast layer to reduce ballast deformation and extend the maintenance cycle by a factor of about 3, or at the top of the subgrade to increase the bearing capacity of the track foundation (Tensar, 2009). The conventional geogrids are produced with high stiffness in longitudinal and transverse directions with square apertures to suit the ballast grading. The triaxial geogrid has evolved which involves a change in grid aperture shape from rectangular to a triangular one which is a more stable geometric shape for structural efficiency (Tensar, 2010). The pull-out interaction mechanisms between particle and geogrid reinforcements are more complex than those between particle and sheet reinforcements. This is because the pull-out resistance of biaxial geogrids includes two main components: the passive resistance that develops against the front of the transverse ribs, and the interface shear resistance that takes place along the longitudinal ribs, and also, but to a lesser extent, along transverse ribs (Koerber et al. 1989 and Teixeira et al. 2007). Although the interface shear component can be quantified using parameters obtained from direct shear tests, the passive resistance can only be evaluated using a pull-out test.

A typical pull-out test performed by Kwan (2006) was conducted in a small wooden box with dimension of 200mm wide x 300 mm long x 400mm deep. However, interpretation of unrepeatable pull-out test results proved to be a difficult task, mostly due to the boundary conditions of the small box and few apertures being tested. Bergado et al. (1993) reported that the pull-out resistance of individual-rib geogrids without transverse ribs yields 80–90% of the pull-out resistance of the corresponding

grids with transverse ribs, attributed to the nodes or ribs on longitudinal members. Palmeira and Milligan (1989) attempted to investigate the influence of boundary conditions on pull-out test results. They found that the internal friction angle between the soil and reinforcement could be severely overestimated because of friction on the internal front wall of the box in small scale tests. They recommended lubricating the front face and increasing the scale of the tests. Dias (2003) (in Palmeira, (2009)) have demonstrated a significant increase in pull-out resistance and a stiffer response by reducing the box height. Further influencing factors like the stiffness of the loading plate, the distance between the first transverse ribs and the front wall, the shape of the geogrid specimen (number of ribs in machine and transverse direction), geogrid length, external clamping, wall friction, normal load and pull-out velocity were described by Alagiyawanna et al. (2001), Moraci and Piergiorgio (2006) and Palmeira (2009). Hence, a detailed description of the sample preparation and test procedure is necessary which has to be considered with the framework of the following large box pull-out simulation in order to reproduce realistic pull-out behaviour. In this chapter, a larger box measuring 400mm wide x 600mm long x 400mm deep which is four times larger than the small box was used in these experimental pull-out tests. These experiments aim to compare the performance of biaxial and triaxial geogrids and also investigate the key parameters that influence geogrid reinforcement.

4.2 Test procedure

Figure 4.1 shows the large box pull-out test set-up in the lab. Figure 4.2 shows the schematic diagram of the large-box pull out test. The box is filled with 140 kg graded ballast with a geogrid layer placed at mid-depth protruding out of the box through a slot in right-hand wall of the box. A thin plastic membrane, placed on either side of the grid, is used to cover the aperture through the opening of the slot to prevent the grid trapping aggregate between the grid nodes and the slot. It has considerably improved the reliability and repeatability of the test results. A load cell with a 3kN capacity is used for measuring the pull-out force applied by the hydraulic jack, which pulls the geogrid out at an approximately constant rate. A dial gauge measures displacement intervals over pull-out distance of 50mm.



Figure 4.1 Large box pull-out test set-up in the laboratory

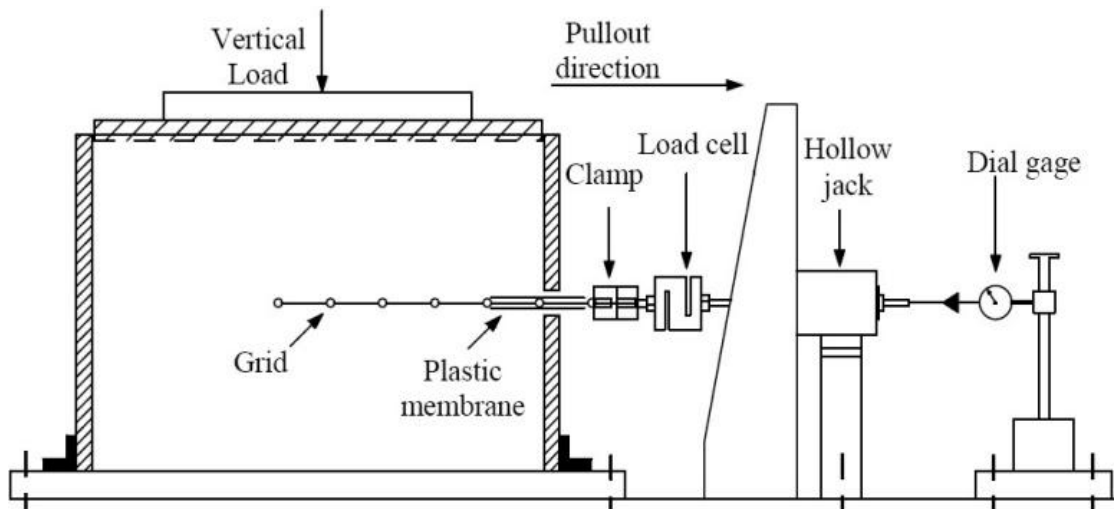


Figure 4.2 Schematic diagram of large-box pull-out test

In these experiments, the ballast used was from the Glensanda quarry in Scotland and is a granite comprising mainly plagioclase (35%), quartz (30%) and alkali feldspar (20%). Physical properties relating to particle shape are quoted in Lim (2004) with his results presented in Table 4.1, where the particle shape is described according to Railtrack (2000) and the relevant British Standard (BSI, 2002). The same type of ballast was used throughout the large box pull-out tests. It can be generally described as a uniformly graded, crushed hard stone which is durable, angular, equidimensional in shape and relatively non flaky. The grading curve of ballast specified by Railtrack (2000) is shown in Fig. 4.3. The ballast particle mean size is approximately 40mm. The coefficient of uniformity C_u is approximately 1.4. The initial density is approximately 1458 kg/m^3 .

Table 4.1 Particle shape according to RT/CE/S/006, Issue 3:2000 and BS EN 13450: 2002 (Modified from Lim, 2004)

Ballast	RT/CE/S006		BS EN 13450	
	Flakiness Index	Elongation Index	Flakiness Index	Length Index
Glensanda	5	20	7	1

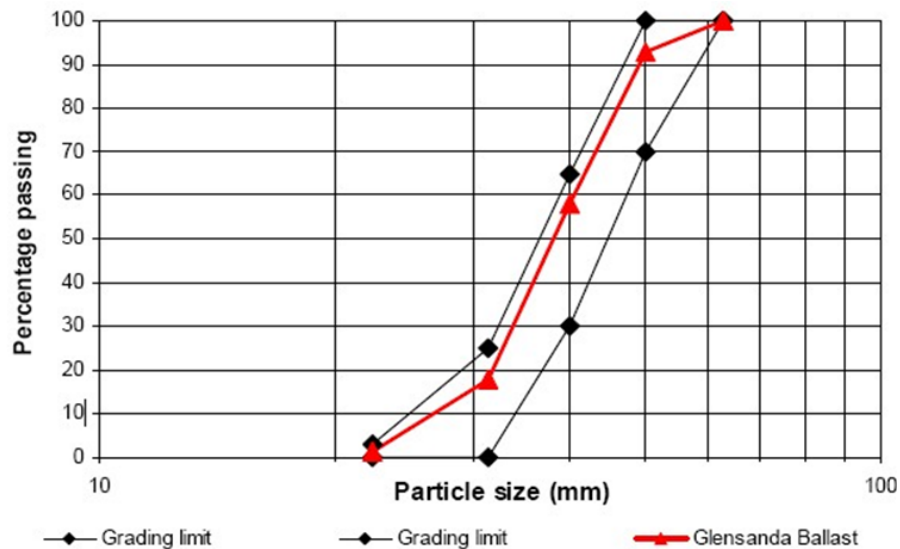


Figure 4.3 Grading curve of ballast (Grading limit from TR/CE/S006, Issue 3:2000)

All tested polymer geogrids of biaxial and triaxial types are shown in Figure 4.4. The key components of the polymer geogrid SSLA30 are identified in Fig. 4.4a. The effective grid areas of all the geogrids were approximately 260mm x 195mm, which

is equal to the area of 12 apertures of geogrid SSLA30. A summary of all the tested geogrids is given in Table 4.2.

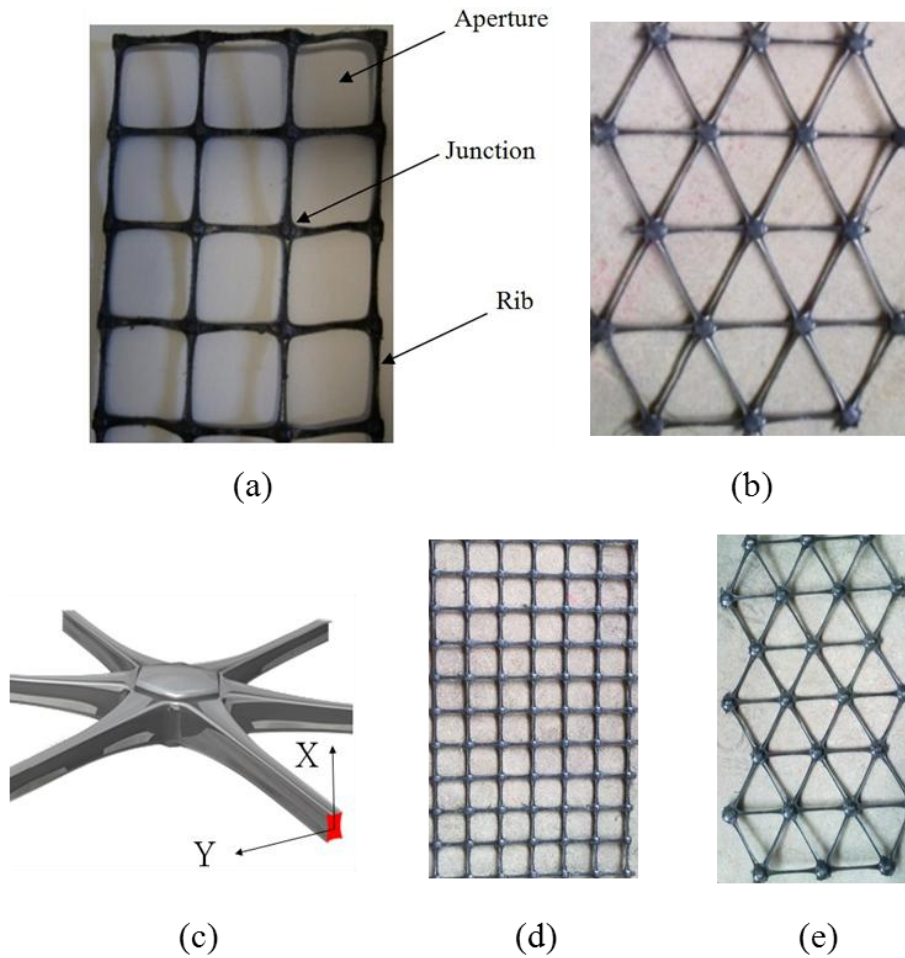


Figure 4.4 Geogrid samples: (a) biaxial geogrid SSLA30; (b) triaxial geogrid TG1; (c) new rib profile of TG1; (d) biaxial geogrid SS40; (e) triaxial geogrid TX130

Table 4.2 Tested geogrids

Geogrid	Aperture shape	Rib tensile strength (kN/m)	Rib length(mm)	Cross-section shape of rib
SS40	Square	40	32	
SSLA20	Square	20	65	
SSLA30	Square	30	65	
TX130	Triangular	N/A	75	
TX160	Triangular	N/A	40	
TG1	Triangular	N/A	75	

The specimens used for the large-box pull-out testing program were prepared by four main steps. Firstly, the ballast was spread evenly in the box until reaching the mid-height of box and then the lower half of the specimen was compacted using a wood plate to make the interface close to horizontal. Afterwards, the geogrid specimen was positioned within the box and attached to the clamp used to apply the pull-out force. After placement of the geogrid, the upper portion of the box was filled with ballast following the same procedures used in the lower portion. In order to maintain consistency of the lower and upper half sample, both halves weighed around 70kg. Finally, a wooden block slightly smaller than the internal dimensions of the box was placed over the top ballast. If a surcharge is required then the weight must be placed on the block to apply a uniformly distributed pressure. The pull-out force and the pull-out displacement were recorded until the ultimate displacement of the jack (50mm) was achieved. The test was performed with the grid being pulled horizontally at a relatively constant rate which is about 0.5mm/s. The pull-out rate should be gradually increased during the initial 2mm, because a larger pull-out rate causes a sharp increase of pull-out force at the beginning. At the end of each test, it was necessary to replace the geogrid if it had a significant deformation. Generally, the peak pull-out forces are relatively small (<10%) compared to the tensile strengths of the geogrids (Table 4.2), which caused little geogrid strain especially without surcharge conditions.

4.3 Results

The pull-out tests were conducted using surcharges of 0 and 0.5 kN for six types of geogrids respectively. The test was performed with the grid being pulled horizontally at a relatively constant rate. Each type of pull-out test was performed three times to ensure repeatability. As the test was designed to investigate the interlocking effect between ballast and grid but not the tensile strength of the ribs, it was decided that the test should proceed at the vertical stress of 5.0kPa (0.5kN load + overburden). In general, the overburden stress in the railway track bed of 300mm thick ballast

equates to approximately 7.0kPa. So the stress achieved in the pull-out tests equates to the overburden stress at 215mm depth in the railway track bed.

Figure 4.5 shows repeated results for the tests in the small box pull-out test (Kwan (2006)), in terms of the pull-out force as a function of displacement for surcharges of 0.0 and 0.5kN. Figures 4.6 to 4.11 show the pull-out forces measured in this research as a function of pull-out displacement for surcharges of 0kN and 0.5kN for the six geogrids. Obviously, higher peak forces and ultimate forces were produced under 0.5kN surcharge. Better results were obtained in the large box pull-out test owing to the improved boundary condition of the large box and more apertures being tested. The jagged natures of the plots illustrate intermittent slippages in the interlocking between ballast and the geogrid. Take Figure 4.6 as an example: it shows results for repeated test results in the large box pull-out test in terms of the pull-out force as a function of displacement for surcharges of 0.0 and 0.5kN. Two lines of average pull-out forces have been added in Figure 4.6 which reduce the oscillations and present a clearer view of the overall behaviour.

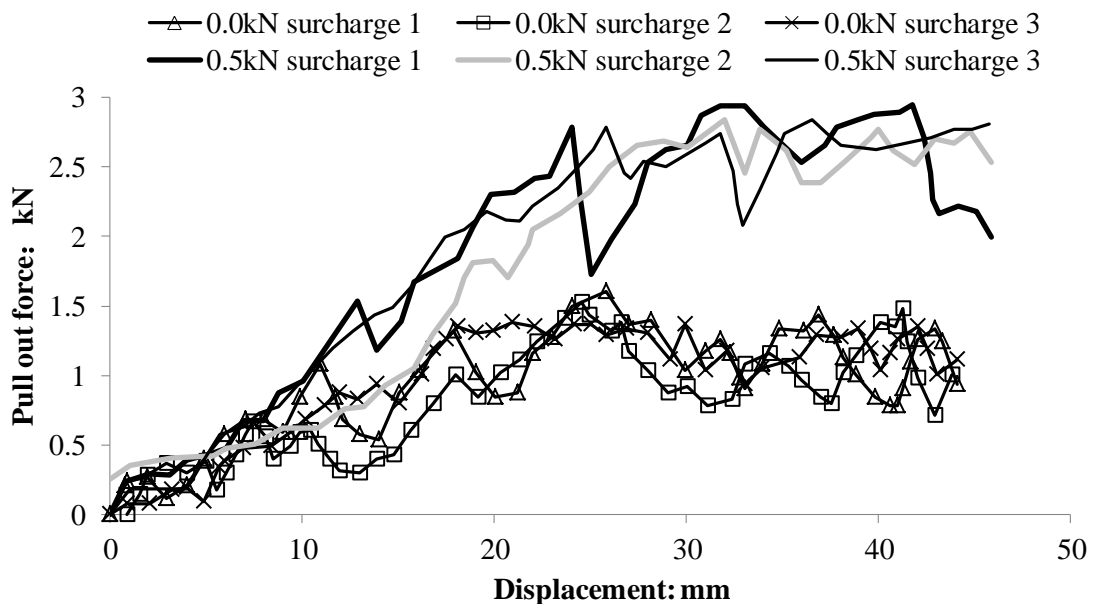


Figure 4.5 Small box pull-out test results: pull-out force against displacement for SSLA30 geogrid under 0.0 and 0.5kN surcharge (Kwan, 2006)

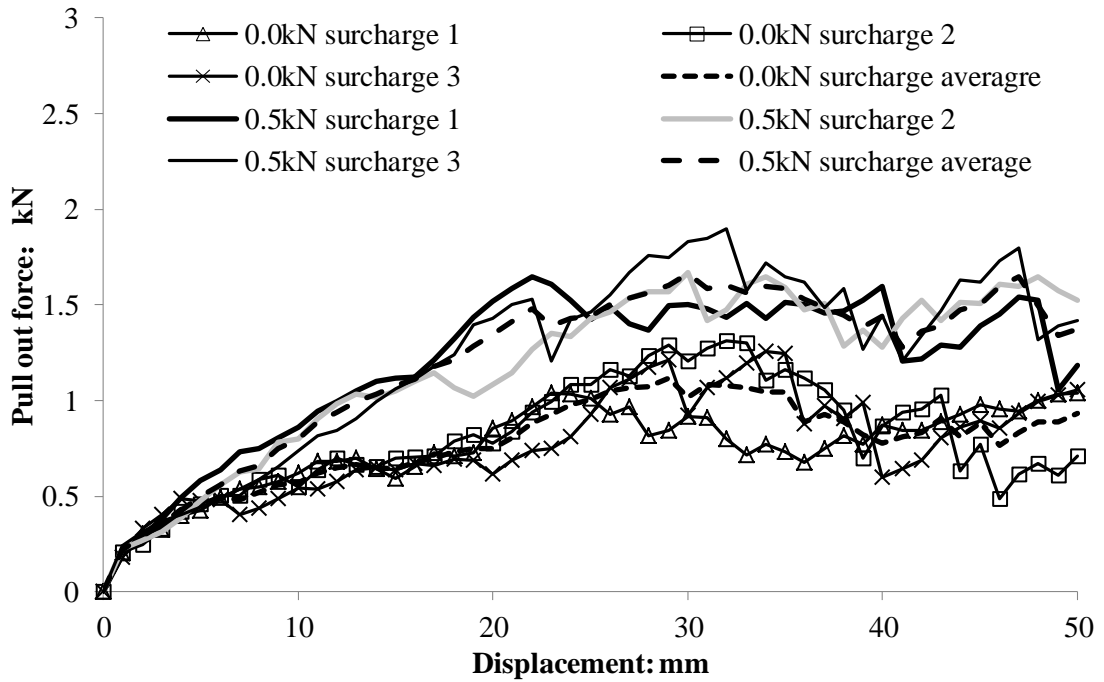


Figure 4.6 Large box pull-out test results: pull-out force against displacement for SSLA30 geogrid under 0.0 and 0.5 kN surcharge

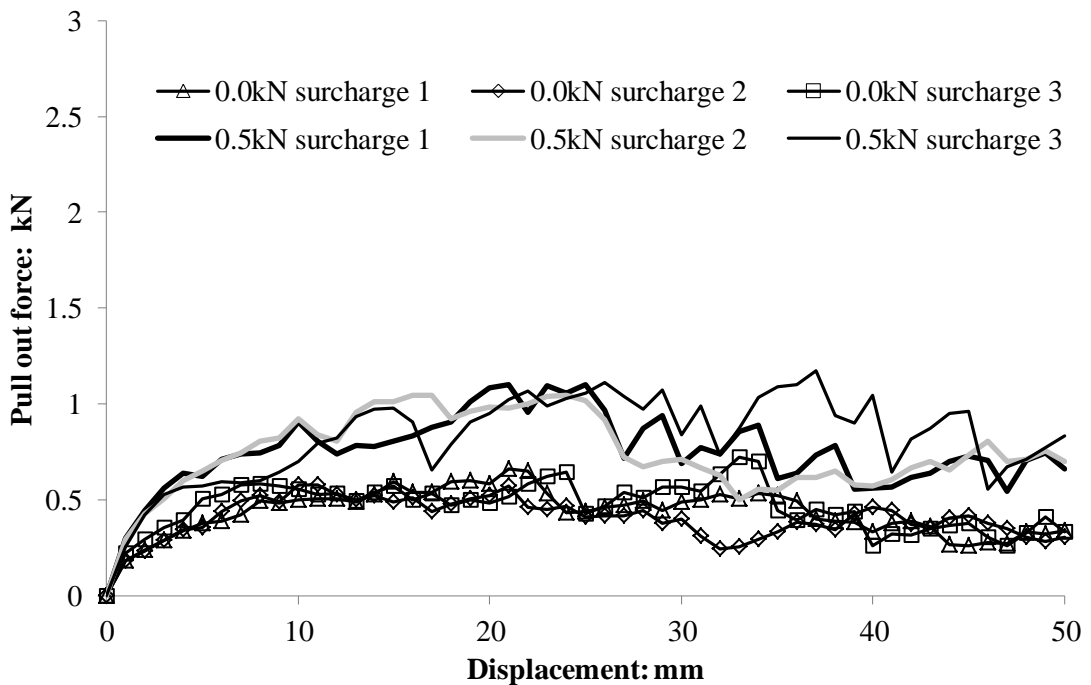


Figure 4.7 Large box pull-out test results: pull-out force against displacement for SS40 geogrid under 0.0 and 0.5 kN surcharge

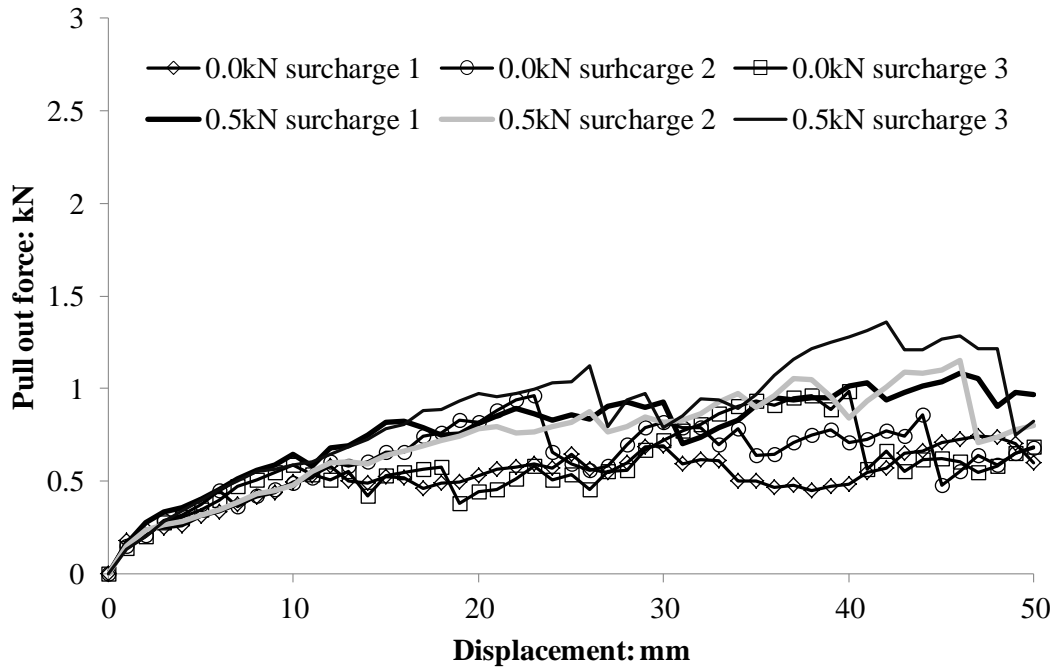


Figure 4.8 Large box pull-out test results: pull-out force against displacement for SSLA20 geogrid under 0.0 and 0.5 kN surcharge

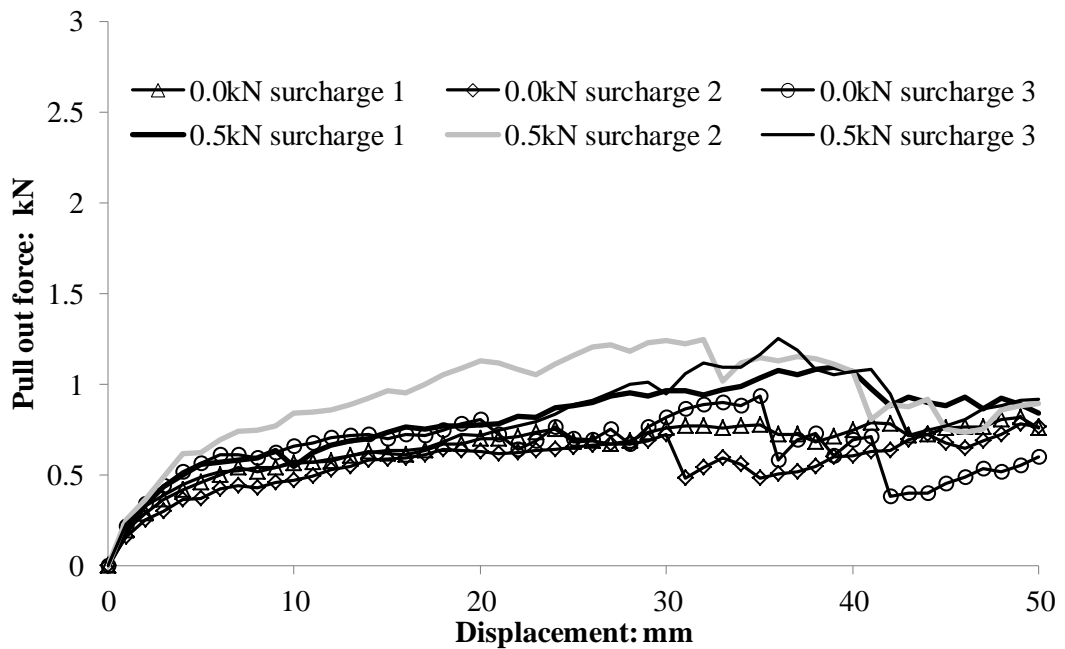


Figure 4.9 Large box pull-out test results: pull-out force against displacement for TX160 geogrid under 0.0 and 0.5 kN surcharge

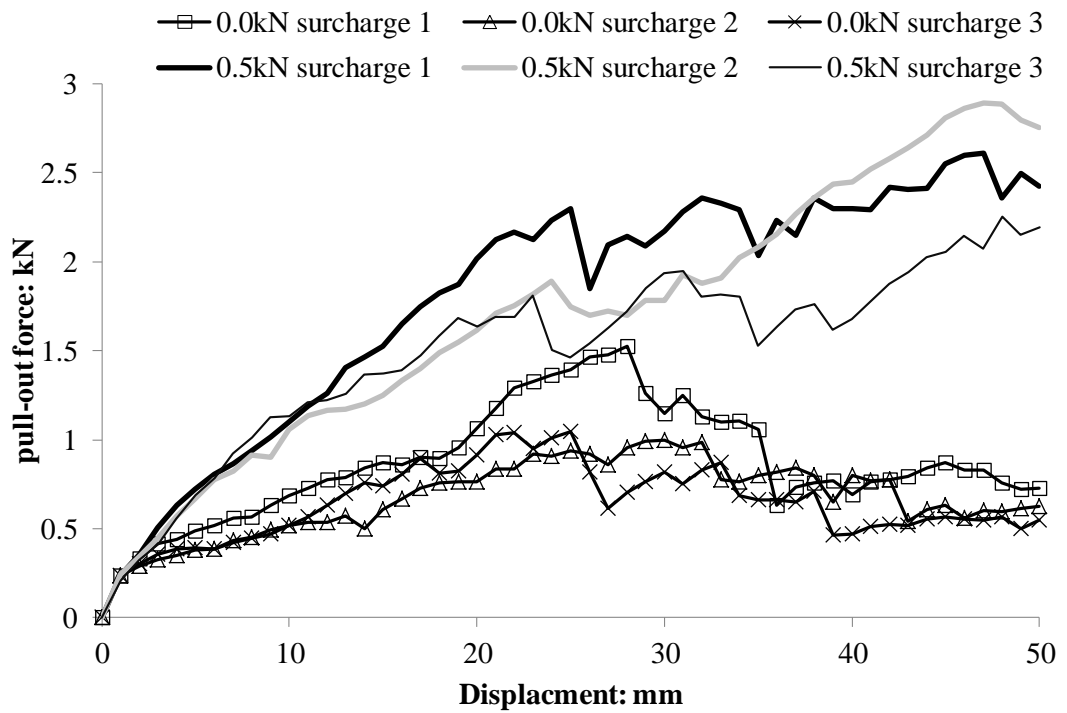


Figure 4.10 Large box pull-out test results: pull-out force against displacement for TX130 geogrid under 0.0 and 0.5 kN surcharge

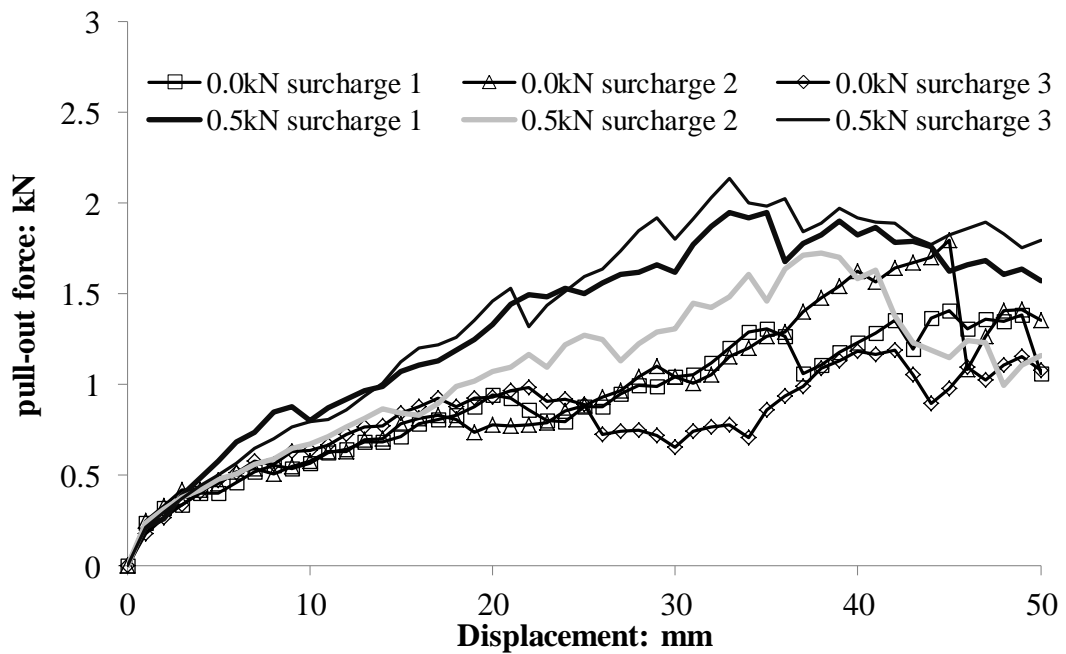
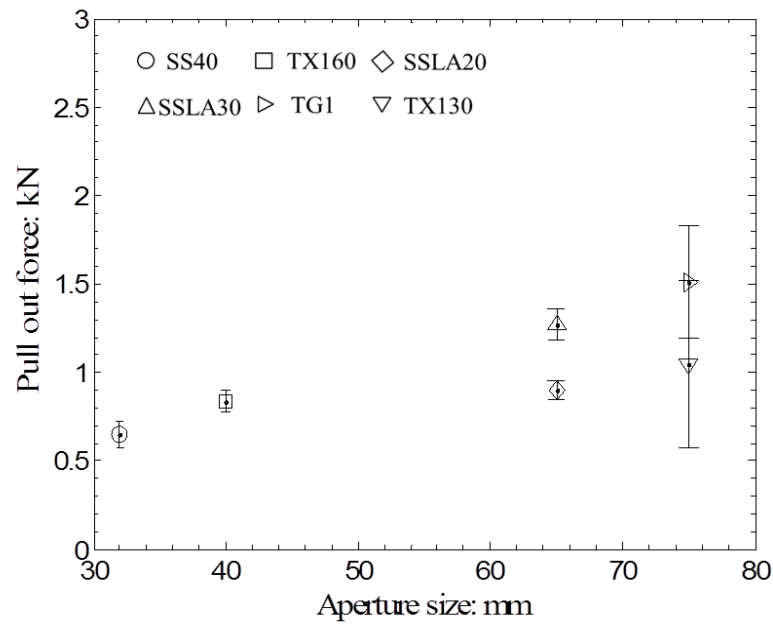


Figure 4.11 Large box pull-out test results: pull-out force against displacement for TG1 geogrid under 0.0 and 0.5 kN surcharge

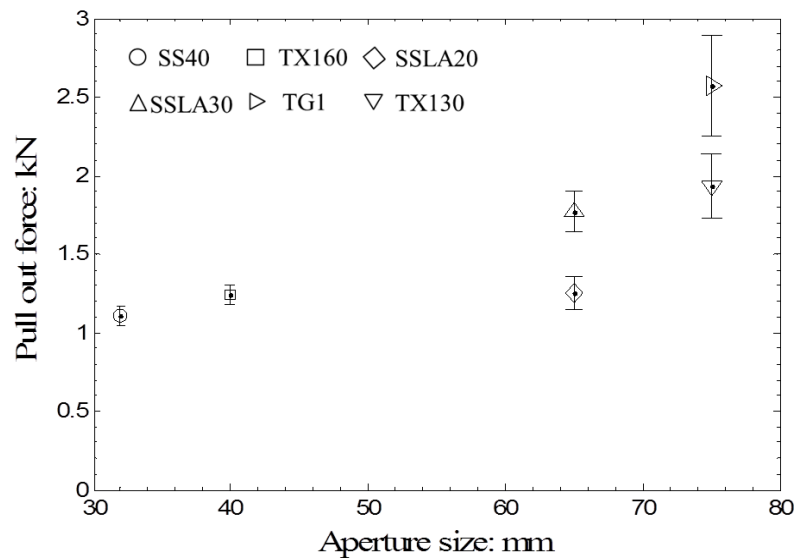
4.4 Discussion

In order to evaluate the geogrid performance effectively, the peak pull out forces for each geogrid are compared as shown in Figure 4.12. The data point (mean pull-out force) is the average pull-out force of the three repeated tests, and the upper and lower values are the maximum and minimum pull-out forces respectively. It is clear that a higher average peak force was recorded as the geogrid aperture size increased, thus confirming that the aperture size of both biaxial and triaxial geogrids have direct influence on the particle-geogrid interlock and therefore pull-out resistance. Moreover, the aperture size of SS40 is 32mm which is too small to allow proper interlock with ballast.

TG1 geogrid has the same aperture shape and size as TX130 geogrid but a different cross-sectional shape of the ribs, as detailed in Table 4.2. Taking the plane of the geogrid to be horizontal, TX130 has a horizontal rectangular cross-section and TG1 has a vertical rectangular cross-section, which makes the ribs of TG1 stiffer in bending in the vertical plane, but less stiff in bending in the horizontal plane, due to the reduced second moment of area about the axis of bending. The relative performance, in Figure 4.12, shows that the peak pull-out forces of TG1 and TX130 are essentially the same at 0kN surcharge when error bars are taken into account. TG1 offers potentially better interlock capabilities at 0.5 kN surcharge. This is likely to be attributed to the different bending stiffness of the ribs owing to the cross-section profile of the rib, as shown in Figure 4.4c and Table 4.2. Under increasing surcharge and interlock, the geogrid is restrained vertically and therefore will tend to deform along the horizontal plane. The ribs of TG1 geogrid can deform more easily in the horizontal plane of the geogrid (the Y direction), with a resulting reduced pull-out resistance compared to the TX130 geogrid.



(a)



(b)

Figure 4.12 Influence of aperture shape and size on pull-out resistance: (a) without surcharge; (b) under 0.5 kN surcharge

The other issue which may be explained by a rib profile effect is the significantly better performance of SSLA30 geogrid compared with SSLA20. SSLA20 and SSLA30 have the same square aperture size of 65mm, but the ribs of SSLA30 are thicker than that of SSLA20 (see Table 4.2), which give better ballast confinement. Comparing SS40 and SSLA20, it is evident that SSLA20 (aperture size of 65mm, rib tensile strength of 20kN/m) gave greater average interlock with the ballast particles than SS40 (aperture size of 32mm, rib tensile strength of 40kN/m) and a higher peak

force. This indicated the aperture size is dominant in interlocking compared with the thickness of ribs.

The pull-out resistance of geogrid includes two components: the interface shear resistance that takes place along the longitudinal ribs (and to a lesser extent along the transverse ribs) and the bearing resistance that develops against the front of transverse ribs (Koerner et al. 1989). As shown in Figure 4.13, TG1, Tx130, SSLA20 and SSLA30 have approximately the same area of coverage for a single reinforcing unit apart from the difference in aperture shape. Figure 4.12 shows that the triaxial geogrids (TX130, TG1) outperform the biaxial geogrids (SSLA20 and SSLA30), especially under the 0.5 kN surcharge. This improvement could be explained by the geometry in Figure 4.13. For the biaxial geogrid, most pull-out resistance comes from the bearing on the transverse ribs. For the triaxial geogrid, non-transverse ribs carry load in both the longitudinal and transverse directions giving extra resistance. Therefore, triaxial geogrids can provide more pull-out resistance than biaxial geogrids for the same geogrid area even though it spends approximately 15% more polymer material. Besides, biaxial geogrids have tensile stiffness predominantly in two directions. Triaxial geogrids have three principal directions of stiffness (Tensar, 2010), which is further enhanced by the triangular geometry providing stiffness through 360°. In these experimental tests, the pull-out directions of geogrid are kept the same. Hence, future work could investigate the effect of pull-out direction on the interaction of ballast and geogrid.

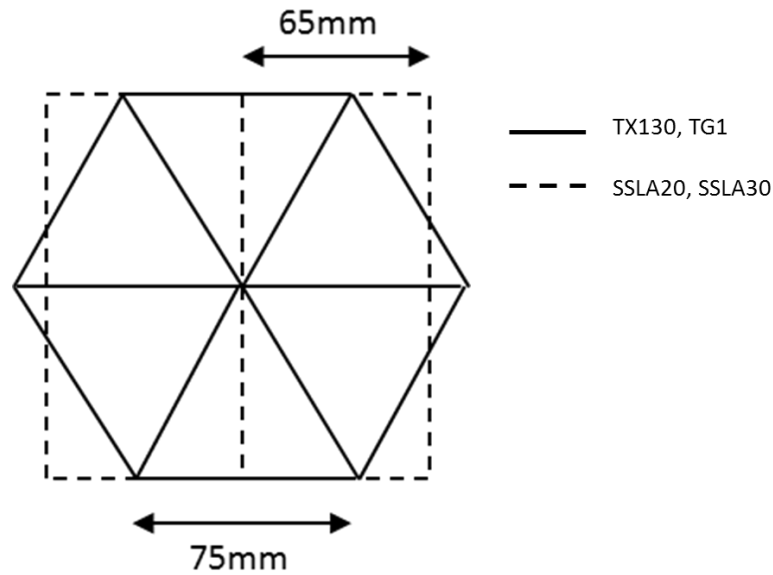


Figure 4.13 The geometry of the reinforcing units of the biaxial and triaxial geogrids

4.5 Conclusions

Laboratory large box pull-out tests have been performed on biaxial and triaxial geogrids embedded within a ballast sample. The pull-out force has been measured as a function of displacement for the different grids and under different surcharges. Experimental results indicate that geogrid aperture size plays a more influential role than the tensile strength or the thickness of the ribs. A higher average peak force was recorded as the geogrid aperture size increased from 32mm to 75mm, thus confirming that the aperture size of both biaxial and triaxial geogrids have direct influence on the particle-geogrid interlock and therefore pull-out resistance. The triangular aperture, coupled with a vertical rectangular rib cross-section and junction efficiency, gives greatly improved ballast confinement and interaction compared to biaxial grids. For the biaxial geogrid, most pull-out resistance comes from the bearing on the transverse ribs. For the triaxial geogrid, non-transverse ribs carry load in both the longitudinal and transverse directions giving extra resistance. Therefore, triaxial geogrids can provide more pull-out resistance than biaxial geogrids for the same geogrid area. For the 40mm ballast that was used, the optimum geogrid is triaxial geogrid with aperture size 75mm.

Chapter 5 Geogrid modelling using PFC^{3D}

5.1 Preliminary study

Zhang et al. (2008) have demonstrated pull-out test simulations in PFC^{2D} using a geogrid consisting of a string of bonded particles. This approach ignores the significant influence of the transverse ribs on the pullout resistance verified by Mulabdic and Minazek (2010) on the basis of laboratory tests. Hence, it follows that only the 3-dimensional case is appropriate to simulate soil-geogrid interaction. As introduced in Section 3.6, Konietzky et al. (2001) built up the geogrid of aperture size 65mm using spherical particles bonded together by contact and parallel bonds. The contact bond acts only at the contact point and can transmit only a force, while the parallel bond acts over a circular cross-section between the two particles in contact and transmit both a force and a moment. The mechanical behaviour of geogrids under tension and torsion loading can be determined and quantified according to Koerner (2005) using standardized laboratory tests (single rib test, single junction strength test and in-plane rotation test). It should also be noted that the numerical geogrid with 9 cells (see Figure 3.7) consists of approximately 31,000 particles (Konietzky et al., 2004), which means the computational time is greatly extended. Further studies by Qian et al. (2011) and Ferellec and McDowell (2010) have demonstrated the possibility of modelling geogrids by using wall elements (Figure 5.1). However, preliminary work should first be performed on the geogrid model to take into account its flexibility.

At the preliminary stage of this research, the geogrid model using walls and the single-ball geogrid model (Figure 5.2) were used. However, neither of them is considered a good geogrid model to reproduce the real geogrid behaviour. For the

geogrid using walls, the geogrid doesn't have any deformation and gravity in PFC^{3D}. For the single-sphere geogrid model, Figure 5.2 shows the view of the single-ball geogrid in form of the arranged particles and the parallel bonds between them. The simulation results show the single-sphere geogrid cannot reveal the real deformation behaviour of geogrid. Therefore, a new geogrid model generation needs to be developed. Ferrellec and McDowell (2012) proved that the performance of two layers of spheres in a cross-section of rib was better than a single layer of spheres and single row of spheres. However, the geogrid model used reduces the accuracy of geometrical shape and also ignores the different bending stiffness of geogrid rib along horizontal and vertical planes. Therefore, a new two-layer geogrid model has been generated, and also the micro parameters have been calibrated in this chapter.

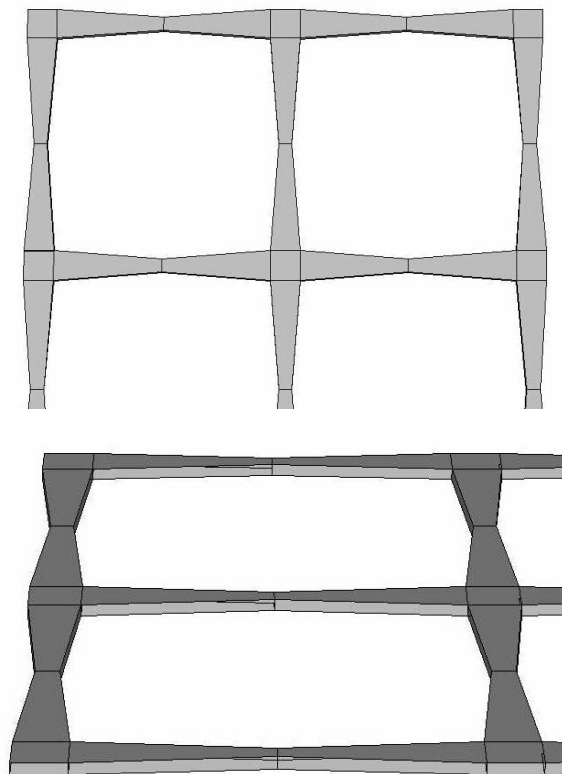
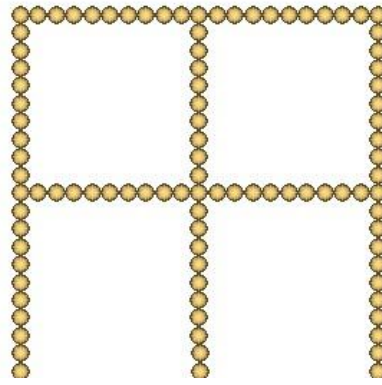
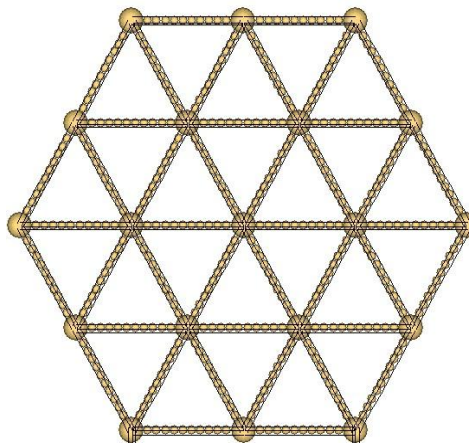


Figure 5.1 Numerical biaxial geogrid model using walls (Ferrellec and McDowell, 2010)



(a)



(b)

Figure 5.2 Numerical single-sphere geogrid models: (a) biaxial geogrid; (b) triaxial geogrid with parallel bonds

5.2 Biaxial geogrid

5.2.1 Numerical modelling procedure

Figure 5.3a shows a new two-layer geogrid model for the Tensar biaxial geogrid, comprising 816 small particles for each aperture. The model set-up was performed first by creating the nodes and then by adding the ribs between the nodes. The ribs comprise balls of different size, with smaller balls at the centre of the ribs, to give the required geometry. A continuous slight decrease of the particle radii from the junction to the centre of each rib is considered. All particles are bonded together by parallel bonds, which act over a circular cross-section between the two particles in

contact and transmit both a force and a moment (Itasca, 2003). It should be noted that, because the bending resistances of ribs along the transverse and longitudinal directions are significantly different, the parallel bonds along the X and Y directions (black), as shown in Figure 5.3b, differ from the parallel bonds along the Z direction (red). The parameters will be calibrated in the following subsection.

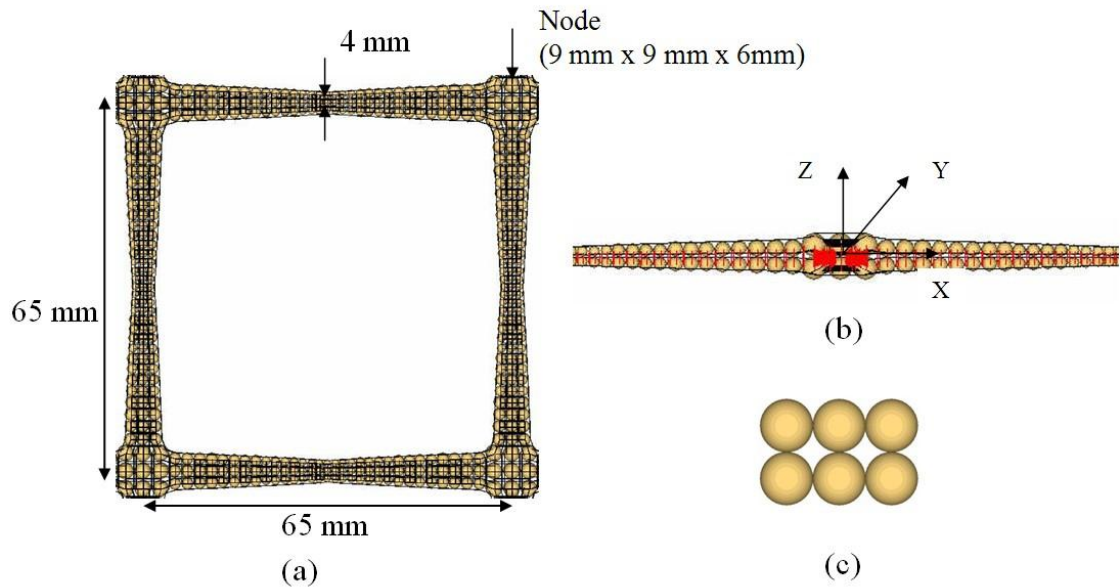
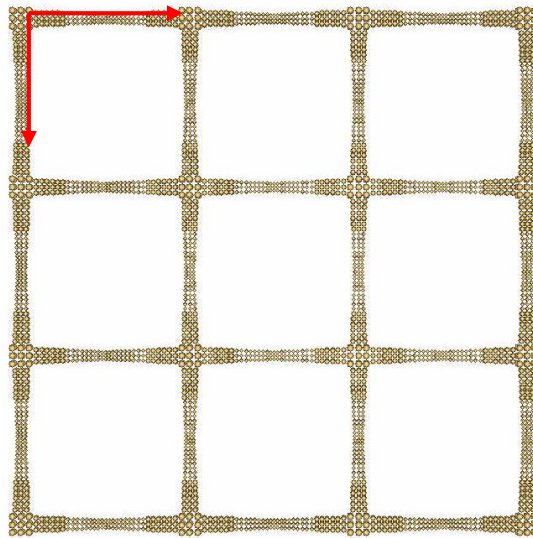


Figure 5.3 Discrete element model of geogrids: (a) aperture of biaxial geogrid and parallel bond locations (black); (b) side view between nodes; (c) cross-section of rib

The system to generate the geogrid in PFC^{3D} is composed of basic square elements which create a simple junction with a rib in both longitudinal and transverse directions. Hence it follows that because of the high flexibility, this system can be used for setting up geogrids with different geometrical properties (e.g. aperture size) and for generating specific specimens which are required in calibration, pull-out tests and box tests. Based on the geometrical properties of the selected biaxial geogrid (SSLA30, as shown in Figure 5.4a), 4752 particles are necessary to create one sample with nine meshes (Figure 5.4b).



(a)



(b)

Figure 5.4 Biaxial geogrid with 16 nodes and 9 meshes: (a) laboratory geogrid sample; (b) PFC^{3D} geogrid model

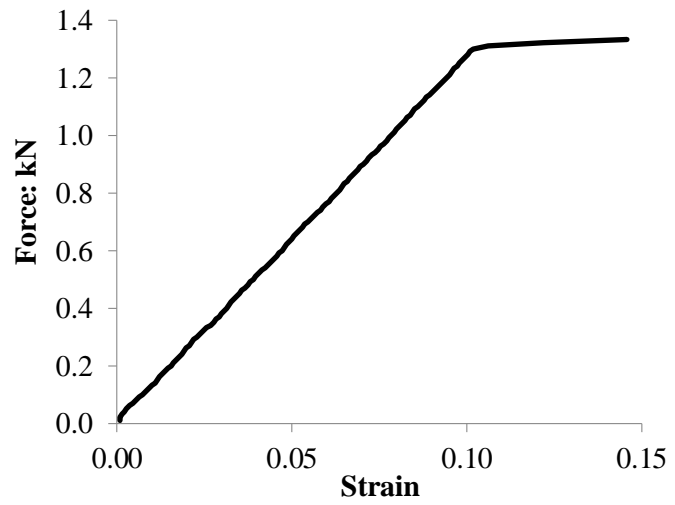
5.2.2 Calibration tests

According to Konietzky et al. (2004), the parameters for the geogrid were calibrated by three different tests: a single rib test, a single junction test and an in-plane rotation test. The force at failure for a single rib test is 1.37 kN at a failure strain of 10.5% and the force at failure for a single junction test is 1.26 kN at a failure strain of 9.2%. For an in-plane rotation test, the in plane rotation stiffness is 0.79 Nm/degree. The calibration was performed in terms of stiffness and strength. Figures 5.5 and 5.6

show the tension test geometries and simulation results. The single junction test was modelled using three nodes. The upper node was fixed to simulate the junction clamp and a constant velocity was applied at the lower row of particles. The same model as used for the single junction test was used to model the single rib test. A constant velocity was applied at both the upper and lower rows of particles of rib nodes. The axial strain and the resulting forces at the upper and lower rows of particles were monitored during the test. The parallel bond is depicted as a cylinder of elastic material in PFC^{3D}. So the geogrid model has such a linear elastic-perfectly behaviour as shown in Figure 5.5b and 5.6b. Experiments show some minor plastic deformation at larger strain but these are considered negligible for the purpose of these simulations. The numerical in-plane rotation test, as shown in Figure 5.7, was then performed to match the experimental results as much as possible. It clearly shows the deflection of ribs during the rotation test (Figure 5.7c). The four circles (cylindrical walls) and the adjoining plane walls are used to define a rigid block with no sharp corners, and used to rotate the grid. The movement of these walls (i.e. the block) defines the rotation and the rotational rigidity was given by the trend line as shown in Figure 5.7b, which is a simple line of best fit. The initial deviation from the trend line is due to the behaviour of the discrete geogrid at the corner as marked. It should be noted that it was not possible to fit all three calibration tests using the same set of parameters. Therefore the chosen set of parameters is based mainly on the calibration of the single junction tests and the single rib tests because the rotational rigidity of geogrid has a little influence on the performance (TRI/Environmental, 2001). Although this match of in-plane rotation test is not perfect, the calibrated set of parameters as shown in Table 5.1 was used in the simulations. It seems that a better calibration of grid would not change the general behaviour in terms of aggregate-grid interlock. These micromechanical parameters can be subdivided into deformation parameters (parallel bond stiffnesses) and strength parameters (parallel bond strengths).



(a)

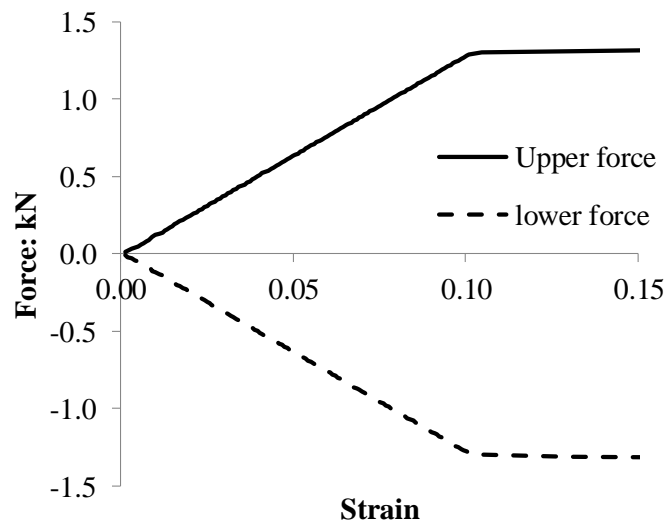


(b)

Figure 5.5 Single junction test: (a) test geometry test geometry and velocity vectors during the test; (b) force-strain plot

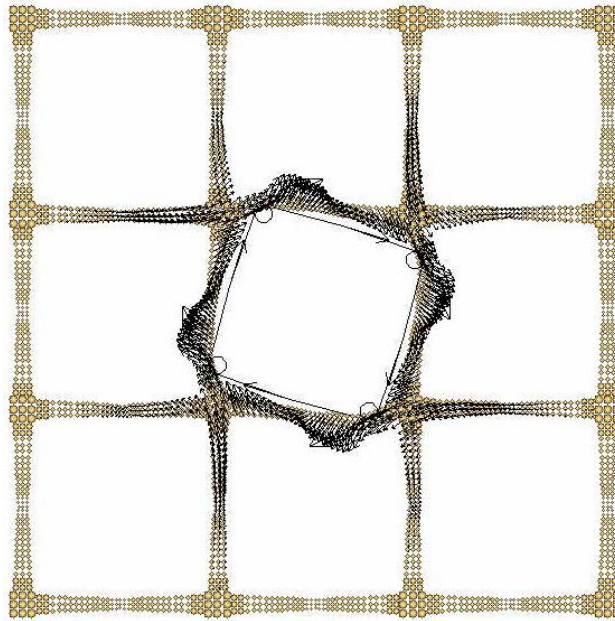


(a)

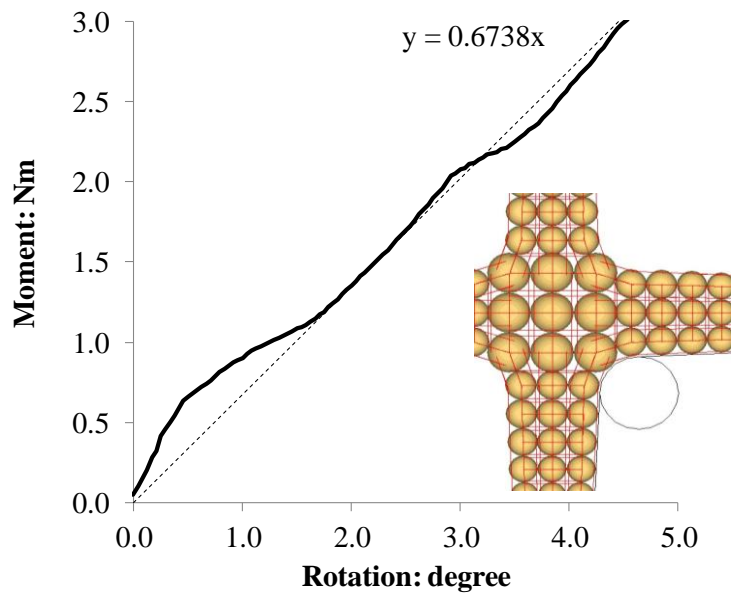


(b)

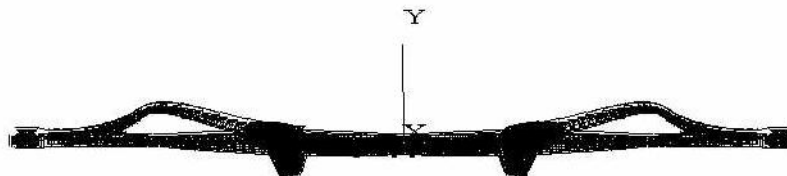
Figure 5.6 Single rib test: (a) test geometry and velocity vectors during the test; (b) force-strain plot



(a)



(b)



(c)

Figure 5.7 In-plane rotation test: (a) test geometry and velocity vectors during the test; (b) Moment Vs angle of rotation; (c) deflection of ribs from side view

Table 5.1 Micromechanics parameters for geogrid model (Chen et al. 2012)

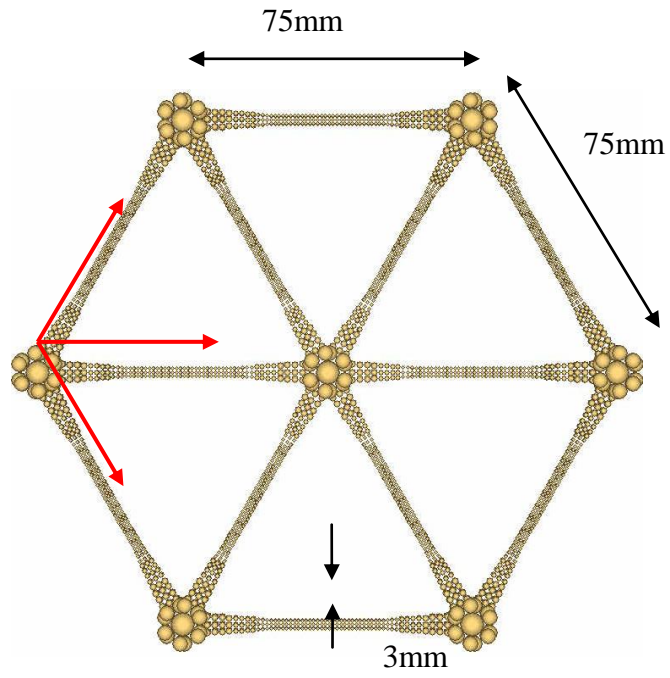
Parameters	Unit	Value
Parallel bond radius	mm	1.0
Parallel bond normal stiffness (LD)	N/m	4.2e11
Parallel bond shear stiffness (LD)	N/m	5e5
Parallel bond normal strength (LD)	N	1.53e8
Parallel bond shear strength (LD)	N	1.2e7
Parallel bond normal stiffness (TD)	N/m	4e9
Parallel bond shear stiffness (TD)	N/m	5e5
Parallel bond normal strength (TD)	N	1.57e7
Parallel bond shear strength (TD)	N	1e7
Friction angle:	Degree	31

* LD: longitude direction; TD: transverse direction

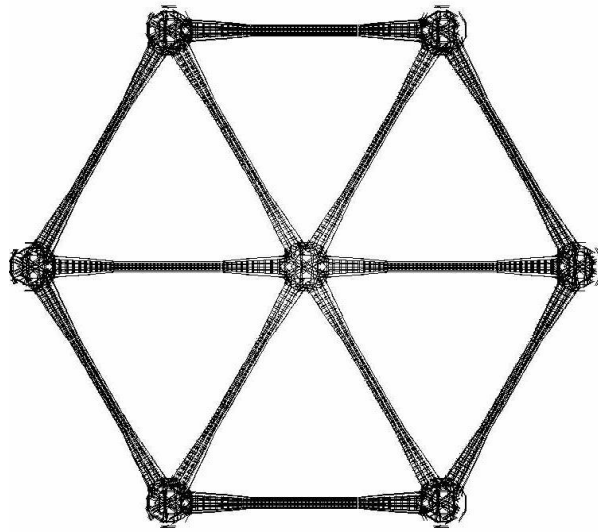
5.3 Triaxial geogrid

Figure 5.8 shows a new two-layer geogrid model for the Tensar triaxial geogrid. The model set-up was performed first by creating the nodes and then by adding the ribs between the nodes. A continuous slight decrease of the particle radii from the junction to the centre of each rib is considered. In addition, twenty five particles have been added between the ribs at each junction to support the rigidity under torsional loading. Similarly, all particles are bonded together by parallel bonds.

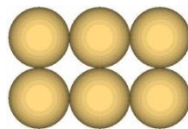
The system to generate the geogrid in PFC^{3D} is composed of basic triangular elements which create a simple junction with a rib in all three directions, as shown in Figure 5.8a. Hence it follows that because of the high flexibility, this system can be used for setting up geogrids with different geometrical properties (e.g. aperture size) and for generating specific specimens which are required in box tests. Based on the geometrical properties of the selected triaxial geogrid TX130 (Figure 5.9a), 11,657 particles are necessary to create one sample with 20 triangular meshes (Figure 5.9b). Due to fewer data of standard triaxial geogrid laboratory tests, the triaxial geogrid model is not calibrated in this project. It was given the same micromechanical parameters as the biaxial geogrid in order to investigate the effect of aperture shape of the geogrid on reinforced ballast performance in box test simulation.



(a)

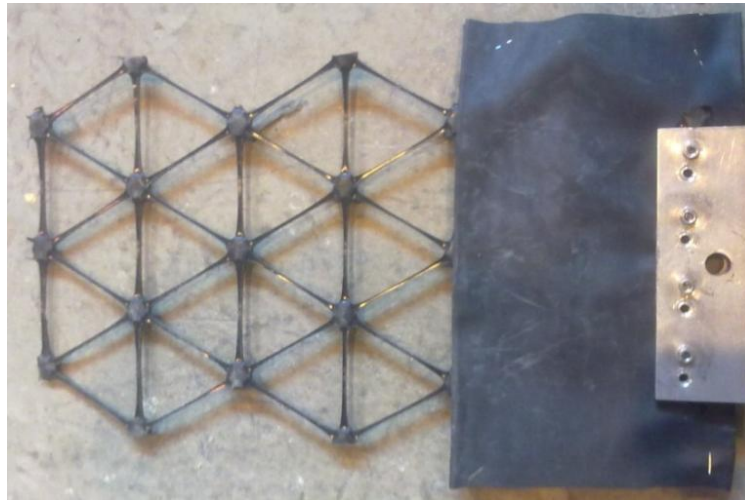


(b)

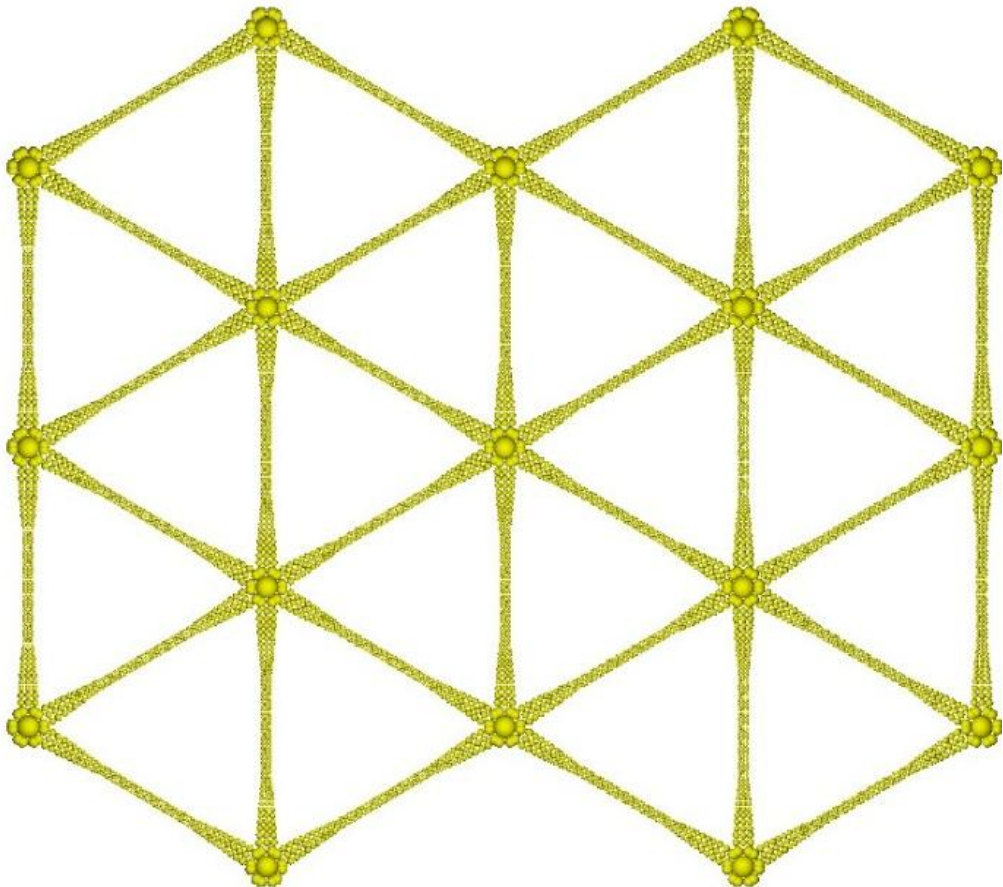


(c)

Figure 5.8 DEM of triaxial geogrid: (a) particle model; (b) parallel bond model; (c) cross-section of rib



(a)



(b)

Figure 5.9 Triaxial geogrid with 17 nodes and 20 meshes: (a) laboratory pull out test geogrid sample; (b) PFC^{3D} geogrid model

5.4 Conclusions

The performed modelling of the new two-layer geogrid has demonstrated that PFC is able to reproduce the deformation and strength characteristics of geogrids at least before reaching the maximum strength values (pre-failure-region). The main characteristics like the load-deformations behaviour, the rotation rigidity, the tensile strength and shear strength of the biaxial geogrid were reproduced by parallel bonds in PFC^{3D}. Further triaxial geogrid standard laboratory tests and calibration are necessary to simulate the triaxial geogrid model.

Due to the fact that the geogrid model is computationally very time-consuming, at present the modelling of a whole practical application (e.g. a slope or railway reinforcement) with detailed modelling of hundreds or thousands of geogrid-meshes is beyond the current computer capabilities. However, the physics of the interlocking mechanism can be studied on a few meshes only in the following simulations, such as pull out test, box test and composite element test simulations. Besides, the geogrid model allows a unique graphical demonstration of the interlocking mechanism which can be used to convince clients about the advantages and the physical behaviour of a geogrid system. It will also enable the user to model other possible prototype geogrids using DEM, to investigate their performance before investing money in the manufacture of such geogrids.

Chapter 6 Discrete element modelling of large box pull-out test

6.1 Introduction

The Discrete element Method has been used for simulating complex soil/aggregate geogrid interaction (Konietzky et al. 2004; McDowell et al. 2006; Zhang et al. 2007, 2008). This numerical simulation approach is fully capable of modelling the interaction of ballast particles and the geogrid by accounting for the aggregate particle shape, reproducing the actual geometry of geogrid and assigning proper properties for the particles and geogrids. In this methodology, force displacement laws for different element bonding conditions and the laws of motion govern the movement and contacts of each element (ball and wall).

Zhang et al. (2007) presented DEM simulations of geogrid pull-out behaviour using PFC^{2D} and compared with experimental results and showed some agreement. However, the 2D geogrid model consisting of a string of bonded particles ignores the significant influence of the transverse ribs on the pull-out resistance. Hence, it follows that only the 3-dimensional case is appropriate to simulate particle-geogrid interaction. Wilson-Fahmy et al. (1994) predicted components of pull-out resistance against pull-out displacement expressed as a percentage of ultimate resistance from theoretical analysis. Figure 6.1 clearly shows the tendency of the pull-out resistance components. Initially, most of the shear resistance is taken by friction along the longitudinal ribs. The component of longitudinal friction decreases as pull-out displacement increases, whilst the component of bearing resistance which is the same as the passive resistance increases, and the transverse friction component is comparatively stable. The importance of modelling ballast particle shape in DEM was investigated by Lu and McDowell (2007) in terms of the load-deformation

response and also by Lim and McDowell (2005). Recent work by Konietzky et al. (2004) and McDowell et al. (2006) focused on aggregate and geogrid interactions and modelling confinement effects. The findings of DEM studies covered interaction between geogrids and surrounding soil/aggregate in both triaxial and small box pull-out tests, contact force distributions, deformations and particle rearrangements. The simulations demonstrated the development of strong contact forces in the vicinity of the geogrid area, due to interlocking. They also found that a well-defined reinforced zone could be seen approximately 10cm above and below the geogrid, although this is expected to depend on aggregate size and geogrid type.

This chapter presents large box pull-out test simulation with biaxial geogrid. Four different shapes of clumps were used to represent each ballast particle to obtain an acceptable shape for modelling railway ballast. The two-layer biaxial geogrid model as described in chapter 5 is tested. The geogrid-reinforced system is then modelled in simulated large box pull-out tests and compared with experimental results in chapter 4, in order to obtain valuable insight into the interlocking mechanism of geogrid-reinforced ballast.

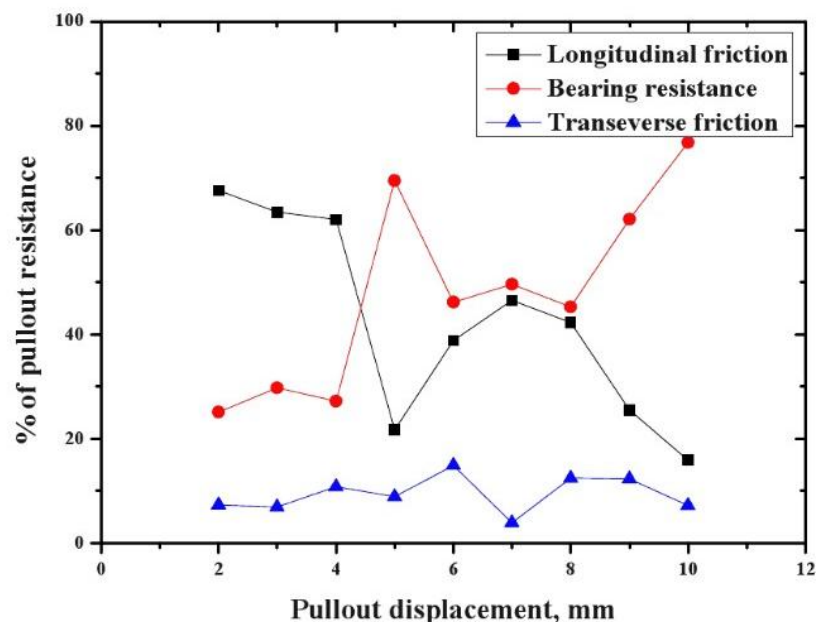


Figure 6.1 Predicted components of pull-out resistance (Zhang et al. 2008)

6.2 Modelling ballast particle shape

Particle shape plays a key role in the behaviour of railway ballast. It influences not only the physical state of the assembly (skeleton and porosity) but also the particle interaction (interparticle friction, contact force and coordination number). In the past, various attempts have been made to characterise particle shape for railway ballast. However, due to the complexity and irregularity of the particle shapes, universally accepted effective shape characteristic parameters have not yet been established. In the railway industry, various shape characteristics (i.e. flakiness, elongation, roughness, angularity and surface texture) are used.

Barrett (1980) reviewed various approaches to analyze particle shape in geology and sedimentology and expressed the shape of a particle in terms of three independent properties, namely form (overall shape), roundness (large-scale smoothness) and surface texture, as shown in Figure 6.2. It should be noted that each of these aspects of shape can itself be represented by more than one dimension. Form reflects variations in the particle scale, while roundness reflects variations at the corners. Surface texture is a property of particle surfaces between and at the corners. To model the angular shapes of ballast particles and also investigate the effect of particle shape on performance, four different shapes of clumps were constructed as shown in Figure 6.3. The two-ball clump is used, following Powire et al. (2005). The 4-ball tetrahedral clump is rounder than the 2-ball clump. The surface texture of 8-ball tetrahedral clump is rougher than the 4-ball tetrahedral clump. The 8-ball flaky clump represents the particle of rectangular form. The dimensions of these clumps are shown in Table 6.1. It should be note that the volumes of these four clumps are the same as a single sphere of radius 20mm.

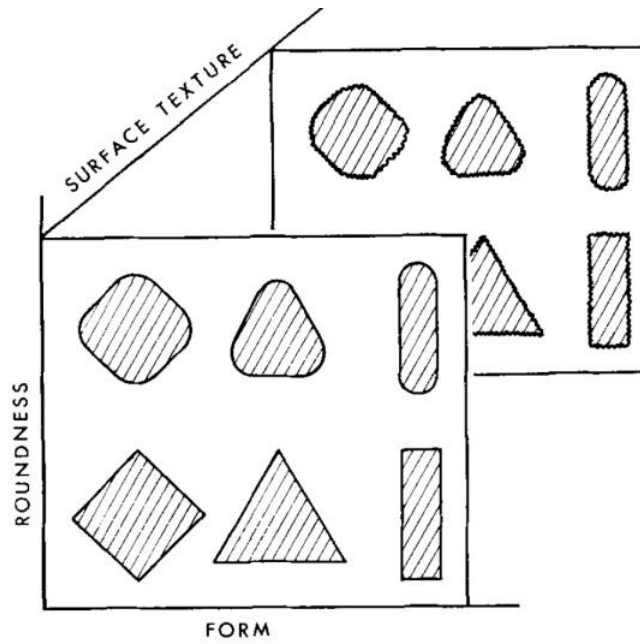


Figure 6.2 A simplified representation of form, roundness and surface texture by three linear dimensions to illustrate their independence (Barrett, 1980)

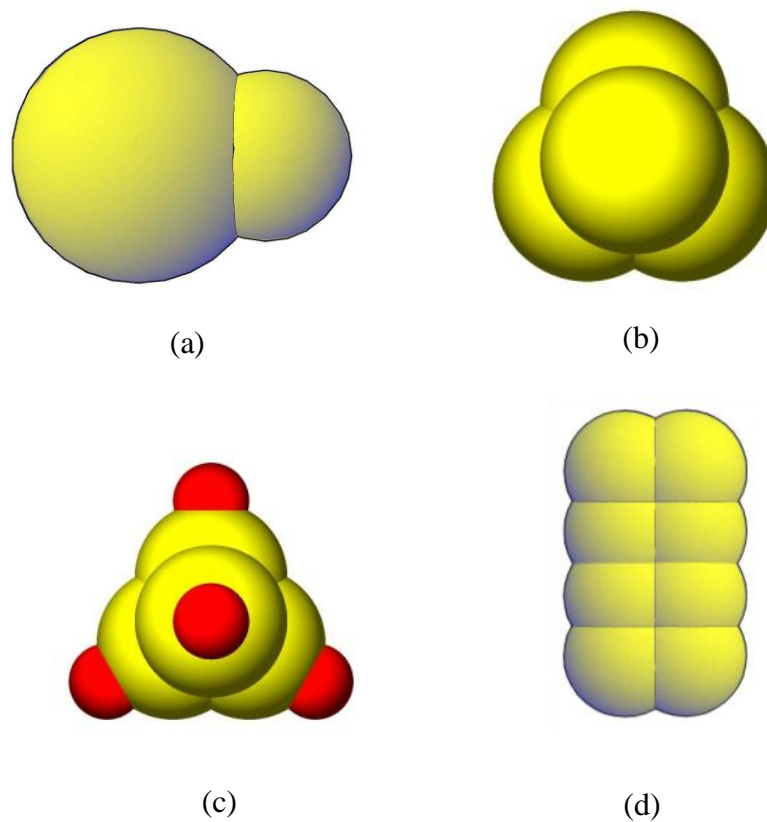


Figure 6.3 Clumps tested in the simulations: (a) 2-ball clump; (b) 4-ball tetrahedral clump; (c) 8-ball tetrahedral clump and (d) 8-ball flaky clump

Table 6.1 Sizes of the tested clumps

Ballast particle shape	Single sphere	2-ball clump	4-ball tetrahedral clump	8-ball tetrahedral clump	8-ball flaky clump
Radius of balls in clump (mm)	R= 20	R _{large} = 18.8 R _{small} = 12.5	R= 14.1	R _{large} = 13.6 R _{small} = 6.8	R= 11.7

6.3 Particle-pouring test simulation

Kwan (2006) showed that for an experimental test in which one flat ballast particle surface was sheared past one another, a particle-particle friction coefficient of approximately 0.6 ($\tan 31^\circ$) was obtained. Figure 6.4 shows a heap of 736 two-ball clumps deposited from a hopper with a 25cm square aperture, 0.7m above the base wall. The spreading of the simulated material demonstrates a realistic physical behaviour of the clumps. The critical state angle of shearing resistance or angle of repose is a function of the ball-ball coefficient of friction and the particle shape. Figure 6.5 shows the ballast heaps using different particle shapes. The heap of spheres of radius 20mm was simulated for comparison. The coefficients of friction for the balls are all set to be 0.6 in order to ignore the influence of the ball-ball friction coefficient. The coefficient of friction for the base wall is also set to be 0.6.

For the heap of spheres or 2-ball clumps, it was possible to calculate the porosity directly using a measurement sphere in PFC^{3D}. However, no facility is available in PFC^{3D} for calculating the porosity of a sample of clumps comprising more than two particles within each clump. Therefore the porosities of the heaps were estimated using a 3-D grid of 9×10^6 small cubes, each of side 0.5mm, in the column directly below the top of the heap (Figure 6.5b). By comparing the porosities of a heap of spheres calculated by PFC^{3D} and MATLAB, it is estimated that the percentage error in the porosity was less than 4%. This was deemed acceptable.

Table 6.2 lists the angles of repose and porosities of the heaps for each aggregate of clumps. There are no results available for particle pouring test. It is to be noted that even recycled ballast exhibits a basic friction angle approximately of 40° . If the slope isn't constant, a visual estimate is made for the particles over the surface of the sample. The angles of repose resulting from the numerical simulations with the 2-ball clumps and 4-ball tetrahedral clumps show agreement with the angle of shearing resistance of real ballast (typically around 40°). In case of the 8-ball tetrahedral clumps and 8-ball flaky clumps, the angle of repose ($43-44^\circ$) is higher. There are some large voids in the middle of heaps resulting from the interlocking of the complex, angular clumps.

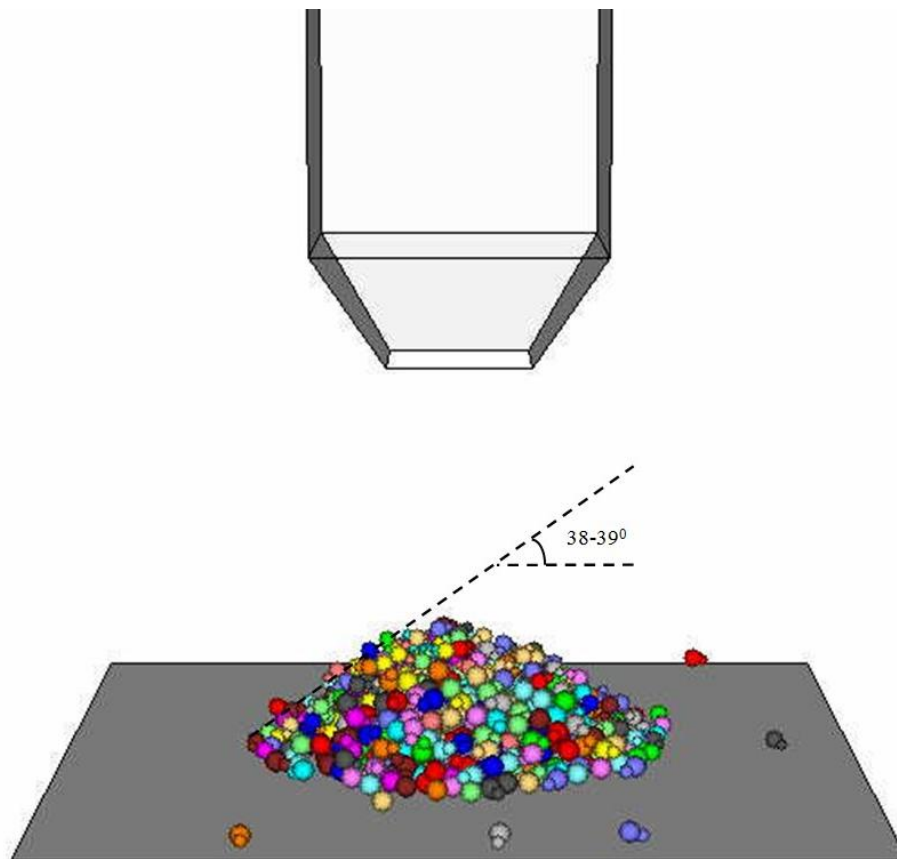


Figure 6.4 Numerical model of the ballast-pouring test using PFC^{3D} two-ball clumps

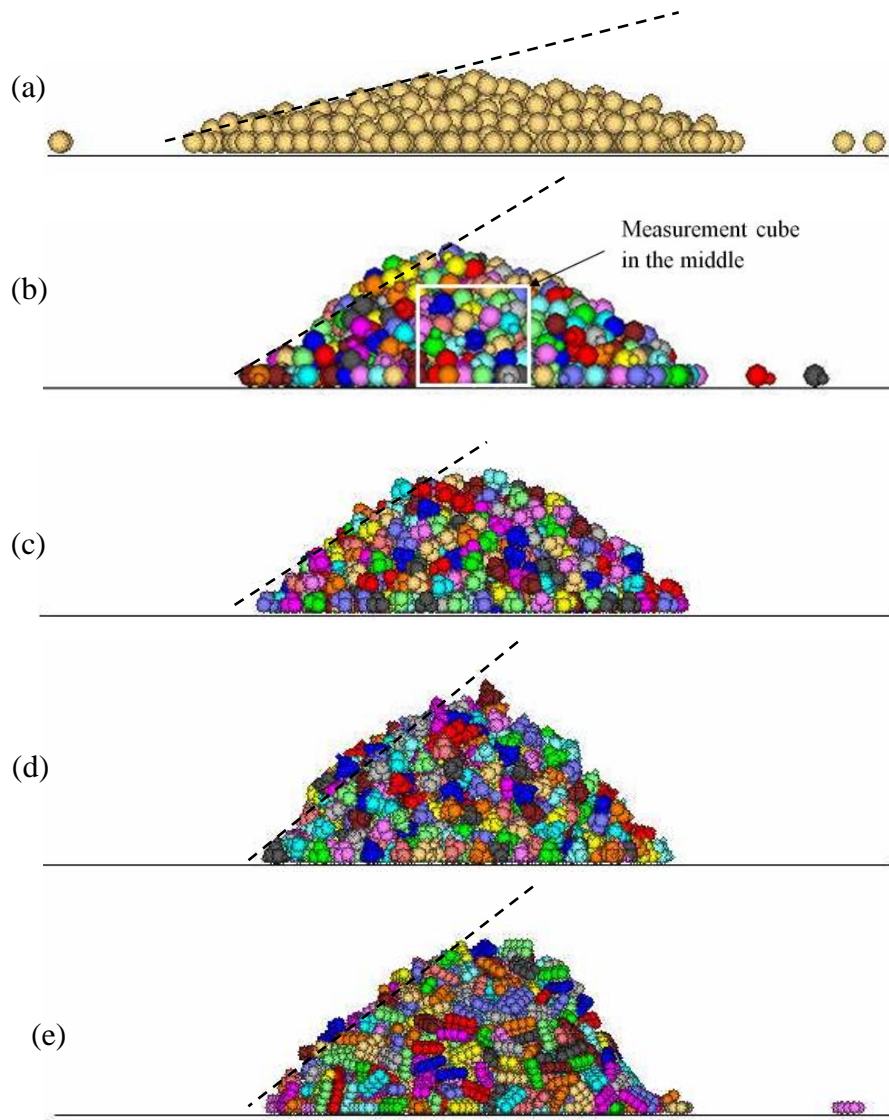


Figure 6.5 Ballast heap simulations using different particles: (a) sphere; (b) 2-ball clump; (c) 4-ball tetrahedral clump; (d) 8-ball tetrahedral clump and (e) 8-ball flaky clump

Table 6.2 The angle of repose and porosity of each heap

Ballast particle shape	Angle of repose	Porosity in the middle
Single sphere	15-16 °	0.409
2-ball clump	38-39 °	0.426
4-ball tetrahedral clump	39-40 °	0.447
8-ball tetrahedral clump	43-44 °	0.499
8-ball flaky clump	43-44 °	0.499

6.4 Numerical modelling procedure

Figure 6.6 shows the biaxial geogrid model in the pull-out test simulation of aperture size 65mm, comprising 6672 parallel bonded balls. The effective geogrid area has 12 square apertures, which is consistent with the experimental tests. The generation and micromechanical properties of the geogrid model were presented in Section 5.2. Figure 6.7 shows the numerical model for the large box pull-out test and the specimen of 2-ball clumps with the embedded geogrid under a 0.5kN surcharge. Single-sized clumps were used even though the size distribution plays an important role for mechanical behaviour. This can be considered satisfactory as ballast is usually reasonably uniformly graded ($D_{60}/D_{10} \approx 1.4$) to provide large enough voids to facilitate good drainage. The dimensions of the pull-out box and the geogrid size and position are the same as those used in the laboratory experiments.

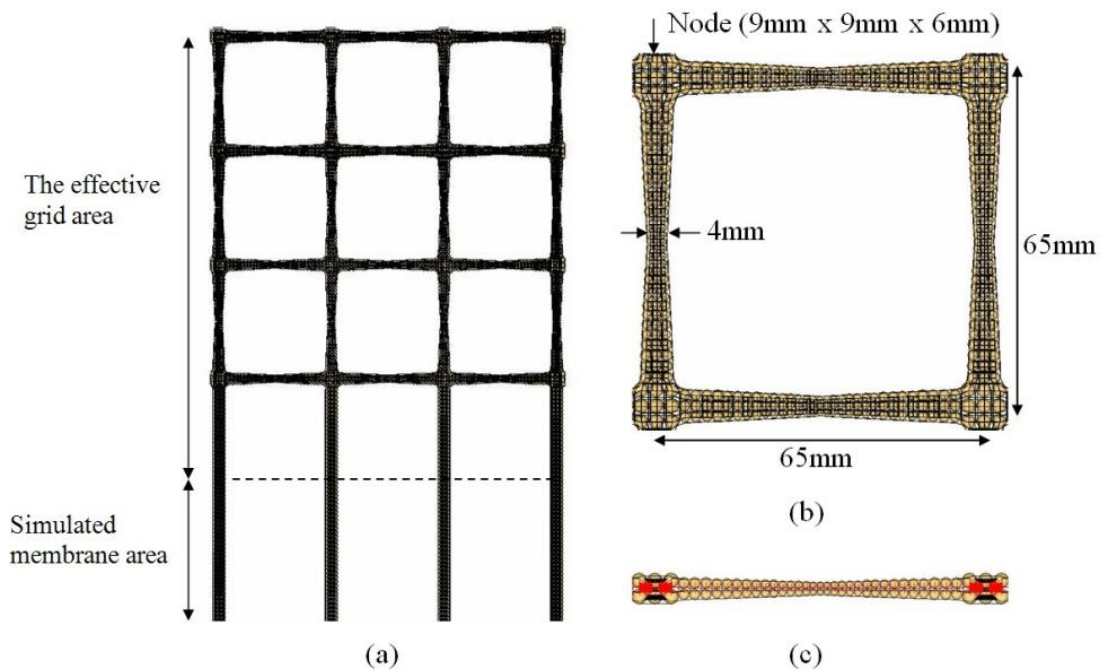
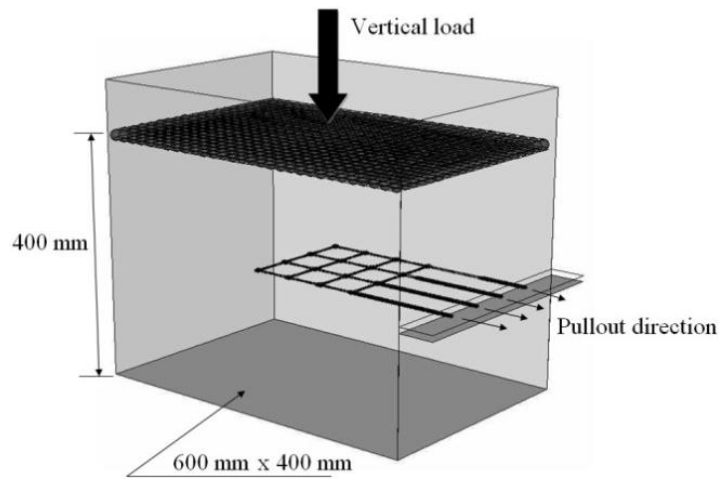
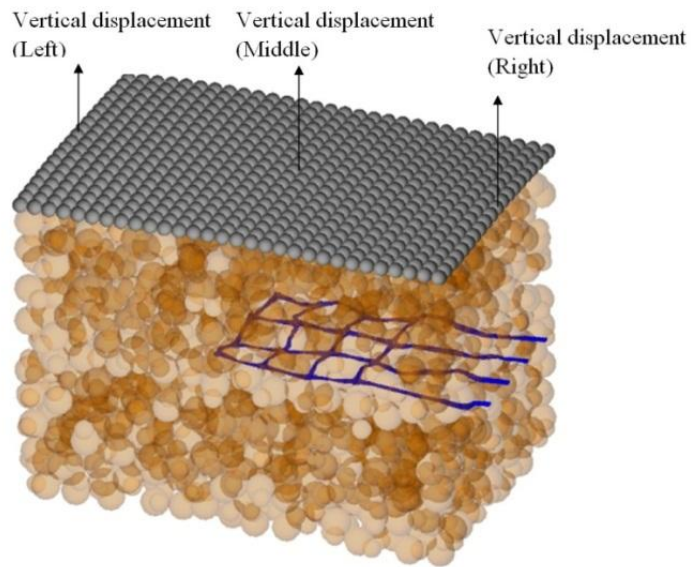


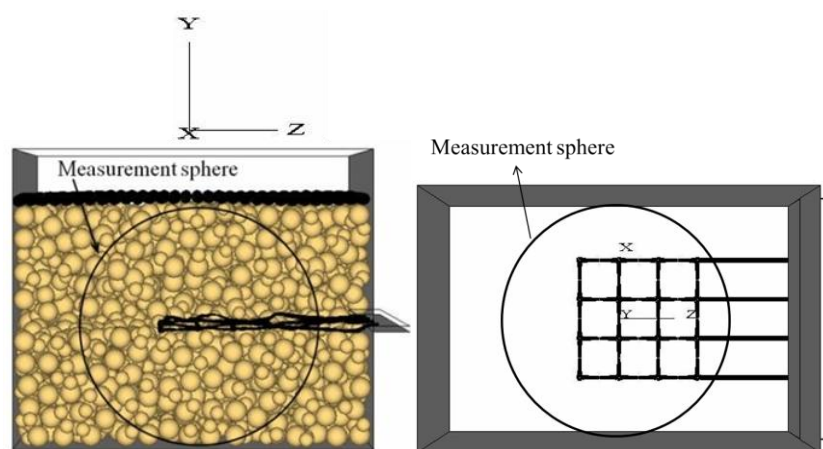
Figure 6.6 Discrete element model of geogrids: (a) biaxial geogrid model; (b) aperture of biaxial geogrid; (c) side view



(a)



(b)



(c)

Figure 6.7 DEM of large box pull-out test: (a) embedded geogrid specimen and simulated surcharge; (b) specimen of two-ball clumps under 0.5kN surcharge; (c) measurement sphere in PFC^{3D}

The DEM sample preparation procedure followed the experimental sample preparation. At the beginning, an initial sample of spheres was generated within the top of the box without overlapping and the spheres were then expanded to their final size (40 mm). After that, the position of each sphere was found, and the spheres were replaced by the 2-ball clumps or other clumps with the same volume, which were given random orientations. The clumps were directly deposited in the pull-out box and cycled to equilibrium under a changing gravitational acceleration which was reduced gradually from 98.1 m/s^2 to 9.81 m/s^2 followed by a monotonic compaction with a horizontal wall to densify the sample. The clumps located higher than the centre of the slot were then deleted. Afterwards, the remaining sample below the slot was compacted using cyclic loading by a horizontal wall. The geogrid specimen was then installed at the centre of the slot, with the geogrid protruding outside of the slot. Two frictionless walls were generated near the slot above and below the grid (Figure 6.7a) to prevent the geogrid layer from overlapping with the right-hand walls above and below the aperture during pull-out. Because of the “soft contact” approach in PFC^{3D}, balls and walls overlap to give contact forces and it is possible for balls to penetrate through walls according to the contact law. This would artificially increase the pull-out resistance if the “membranes” above and below the grid were not installed to prevent particles from becoming trapped around the aperture. The upper half sample was again generated using the same expansion method, replaced by the clumps. After that, the whole sample was compacted and cycled to equilibrium. In the experimental pull-out test, a wooden block slightly smaller than the internal dimensions of the box was placed to distribute the surcharge. Similarly, a simulated block that consists of 600 parallel bonded balls was used at the top surface to apply a vertical load, as shown in Figure 6.7a. The parallel bond stiffness (uniformly distributed over the bond area) is 600 MPa/m. The parallel bond normal strength and shear strength are both set to 100MPa. The spheres around the perimeter of the simulated block are smooth to prevent trapping between the simulated block and the pull-out box. The constant surcharge was provided by the self-weight of the loading spheres using an appropriate density for these spheres to give the required surcharge.

The volume of the clump is equal to a single sphere of radius 20mm, so the total volume of the clumps V_{cl} is computed. The porosity n of the sample can be calculated with the total volume of the specimen V_{tol} by

$$n = 1 - \left(\frac{V_{cl}}{V_{tol}} \right) \quad (6.1)$$

The initial porosity of sample in lab is approximately 0.44. The numbers and sizes of particles for the four simulated samples are listed in Table 6.3. The porosity of the sample of 8-ball clumps is a bit higher but shows good agreement with the lab tests. Besides, porosity in particle-pouring test (Table 6.2) may be larger than the initial porosity of the pull-out test specimen after compaction. However, in the 2-ball clump model, the porosity in particle-pouring test is smaller than the initial porosity of the pull-out test specimen after compaction. That is because of the interlocking effect of the geogrid in the pull-out specimen, which leads to more voids in the geogrid/ballast interaction zone.

Table 6.3 Numbers of particles and initial porosity for each sample

	Ballast particle shape	Number of clumps	Initial porosity (n)
Sample 1	2-ball clump	1605	0.44
Sample 2	4-ball tetrahedral clump	1624	0.43
Sample 3	8-ball tetrahedral clump	1573	0.45
Sample 4	8-ball flaky clump	1507	0.47

Stress in a PFC^{3D} model is defined with respect to a specified measurement volume. The measurement volume in PFC3D is a sphere and will be referred to as a “measurement sphere”, as shown in Figure 6.7c. Table 6.4 shows the average stress tensor in the measurement sphere for each sample at the initial state. It indicates that the stress along the Y direction (gravity) is larger than the stress to the side walls.

Moreover, the vertical stresses of the samples vary considerably, especially for the 2-ball clumps. This could be attributed to the gravity of the overlapping of spheres within clumps. In these simulations, when spheres overlap to be a clump, the total volume of spheres in a clump is greater than the volume of the clump and the mass of the clump is therefore greater than the mass of an equivalent clump with a uniform density; such an entity is currently not available with PFC^{3D}. It can be seen that the sample with more overlapping spheres within clumps, has larger initial vertical (yy) stress. Besides, there is such a difference between K_0 in the X and Z directions as shown in Table 6.4. This could be caused by the different reinforcing areas along the X and Z directions in the measurement sphere as shown in Figure 6.7c. Surely the ballast-geogrid interaction is influenced by the initial stress state, especially stress of zz component along pull-out direction. In these simulations, all initial stresses of these samples along pull-out direction are similar.

Table 6.4 Initial average stress tensor in the measurement sphere for each sample

	Ballast particle shape	Stress (xx component)	Stress (yy component)	Stress (zz component)	Stress intensity factor: K_0
Sample 1	2-ball clump	64	110	58	$K_{0x} \approx K_{0z} = 0.55$
Sample 2	4-ball tetrahedral clump	134	216	65	$K_{0x} = 0.62$ $K_{0z} = 0.3$
Sample 3	8-ball tetrahedral clump	108	198	69	$K_{0x} = 0.54$ $K_{0z} = 0.35$
Sample 4	8-ball flaky clump	65	237	66	$K_{0x} = 0.28$ $K_{0z} = 0.55$

For Samples 2, 3 and 4, two different vertical loads were considered: 0.0 and 0.5 kN. For these simulations, the normal and shear stiffness of the particles were 1.0×10^8

N/m and the stiffnesses of the walls were set to have the same values as the particles. The ball, box and geogrid friction coefficients were all set to be 0.6. The density of the ballast particles was 2600 kg/m^3 . A horizontal pull-out rate of 5 mm/s was given to the spheres at the right-hand end of the geogrid. To avoid any dynamic effects, the pull-out rate was gradually increased linearly with time from zero to the final rate after an initial 2 mm displacement. The simulation was terminated at a total pull-out displacement (i.e. the displacement of the right-hand end of the geogrid) of 60 mm for comparison with experiments of 50 mm . During the simulation, the pull-out force, the pull-out displacement, the axial deformation of longitudinal ribs and the porosity (using a measurement sphere in PFC^{3D}) were recorded. As no facility is available in PFC^{3D} for calculating the porosity of a sample of clumps comprising more than two particles within each clump, the average vertical displacement of the surcharge (as shown in Figure 6.7b) was recorded to represent the volumetric strain for the sample of 8-ball clumps.

6.5 Results and discussion

6.5.1 Simulation results using 2-ball clumps

For the Sample 1, three different vertical loads were considered: 0.0 , 0.5 and 1.0 kN . Figure 6.8 shows the development of the total pull-out force for the sample of two-ball clumps under different loading conditions. It clearly shows that up to a displacement of approximately 20 mm , the peak force was larger for a greater surcharge. However, the confinement caused by 1.0 kN surcharge does not seem to have enhanced the interlocking effect beyond the peak pull-out force. This could be attributed to a severe unrecoverable deformation of the geogrid after the peak force under 1.0 kN surcharge. Figure 6.9 shows evolution of the particle porosity within the measurement sphere for the sample of two-ball clumps. It indicates that the sample contracted until a displacement about 8 mm and then dilated. Moreover, the displacement at the peak pull-out force is associated with the maximum rate of dilation of the sample given by the measurement sphere.

Compared to the experimental results, it can be seen from Figure 6.10 that the pull-

out force was well predicted by the DEM simulations especially up to approximately 20 mm displacement without surcharge. However, it appears that the DEM simulations underestimate the pull-out force after a displacement of approximately 20 mm, and also the response for 0.5kN surcharge is not predicted well after 10mm displacement. It is believed that, owing to less angularity of the two-ball clumps, interlocking between the particle and geogrid and between particles is reduced compared to the real experiments comprising more angular particles.

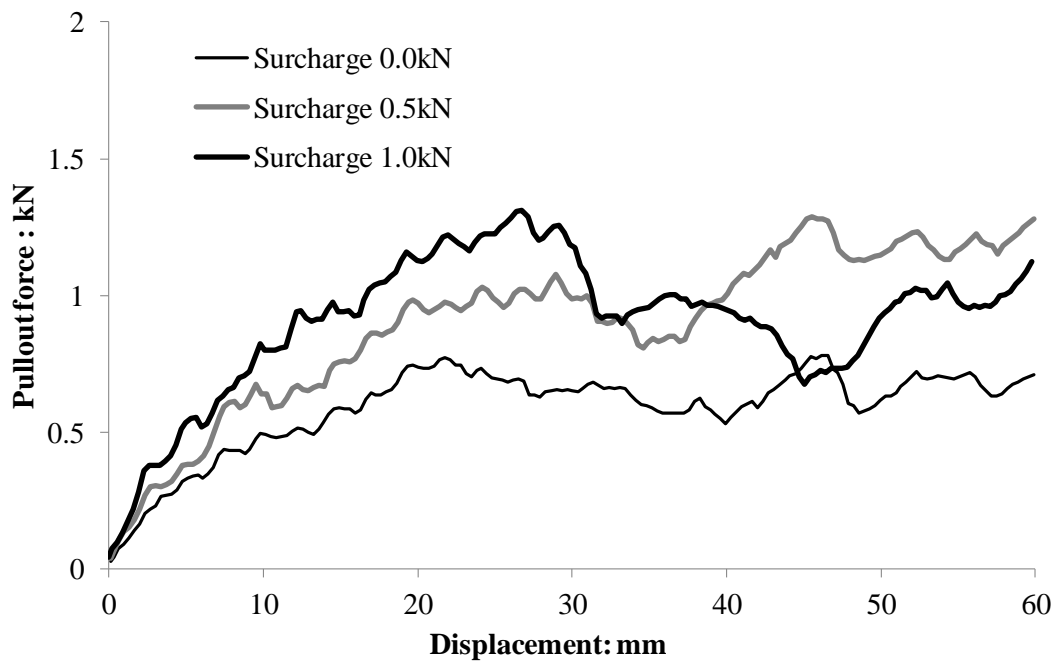


Figure 6.8 Pull-out force as a function of displacement for different values of surcharge

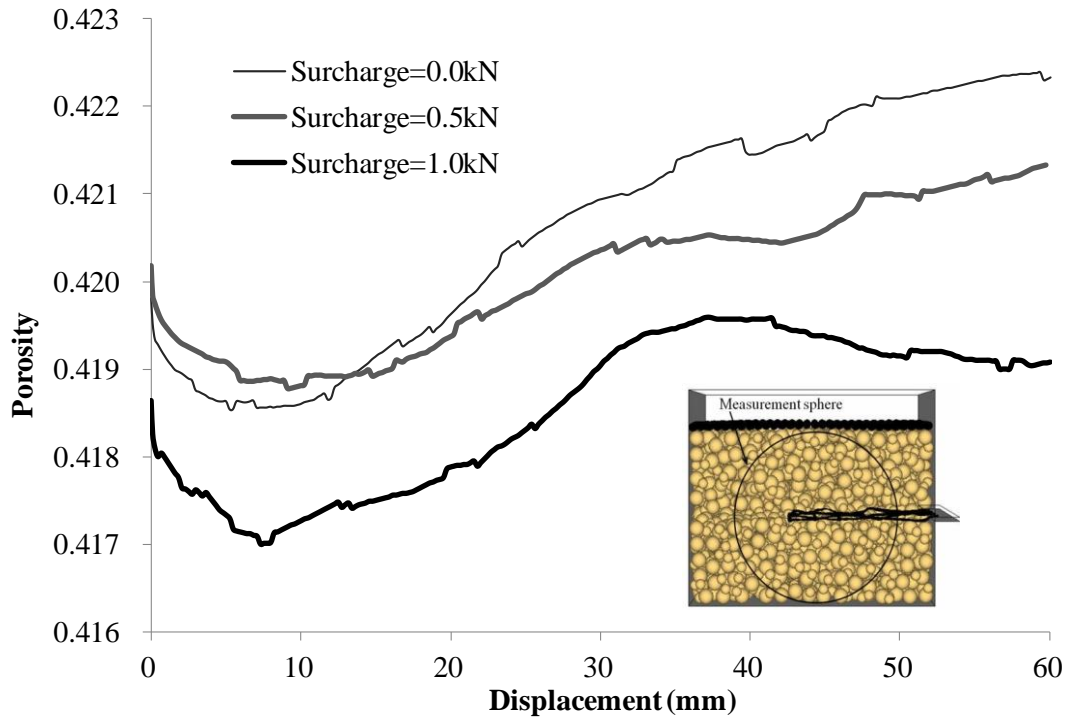


Figure 6.9 Particle porosity as a function of pull-out displacement for different values of surcharge

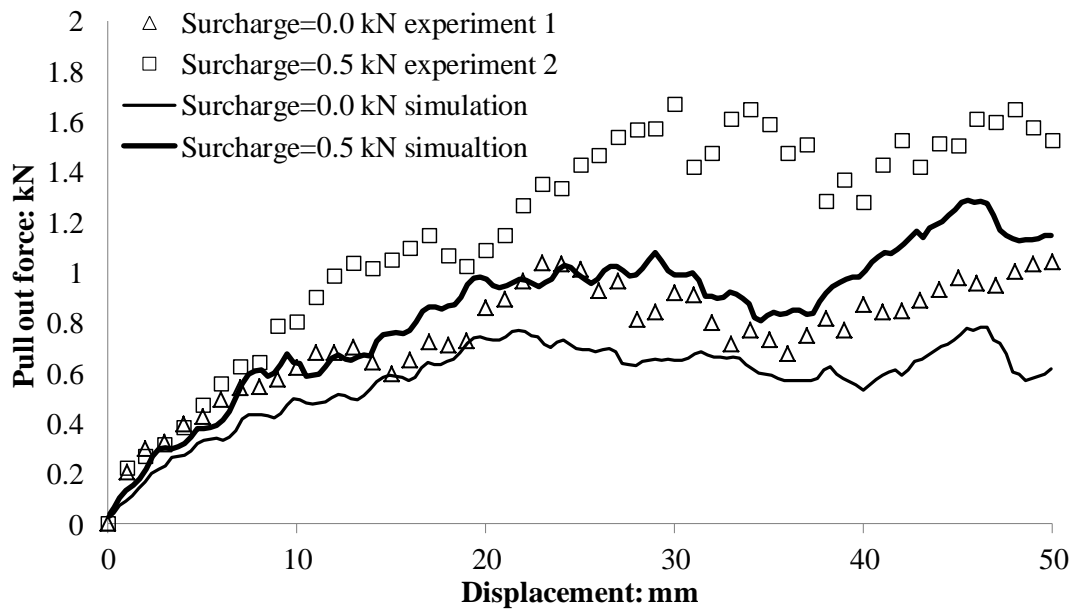
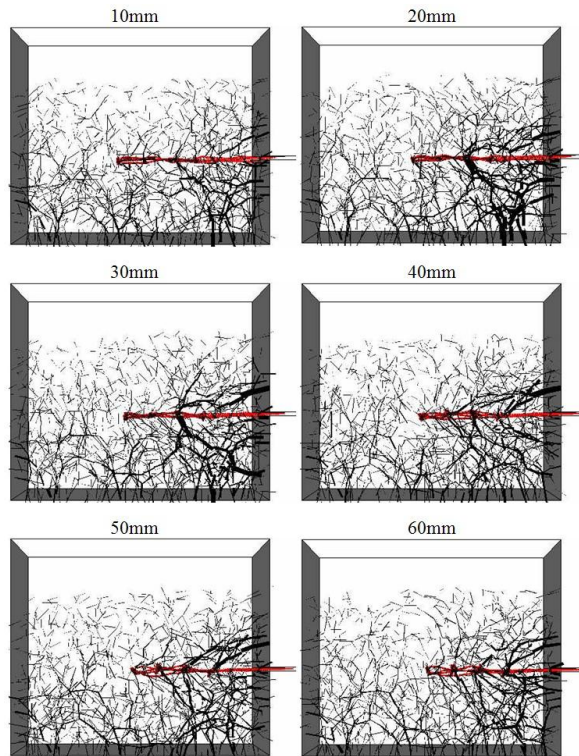


Figure 6.10 Comparison of DEM with laboratory experiment: pull-out force against displacement

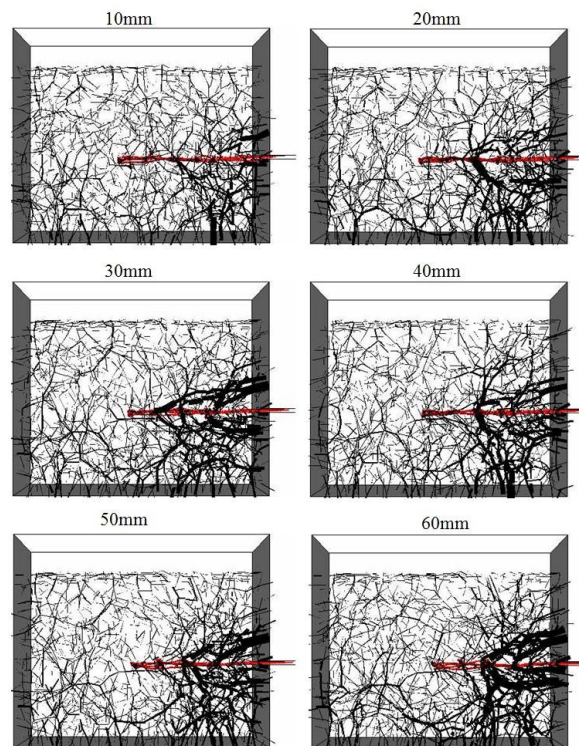
Figure 6.11 show the development of contact force distributions for several stages during the pull-out test. It should be noted that contact forces are all drawn at the

same scale. These figures display the strong contact forces in the vicinity of the geogrid area, which clearly shows the interlocking effect. This is in agreement with the simulation modelled by McDowell et al. (2006). It can be seen that, the clump ballast particles arch around each transverse rib during pull-out. Furthermore, the arching is concentrated on the back two transverse ribs after approximately 50 mm displacement. The principal interlocking area has a range of about 10 cm thickness either side of the geogrid.

Figure 6.12 shows the evolution of axial strain between several observation points of the longitude rib AE. The positive value means that the geogrid nodes are further apart; the negative value means that the grid nodes are closer together. With an increase in the surcharge, the axial strain of each ribs apart from rib BC increased and more nodes move further apart. The deformations of geogrids under 0.5 kN surcharge in the laboratory experiment and simulation (the sample of two-ball clumps) are shown in Figure 6.13, which clearly displays the extensive deformation of the grid, and deflection of the ribs can be seen in the side view. This deflection explains why, for the longitudinal ribs AB and BC, negative strains are observed in Figure 6.12b, as the nodes are closer together than before pull out. Besides, the geogrid in the simulation seems to have more evident deformation compared with the experimental geogrid sample. This is because the geogrid deformation in the simulation was captured during the pull-out test, whereas it is not possible to view the whole deformed geogrid during the pull-out test in the laboratory, but only after the test when the geogrid has been removed.



(a)



(b)

Figure 6.11 Contact force (scaled) distribution for sample of 2-ball clump during pull-out: (a) surcharge= 0.0 kN; (b) surcharge= 0.5 kN

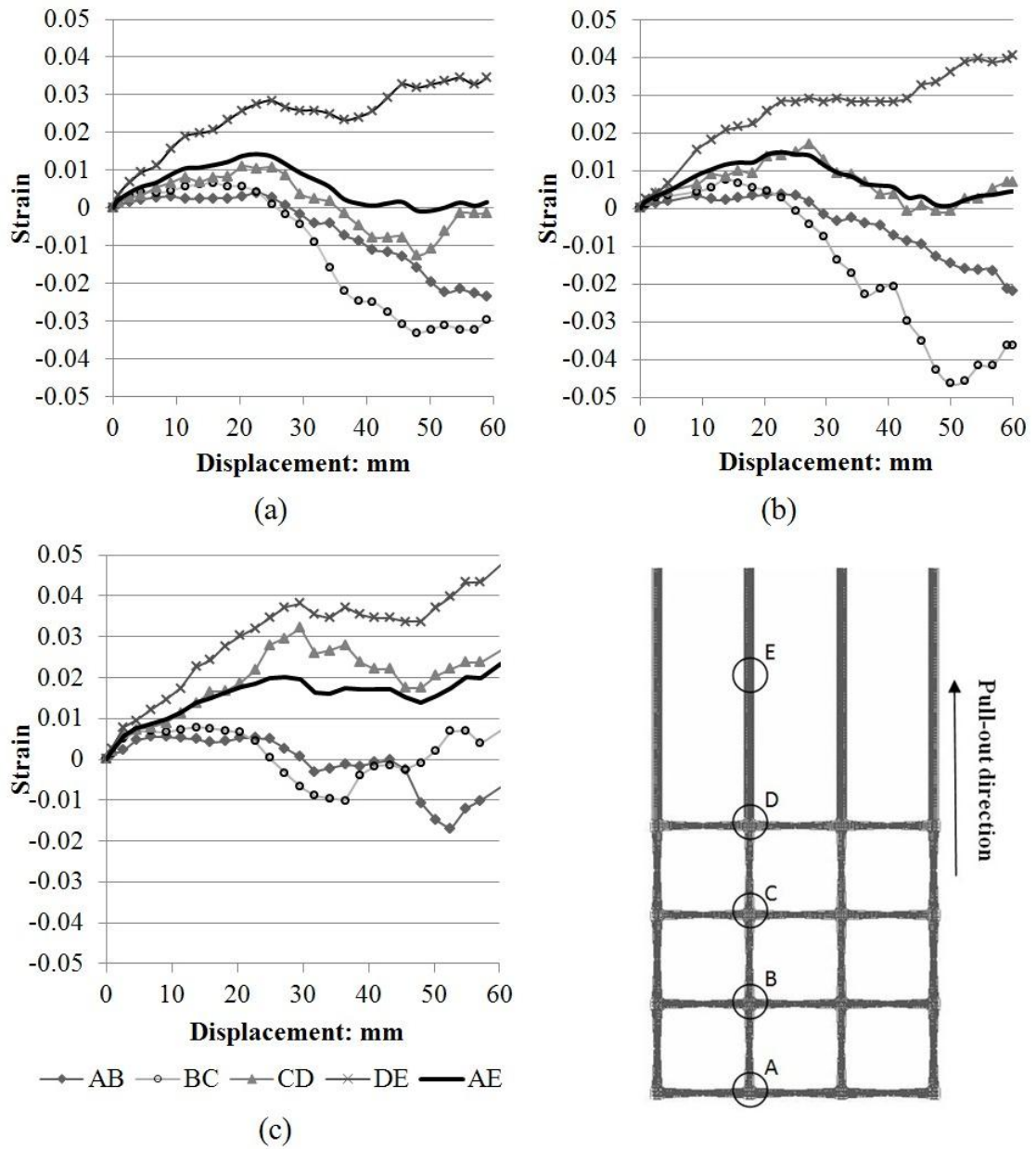
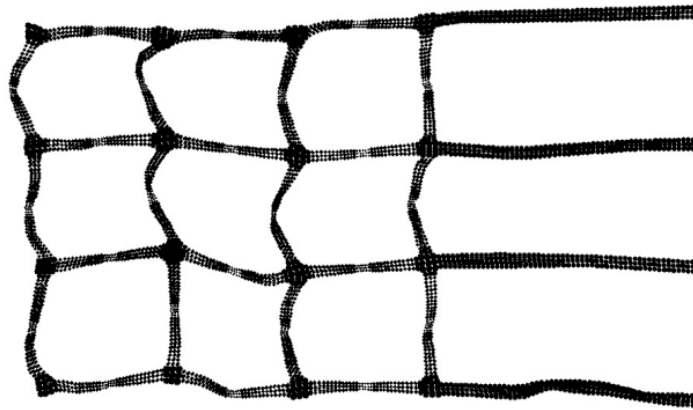


Figure 6.12 Axial strains of longitudinal ribs under different values of surcharge:
 (a) 0.0 kN; (b) 0.5 kN; (c) 1.0 kN



(a)



(b)



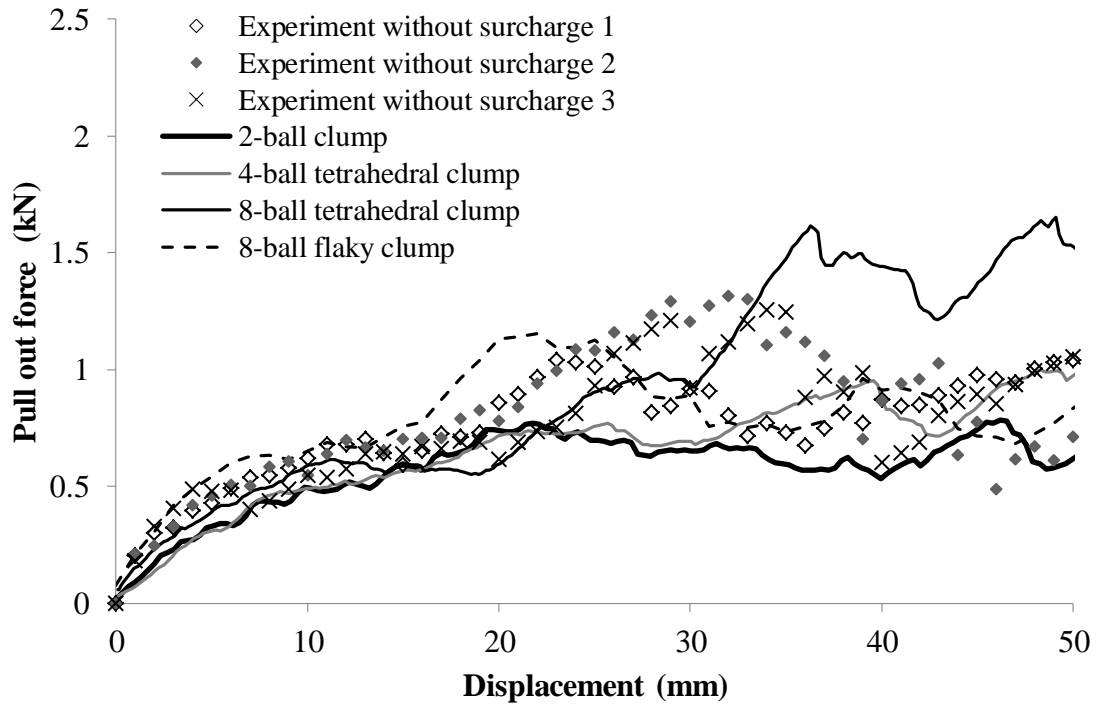
(c)

Figure 6.13 Geogrid deformation after 50mm displacement: (a) experiment; (b) simulation; (c) simulation (side view)

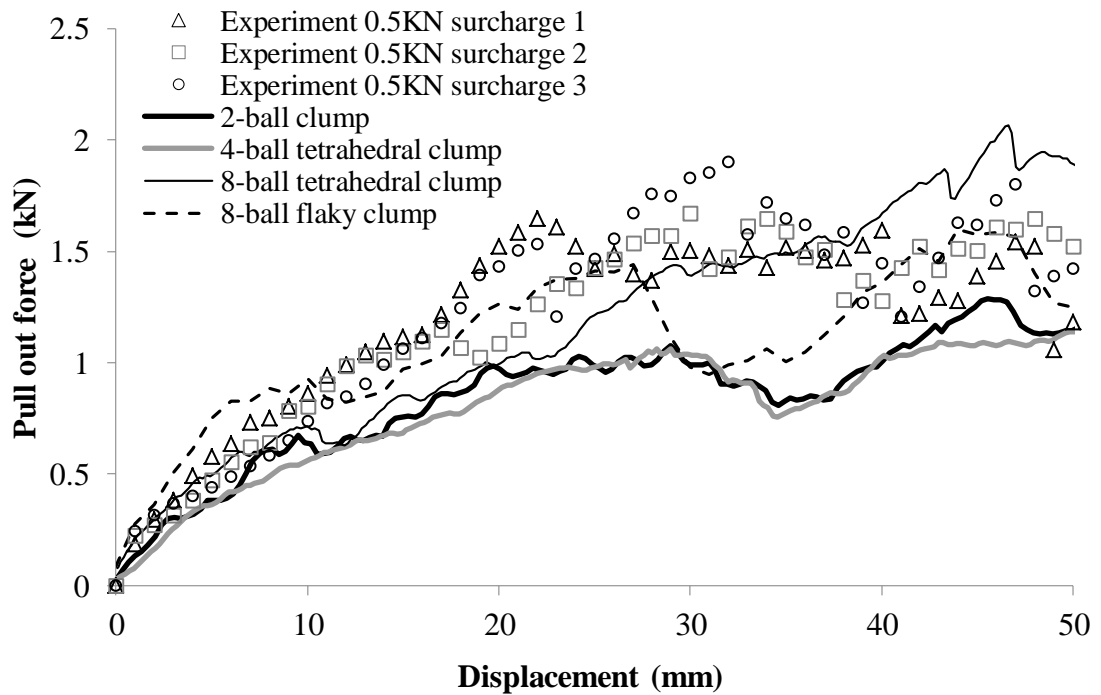
6.5.2 Effect of ballast particle shape

Selig and Waters (1994) reviewed experimental data for granular materials and pointed out that increasing both angularity and particle surface roughness increases the shear strength of the assembly. In order to evaluate the influence of particle shape on the aggregate-geogrid interlock, the four clumps with different shapes as

mentioned in Section 6.2 were simulated. Figure 6.14 shows the development of pull-out force for all four samples under different loading conditions and compares the simulation results with the experimental results. It clearly shows that up to a displacement of approximately 20 mm, the pull-out force is well predicted by the DEM simulation and the peak force is larger for a greater surcharge. Moreover, the particle shape seems to have little effect during the initial 20mm displacement. However, it appears that the DEM simulations for 2-ball clumps and 4-ball tetrahedral clumps underestimate the pull-out force after approximately 20mm displacement. It is believed that, due to lower angularity of the 2-ball clumps and roundness of the 4-ball tetrahedral clumps, interlocking between the particles and geogrid is reduced compared to the real experiments comprising more angular and rougher particles. In the case of the 8-ball tetrahedral clump and 8-ball flaky clump, the pull-out forces are closer to the experimental results. However, flaky ballast is not considered to be good quality ballast. After having conducted a set of triaxial ballast tests to investigate the ballast shape on ballast performance, Roner (1985) found that randomly placed flaky material had a higher deviator stress and angle of internal friction than did nonflaky material at the same void ratio. Similarly, Selig and Waters (1994) concluded that any quantity of flaky particles, either randomly oriented or oriented other than generally parallel to the failure plane, increases the shear strength of the granular specimen. This offers a possible explanation as to why the pull-out force was higher than expected. Besides, orientation parallel to the failure plane, when a significant proportion of the particles are flaky, will cause a substantial strength reduction. The disadvantage of increased flakiness appears to be increased abrasion, increased breakage, increased permanent strain accumulation under repeated load, and decreased stiffness. Therefore, for the four alternative clumps presented here, the 8-ball tetrahedral clump seems most representative of real ballast.



(a)



(b)

Figure 6.14 Comparison of DEM with laboratory experiment: (a) pull-out force against displacement without surcharge; (b) pull-out force against displacement for a surcharge of 0.5 kN

6.5.3 Simulation results using 8-ball tetrahedral clumps

For the sample of 8-ball tetrahedral clumps, the displacement at peak pull-out force (approximately 47mm) is associated with the maximum rate of dilation of the sample given by the average vertical displacement of the loading spheres, as shown in Figure 6.15. Each average is the mean displacement of the central sphere and the two adjacent transverse spheres on either side, at the left-hand end, centre and the right-hand end of the surcharge (Figure 6.7b). It should be noted that volumetric strains cannot be obtained for these clumps including more than two balls using measurement spheres in PFC^{3D}. Figure 6.15 also indicates that the dilative behaviour is more obvious in the reinforced zone at the right-hand end of the sample. This can also be seen in Figure 6.16. It is clear in Figure 6.16 that the upwards displacement is noticeably greater at the right-hand end after pull out of approximately 30mm and 50mm, respectively. The top surcharge block can tilt during the pull out, potentially causing non-uniform distribution of the surcharge, which is consistent with the experimental tests.

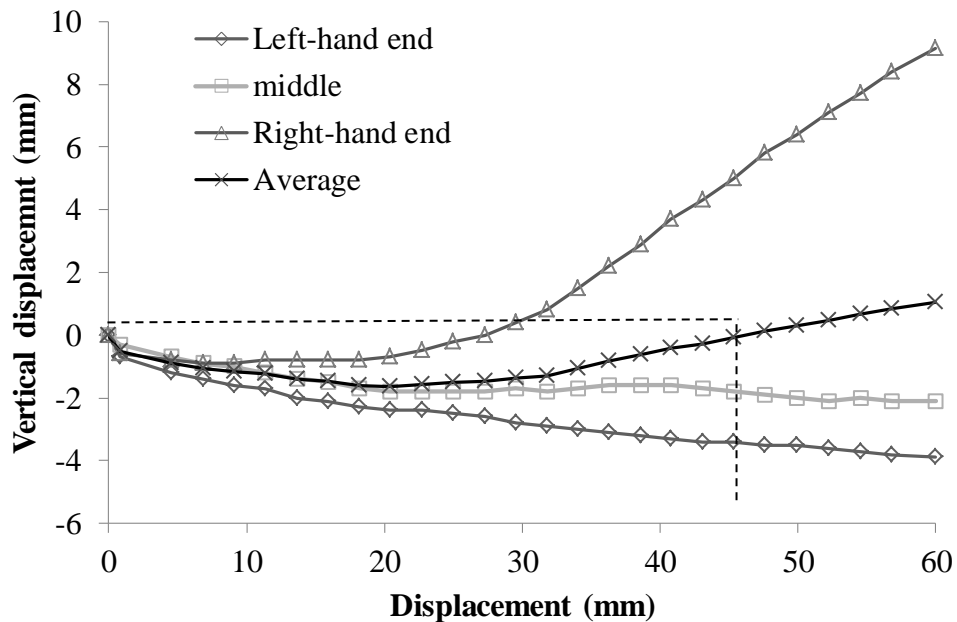


Figure 6.15 Vertical displacement of surcharge block for sample 3

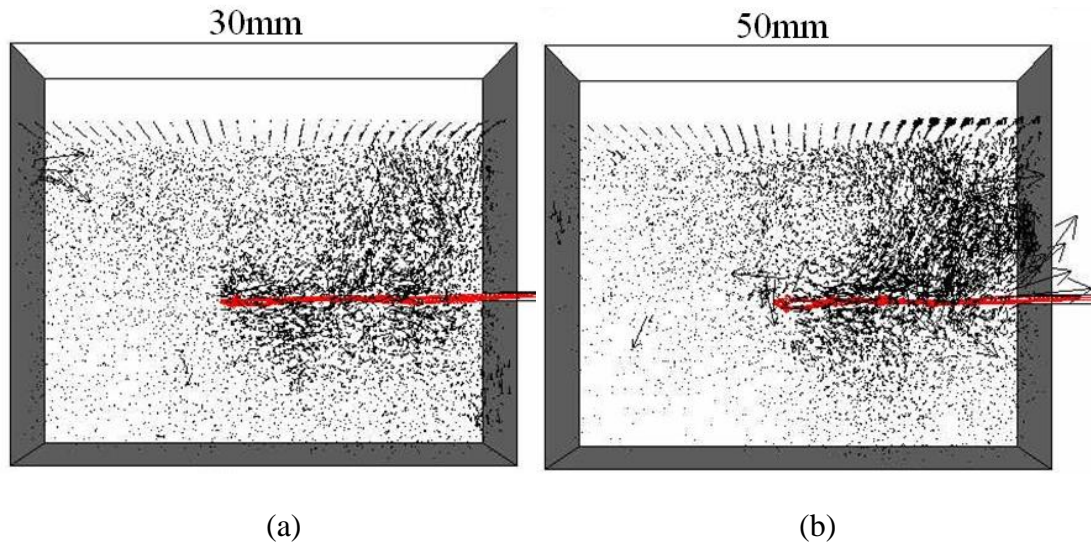
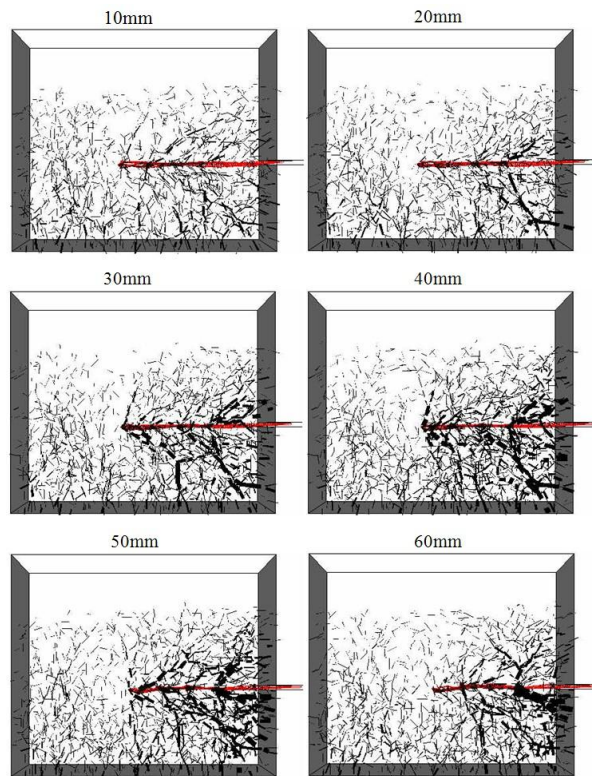
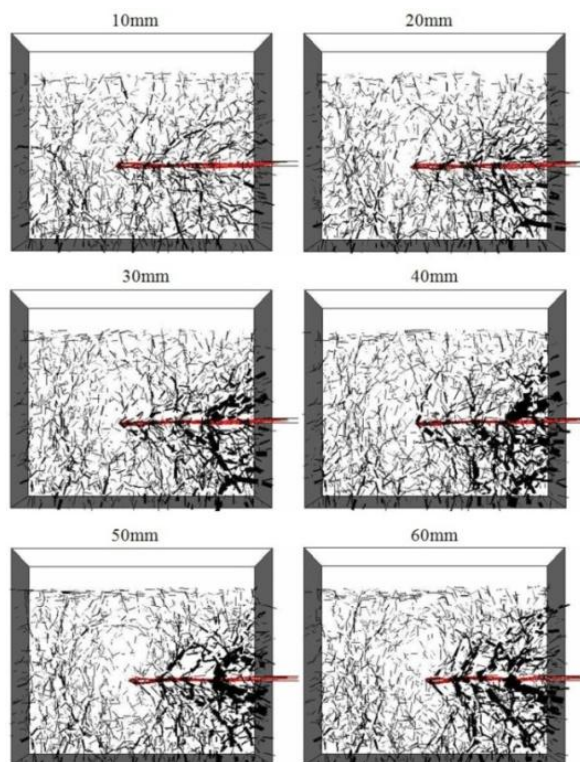


Figure 6.16 Displacement vectors of ballast particles in pull-out box (length of arrow proportional to magnitude): (a) at 30mm pull-out displacement (maximum magnitude of displacement vector = 12.0 mm); (b) at 50mm pull-out displacement (maximum magnitude of displacement vector = 22.6 mm))

Figure 6.17 shows the development of the contact force chains under 0.5 kN surcharge for Sample 1 and Sample 3 respectively (geogrid is shown in red). It should be noted that contact forces are all drawn at the same scale. These figures show the strong increase in the contact forces in the geogrid area, due to aggregate-geogrid interlock. It can be seen from the 3D view (Figure 6.18) that the clump ballast particles have arched around the transverse ribs during the pull-out. According to Tensar (2007), load is carried mainly by bearing on the thick transverse ribs, and transferred through the junctions to the longitudinal ribs at very small deformations. Comparing Figures 6.11 and 6.17, the magnitude of the average of the contact force for the 8-ball clumps in Sample 3 is less than for the 2-ball clumps in Sample 1 due to the higher number of contacts for the 8-ball tetrahedral clumps leading to a more homogeneous stress distribution.



(a)



(b)

Figure 6.17 Contact force (scaled) distribution for sample of 8-ball tetrahedron clump during pull-out: (a) surcharge= 0.0 kN; (b) surcharge= 0.5 kN

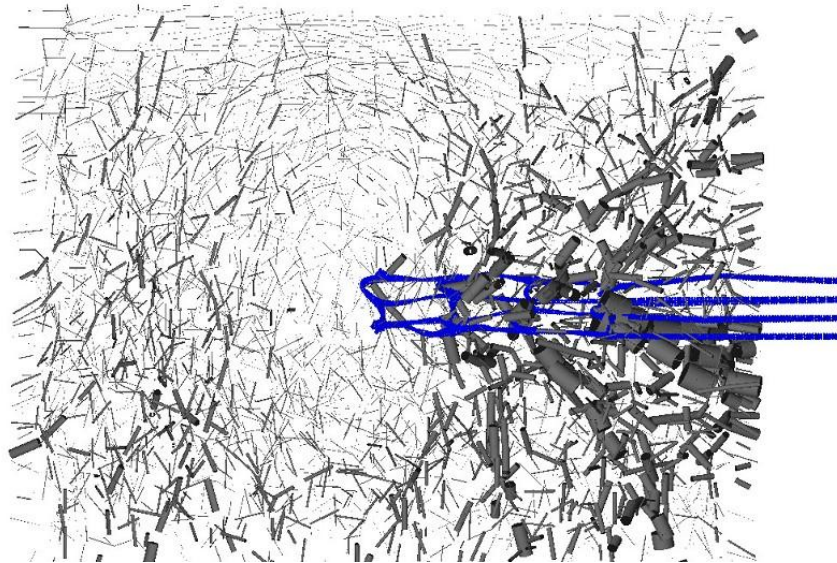


Figure 6.18 The interaction mechanism: 3D view of contact force from the transverse ribs

In a mechanically stabilised layer, ballast particles interlock within the geogrid and are confined within the apertures, creating an enhanced composite material with improved performance. The structural properties of the mechanically stabilised layer are influenced by depth of the confined zones. As shown in Figure 6.19, the interlocking effect is largest for approximately 75mm on both sides of the geogrid, and decreases during the transition zone, and vanishes at a distance greater than about 150mm. For the case without surcharge, the contact forces below the geogrid are larger than that above the geogrid due to the non-confinement on the top (i.e. gravity). For the case with surcharge, the contacts forces below and above geogrid are relatively symmetrical due to both confinement at the top and bottom (gravity negligible in comparison). This can explain that the peak of the contact force is below the geogrid for the case without the surcharge and approximately at the geogrid level for the case with the surcharge.

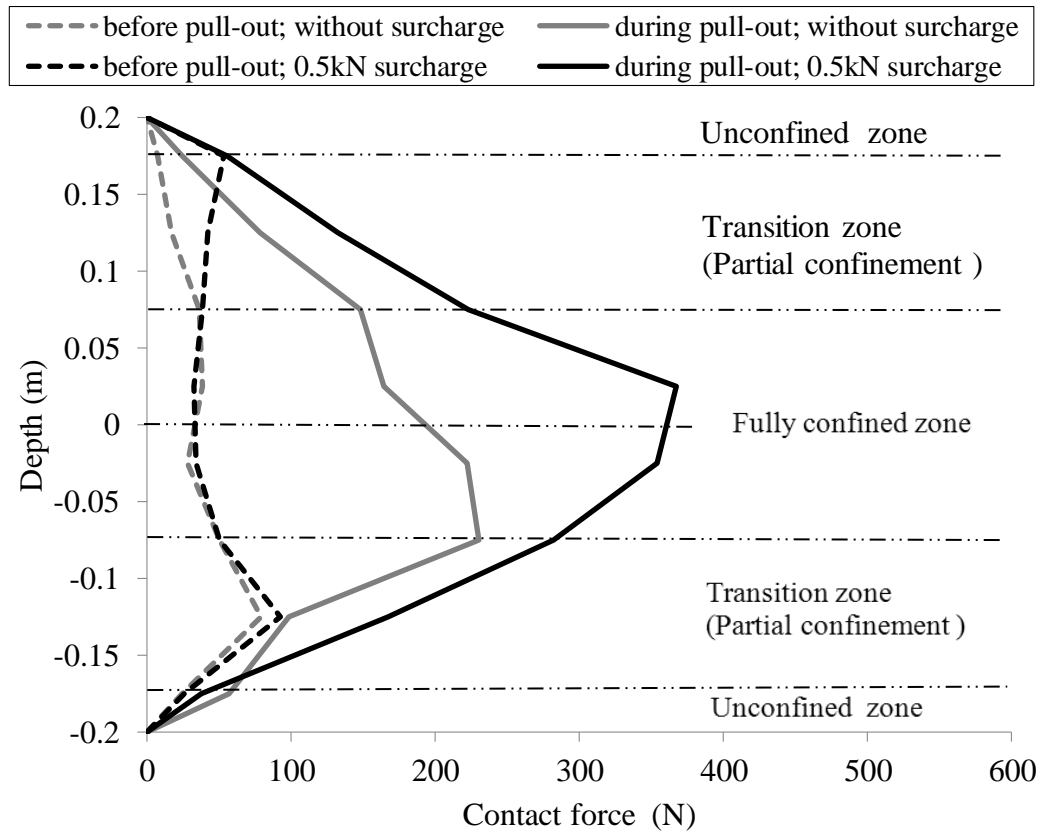


Figure 6.19 Contact force applied on the front wall before and during the pull-out test for sample 3

6.6 Conclusions

Laboratory large box pull-out tests have been performed on typical geogrids embedded within a ballast sample. The pull-out force has been measured as a function of displacement under different surcharges. A new DEM model for the geogrid has been developed by bonding two layers of small balls together to form the required geometry using parallel bonds, and calibrated by simulating standard tests. Four kinds of clumps, namely a 2-ball clump, 4-ball tetrahedral clump, 8-ball tetrahedral clump and 8-ball flaky clump were used to represent the real ballast particles. All four kinds of clumps have been shown to give an acceptable angle of repose, comparing with real ballast. The DEM simulations have been shown to provide good predictions of the pull-out force as a function of displacement especially for the initial 20mm displacement. The particle shape seems to have little

effect on the initial development of the pull-out force. The simulations also have given valuable insight into the interaction between ballast and geogrid under different surcharges, although the DEM simulations using 2-ball clumps or 4-ball tetrahedral clumps, underestimate the pull-out force after a displacement of about 20mm. This is thought to be a function of the uniform particle size, angularity and roundness of the simulated clumps, compared to the well-graded, angular ballast particles in the laboratory tests. Considering the four kinds of clumps, the 8-ball tetrahedral clump which has more angularity and roughness, seems more representative of real ballast. The fully reinforced zone is approximately 75mm above and below the geogrid.

Chapter 7 Discrete element modelling of cyclic loading of geogrid-reinforced ballast under confined and unconfined conditions

7.1 Introduction

Due to the increasing number of faster and heavier trains, additional and greater cyclic loading is causing much track deterioration. The essence of track deterioration is settlement due to permanent deformation within the ballast layer, sub-ballast layer and subgrade (Selig and Waters, 1994). The application of reinforcing geogrid has been proved to be a simple and economic way which can reduce the permanent deformation in the ballast layer. Understanding the behaviour of ballast/geogrid system could lead to the better design of railways that will reduce maintenance costs.

Previous researchers such as Shenton (1974) and Indraratna et al. (1998) studied the permanent deformation of ballast under cyclic loading in the triaxial test. They found the permanent axial strain accumulation is proportional to the logarithm of the number of load cycles. The behaviour of geogrid-reinforced ballast under cyclic loading has also been investigated. The geogrid reinforcement has been found to reduce permanent settlement, and to also have a more beneficial effect on softer subgrade (Raymond, 2002 and Brown et al. 2007). McDowell and Stickley (2006) found that in box tests, the sample with geogrid at 100mm from the base gave a better performance than the sample with geogrid at 200 mm from the base, or using two geogrid layers at both locations. It should be noted that the experiments alone cannot provide full insight into the complex interlocking between ballast and geogrid under cyclic loading. The discrete element method (DEM) pioneered by Cundall and Stack (1979) has therefore been used to complement the laboratory experiments and provide much needed micro mechanical insight.

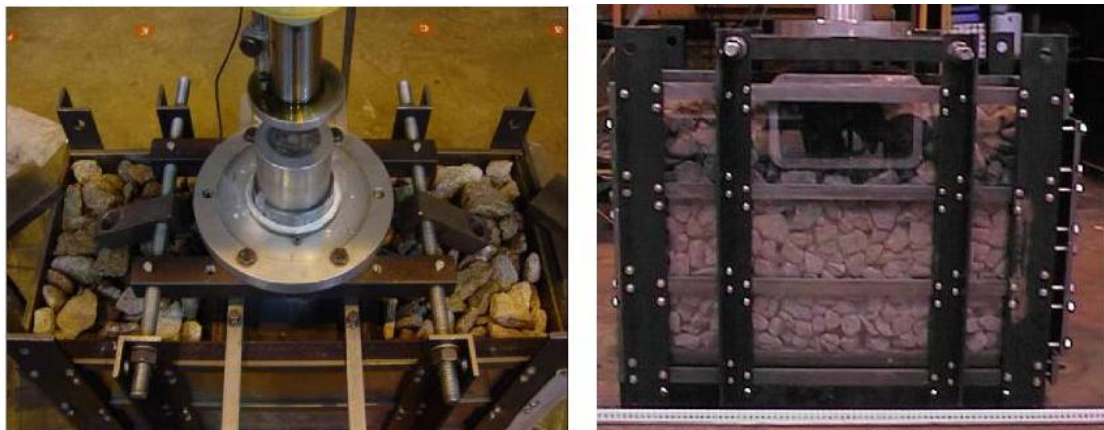
This chapter aims to use the discrete element method to model cyclic loading of geogrid-reinforced ballast under confined and unconfined conditions. For the confined condition, a box test is simulated on unreinforced and reinforced samples which have different geogrid positions and geogrid apertures. Performance is measured in terms of permanent settlement, resilient modulus and stress-deformation behaviour. The effect of the geogrid on the distribution of contact forces and also the cyclic response of the geogrid-reinforced ballast are studied. For the unconfined condition, cyclic loading of a trough of ballast (the Composite Element Test (CET) devised by Brown et al. (2007)), is simulated using the code PFC^{3D} (Itasca, 2003) to examine the effect of position and number of geogrids as well as subgrade stiffness on the performance of reinforced ballast.

7.2 Box test simulation

7.2.1 Box test description

McDowell et al. (2004) described a box test involving the application of cyclic loading to a simulated sleeper on ballast in a box of dimensions 700 mm x 300 mm x 450 mm. Figure 7.1 shows the laboratory box test set-up. The test can simulate traffic loading on the rail section shown in Figure 7.2. The ballast properties such as stiffness, permanent settlement and degradation have been investigated. McDowell and Stickley (2006) investigated the performance of geogrids placed at 200mm and 100mm from the base in the laboratory box test. The sample with the grid at 100mm from the base performed better than the sample with the grid at 200 mm from the base, as shown in Figure 7.3. However, not much micro mechanical insight can be gained from the laboratory tests. McDowell and Lim (2005) described discrete element modelling of ballast using a sphere as well a simple 8-ball “cubic” clump to represent each ballast particle, and found that interlocking of ballast can be modelled using clumps. Lu and McDowell (2005) devised new clumps to examine the effect of clump shape on the distribution of contact forces and the cyclic response of the aggregate. Lu and McDowell (2006) used a two-ball clump with two bonded

asperities (small spheres) bonded to model the abrasion of ballast particles in the box test using the discrete element method, and showed that most of the abrasion occurs directly under the sleeper. Konietzky et al. (2004) investigated the interlocking of ballast and geogrid in DEM simulations of pull-out tests and cyclic triaxial tests. Bhandari and Han (2010) investigated the geotextile-soil interaction under a cyclic wheel load using PFC^{2D}. The DEM results show that the depth of the geotextile significantly affects the degree of interaction between the geotextile and the aggregate. Moreover, results from two-dimensional models do not provide sufficient micromechanical insight for this boundary value problem because the kinematic constraints are completely different in three dimensions. Therefore, the aim of the box test simulations on geogrid-reinforced ballast is to gain an improved understanding of the micro-mechanical response of the reinforced ballast layer and the respective influences of the locations of the geogrids and the geometry of the geogrid apertures.



(a)

(b)

Figure 7.1 Box test set-up: (a) view from the top of the box and (b) front view (Lim, 2004).

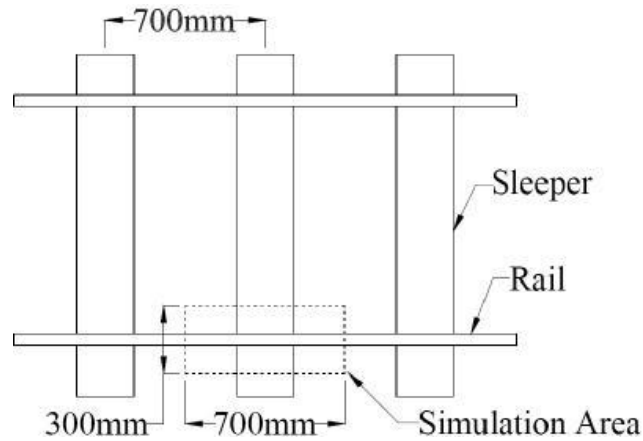


Figure 7.2 Plan of rail and sleepers showing section represented by the box test (Lim, 2004).

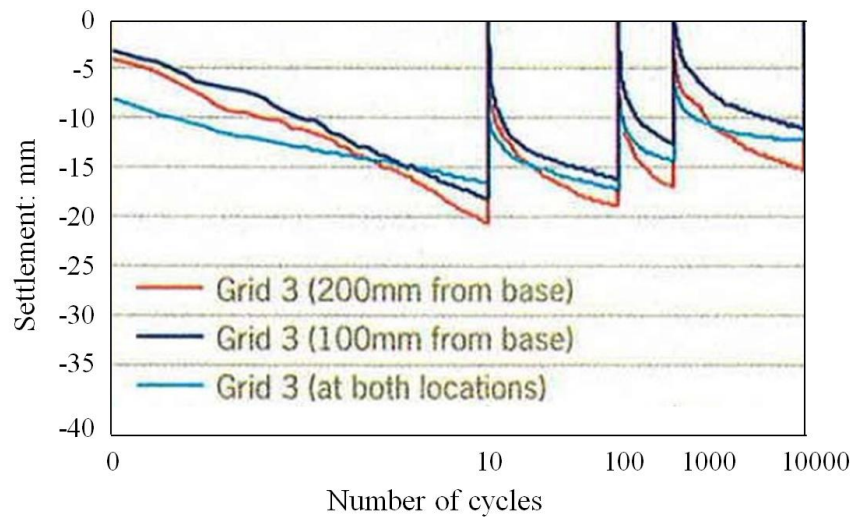


Figure 7.3 Settlement of ballast reinforced with grid at 100mm from base, at 200mm from base, and both grids (McDowell and Stickley, 2006).

7.2.2 Modelling procedure

Figure 7.4 shows the details of new two-layer biaxial and new triaxial geogrid models which were used in the following simulations. Figures 7.4a and b shows the reinforcing units of the biaxial and triaxial geogrids, respectively. For the triaxial geogrid, the rib length between two nodes is 75mm. This was chosen to give a similar geogrid area as the 65mm biaxial geogrid. All particles are bonded together by parallel bonds, which act over a circular cross-section between two particles in contact and transmit both a force and a moment (Itasca, 2003). It should be noted that

the triaxial geogrid was given the same micro mechanical parameters as the biaxial geogrid (see Table 5.1) in order to investigate the effect of aperture shape of the geogrid on reinforced ballast performance.

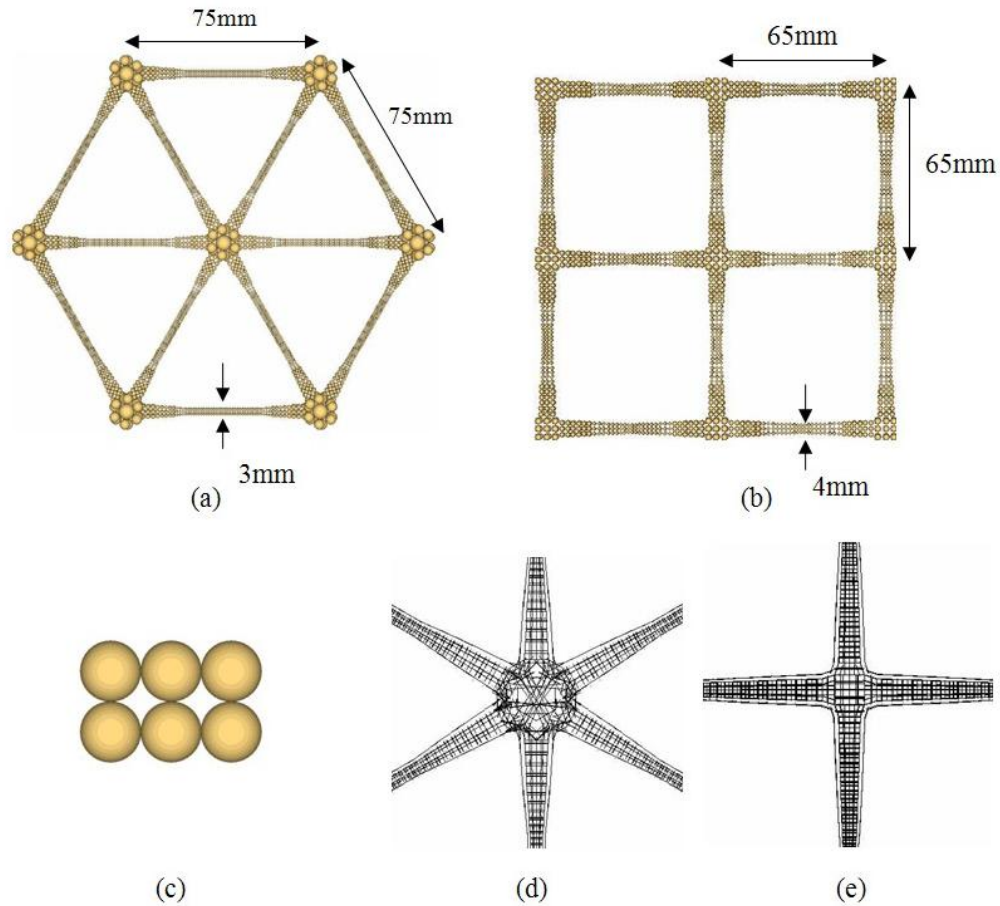


Figure 7.4 DEM of geogrid: (a) triaxial geogrid; (b) biaxial geogrid; (c) cross-section of rib (d) parallel bonds of triaxial geogrid; (e) parallel bonds of biaxial geogrid

Since McDowell et al. (2005) found that the breakage in the box test was minimal, uncrushable clumps were used in the simulations here. Due to the high computational time required to simulate the biaxial and triaxial geogrid layers with 18483 and 38451 parallel-bonded balls respectively (measured in PFC^{3D}), a simple 2-ball clump was used to represent each ballast particle. Figure 7.5 shows the PFC^{3D} models of geogrids and ballast particles as well as a reinforced sample with a geogrid 100 mm from the base. The dimensions of both the box and the sleeper in the simulations are equal to the real dimensions in the laboratory: 700 mm x 300 mm x 450 mm for the

box and 250 mm x 300 mm x 150 mm for the sleeper. In these simulations, biaxial geogrids were placed at four different heights above the base: 50mm, 100mm, 150mm and 200mm, to investigate the influence of location of the geogrid on the performance of the reinforced ballast system. In addition, a triaxial geogrid was also placed at 100mm depth to compare with the performance using a biaxial geogrid at the same depth. Table 7.1 shows the details of the simulations. According to Lim and McDowell (2005), the normal and shear stiffness (linear-elastic) of the balls were 5.08×10^9 N/m. However, they pointed out that the stiffnesses of the assembly were higher than expected even though the normal and shear stiffnesses of the balls were supposed to correspond to the Young's modulus of the granite. Therefore, following Lu and McDowell (2006), the normal and shear stiffness of the particles were set to be 10^8 N/m and the stiffnesses of the walls and sleeper were set to the same values as the particles. In the laboratory box test, a stiff rubber mat was used to represent the sub-ballast and subgrade layers. For this simulation, the stiffness of base wall was set to be 5×10^5 N/m, following Lu and McDowell (2006).

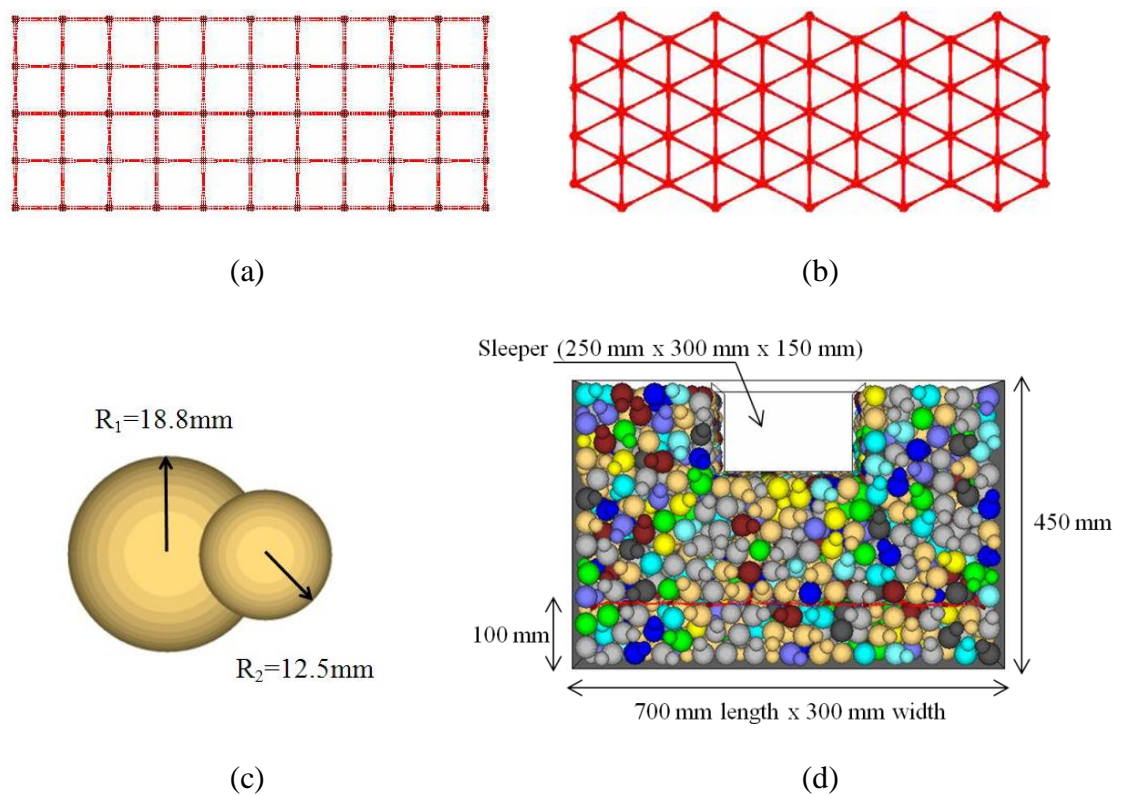


Figure 7.5 PFC^{3D} model (a) biaxial geogrid layer; (b) triaxial geogrid layer; (c) two-ball clump as a ballast particle ($R_1=18.8$ mm, $R_2=12.5$ mm); (d) reinforced sample with a geogrid layer at 100 mm above base

Table 7.1 Schedule of the box test simulations

	Type of geogrid	Location of geogrid (from the base)	Number of two- ball clumps
Unreinforced sample	N/A	N/A	1579
Reinforced sample 1	Biaxial geogrid	50 mm	1574
Reinforced sample 2	Biaxial geogrid	100 mm	1576
Reinforced sample 3	Biaxial geogrid	150 mm	1574
Reinforced sample 4	Biaxial geogrid	200 mm	1574
Reinforced sample 5	Triaxial geogrid	100 mm	1576

The critical state angle of shear resistance or angle of repose is a function of the ball-ball coefficient of friction and the particle shape. Kwan (2006) showed that experimental test on flat ballast particle surface sheared past one another gave a particle-particle friction coefficient of approximately 0.6 ($\tan 31^\circ$). Figure 7.6 shows a heap of 1472 two-ball clumps deposited from a hopper with a 12.5cm square aperture, 0.7m above the base wall; the angle of repose is approximately 39° , which is consistent with the angle of shearing resistance of real ballast. Therefore, the coefficients of friction for the balls, box and sleeper were all set to be 0.6. The density of the particles was 2600kg/m^3 . For the sample of two-ball clumps, it was possible to calculate the porosity directly using a measurement sphere in PFC^{3D}. It should be noted that the permanent deformation depends mainly on the initial compacted density of the ballast (Selig and Waters, 1994). It was found that the initial sleeper deformation increased with the increasing initial porosity of sample. A porosity of 0.38 was used for all the simulated tested samples. Even though the particle shape and size distribution plays an important role for mechanical behaviour as documented by Stahl and Konietzky (2011), the simplified approach using uniformly-graded particles can be used to show differences between the geogrid type and location. This can be considered satisfactory as ballast is usually reasonably uniformly graded ($D_{60}/D_{10} \approx 1.4$) to provide large enough voids to facilitate good drainage.

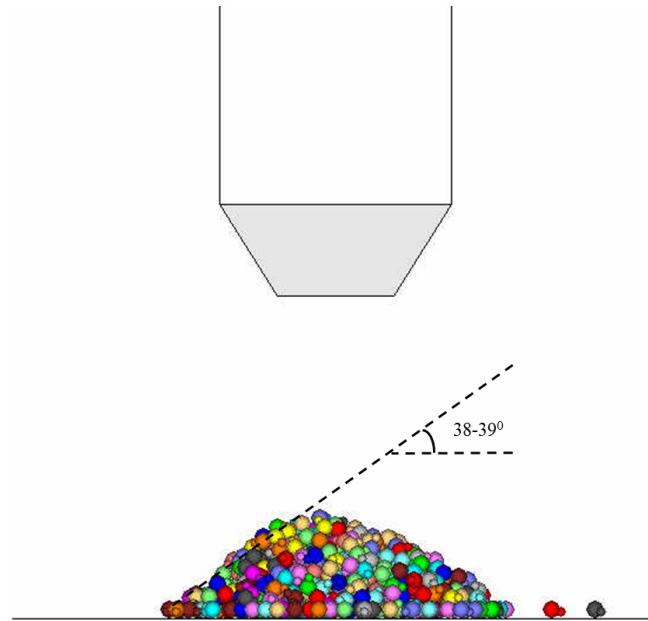


Figure 7.6 The particle-pouring test using the PFC^{3D} two-ball clumps

To prepare the sample, small spheres were first generated with the box away from the geogrid area between two stiff walls. Then the spheres were expanded by a factor 1.6 to their final size (40mm) and replaced by two-ball clumps (major axis of 44mm, minor axis of 37.6mm) with the same total volume, at random orientation. It should be noted that, for all these simulations, the particle shape, the initial porosity of sample and the numbers of particles used in each sample are almost the same (Table 7.1); that is all particles were regarded as being in similar positions at the start of each test. Once the geogrid was installed, the two walls above and below the geogrid area were deleted. Then the assembly was compacted under a high gravitational acceleration of 98.1 ms^{-2} . After the assembly was compacted to equilibrium, the gravity was reduced gradually to 9.81 ms^{-2} . During the preloading stage, all samples were loaded by moving the sleeper towards the assembly to give an initial load equivalent to the self-weight of the sleeper in the laboratory (34kg). Once the required initial stress was achieved, the samples were then loaded by the sleeper base wall using a sinusoidal load pulse with a minimum load of 3kN and a maximum load of 40kN, at a frequency of 3Hz (following McDowell et al., 2005). The required loading was achieved by the PFC^{3D} servo-control mechanism. Figure 7.7 shows the simulated sinusoidal loading curve represented in the form of an applied cyclic stress with the number of cycles (Mean stress= 289 kPa; Amplitude= 489 kPa) for a

frequency of 3 Hz. Unless dynamic increments occur due to rail or wheel imperfections, the load applied has been shown to be frequency-independent; with the result that settlement is only a function of number of cycles (Shenton, 1974).

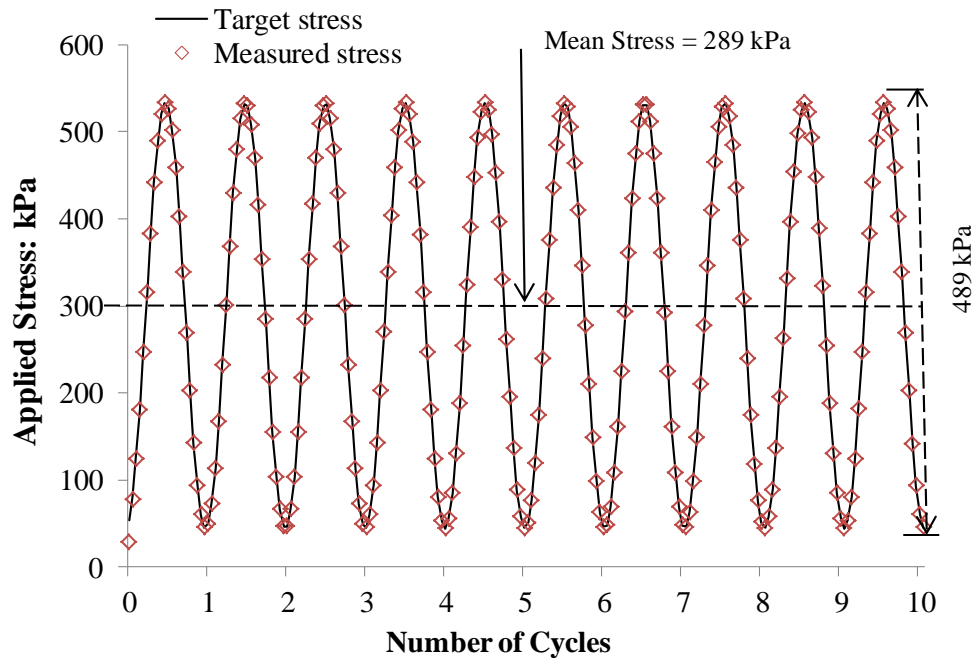


Figure 7.7 Typical applied sinusoidal stress at 3 Hz for box test simulation

7.3.3 Results and discussions

It is unrealistic to perform simulations with a large number of cycles due to the limitations in computing time. In each simulation, only 50 load cycles were performed, taking almost two months of computational time. Figure 7.8 shows the deformation of the simulated sleeper as a function of applied stress for Reinforced Sample 2 (grid at 100mm from the base) during the 50 cycles. It is evident from Figure 7.8 that reinforced ballast gives both resilient and permanent deformations. However, with an increase in the number of cycles, the area inside each loop becomes smaller and the increments of plastic deformation generally decreased. The hysteresis loops are very similar to those obtained in laboratory triaxial experiments and simulations (Selig and waters, 1994; Shenton, 1974; Lu and McDowell, 2006; Lobo-Guerrero and Vallejo, 2006).

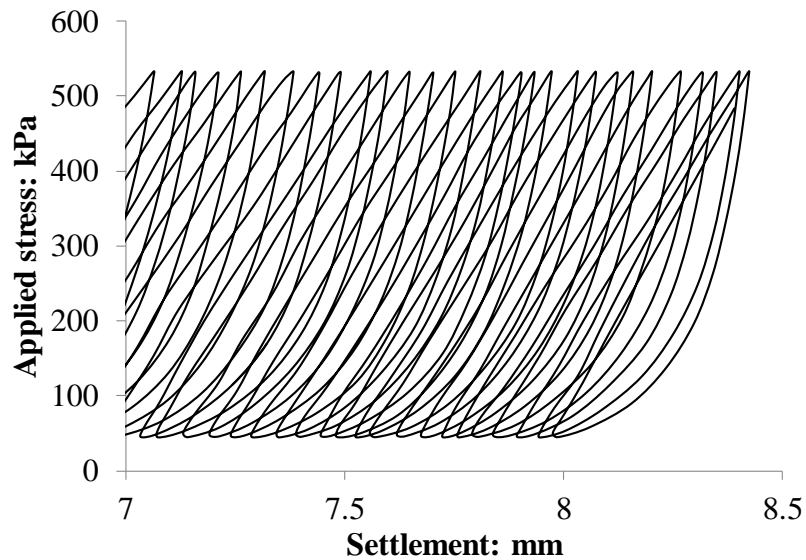
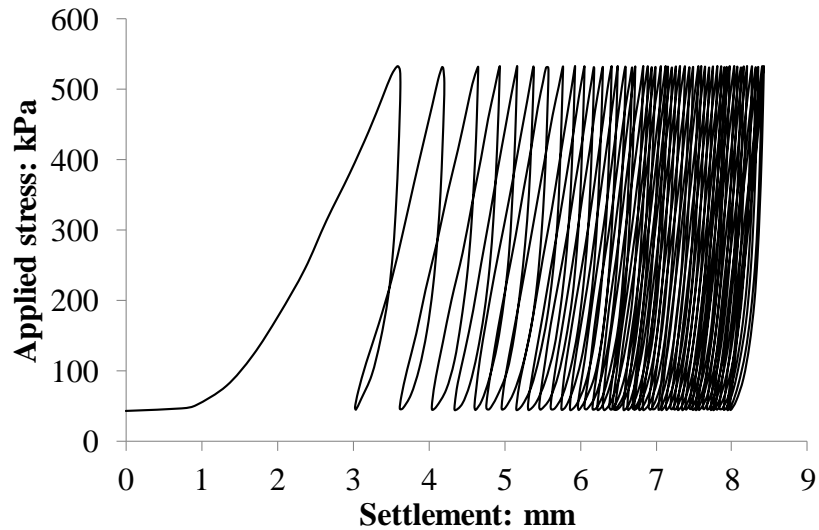


Figure 7.8 Applied stress vs. settlement response for Reinforced Sample 2 (geogrid at 100mm above base)

Figure 7.9 presents the permanent deformation of the sleeper against number of cycles for each of the samples. It is evident that the location of the geogrid layer has a significant influence on the settlement of the ballast. It also can be seen that significant settlements occurs during the early stages; the rate of settlement gradually reduces with the increasing number of cycles until approximately the 15th cycle when the rate of displacement stabilises at this stage. Settlement is only caused by the rearrangement of uncrushable particles in these simulations. It can be seen from Figure 7.9 that the permanent settlement is approximately linear with number of cycles for all samples after 20 cycles: this is due to insufficient interlock provided by the simplistic two-ball clumps. During the first cycle, the settlements of reinforced

samples are obviously smaller than unreinforced sample due to the confinement caused by the geogrid. However, the settlement of Reinforced Sample 1 becomes larger than the unreinforced sample after approximately 13 cycles, which means it cannot provide an effective reinforcement at 50 mm depth. This could be because the single ballast layer (size 40mm) under the geogrid has poor interlock with the geogrid, allowing relatively easily movement of the ballast particles on the base. Generally, the best position of the geogrid is at 100 mm followed by 150mm and 200 mm from the base. This is in agreement with results reported from the experimental box tests conducted by McDowell and Stickley (2006), which showed that the sample with the geogrid at 100mm from the base gave smaller permanent settlements (and hence better performance) than the sample with the grid at 200 mm from the base (see Figure 7.3).

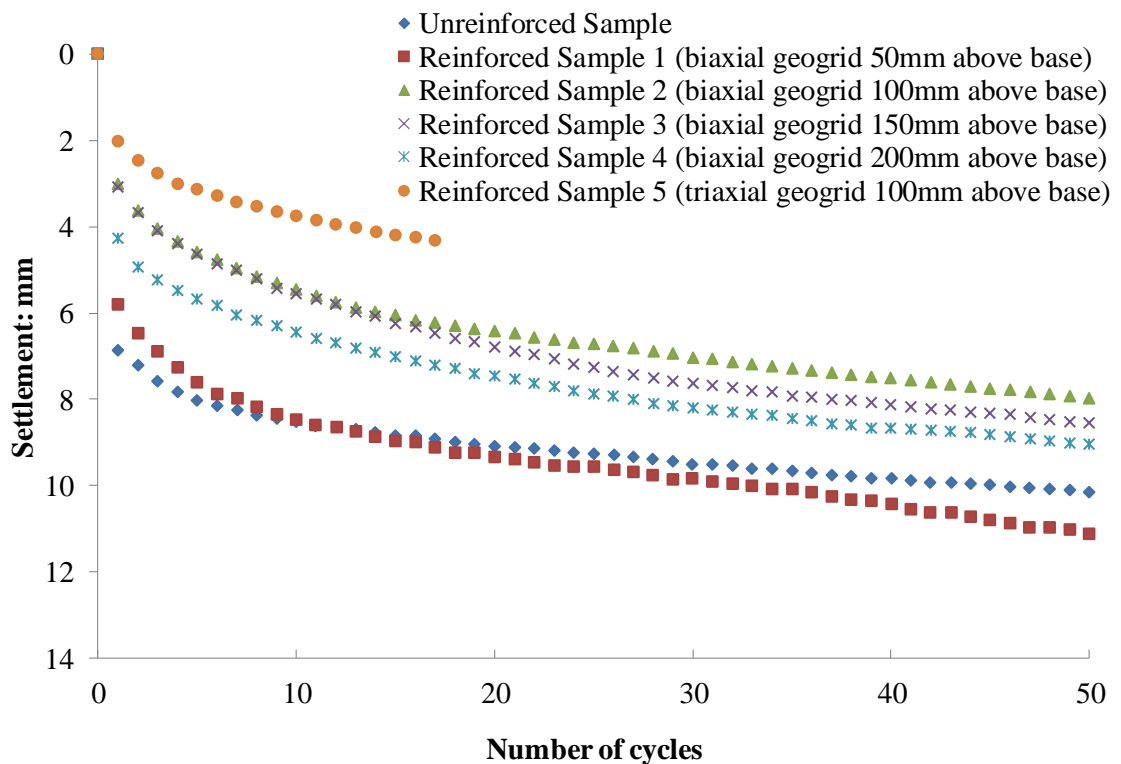


Figure 7.9 Settlement plotted against number of load cycles for all samples

The influence of the geogrid aperture shape has also been investigated. Given that the sample reinforced with the biaxial geogrid at 100mm from the base performed best, a simulation was also performed using the triaxial grid at the same depth to

study the influence of the grid geometry. Comparing the results of Reinforced Sample 2 (biaxial geogrid) and Reinforced Sample 5 (triaxial geogrid), shown in Figure 7.9, it can be seen that the triangular apertures provide better interlock with the aggregate than the square apertures at the same depth. Even though the triaxial geogrid (75mm) has approximately 15% more polymer material than the biaxial geogrid (65mm) per unit area, the triaxial geogrid improved the performance by 33% after 18 cycles. Therefore this improved performance using the triaxial geogrid may be attributed to not only the presence of more material but also the near isotropic radial stiffness, shown in Figure 7.10 (Tensar, 2010). As can be seen from Figure 7.10, the stiffness of biaxial geogrid is greatest when measured in the direction of ribs and is minimum when measured at 45° to the ribs. By comparison, the stiffness of triaxial geogrid is nearly consistent in all directions. It would appear that this grid geometry has improved the performance of the grid-ballast system.

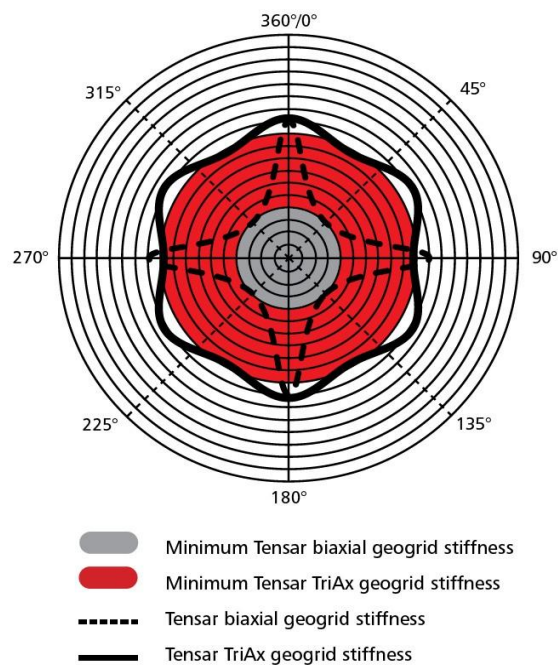


Figure 7.10 Radial stiffnesses of biaxial and triaxial geogrids (Tensar, 2010)

Figure 7.11 shows the resilient modulus for each sample against the number of cycles. The resilient modulus (M_r) of materials is defined as the repeated applied stress divided by the sleeper strain.

$$M_r = \frac{\sigma_{\max} - \sigma_{\min}}{\epsilon_{\max} - \epsilon_{\min}} \quad (7.1)$$

The M_r of Reinforced Sample 1 has an inflection point after approximately 30 cycles, which explains the sudden increase of settlement of Reinforced Sample 1 after 30 cycles (Figure 7.9). In contrast, the M_r of Reinforced Sample 2 and 3 gradually increased until approximately 30 cycles and then tended to a constant value, which implies that the sample became denser and stiffness increases with density. Overall, the resilient modulus did not vary much during cyclic loading and, more significantly, there was no increase owing to the presence of reinforcement. Therefore, the geogrid is likely to be useful for reducing the plastic strain but not resilient strain, which is similar to the conclusion by Brown et al. (2007).

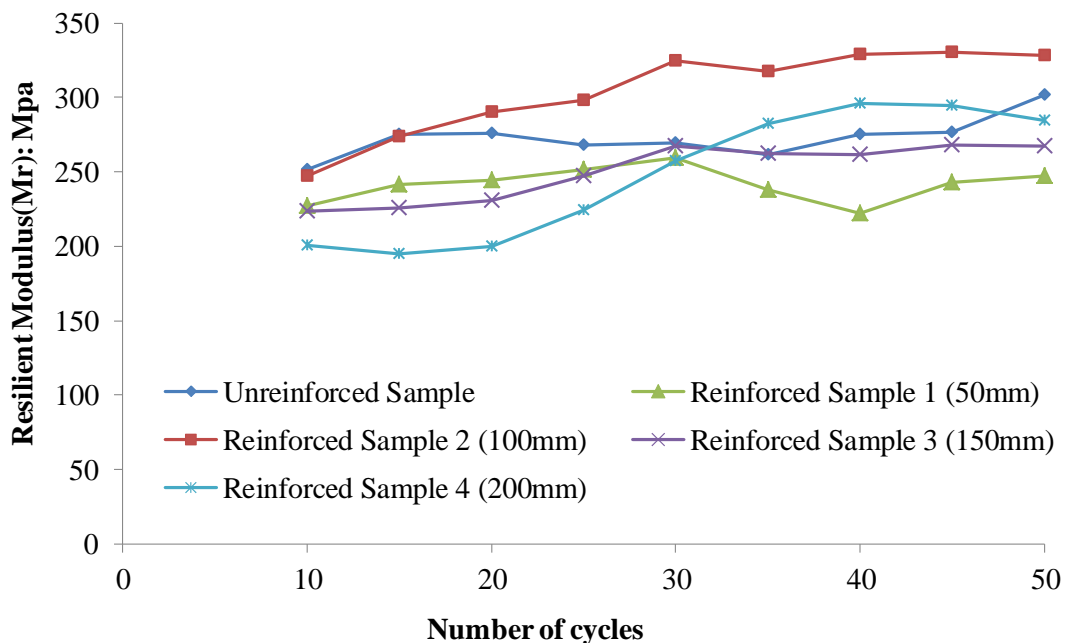


Figure 7.11 Resilient Modulus plotted against number of load cycles for all samples

In order to obtain insight into the interlocking between the ballast particles and the geogrid, contact force distributions and displacement vectors during cyclic loading were investigated. Figure 7.12 shows the contact force chains for Reinforced Sample 2 (100 mm from base) at different stages of cyclic loading: at minimum load before the first loading cycle, at maximum load during the first cycle, and after unloading.

The major contact force chains were developed beneath the sleeper during first cycle of loading. Figure 7.13 shows the contact force distributions for each of the samples at peak load during the tenth cycle. The contact force distributions show how the applied load is transferred to the sample. Figure 7.13 shows that mean angle of load spread is smaller for the unreinforced sample than the reinforced sample. If the geogrid is placed too high the major interlocking occurs in the middle of the grid under the sleeper. If the grid is too low, then load is transferred to the side walls. Placing the grid at 100mm from the base gives the best results in terms of confining most of the ballast across the entire section of grid, so that the grid-ballast system is essentially acting as a beam in bending. These results are in agreement with a technical report by Oxford University (1980). Figure 7.14 shows the particle displacement vectors, drawn at the same scale to allow visualization of the local deformation mechanisms, for unreinforced and reinforced samples. The average displacement is the mean magnitude of the displacement vectors for all ballast clumps. The average displacements calculated by the displacement vectors show that displacement for the triaxial grid is by far the lowest and the displacement for the biaxial geogrid at 50mm above the base is the largest. This is consistent with the settlement of each sample as shown in Figure 7.9. Besides, it can be seen that the contact forces are consistent with the particle displacements, comparing Figure 7.13 and Figure 7.14.

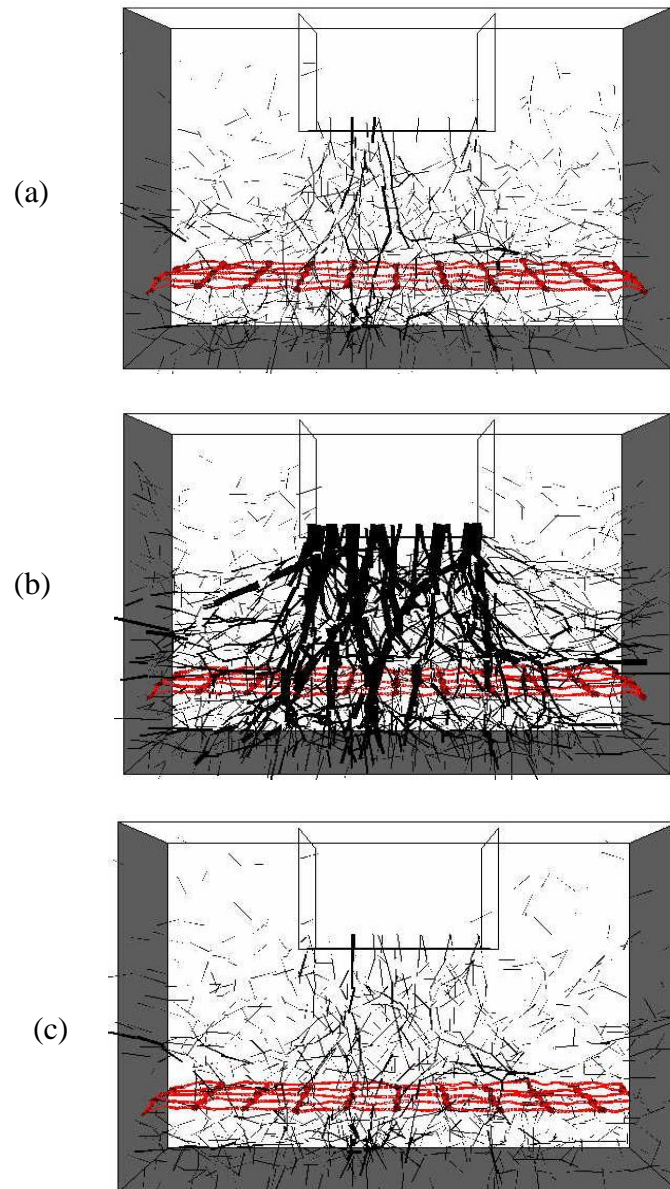


Figure 7.12 Contact forces for reinforced sample with a geogrid at 100mm above the base: (a) at minimum loading (maximum contact force= 883N); (b) at maximum load (maximum contact force= 3910 N); (c) after unloading to 3 kN (maximum contact force= 938 N)

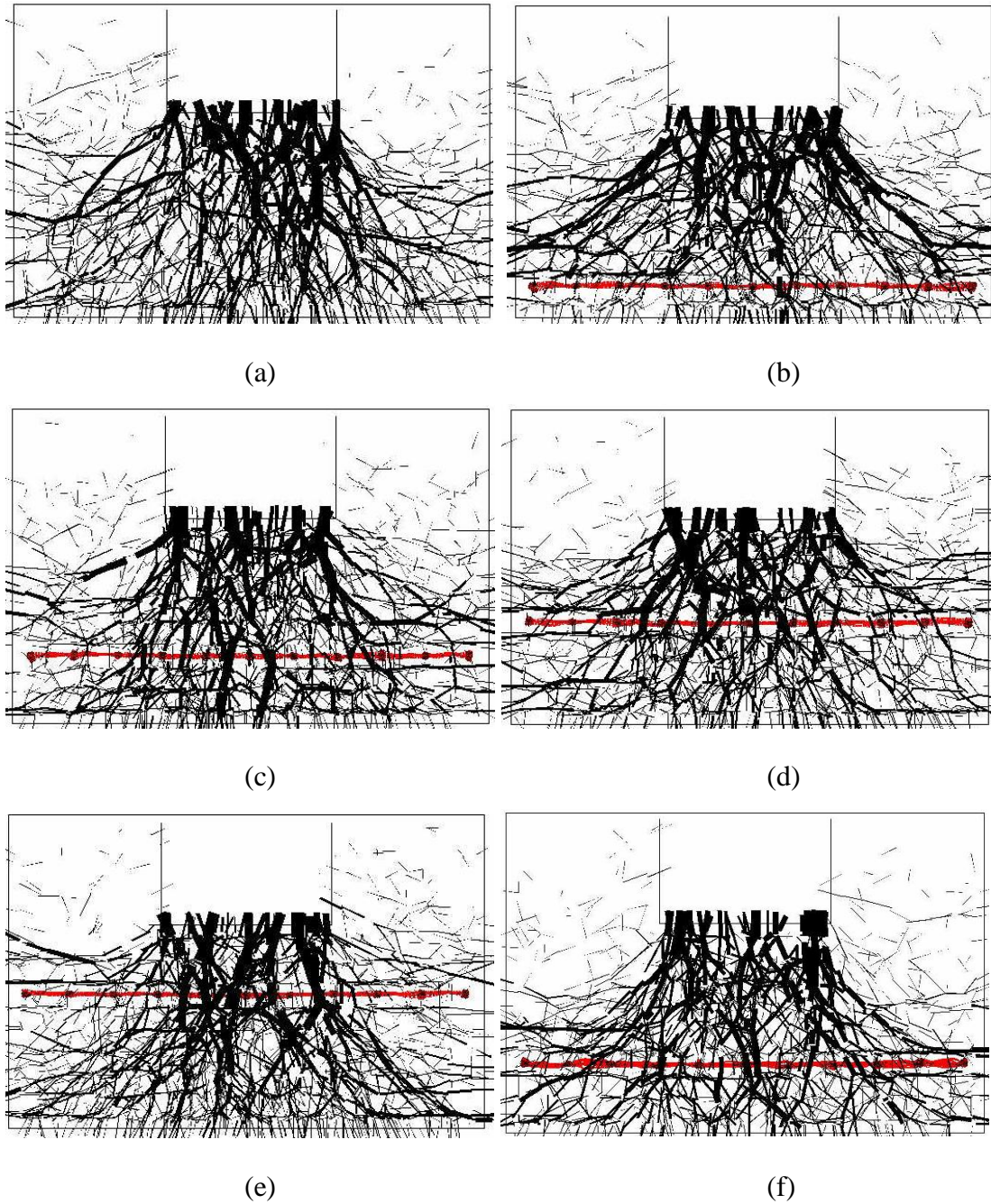


Figure 7.13 Contact force distributions at maximum load during the tenth cycle: (a) unreinforced sample (maximum contact force= 3527N); (b) Reinforced Sample 1 (maximum contact force= 2932N); (c) Reinforced Sample 2 (maximum contact force= 2995N); (d) Reinforced Sample 3 (maximum contact force= 3290N); (e) Reinforced Sample 4 (maximum contact force= 3404N); (f) Reinforced Sample 5 (maximum contact force= 4547 N)

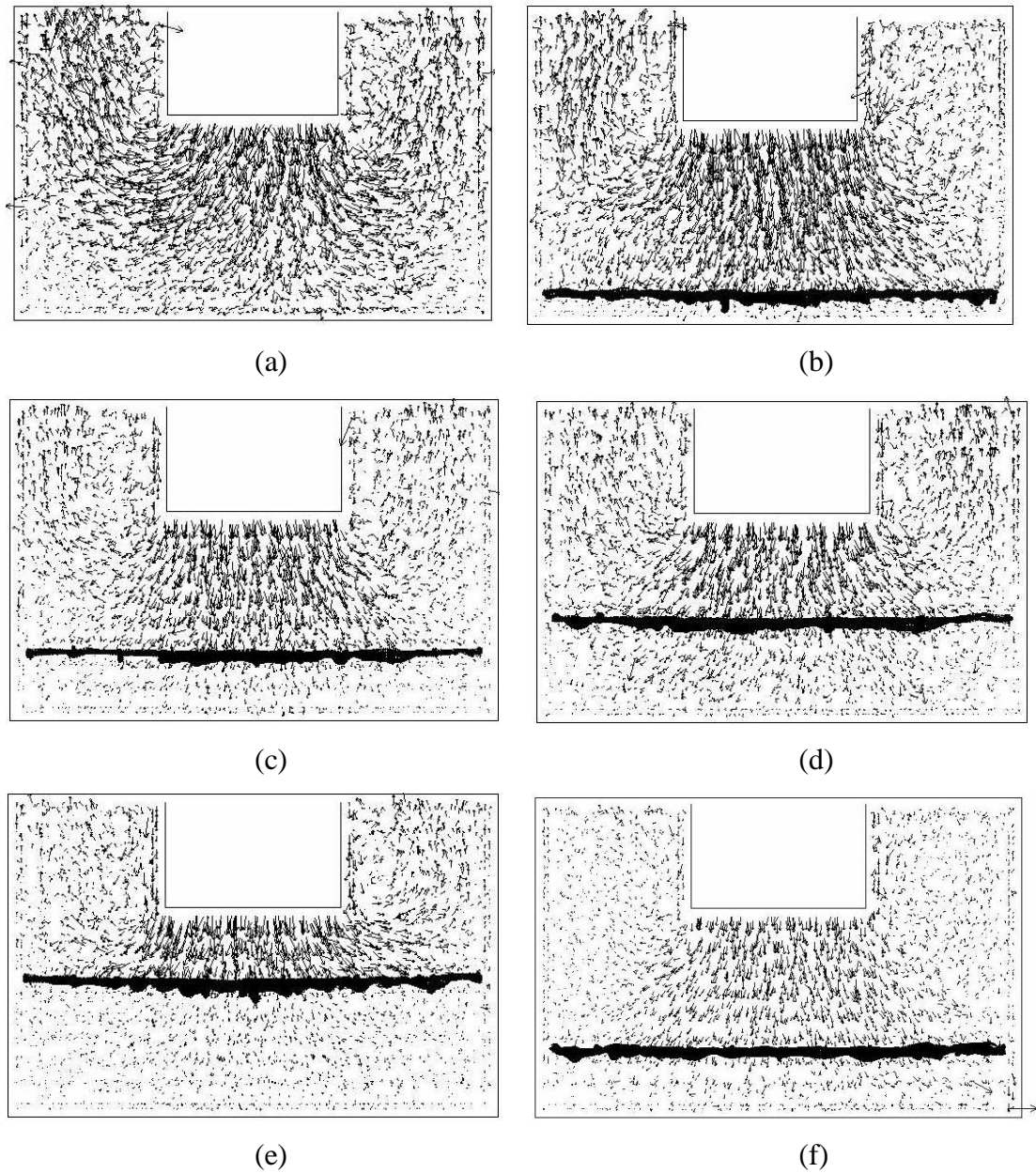


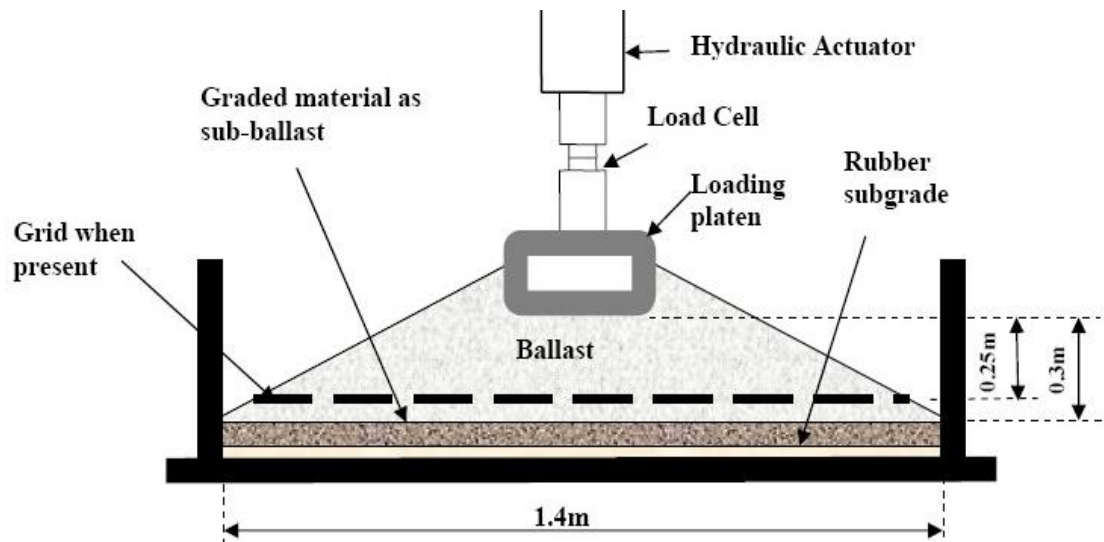
Figure 7.14 Total displacement vectors drawn at same scale at maximum load during the tenth cycle: (a) unreinforced sample (average displacement =2.80mm); (b) reinforced sample 1 (average displacement= 3.17mm); (c) reinforced sample 2 (average displacement=2.12mm); (d) reinforced sample 3 (average displacement=2.21mm); (e) reinforced sample 4 (average displacement=2.15mm); (f) reinforced sample 5 (average displacement= 1.85mm)

7.4 Composite Element Test (CET)

7.4.1 The test description

The Composite Element Test (CET) apparatus, as shown in Figure 7.15, was designed to investigate various design variables (e.g. geogrid geometric properties, subgrade stiffness and location of the geogrid layer for use in trackbed design) under simplified full-scale conditions of the field situation (Brown et al. 2007). It consists of a 'channel' of 1.4m long, 0.7m wide and 0.3m thick in keeping with normal ballast depth on site. A cyclic load of 20kN at 2 Hz was applied for 30,000 cycles through a loading platen consisting of a section of rectangular hollow steel, 0.7m long and 0.25m wide, giving a contact stress of 114kPa beneath the beam, which is approximately half of the maximum expected on an actual track (Brown et al. 2007). Rubber sheets were used to form the subgrade: a single sheet for the 'stiff' condition and three sheets for 'soft'. The soft condition was found to be approximately equivalent to a subgrade with resilient modulus of 30MPa and the stiff condition to a subgrade with resilient modulus of 90MPa. A 50mm thin well-graded sub-ballast layer was placed over the rubber, which provided a transition from the rubber to the ballast thus allowing more realistic behaviour than if ballast and rubber had been used alone. Figure 7.15b shows the ballast sample after it was compacted with a pneumatic vibro-tamper in a consistent manner for each test installation.

The primary objective of the CET experiments was to investigate whether or not accumulated settlement could be reduced by use of the reinforcing geogrid. Brown et al. (2006) carried out CET tests with a range of different aperture sizes. They found that an aperture size of 65mm gave optimum performance for the 50mm ballast. This conclusion was confirmed by the theoretical analysis of pull-out tests reported by McDowell et al. (2006). Figure 7.16 shows the 40-32 geogrid (tensile strength of 40kN/m and 32mm nominal aperture) is seen to result in higher settlement than for the unreinforced case. However, the larger aperture, 30-65 geogrid (tensile strength of 30kN/m and 65mm nominal aperture) shows a much better performance.



(a)



(b)

Figure 7.15 The Composite Element Test apparatus: (a) front view; (b) side view (Brown et al, 2007)

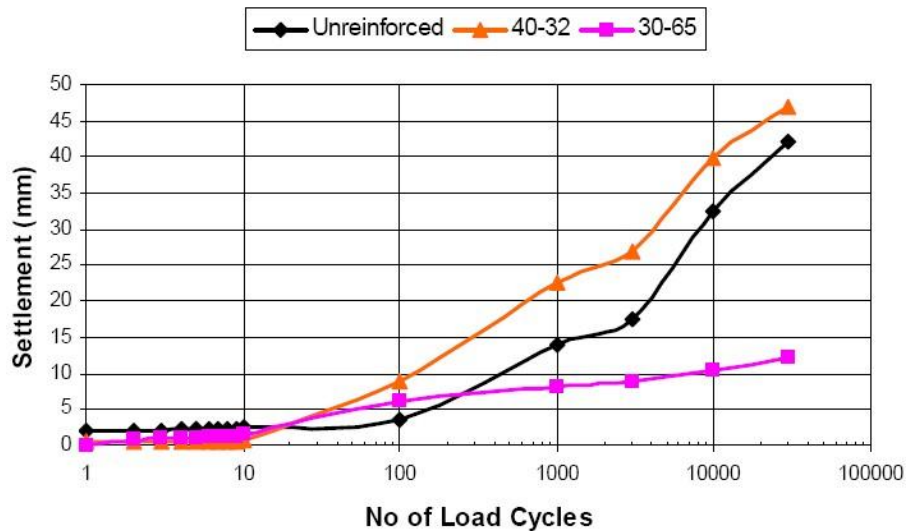


Figure 7.16 CET data comparing reinforced and un-reinforced ballast performance (Brown et al, 2006)

7.4.2 Modelling procedure

The presented box test simulation has modelled cyclic loading of geogrid-reinforced ballast under confined condition. The aim of CET simulation is to examine the performance of geogrid-reinforced ballast under unconfined condition. The full-scale CET model is too computationally time-consuming owing to the complicated geogrid layer and too many ballast particles, and is beyond current computer capabilities. Therefore, the width of sample was decreased from 700 mm to 300 mm to reduce the number of balls and therefore reduce the computation time. Nevertheless, there are still more than 100,000 spheres for a reinforced sample. In order to focus on the settlement in ballast layer, the settlements in the sub-ballast and subgrade layer were ignored in this simulation. Therefore, the sub-ballast layer, as shown in Figure 7.17, was simulated by a rectangular agglomerate (i.e. bonded particles) of graded two-ball clumps which have the same volumes as spheres with radius from 5mm to 8mm. The ballast layer was generated using the same dynamic method as the box test simulation. During the generation procedure, an initial sample of spheres was generated within the trapezoidal prism without overlapping and then expanded to their final size. Afterwards, these spheres were replaced by two-ball clumps with the same volume. The micromechanical parameters for the ballast particle and geogrid model are the same as used in the box test simulations. For the reinforced sample, similarly, two stiff walls were generated above and under the

geogrid to prevent overlapping between geogrid and ballast particles. Once the geogrid was installed, the two walls were deleted and the system cycled to equilibrium. Then the two side sloping walls were removed and the ‘sleeper’ velocity was applied using the PFC^{3D} servo-control mechanism. Once the required initial stress was achieved, a sinusoidal load pulse was applied on the sleeper walls with a minimum load of 1.5 kN and a maximum load 10 kN at a frequency of 2 Hz, which is half the cyclic load in the lab due to the DEM sample being approximately half as wide as the lab sample.

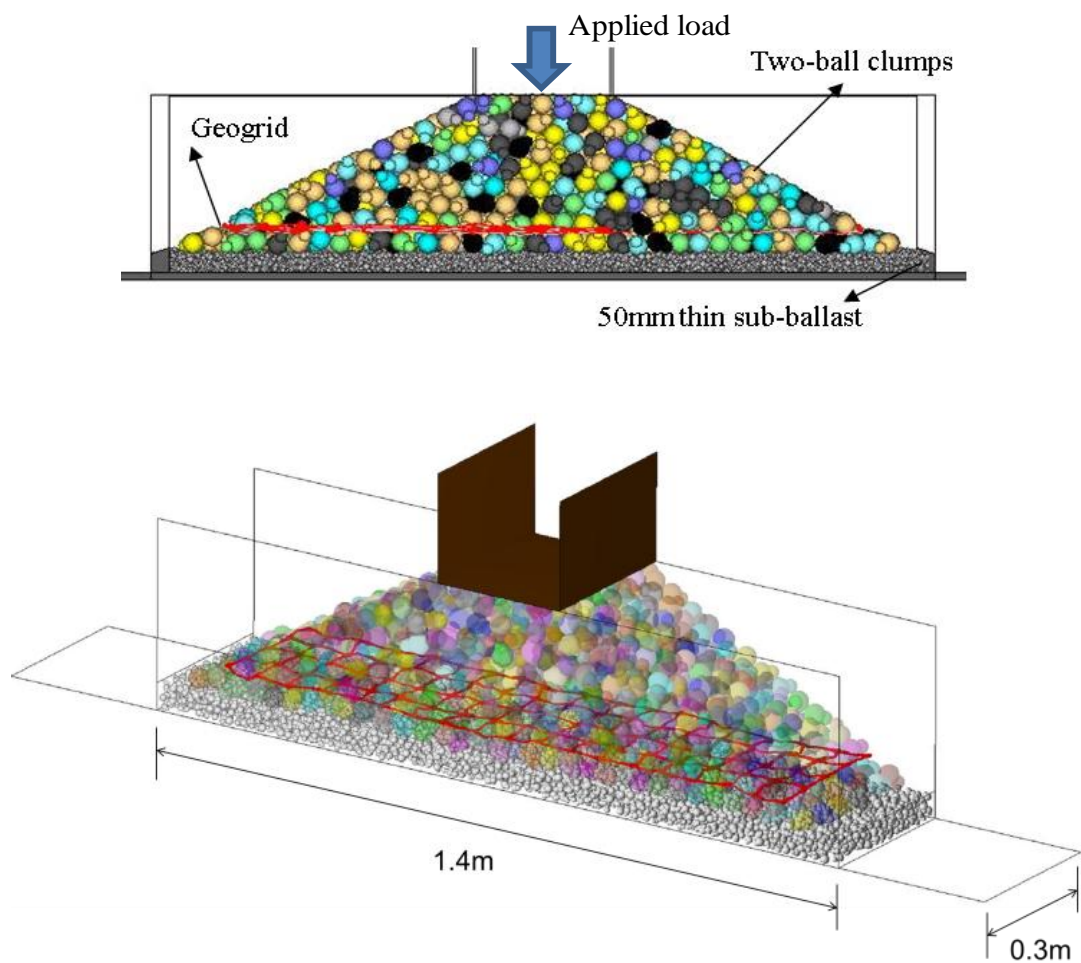


Figure 7.17 Geometry of the simulated CET apparatus

7.4.3 Results and discussion

It should be noted that the geogrid models comprise too many small spheres, which causes the computing speed for reinforced samples to be very slow. The number of

applied cycles is 50 cycles, still taking one month of computational time. Figure 7.18 shows a comparison of performance with the geogrid in its usual position at the bottom of ballast layer (50mm above sub-ballast), 100mm above the sub-ballast and mid-depth (150mm above sub-ballast). The figure also shows the results of using geogrids at both locations; one at 50mm above sub-ballast bottom and one at mid-depth. The results indicate that the settlement could be reduced by use of the reinforcing geogrid and also demonstrates that the position of the geogrid has a major influence, which is in agreement with the results of the CET experiments (Brown et al., 2007) and box test simulations presented earlier. Generally, for a single geogrid layer, the location of the grid at the bottom of the ballast layer (50mm) is better than at 100mm from the sub-ballast or at mid-depth. It's surprising that the geogrid placed at the mid-depth performs worst. This will be explained by the following analysis of contact force distribution. For the double geogrid layer, it seems to give a small improvement in term of reducing settlement, but it would be considered uneconomical to use two layers when the improvement is only marginal when comparing with the performance with the single grid at 50mm above the sub-ballast.

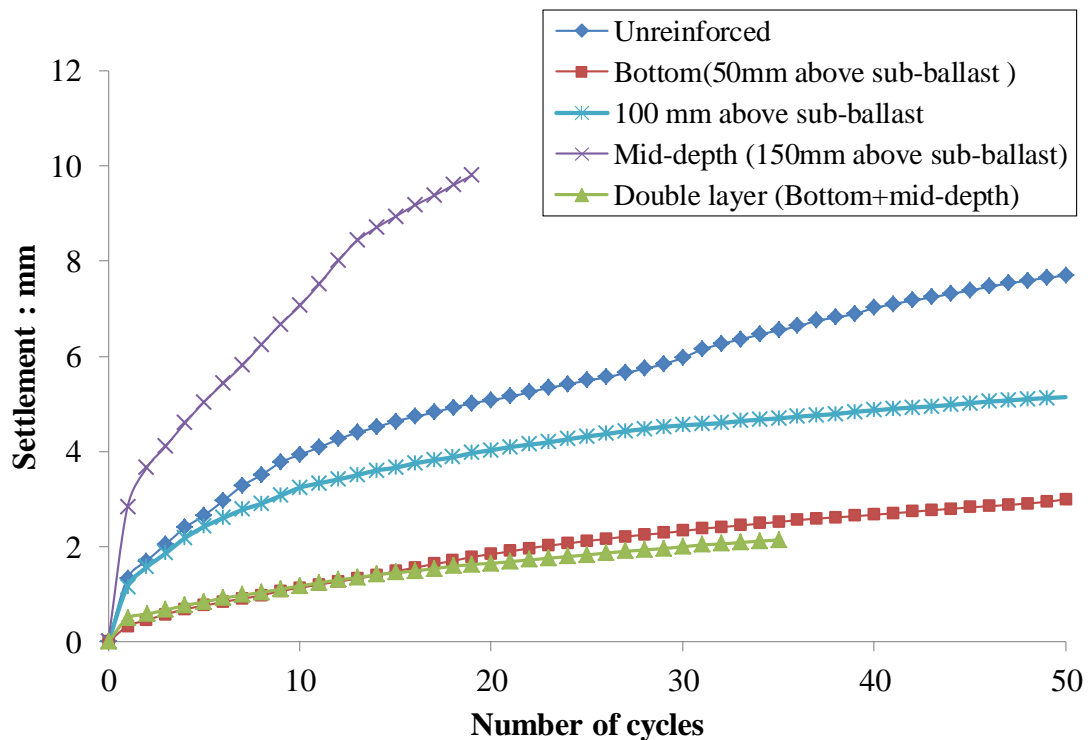


Figure 7.18 Comparison of performance for different arrangements of geogrids

The CET experimental data (Brown et al. 2007), shown in Figure 7.19, shows that the geogrid reinforcement effect is more pronounced for a soft subgrade than a stiff one. In this simulation, the subgrade was represented by the base wall: a stiffness of $5 \times 10^5 \text{N/m}$ for the 'soft' condition and a stiffness of 10^8N/m for the 'stiff' condition. Even though ballast gradations are different and also the base wall in the simulation is not deformable but the rubber subgrade in the lab is deformable, the simulation results from Figure 7.20 simply show the same conclusion as for the experimental results, namely that the subgrade stiffness has an influence on the settlement of ballast layer. However, the difference between stiff and soft subgrade is very small in both experimental and numerical results up to 20 cycles. More cycles are required before confident conclusions can be drawn.

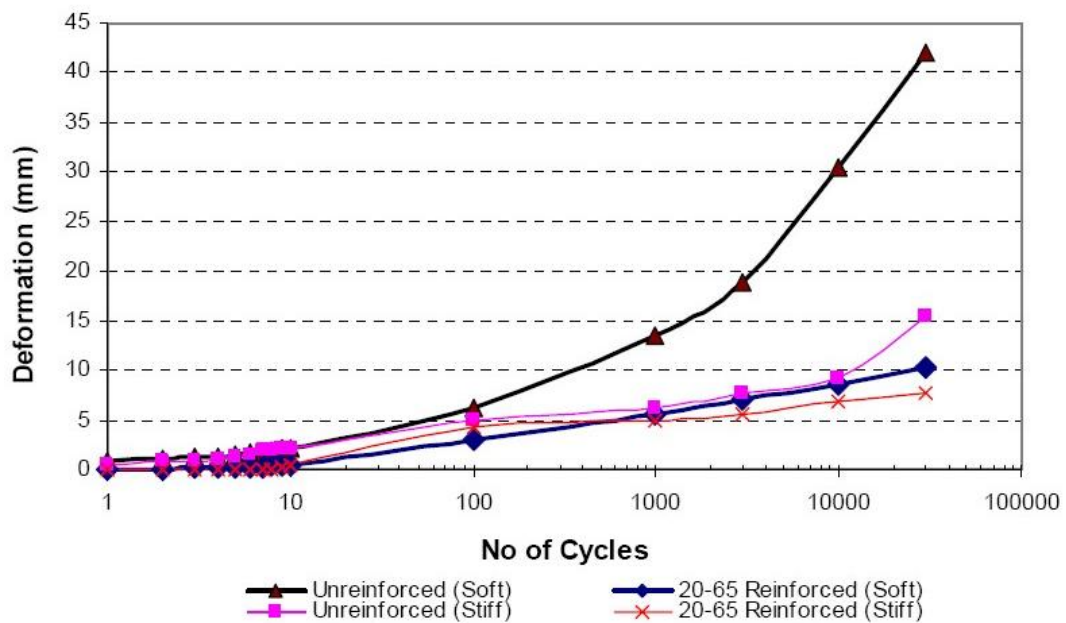


Figure 7.19 CET data comparing reinforced and unreinforced ballast (Brown et al, 2007)

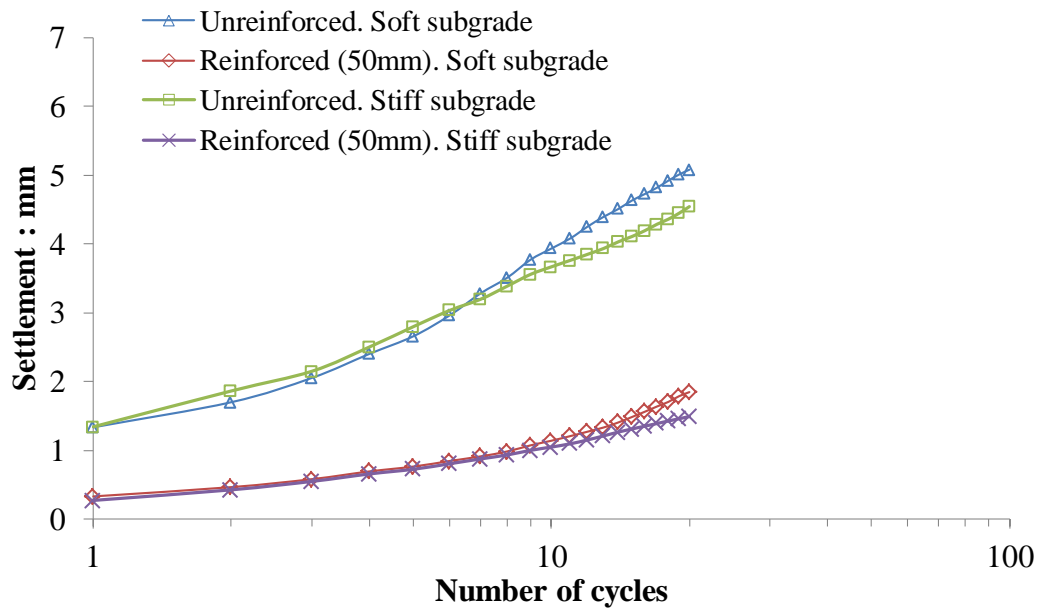


Figure 7.20 Effect of subgrade stiffness and of geogrid reinforcement (logarithmic scale)

Figure 7.21 presents contact force distributions at maximum load. It can be seen that Figure 7.21b shows improved confinement, with a well-defined vertical channel of contact forces. However, in Figure 7.21c and 7.21d with the geogrid at 100mm above subballast and mid-depth, there are very high contact forces directly under the sleeper with low contact forces away from the sleeper; this is consistent with the poor performance in terms of settlement. Figure 7.22 shows that the lateral displacement was significantly reduced in the reinforced zone which is approximately 50 mm above and below the geogrid. Moreover, Figure 7.23 shows the reduced displacements for the reinforced sample compared to the unreinforced sample.

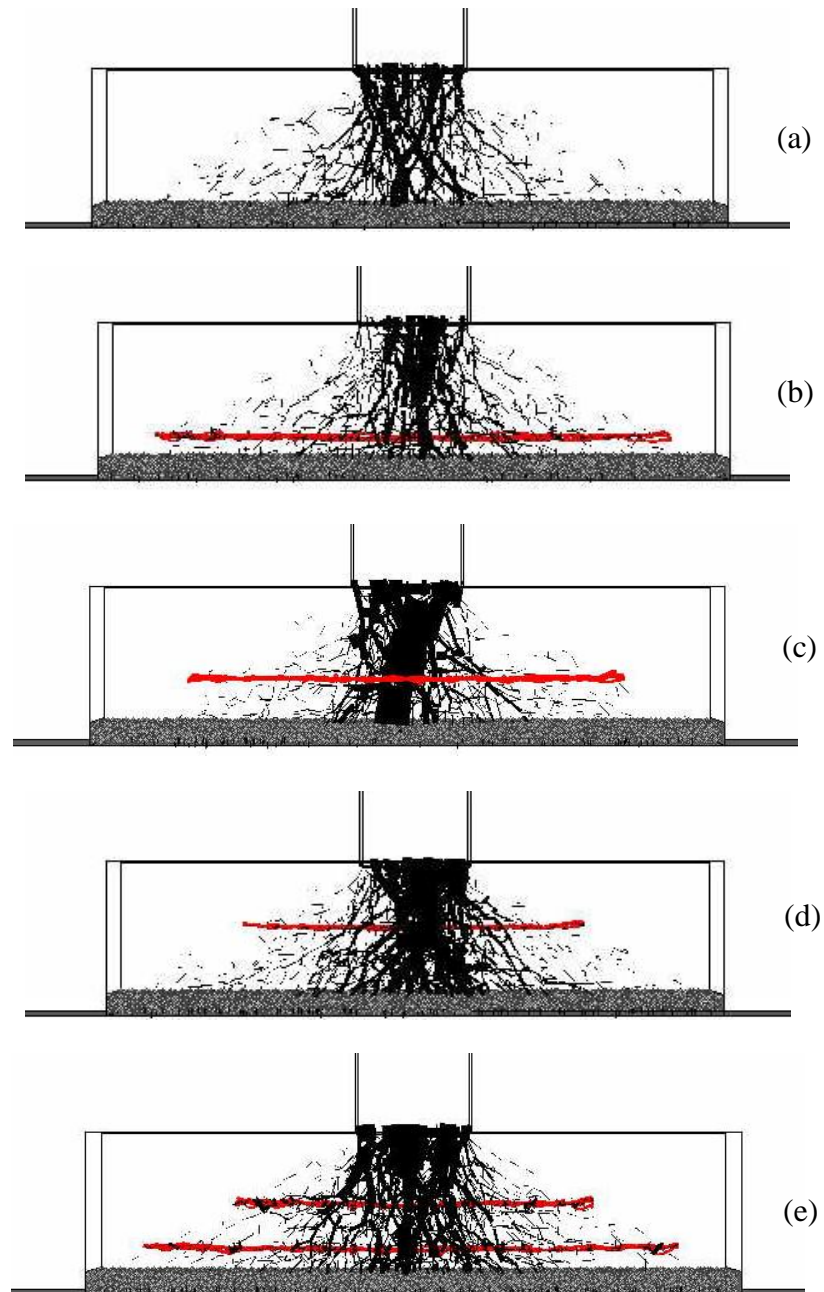


Figure 7.21 Contact forces (scaled) at maximum load during the ninth cycle: (a) unreinforced sample; (b) reinforced sample (bottom); (c) reinforced sample (100mm above subballast); (d) reinforced sample (mid-depth); (e) reinforced sample (double layer)

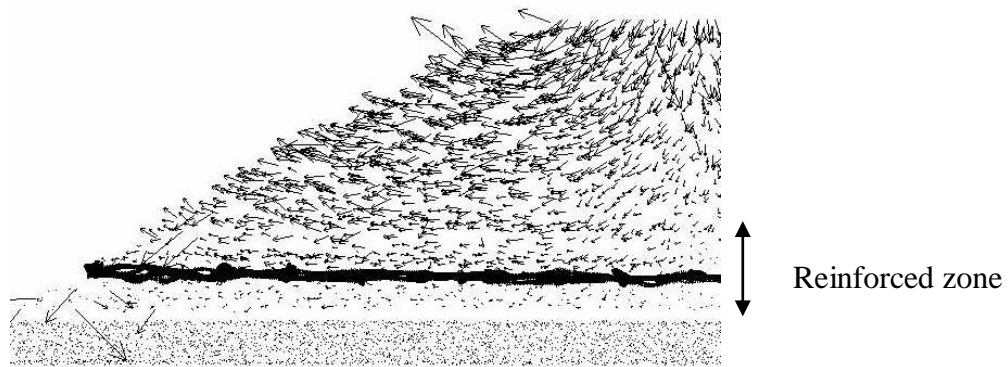


Figure 7.22 Total displacements at maximum load in the left half sample

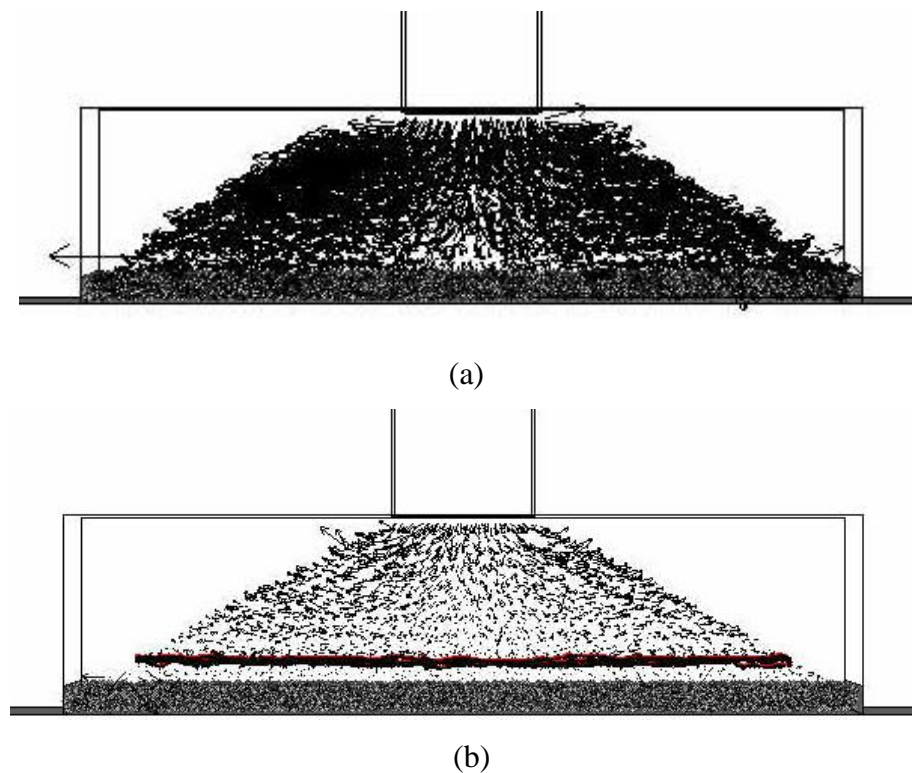


Figure 7.23 Displacement vectors of ballast particles at maximum load during the ninth cycle: (a) unreinforced sample (Maximum magnitude of displacement vector = 13.0); (b) reinforced sample (Maximum magnitude of displacement vector= 8.4)

7.5 Conclusions

A discrete element model for geogrid-reinforced ballast has been developed using two-ball clumps for the ballast particles and alternative biaxial and triaxial two-layer geogrid models. The two-ball clumps have been shown to give a similar angle of

reponed to real ballast. The geogrid models have been developed by bonding small balls together regularly to form the desired geometry using parallel bonds, and the micro mechanical parameters chosen to calibrate the grid behaviour against simple laboratory tests. Geogrid-reinforced ballast under cyclic loading has been simulated for both confined and unconfined conditions. Results in both cases confirmed that the geogrid reinforcement can reduce the settlement of ballast significantly when placed at the optimum location. For the confined condition (box test), the optimum location of geogrid is 100 mm above the base, and the triaxial geogrid of aperture (rib) size 75mm outperforms the biaxial geogrid of aperture (rib) size 65mm. The resilient behaviour is not affected much by the presence of the geogrid, but permanent settlements are significantly reduced, thereby reducing maintenance operations and associated costs in real trackbed. For the unconfined case, the geogrid layer positioned 50mm from the sub-ballast layer gives a better performance than that at 100mm from the sub-ballast layer or at mid-depth in the ballast layer in agreement with experimental results by Brown et al. (2007). The use of two geogrid layers located both near the base and at mid-depth leads to a slight improvement in performance. The geogrid limits the lateral displacement of particles in the reinforced zone, which is approximately 50mm above and below the geogrid. The subgrade stiffness has an influence on the settlement of ballast layer. The next chapter will examine the differential settlements caused by train loading over a trackbed of variable subgrade stiffness.

Chapter 8 Discrete element modelling of track transition zones

8.1 Introduction

Transition zones span between railway track on natural ground and rigid substructures such as culverts, tunnels and bridges (Figure 8.1). The abrupt change in the stiffness of the track support leads to the pumping ballast, hanging sleepers (gaps between sleeper and ballast), ballast breakdown, rail battering, concrete sleeper cracking and differential settlement. Therefore, transition zones typically require extensive maintenance to preserve track geometry and ride quality. These high maintenance costs and the potential to cause delays to train services are of major concerns for railway infrastructure managers. However, in many countries transition design is still based on empirical methods using trial and error (for example in the UK there is no standard for transition design). Thus, at present, there is no detailed understanding of the mechanisms of track geometry deterioration at transition zones.



Figure 8.1 Transition section between an embankment and a bridge (Li and Davis, 2005)

This chapter aims to use the discrete element method (DEM) (Cundall and Strack, 1979) to investigate transition zones from a micro mechanical perspective. DEM enables the monitoring of the evolution of the inter-particle contact forces, displacements and velocities of particles which cannot easily be investigated in the field. Hence, a track transition model with dimensions 2.1m x 0.3m x 0.45m was simulated by using PFC^{3D}. In this simulation, ballast particles were represented by two-ball clumps; sleepers and subgrade were represented by walls with various stiffnesses. The stiffness of the base wall was determined by simulating a simple compaction test. In order to identify and evaluate appropriate mitigation methods, two kinds of transition patterns, including a single step change and a multi step-by-step change for subgrade stiffness distributions, were tested. Due to faster and heavier modern trains, existing railway transition zones are experiencing problems, such as deterioration and/or loss of ballast material, and the increase of differential settlements. The influences of train direction, speed and axle load on the transition were also investigated. In addition, geogrid was used in the ballast layer (100mm from base) on the soft subgrade, to examine the effect of geogrid reinforcement. The biaxial geogrid model with aperture size 65mm was developed by using many small balls bonded together. In order to replicate realistic traffic loading, a sinusoidal load applied on the three sleepers was simulated in a controlled manner using out of phase loading. A 90 degree out of phase loading was used. This chapter provides insight into the factors that can cause or accelerate track degradation at the transition zones, in order to identify and evaluate appropriate mitigation design.

8.2 Problem definition

Track transition issues affect all types of rail operation. It should be noted that there are few papers specific to railway transition; much of existing literature is related to normal track. The purpose of this section is to summarize the existing literature in terms of problem definitions, analytical and numerical methods, and recommended designs and proposed mitigation techniques.

According to Davis and Li (2006), track transition problems specifically occur at bridge approaches, and can be attributed to the following three major factors:

(1) An abrupt stiffness change in the track support leads to uneven track deflection that can increase dynamic vehicle/track interaction. The increased dynamic wheel/rail forces, together with a uniform distribution of internal forces between the rails and sleepers, accelerate differential settlement, which leads to even higher forces (Kerr and Moroney, 1993; Frohling et al. 1995; Hunt and Winkler, 1997). Moreover, the effect of the load increase depends on the moving direction of the train. In addition to track stiffness change, vehicle axle loads, speeds, and suspension characteristics all influence differential settlement.

(2) The ballasted approach section inherently settles more than the bridge section because of underlying soil layers, thus producing an uneven profile or differential settlement that leads to adverse dynamic vehicle/track interaction.

(3) Settlement of ballasted track can be highly variable because of geotechnical issues affecting the subgrade performance such as low strength soils, deficient soil placement and compaction, poor drainage and erosion (Briaud et al. 1997; Hoppe 2001). Environmental factors such as wet/dry and freeze/thaw cycles also affect subgrade settlement behaviour.

Li and Davis (2005) carried out a comparison of the results of tests for average track settlement on four ballast deck railway bridges and their approaches. The results show that the approaches experienced more track geometry degradation than the tracks on the bridges and the open track. The literature indicates that transitions were designed to (1) equalize the stiffness and rail deflection of the ballasted and non-ballasted tracks, usually by controlling the resilience of the rail on the non-ballasted track, or (2) provide a gradual track to match that of the non-ballasted track. Several designs seek to increase the stiffness of the ballasted track by placing a structural element, such as a concrete slab, Geocell reinforcement or an asphalt pavement layer,

between the track granular layers (ballast/subballast layers) and the subgrade (Li 2000; Rose et al., 2002; Bilow and Li, 2005). These structural layers are generally tapered or stepped to allow a gradual increase, or ramping up, of the stiffness within about 20ft of the non-ballasted track interface. Davis and Li (2006) analysed track transition designs using the GEOTRACK computer model (Selig and Waters, 1994). They found that the track modulus and rail deflection of ballasted track were dominated by the subgrade stiffness. Therefore, to significantly increase the stiffness of ballasted track, modification or reinforcement of the subgrade is required. Concrete approach slabs placed between the ballast and subballast layers produced the most substantial track modulus /rail deflection benefits comparing with Hot-Mixed Asphalt underlay and Geocell reinforcement in the subballast layer.

Some other numerical approaches have used the finite element method to investigate the dynamic behaviour of track transition (Banimahd and Woodward, 2007; Lei and Zhang, 2010; Banimahd et al. 2011; Varandas et al. 2011). However, there is no analysis of transition zones from a micro mechanical perspective, as far as the author is aware. In this thesis, the discrete element method (DEM) has therefore been used to simulate the transition zones and provide much needed micro mechanical insight.

8.3 DEM of track transition

8.3.1 Sample preparation

Even issues surrounding transition are more complex than simply a change in track stiffness. Figure 8.2 shows a schematic layout of railway track stiffness transition. It is unrealistic to perform transition zone simulations at full scale due to limitations in computing time. Therefore, a simple 3-sleeper box test model was simulated. Figure 8.3 shows three simulated sleepers of dimensions 250 mm x 300mm x 150mm on ballast particles in a box of dimensions 2100mm x 300mm x 450mm. According to RT/CE/S/102 (Railway PLC, 2002), the minimum ballast depth and sleeper spacing for mainline track are 300mm and 600mm respectively. The ballast depth and sleeper spacing in this simulation are 300mm and 650 mm respectively. The box contains 4890 2-ball clumps which were used to represent ballast particles. To prepare the

sample, small spheres were first generated within the box apart from where the three sleepers are located. Then the spheres were expanded by a factor 1.6 to their final size (40mm) and replaced by two-ball clumps (major axis of 44mm, minor axis of 37.6 mm, see Figure 8.3b) with the same total volume, at random orientation. Then the assembly was compacted under a high acceleration of 98.1ms^{-2} , and the friction coefficient of particles was 0.1. After the assembly was compacted to equilibrium, the gravity was reduced gradually to 9.81ms^{-2} . Meanwhile, the friction coefficient of particles was increased gradually to 0.6. Following Chen et al. (2012b), the normal and shear stiffnesses of the particles were 10^8N/m and the stiffness of the sleepers and the walls of the box (except the base) were all set to the same values as the particles. The coefficient of friction for the balls, side walls and sleepers were all set to be 0.6. The micromechanical parameters of the base wall will be calibrated to represent ‘soft’ or ‘stiff’ conditions in following section.

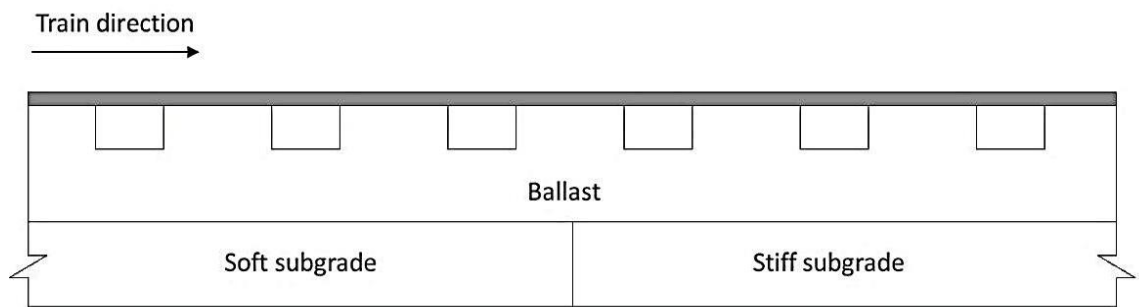
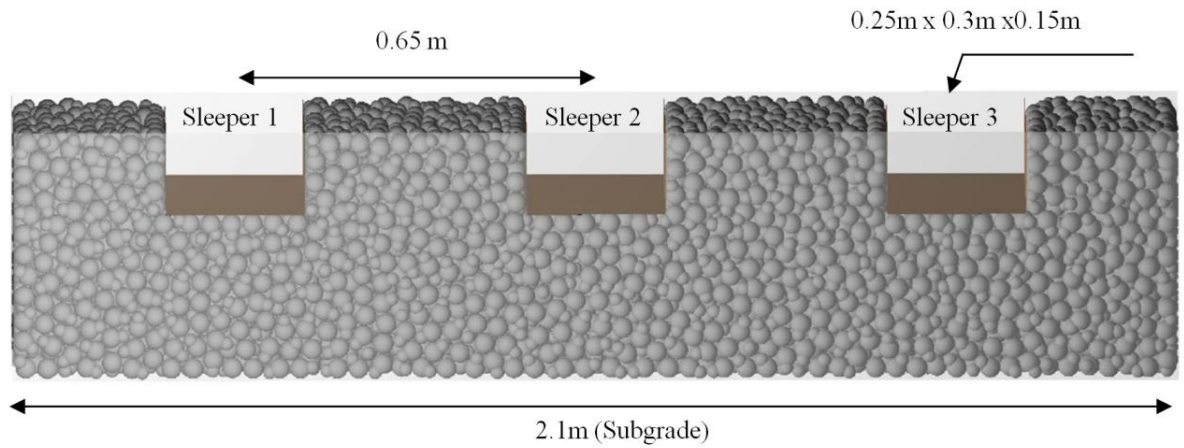
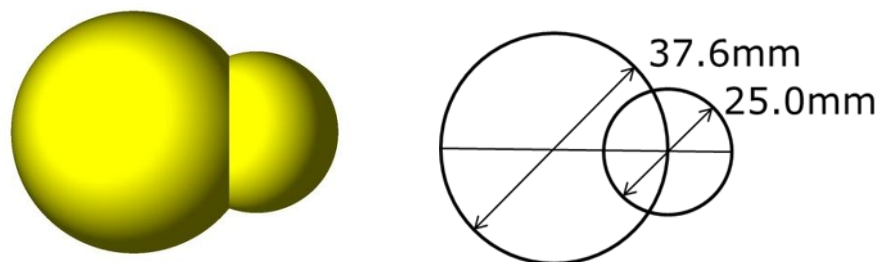


Figure 8.2 A schematic layout of railway track stiffness transition

During the preloading stage, the sample was loaded by moving the sleeper towards the assembly to give an initial load equivalent to the self-weight of the sleeper (34kg). Once the required initial stress was achieved, the sample was then loaded by the sleeper base walls using a phase related loading to replicate realistic traffic loading. The detail of the phase loading pattern will be described in a subsequent section.



(a)



(b)

Figure 8.3 PFC^{3D} model: (a) geometry of the simulated transition zone; (b) two-ball clump as a ballast particle

8.3.2 Determination of the subgrade stiffnesses through a plate bearing test simulation

The idea of modelling soil as an elastic medium was first introduced by Winkler (1867) and this principle is now referred to as the Winkler soil model. The subgrade reaction at any point on the plate is assumed to be directly proportional to the vertical displacement of the plate at that point. In other words, the soil is assumed to be elastic and obey Hooke's Law. The subgrade was simulated by a wall using PFC^{3D} with the same contact and shear stiffnesses. A square clump of length 234mm that consists of 9 x 9 balls was used at the wall to apply a uniform vertical load, as shown in Figure 8.4. The normal and shear stiffnesses of these spheres of the square plate were set to be 10^8 N/m.

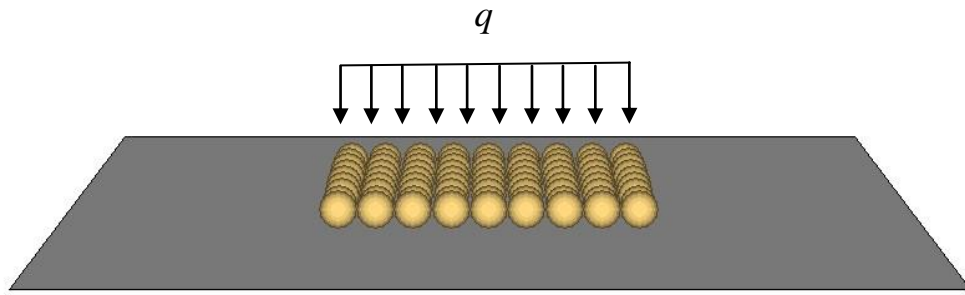


Figure 8.4 Plate bearing test simulation in PFC^{3D}

According to Tomlinson (1995), the settlement (w) of a rigid foundation on a semi-infinite, homogeneous linear-elastic base is given by

$$w = \frac{q}{E} B(1 - \nu^2)(I_s) \quad (8.1)$$

Where w is the vertical displacement of the foundation, m,

q is the bearing pressure under plate (F/B^2), N/m^2 ,

B is the side of square plate, m,

ν is the Poisson's ratio of the soil

E is the modulus of elasticity of the soil, Pa,

I_s is the influence factor

The Poisson's ratio ν was set to be 0.2. The influence factor I_s for settlement depends on the geometry of the plate. For the square rigid plate, the influence factor is 0.82. In this study, the elastic modulus of the subgrades in the open track (soft) and the bridge (stiff) were set to $25MN/m^2$ and $100MN/m^2$, respectively. Because of the soft contact approach in PFC^{3D}, it is possible for balls to penetrate through walls according to the force-displacement law. The magnitude of the overlap also means the vertical displacement (w) is related to the contact force via the force-displacement law, and all overlaps are small in relation to particle size. According to the equation above (Eq. 8.1), when applying a 200N vertical load, the magnitude of overlaps (vertical displacements) in PFC^{3D} were 6.3×10^{-3} mm for soft condition and

1.57 x10⁻³ mm for stiff condition. As a result, the calibrated normal and shear stiffnesses of the base walls in PFC^{3D} were 4.9 x10⁶ N/m at soft end and 2.0x10⁷N/m at the stiff end.

8.3.3 90 degrees out of phase loading

Rigid walls can be used to simulate inclusions or machinery interacting with the granular material. For example, walls were used to represent the railway sleeper in the following simulations. For simulations that require constant loading throughout the test, the servo-control mechanism is implemented. The servo-control mechanism is a function in PFC^{3D} to achieve a required constant stress throughout the simulation. This servo function is called on every calculation cycle to determine the current wall stresses and then adjusting the wall velocities ($\dot{u}^{(w)}$) in such a way to reduce the difference between measured stress ($\sigma^{measured}$) and required stress ($\sigma^{required}$). The calculation algorithm for servo-control mechanism is described as below (see Section 3.4.1):

$$\dot{u}^{(w)} = G(\sigma^{measured} - \sigma^{required}) = G\Delta\sigma \quad (8.2)$$

where G is the ‘gain’ parameter.

The required stresses of these three sleepers are given by

$$\sigma^{required,sleeper 1} = q_{min} + A + A * \sin(2\pi * f * t - \frac{\pi}{2}) \quad (8.3)$$

$$\sigma^{required,sleeper 2} = \begin{cases} q_{min} , & t \leq T/4 \\ q_{min} + A + A * \sin\left(2\pi * f * \left(t - \frac{T}{4}\right) - \frac{\pi}{2}\right), & t \geq T/4 \end{cases} \quad (8.4)$$

$$\sigma^{required,sleeper\ 3} = \begin{cases} q_{min} , & t \leq T/2 \\ q_{min} + A + A * \sin\left(2\pi * f * \left(t - \frac{T}{2}\right) - \frac{\pi}{2}\right), & t \geq T/2 \end{cases} \quad (8.5)$$

$$A = \frac{q_{max} - q_{min}}{2} \quad (8.6)$$

where t is the real time

f is the frequency of the load

A is the amplitude of the applied stress

q_{min} is the minimum applied stress

q_{max} is the maximum applied stress

As shown in Figure 8.5, the simulated traffic loading is achieved by applying sinusoidal loading with a maximum magnitude of 40kN and 90 degrees phase lag between each servo-controlled wall (sleeper). This loading pattern was suggested by Awoleye (1993). It is intended to simulate a train running over three sleepers with 50% of the wheel load on the current loaded sleeper and 25% of the wheel load on the adjacent sleepers (Aursudkij et al. 2009). According to Figure 8.6, it can be seen that the loading pattern in the transition simulation is very similar to that in the real track. The replication of load distribution in the simulation indicates a relatively good simulation of real track. The model simulates a quarter of axle load of approximately 16 tonnes which is comparable to a typical heavy axle load on top of the middle sleeper. The loading frequency varies from 3, 10, 20, 30 and 40Hz to represent train speeds of approximately 28, 94, 187, 281 and 374km/h for investigating the influence of train speed. The DEM model treats the applied wheel loads as vertical only. Only single wheel loads were used in these simulations. The effects of rotating principal stresses have been neglected in this study. With 7.8m/s train speed or 28 km/h, this meant that the test simulated a 2.6 m axle spacing (7.8m/s x 1/3s). The spacing of the front pair of axles of a Bombardier BiLevel passenger rail vehicle in Montreal, Canada is also approximately 2.6 m (Bombardier Inc., 2007).

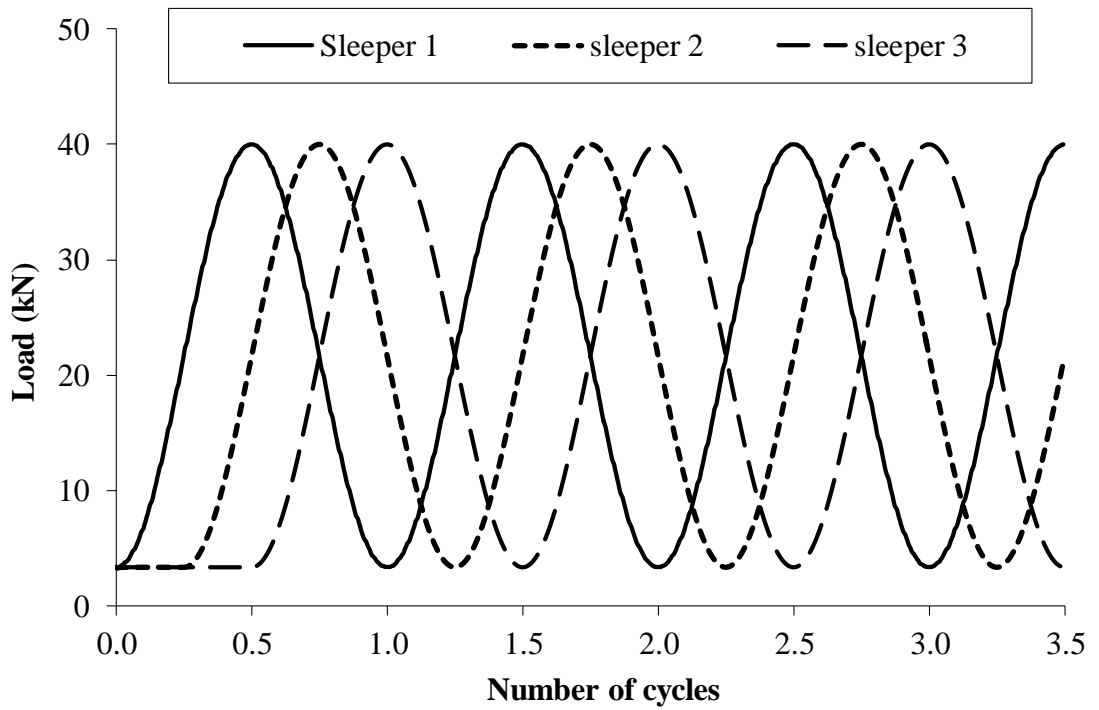


Figure 8.5 Loading pattern in the 3-sleeper box test simulation

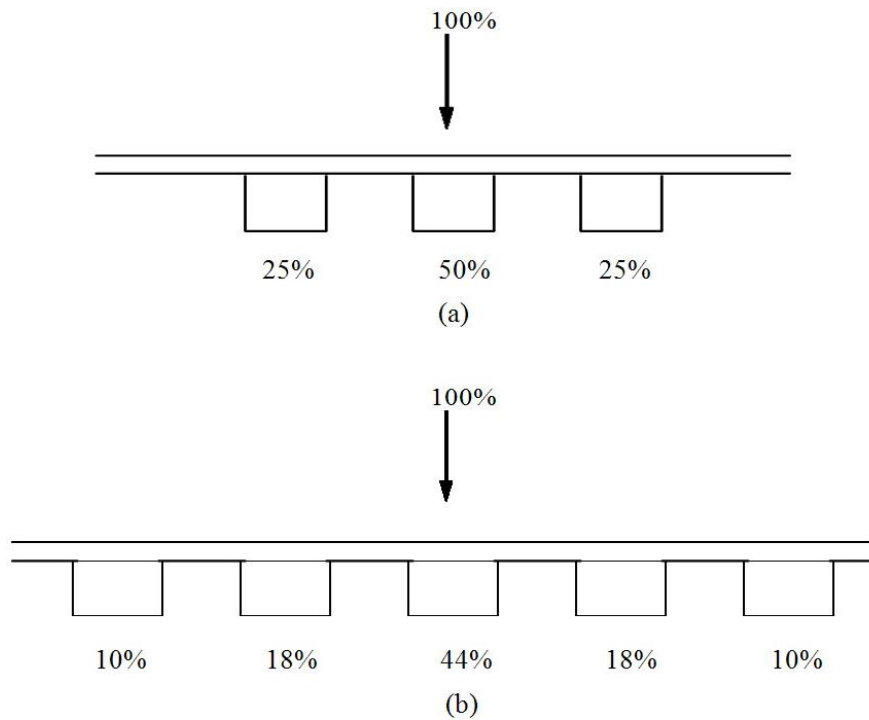


Figure 8.6 Load distributions along successive sleepers (a) suggested by Awoleye (1993) and (b) on a real track based on elastic beam on foundation calculation (Kwan, 2006).

8.4 Results and discussion

8.4.1 Influence of phase loading

Before studying the effect of different subgrade stiffness, it is important to run a simulation on a subgrade with uniform stiff or soft stiffness to check the influence of phase loading. The settlement for each sleeper is shown in Figure 8.7. From the figure, it can be seen that sleeper 1 has slightly more settlement than the sleepers 2 and 3 for both uniform stiff and soft conditions. The difference between sleepers is likely to be due to the random package of clumps during the sample preparation. This differential settlement was deemed acceptable. Figure 8.8 shows the development of the contact force distribution for each quarter cycle of phase loading. It clearly shows that the contact force chains under each sleeper were periodically increased and decreased. Therefore, it can be concluded that it is possible to simulate a 90 degree out of phase loading using PFC^{3D}.

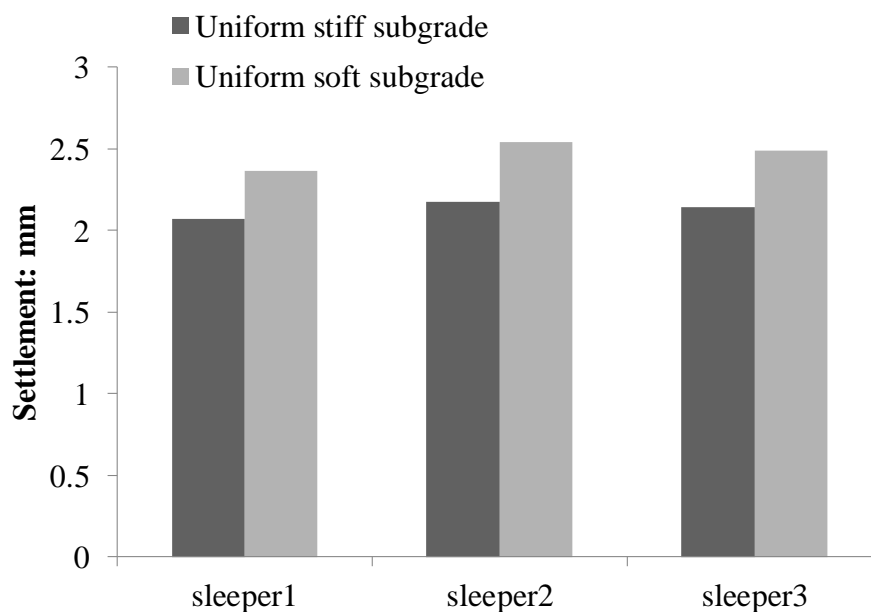


Figure 8.7 Comparison of sleeper settlements on uniform stiff and soft subgrades under out of phase loading after 50 cycles

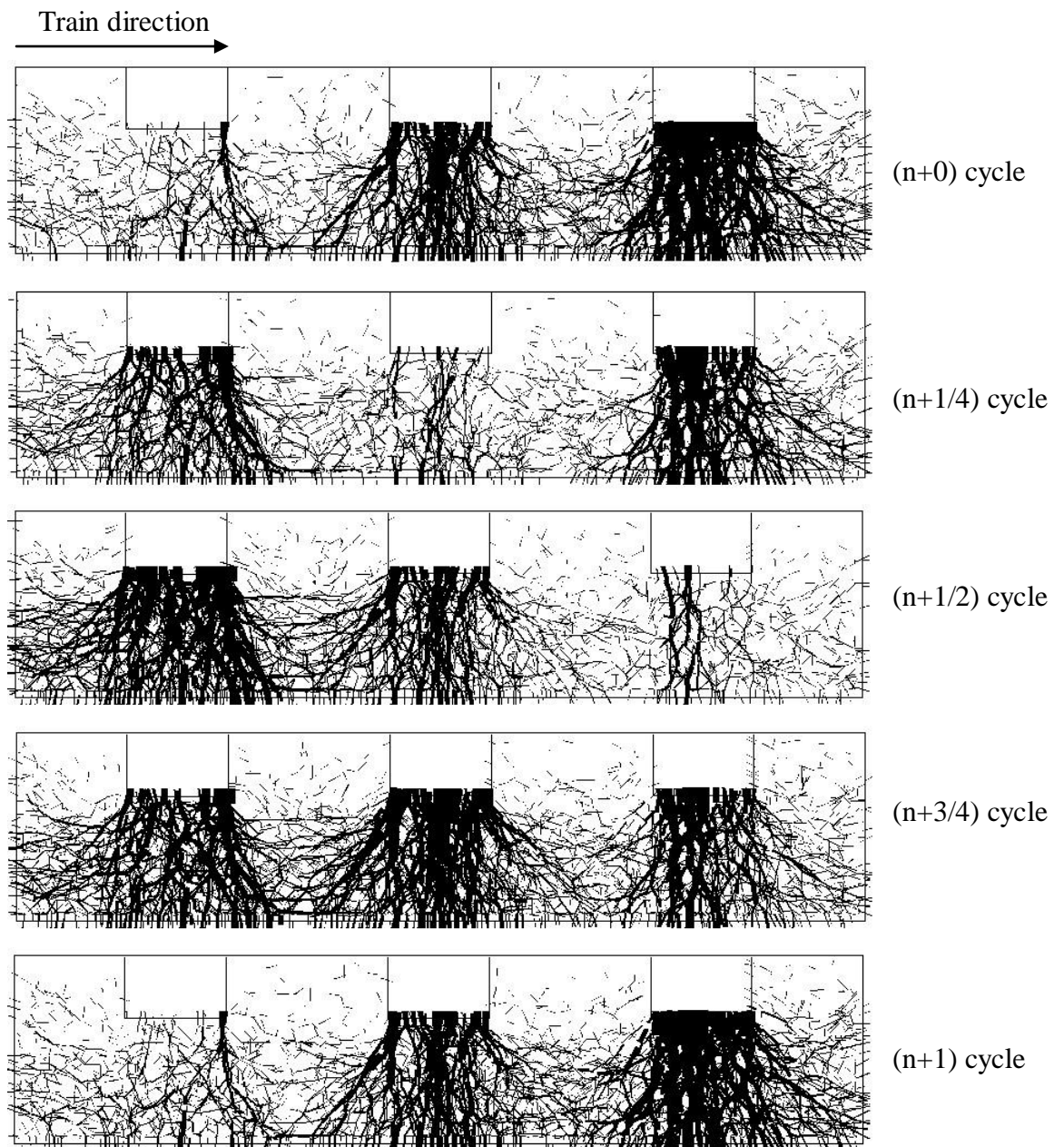


Figure 8.8 Contact force distribution during one cycle of 90 degree out of phase loading

8.4.2 Influence of different subgrade stiffness

A previous study has shown that the track settlements were dominated by the subgrade stiffness. Therefore, to significantly increase the soft subgrade stiffness, modification or reinforcement of the soft subgrade is required. In practice, a concrete slab is usually installed as a structural element in the track substructure to increase

the stiffness or modulus of the track. Most slabs are designed either with a taper to gradually increase the stiffness over an approach distance, or are uniform in thickness but placed at an angle with tapering of the ballast depth to achieve the same ramping effect.

The influences of two alternative kinds of transition patterns: a single step change and a multi step-by-step change for the subgrade stiffness, on the dynamic behaviour of the track were investigated. Figure 8.9 shows the stiffness distribution and also friction coefficients of the subgrades for the two transition patterns. As calibrated by the plate loading test simulation before, the stiffness of the soft subgrade is 4.9×10^6 N/m, and the stiffness of the stiff subgrade is 2.0×10^7 N/m. For the transition pattern A (single step change), sleepers 1 and 2 are on the soft subgrades, and sleeper 3 is on the stiff subgrade as shown in Figure 8.10a. This is to represent the typical transition zone with an abrupt change of vertical stiffness for the subgrade. For the transition pattern B (multi step-by-step change), the transition zone is divided into 21 segments, each having a length of 0.1m with different stiffness and friction coefficient, as shown in Figure 8.10b. The subgrade stiffness gradually increases from 4.9×10^6 N/m at soft end ($E=25$ MPa) to 2.0×10^7 N/m at the stiff end ($E=100$ MPa), while the friction coefficient of the subgrade (base wall) also gradually increases from 0.2 at soft end (e.g. clay) to 0.6 at stiff end (e.g. concrete).

As introduced in Section 8.2, track transition problem specifically occur at bridge approaches, where the ballasted approaches experienced more track geometry degradation than the tracks on the bridges and the open track (Figure 8.11). Comparing the performances of these two kinds of transition patterns, shown in Figure 8.12, an abrupt change of subgrade stiffness provides a similar result as field data (Figure 8.11): sleeper 2 on the approach has the largest settlement, followed by the sleeper on the soft subgrade and the sleeper on the stiff subgrade. In the case of the multi step-by-step change of subgrade stiffness, this has effectively reduced the differential settlement of the three sleepers at the transition zone.

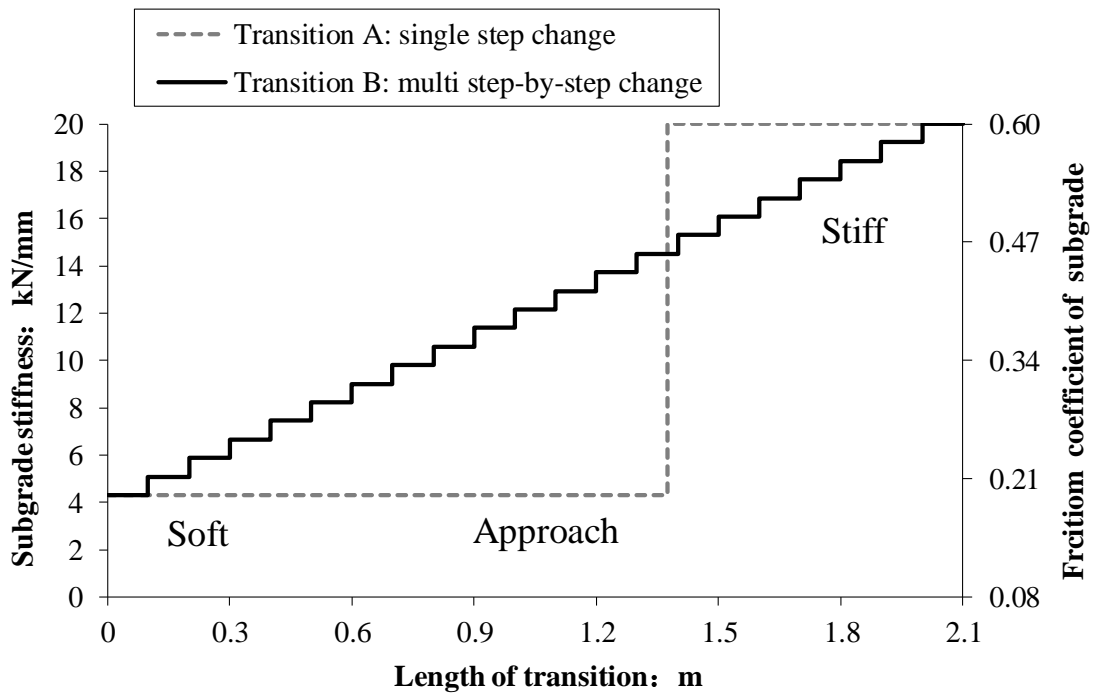


Figure 8.9 Two kinds of transition pattern for subgrade stiffness distribution and coefficient of friction

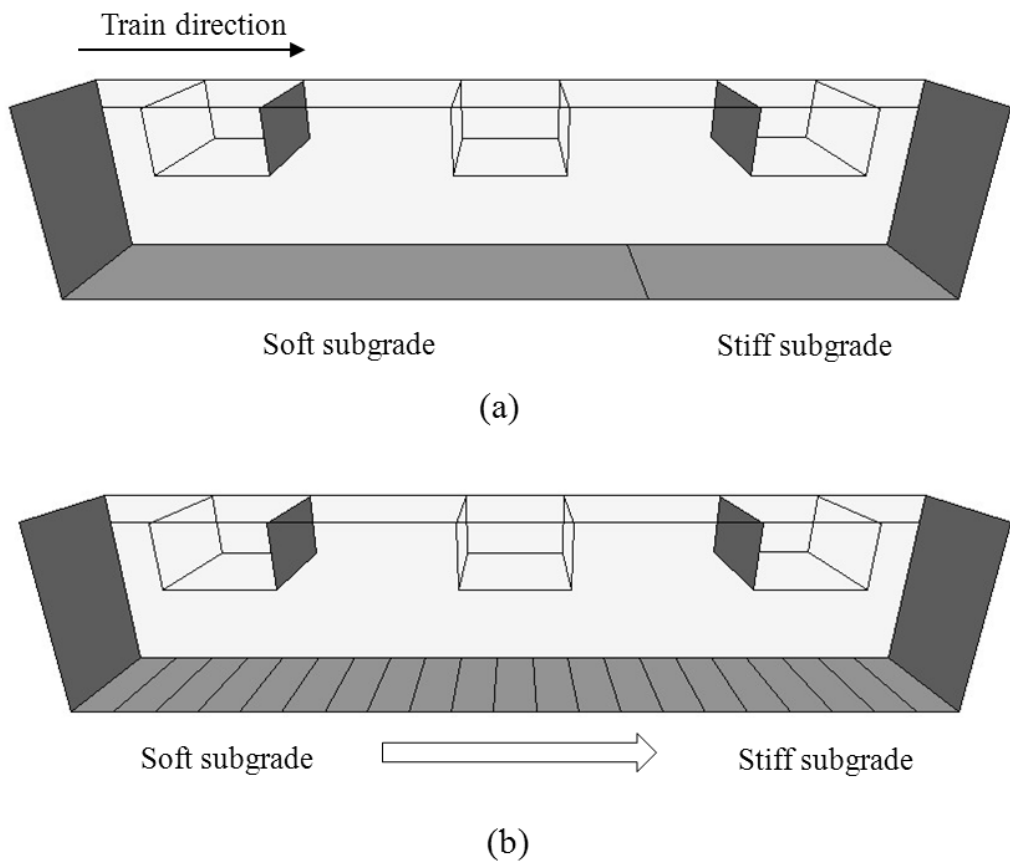


Figure 8.10 Two types of transition patterns represented by the walls in PFC^{3D}: (a) single step change and (b) multi step-by-step change

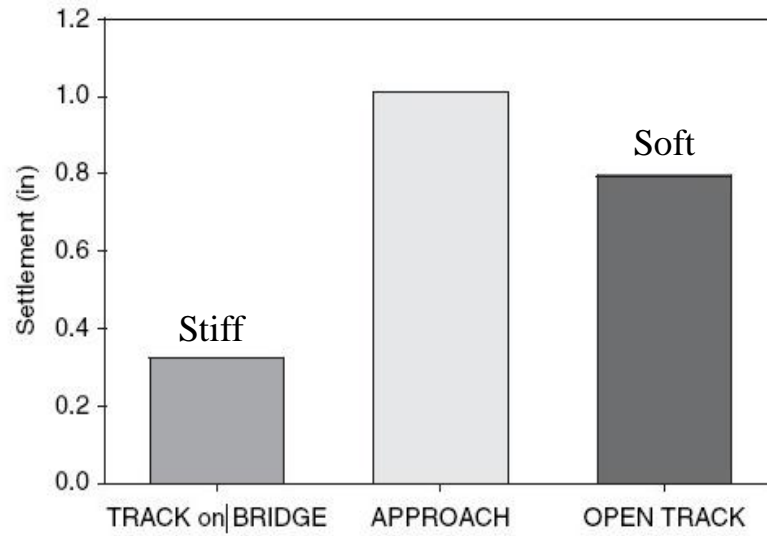


Figure 8.11 Field data: comparison of track settlement accumulated over a maintenance interval (Li and Davis, 2005)

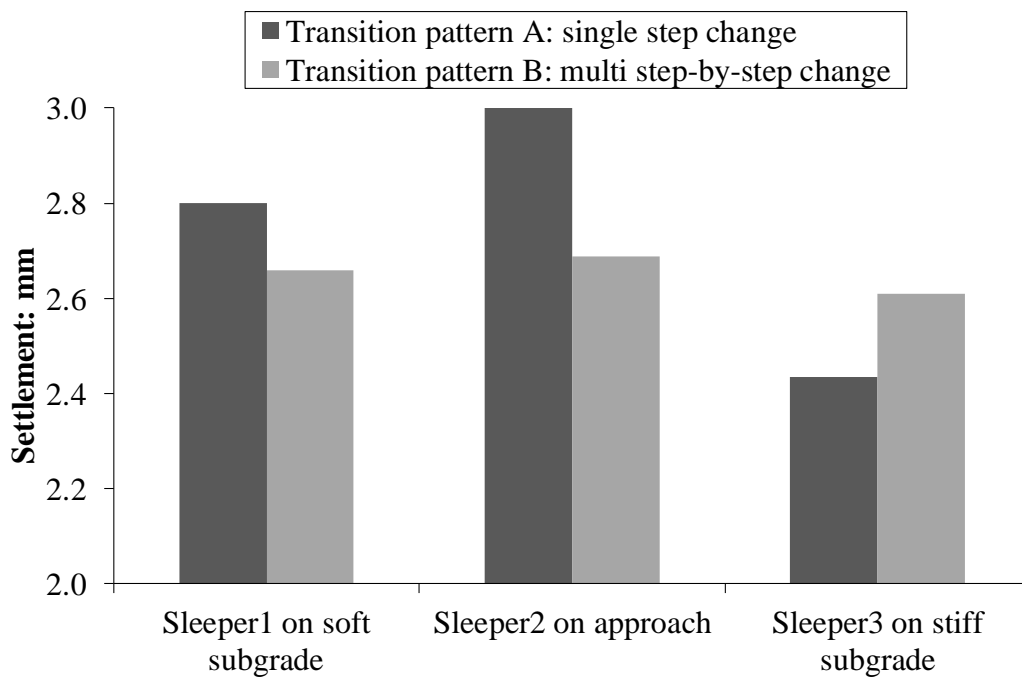


Figure 8.12 Comparison of sleeper settlement after 100 cycles (Frequency=10Hz, train speed= 93.6km/h)

8.4.3 Influence of moving direction

Figure 8.13 shows the results for both directions of travel; Sleeper 2 always settled more than other sleepers. Moreover, moving from stiff to soft subgrade causes larger differential settlement than moving from soft to stiff. This could be explained by the different boundary conditions of sleeper 2 on the approach. When the train was moving from soft to stiff condition the sleeper 1 on soft subgrade has a large settlement; when moving from stiff to soft condition sleeper 3 on stiff subgrade had a small settlement. This causes different boundary conditions for sleeper 2, and therefore different settlements.

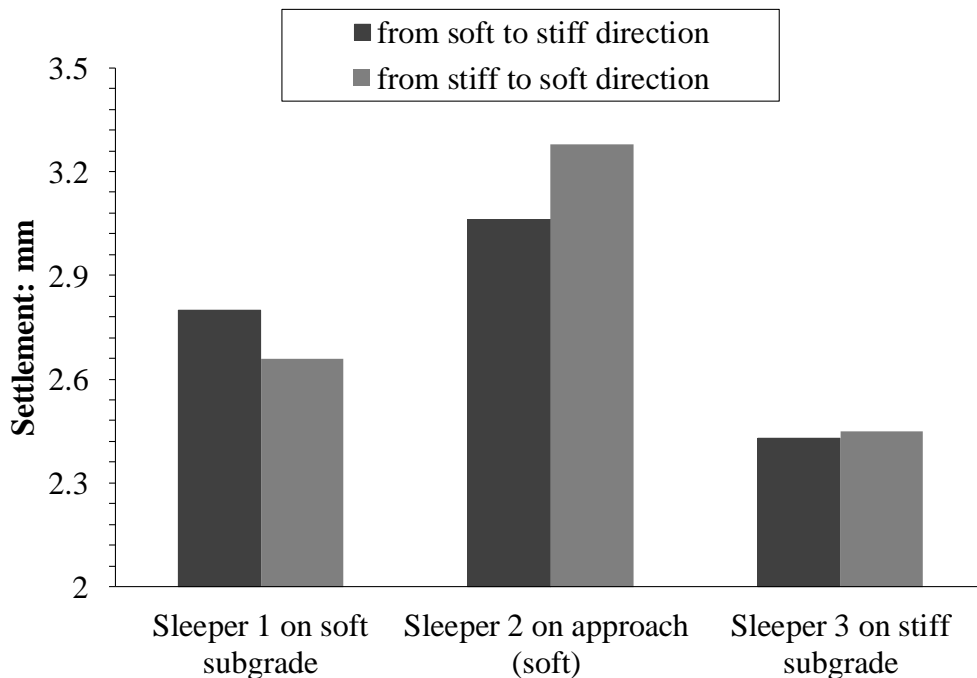


Figure 8.13 Effect of train moving direction after 100 cycles (Frequency=10Hz, train speed= 93.6km/h)

8.4.4 Influence of different frequency of cyclic load (train speed)

Figure 8.14 shows the effect of vehicle speed on displacement of the sleepers for the case of the step change. The speed range can be divided into two regions as follows: in the low speed range (<100 km/h), the displacement does not change significantly with increasing vehicle speed. In the high speed region (>100 km/h), the

displacement increases with vehicle speed. However, the train speed has little influence on the sleeper settlement for the multi step-by-step change condition shown in Figure 8.15. Therefore, the multi step-by-step change of subgrade stiffness appears to be an effective way of reducing differential settlement and also allowing the passing of a high-speed train. A gradual adjustment of the subgrade stiffness will have a beneficial effect in reducing dynamic effects.

The accelerations of all sleepers in both transition patterns have been calculated and shown in Figure 8.16. The trends of the accelerations increase with the increasing speed. It also can be seen that the acceleration of sleeper 2 for the case of the multi step-by-step change has been reduced in the high speed region (200-300km/h) compared to that for the case of the single step change.

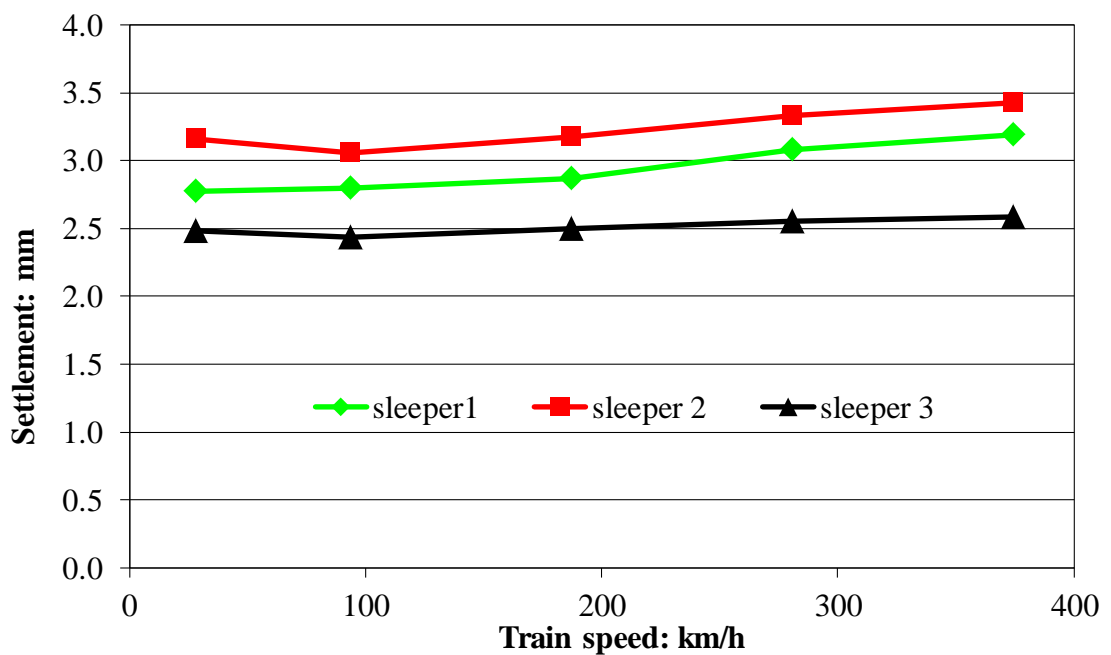


Figure 8.14 Transition pattern A: vertical displacements of the sleepers after 100 cycles

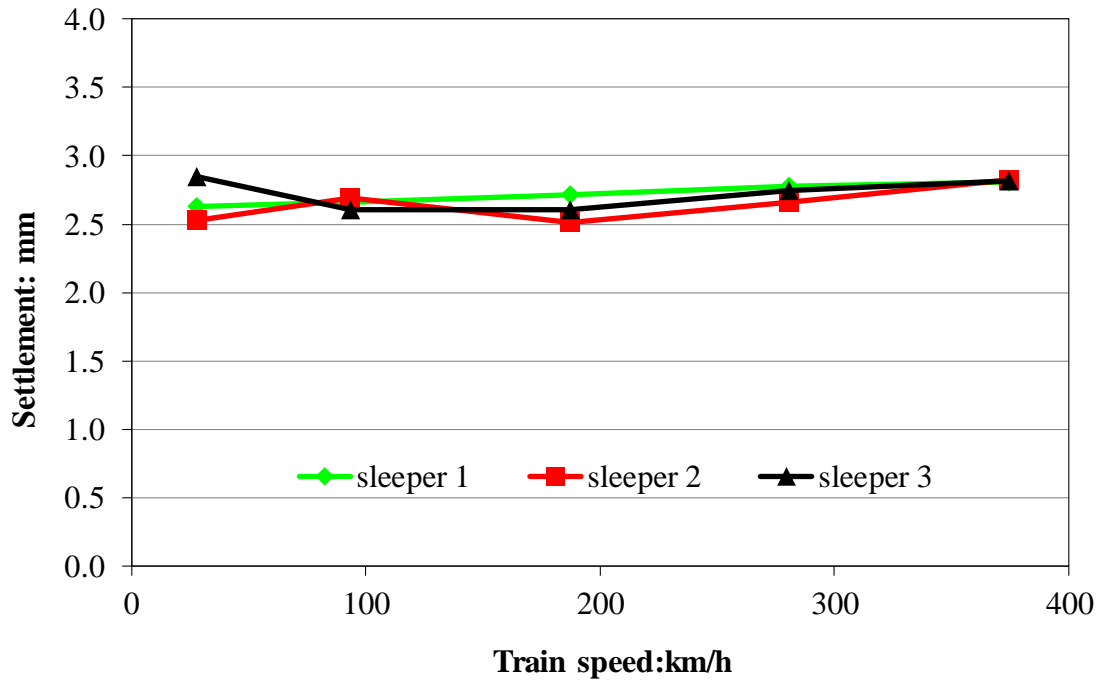


Figure 8.15 Transition pattern B: vertical displacements of the sleepers after 100 cycles

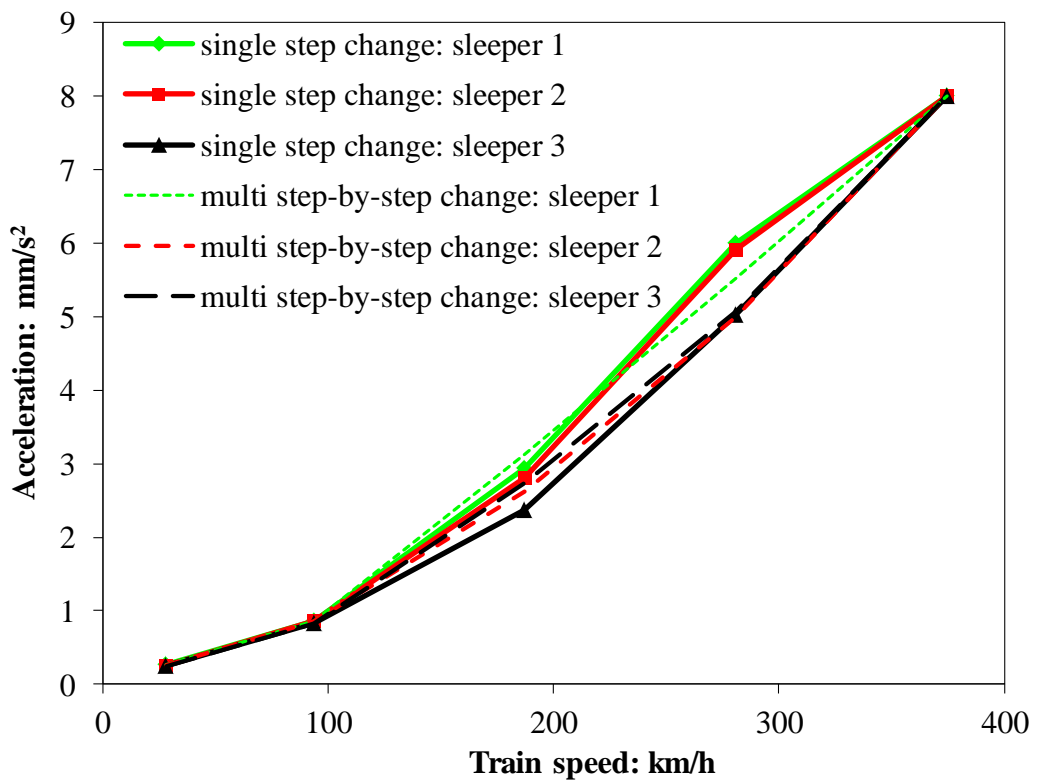


Figure 8.16 Maximum accelerations of sleepers for different transition patterns

8.4.5 Influence of axle load

The model simulates a quarter of axle load of approximately 16 tonnes which is comparable to a typical heavy axle load on top of the middle sleeper. With the heavier cyclic loading applied to existing tracks, the effect of axle load on the transition zones also need to be investigated. Therefore, axle loads of approximately 24 and 32 tonnes have also been applied in the simulations. Figure 8.17 shows the results of the effect of different axle loads on the different sleeper settlement at the speed of 96.4km/h. It shows that the differential settlement of the three sleepers becomes larger with the increasing axle load. This is consistent with the experienced problems in which the track geometry becomes worse when heavier trains pass at transition zones.

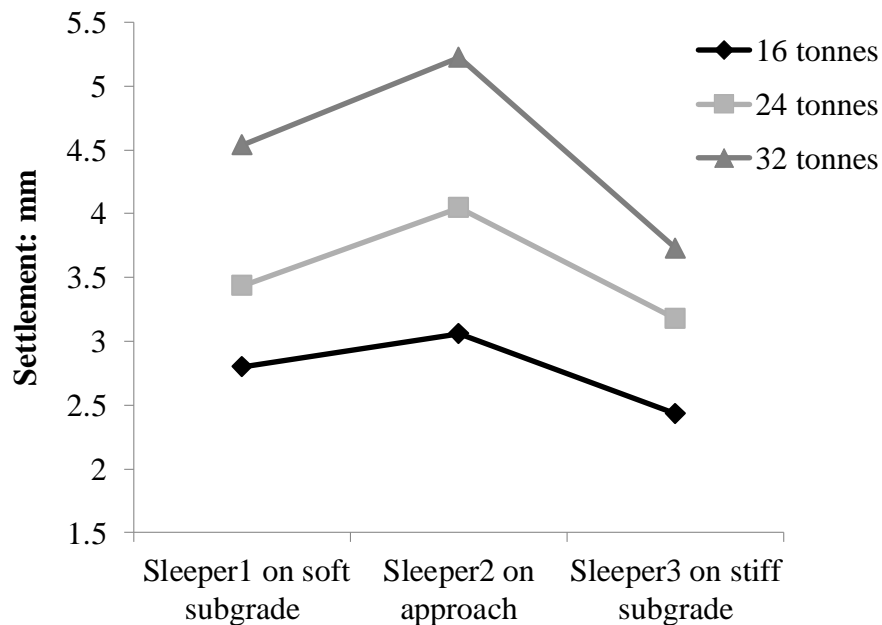


Figure 8.17 The effect of axle load on sleeper settlement (Frequency=10Hz, train speed= 93.6km/h)

8.4.6 Influence of geogrid in transition zones

The application of reinforcing geogrid has been proved to be a simple and economic means of reducing the permanent deformation in the ballast layer and increasing the bearing capacity of the track foundation in the subgrade (Tensar, 2009). A two-layer biaxial geogrid model of 65mm aperture size which is the same as the geogrid was

used in previous simulations (pull-out test, box test and CET), as shown in Figure 8.18a. Chapter 7 has described that the optimum geogrid location in the ballast layer is 100mm above the base (subgrade) in box test simulations. Therefore, in this simulation, the biaxial geogrid model of aperture size 65mm was placed 100mm above the base wall as shown in Figure 8.18b, to investigate the performance of the geogrid in a ballast layer over weak subgrade.

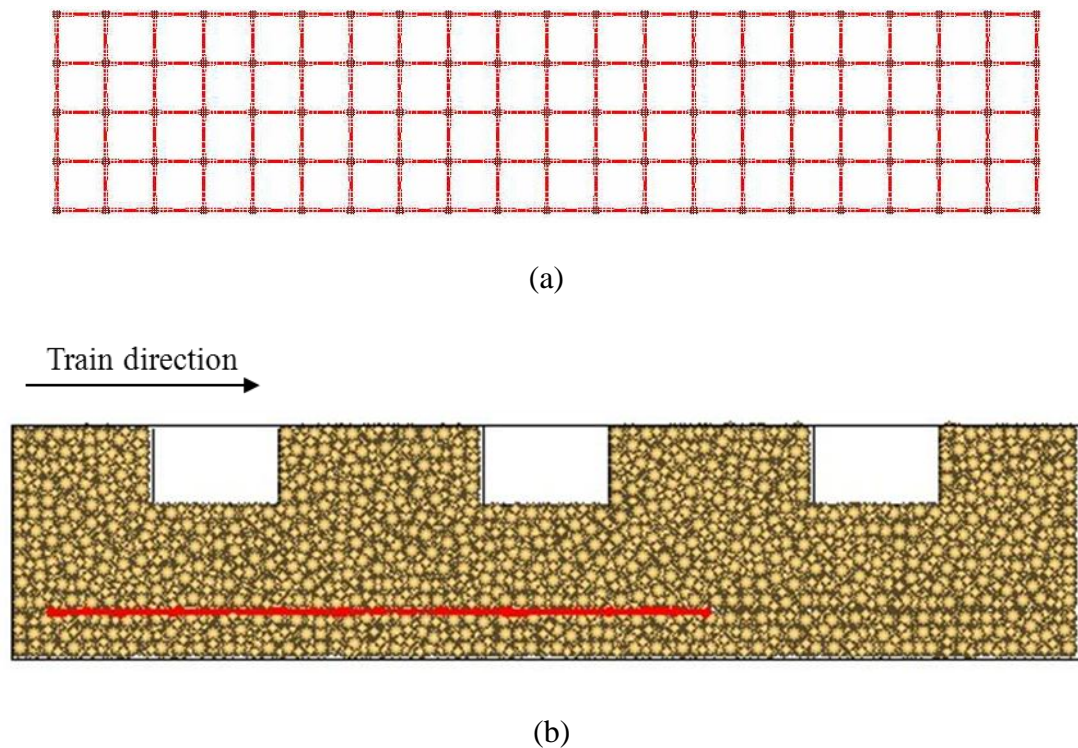


Figure 8.17 (a) Biaxial geogrid model of aperture (rib) size 65mm; (b) reinforced sample with a geogrid layer placed at 100mm above the soft subgrade

It should be noted that, the geogrid model comprises more than 35,000 spheres, which causes the computing speed to be very slow. Figure 8.19 shows the simulation results after 50 cycles, still taking two months of computational time. Comparing the performance with and without geogrid, the geogrid layer installed in the ballast layer was not effective in increasing the stiffness of the track on very low-stiffness subgrades as shown in Figure 8.19. This could be because the particles were allowed more movement on the base due to the low friction coefficient of base (soft subgrade), which decreases the geogrid reinforcement effect. Therefore, the geogrid

performance maybe also related to the subgrade condition. It's suggested that a geogrid is placed in the sub-ballast layer to increase the bearing capacity, especially over soft subgrade, with significant thickness reductions and savings in both the capital and environmental costs (Tensar, 2009).

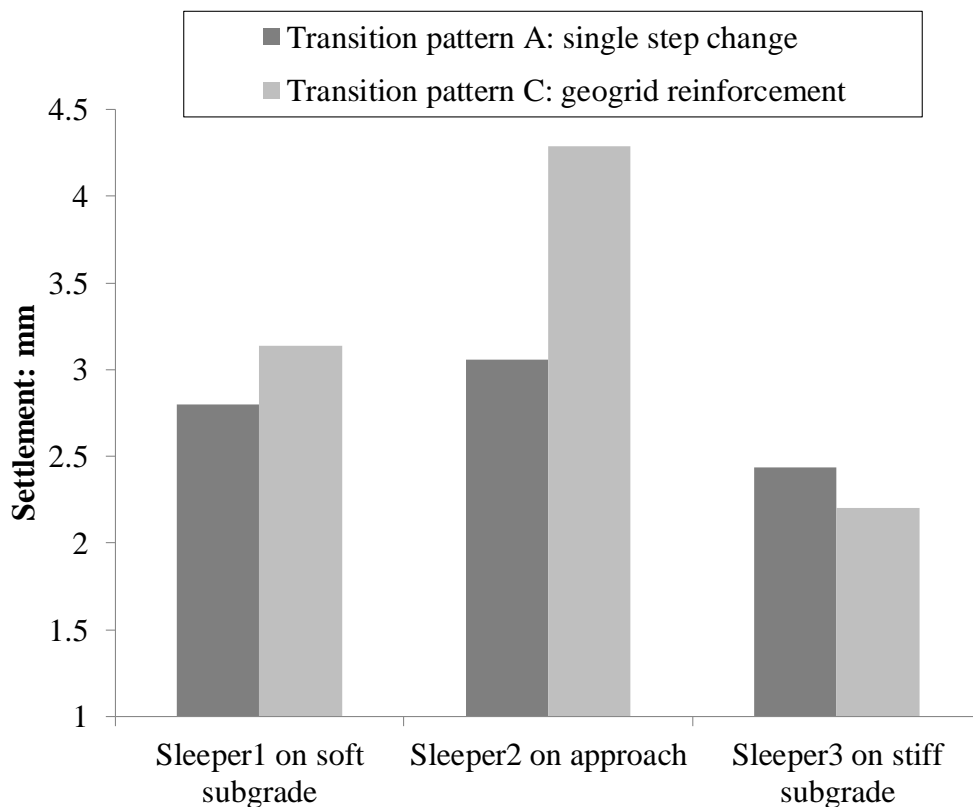


Figure 8.18 Comparison of sleeper settlement after 100cycles (Frequency =10Hz, train speed= 93.6km/h)

8.5 Conclusions

Track transition zones have been modelled by a simple 3-sleeper box test simulation using two-ball clumps for the ballast particles and walls with different stiffnesses for the subgrades. Both the stiffnesses of the soft and stiff subgrades were determined with the plate bearing test simulation in PFC^{3D}. A calibration loading test on uniform stiff subgrade has proved that the 90 degree out of phase loading has little influence on the differential settlement of the three sleepers. Two kinds of transition patterns, including a single step change and a multi step-by-step change for the subgrade

stiffness distribution, were tested. In addition, geogrid was used in the ballast layer (100mm from base) on the soft subgrade to examine the effect of geogrid reinforcement. The simulation results provide a good prediction that the abrupt stiffness change accelerated the sleeper settlement on the approach between soft and stiff subgrade, which is typically found in practice. Moreover, moving from stiff to soft subgrade causes larger differential settlement than moving from soft to stiff. From the point of view of reducing the track degradation, the multi step-by-step change has effectively reduced the differential settlements at the transition zone. With increasing train speed, the sleepers have settled more for the case of the step stiffness change; for the case of the multi step-by-step stiffness change, the train speed has little influence on the sleeper settlement. With increasing train axle load, the track geometry becomes worse: that is to say the differential settlement of the three sleepers increases. The geogrid placed in the ballast layer over the soft subgrade was not effective in the transition simulation. Therefore, for the weak subgrade condition, the geogrid is suggested to be installed in the subballast or subgrade, to increase the bearing capacity.

Chapter 9 Conclusions and suggestions for further research

9.1 Conclusions

Laboratory large box pull-out tests have been performed on biaxial and triaxial geogrids embedded within a ballast sample to examine the key parameters influencing the interaction between ballast and the geogrid. The pull-out force has been measured as a function of displacement for the different grids and under different surcharges. Experimental results indicate that geogrid aperture size plays a more influential role than the tensile strength or the thickness of the ribs. A higher average peak force was recorded as the geogrid aperture size increased from 32mm to 75mm, thus confirming that the aperture size of both biaxial and triaxial geogrids have direct influence on the particle-geogrid interlock and therefore pull-out resistance. The triangular aperture, coupled with a vertical rectangular rib cross-section and junction efficiency, gives greatly improved ballast confinement and interaction compared to biaxial grids. For the biaxial geogrid, most pull-out resistance comes from the bearing on the transverse ribs. For the triaxial geogrid, non-transverse ribs carry load in both the longitudinal and transverse directions giving extra resistance. Therefore, triaxial geogrids can provide more pull-out resistance than biaxial geogrids for the same geogrid area. For the 40mm ballast that was used, the optimum geogrid is triaxial geogrid with aperture size 75mm.

A new DEM model for the biaxial geogrid has been developed by bonding two layers of small balls together to form the required geometry using parallel bonds, and calibrated by simulating standard tests. Four kinds of clumps, namely a 2-ball clump, 4-ball tetrahedral clump, 8-ball tetrahedral clump and 8-ball flaky clump were used

to represent the real ballast particles. All four kinds of clumps have been shown to give an acceptable angle of repose, comparing with real ballast. The DEM simulations have been shown to provide good predictions of the pull-out force as a function of displacement especially for the initial 20 mm of displacement. The particle shape seems to have little effect on the initial development of the pull-out force. The simulations also have given valuable insight into the interaction between ballast and geogrid under different surcharges, although the DEM simulations using 2-ball clumps or 4-ball tetrahedral clumps, underestimate the pull-out force after a displacement of about 20mm. This is thought to be a function of the uniform particle size, angularity and roundness of the simulated clumps, compared to the well-graded, angular ballast particles in the laboratory tests. Considering the four kinds of clumps, the 8-ball tetrahedral clump which has more angularity and roughness, seems more representative of real ballast. The fully reinforced zone is approximately 75mm above and below the geogrid.

The discrete element method has been used to simulate cyclic loading of geogrid reinforced ballast under confined and unconfined conditions. Results in both cases confirmed that the geogrid reinforcement can reduce the settlement of ballast significantly when placed at the optimum location. For the confined condition, box tests have been simulated on unreinforced samples and reinforced samples with different geogrid positions and geogrid apertures. The response of the ballast layer reinforced with geogrid under repeated loading agrees with experimental results. It was found that the optimum location of geogrid is 100 mm above the base, and the triaxial geogrid of aperture (rib) size 75mm outperforms the biaxial geogrid of aperture (rib) size 65mm. For the unconfined condition, cyclic loading of a channel of ballast (the Composite Element Test (CET) has also been simulated, and the sample with the geogrid at 50mm from the sub-ballast layer performs better than that at 100 mm or 150 mm from the subballast in agreement with experimental results by Brown et al. (2007). It was also found that the use of two geogrids at both 50mm and 150mm from the subballast gave smaller settlement than using a single layer geogrid, or the unreinforced ballast. However the double-reinforced ballast performs only marginally better than the sample reinforced 50mm above the sub-ballast. The geogrid reinforcement limits the lateral displacement in the reinforced zone, which is

approximately 50mm above and below the geogrid. The subgrade stiffness has an influence on the settlement of ballast layer.

Track transition zones have been modelled by a simple 3-sleeper box test simulation using two-ball clumps for the ballast particles and walls with different stiffnesses for the subgrades. Both the stiffnesses of the soft and stiff subgrades were determined with the plate bearing test simulation in PFC^{3D}. A calibration loading test on uniform stiff subgrade has proved that the 90 degree out of phase loading has little influence on the differential settlement of the three sleepers. Two kinds of transition patterns, including a single step change and a multi step-by-step change for the subgrade stiffness distribution, were tested. In addition, geogrid was used in the ballast layer (100mm from base) on the soft subgrade to examine the effect of geogrid reinforcement. The simulation results provide a good prediction that the abrupt stiffness change accelerated the sleeper settlement on the approach between soft and stiff subgrade, which is typically found in practice. Moreover, moving from stiff to soft causes larger differential settlement than moving from soft to stiff. From the point of view of reducing the track degradation, the multi step-by-step change has effectively reduced the differential settlements at the transition zone. With increasing train speed, the sleepers have settled more for the case of the step stiffness change; for the case of the multi step-by-step stiffness change, the train speed has little influence on the sleeper settlement. With increasing train axle load, the track geometry becomes worse: that is to say the differential settlement of the three sleepers increases. The geogrid placed in the ballast layer over the soft subgrade was not effective in this transition simulation. Therefore, for the weak subgrade condition, the geogrid is suggested to be installed in the subballast or subgrade, to increase the bearing capacity.

9.2 Suggestions for further research

Pull-out test:

Additional laboratory large pull-out experiments are needed to further validate the development of volumetric strain of geogrid-reinforced ballast samples during the

pull-out. The vertical displacement of the specimen can be measured by attaching three LVDTs (linear variable differential transformers), see Figure 9.1. Besides, image analysis could also be used to get a good measurement of the displacement of the top of the large box pull-out test apparatus.

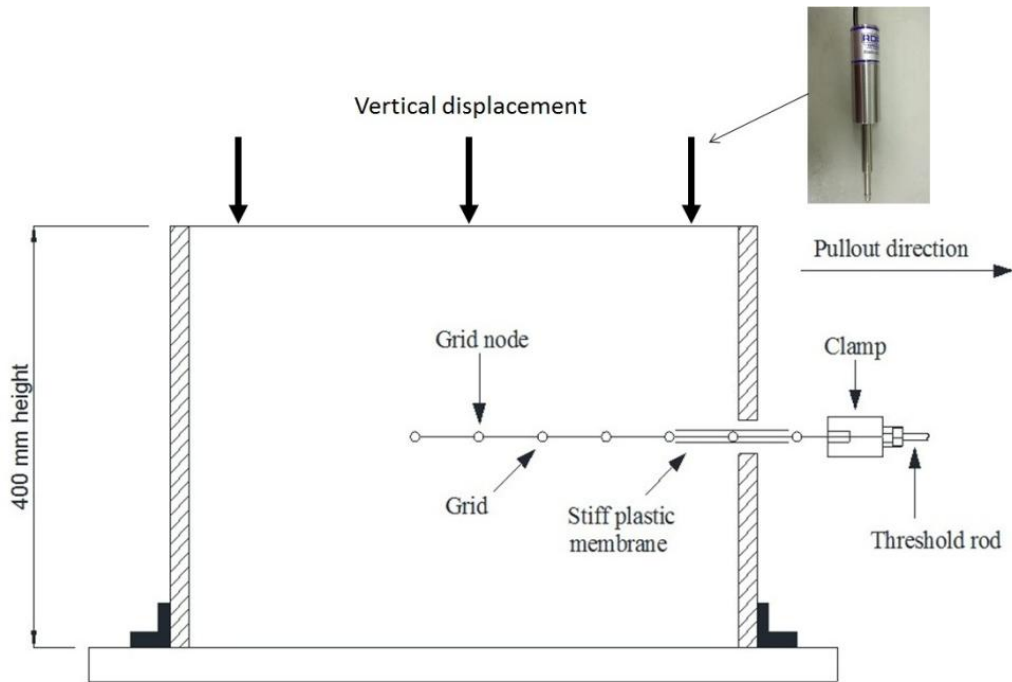


Figure 9.1 Use of LVDT displacement transducers to measure vertical displacements on the top

As shown in Figure 9.2, there is one additional pull-out directions for the biaxial and triaxial geogrids apart from the two directions which have been tested already. Therefore, additional laboratory large pull-out experiments are needed to further understand interlocking of the ballast/geogrid system along different pull-out directions.

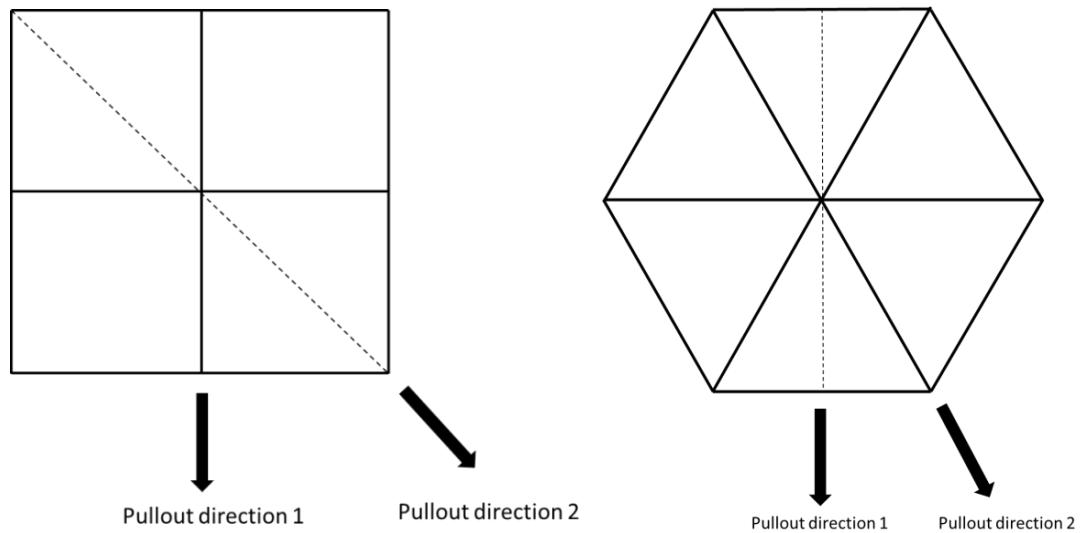


Figure 9.2 Two kinds of Pull-out direction for biaxial and triaxial geogrids respectively

Ballast modelling:

Since ballast is usually a reasonably uniformly graded material, the simulations carried out in this research assumed that the sample consisted of single sized particles. However, this approximation is aimed at reducing the complexity in the simulations and it may not represent entirely a real gradation of ballast. Therefore, future research could be aimed at investigating the effect of aggregate size distribution on the stress-strain response and volumetric behaviour of a ballast assembly.

The effects of particle shape properties on the ballast constructability and compactability can be studied. It has been proven that angular particles perform better than rounded particles in terms of both strength and stability. This is, however, based on the fact that all samples were actually compacted to more or less the same voids ratio. The same voids ratio condition may not be achieved easily since it is known that angular particles tend to have larger voids than rounded particles under the same field compaction effort. It is suggested that the optimum combination of aggregate angularity and compactability be further investigated.

New and more advanced DEM capabilities need to be developed to consider more realistic railroad ballast conditions such as particle breakage. It will also be more

realistic in the future to account for the pore water pressure in the DEM simulations. With such DEM capabilities, ballast fouling can be more comprehensively and realistically investigated.

Geogrid modelling and calibration

In these simulations, the rib cross-section of both biaxial and triaxial geogrid model are rectangular (length/width=3/2). However, previous research and the laboratory pull out test results have revealed that the importance of a combination of the depth and shape of the rib profile. So different shapes of the rib cross-section should be investigated, and the cross-section of rib could be optimized in further research, resulting in the manufacture of new prototypes.

As present in Section 5.3, the shape of the triaxial geogrid is modelled using a set of spherical particles bonded together to form the triangular apertures. However, until now there are not enough index load test results for the triaxial geogrid used to determinate the micromechanical parameters of the bonded geogrid particles required to model the triaxial geogrid. Therefore, in order to calibrate the micro mechanical parameters of triaxial geogrid in PFC^{3D}, laboratory simple standard tests should be tested in the future, such as the single rib test, single aperture (triangular) pull-out test and in-plane rotation test.

Transition modelling:

In this transition model, boundaries were generated by walls which cannot simulate the real condition. To eliminate boundary effects in the computation, simulations using periodic boundary need to be developed in the future. The optimum ramp structure also could be investigated in further research, by using walls or large clump to simulate passage on to a stiff concrete foundation from a soft subgrade, for example.

Field modelling

With increased computing power, it should be possible to model entire sections of ballasted track. This should enable the modelling of track with banked, curved rails and a study of the ballast mechanisms for this boundary value problem.

References

- Alagiyawanna, A. M. N., Sugimoto, M., Sato, S. and Toyota, H. (2001). Influence of longitudinal and transverse members on geogrid pullout behavior during deformation. *Geotextiles and Geomembranes* **19**, pp 483-507.
- Allen, J. (1973). The effect of non-constant lateral pressures of the resilient response of granular materials. Ph.D. Thesis, University of Illinois at Urbana-Champaign, Urbana, Illinois.
- Allen, J. J. and Thompson, M. R. (1974). Resilient response of granular materials subjected to time dependent lateral stresses. *Transp. Res. Rec.* 510, Transportation Research Board, Washington, D.C., 1-13.
- Alva-Hurtado, J. E. (1980). A methodology to predict the elastic and inelastic behaviour of railroad ballast. Ph.D. Thesis, University of Massachusetts, Amherst, Massachusetts.
- Aursudkij, B. (2007). A laboratory study of railway ballast behaviour under traffic loading and tamping maintenance. Ph.D. Thesis, The University of Nottingham.
- Aursudkij, B., McDowell, G.R., Collop, A.C. (2009). Cyclic loading of railway ballast under triaxial conditions and in a railway test facility. *Granular Matter* 11(6), pp391-401.
- Awoleye, E.O.A. (1993). Ballast type-ballast life predictions. Derby, British rail research LR CES 122.
- Banimahd, M. and Woodward, P.K. (2007). Numerical study of train speed effect on railway track response. Preceding's 9th International Conference on Railway Engineering, London.

- Banimahd, M., Woodward, P.K., Kenndy, J. and Medero, G.M. (2011). Behaviour of train-track interaction in stiffness transitions. *Proceedings of the Institution of Civil Engineers, Transport*, 164, Issue TR1, 1-10.
- Barbosa, R. E. (1990). *Discrete Element Models for Granular Materials and Rock Mass*. PhD Thesis, University of Illinois at Urbana Champaign.
- Bilow, D.N., Li, D. (2005). Concrete slab track test on the high tonnage loop at the transportation technology center. In *proceedings of the 2005 AREMA Annual Conference*. AREMA.
- Briaud, J., James, R.W. and Hoffman, S.B. (1997). *Settlement of Bridge Approaches (the Bump at the End of the Bridge)*. Transportation Research Board, National Research Council, Washington. DC.
- Barrett, P. J., (1980). The shape of rock particles, a critical review. *Sedimentology* 27, 291-303.
- Bergado, D. T., Bukkanasuta, A. and Balasubramaniam, A. S. (1987). Laboratory pull-out tests using bamboo and polymer geogrids including a case study. *Geotextiles and Geomembranes*, 5, 153-189.
- Bergado et al. (1993) Interaction between cohesive-frictional soil and various grid reinforcements. *Geotextiles and Geomembranes* 12(4) 5, 327-349.
- Bhandari, A. and Han, J. (2010). Investigation of geotextile-soil interaction under a cyclic verticle loading using the discrete element mothod. *Geotextiles and Geomembranes*, Vol. 28, Issue 1, 33-43.
- Bombadier Inc. (2007). *Commuter trains*. [online], Available at <URL: <http://www.bombadier.com>>
- British standard, (2002). *Aggregates for railway ballast*, British standard Insitution, London.
- British standard, (2012). *Aggregates for railway ballast*, British standard FprEN 13450, London.
- Brown, S.F., Thom, N.H. & Kwan, J. (2006). *Optimising the Geogrid Reinforcement of Rail Track Ballast*. *Railway Foundations: Proceedings of Railfound*, University of Birmingham, 346-354.
- Brown, S.F., Thom N.H. and Kwan, J. (2007). Identifying the Key Parameters that Influence Geogrid Reinforcement of Railway Ballast. *Geotextiles and Geomembranes*, Vol. 25, Issue 6, 326-335.

- Chan, W.K. (1990). Permanent Deformation Resistance of Granular Layers in Pavement, PhD Thesis, University of Nottingham, United Kingdom.
- Chen, C., McDowell, G. R. and Thom, N. H. (2012a). Discrete element modelling of cyclic loads of geogrid-reinforced ballast under confined and unconfined conditions, *Geotextiles and Geomembranes* **35**, 76-86.
- Chen, C., McDowell, G. R. and Thom, N. H. (2012b). A study of geogrid-reinforced ballast using laboratory pull-out tests and discrete element modelling. *Geomechanics and Geoengineering: An International Journal*. (Accepted).
- Chen, C., McDowell, G. R., Thom, N. H., 2013. Investigating geogrid-reinforced railway ballast: experimental pull-out tests and discrete element modelling. Special issue of *Soils and foundations*. August, (Accepted).
- Cheung, G. and O'Sullivan, C. (2008). Effective simulation of flexible lateral boundaries in two and three-dimensional DEM simulations. *Particuology* **6**, 483-500.
- Cui, L. O'Sullivan, C. and O'Neill, S. (2007). An analysis of the triaxial apparatus using a mixed boundary three-dimensional discrete element model. *Geotechnique* **57**(10), 831-844.
- Cundall, P. A. (1971). A computer model for simulating progressive large scale movements in blocky rock systems. Proceedings of the Symposium of the International Society of Rock Mechanics, Nancy, France, Vol. 1, Paper No. II-8.
- Cundall, P. A. and Strack, O. D. L. (1979). A discrete numerical model for granular assemblies. *Geotechnique* **29**, No. 1, 47-65.
- Cundall, P. A., and Hart, R. D. (1992) Numerical Modelling of Discontinues. *Engineering Computations* **9**, No. 2, 100-113.
- Dahlberg, T. (2001). Some railway Settlement Models - A Critical Review. *Proc. Institute of Mechanic Engineers*, Vol 215, Part F.
- Davis, D. and Li, D. (2006). Design of track transitions. Research Results Digest 79, Transportation Technology Centre, Inc.
- Dias, A. C. (2003). Numerical Analyses of Soil-Geosynthetic Interaction in Pull-out Tests. M.Sc thesis, Univeristy of Brasilia, Brasilia, Brazil, pp115. (in Portuguese)
- Eisenmann, J., Leykauf, G. and Mattner, L. (1994). Recent development in German

- railway track design. *Proceedings of the Institution of Civil Engineers: Transport* 105, No. 2, 91-96.
- Esveld, C. (2001). *Modern Railway Track*, second edition. MRT-Productions, the Netherlands.
- Fellerec, J. F. and McDowell G. R. (2008). A simple method to create complex particle shapes for DEM. *Geomechanics and Geoengineering: An International Journal* 3, No.3, 211-216.
- Fellerec, J. F. and McDowell G. R. (2010). A method to model realistic particle shape and inertia in DEM. *Granular Matter* 12, 459-467.
- Fellerec, J. F. and McDowell G. R. (2012). Modelling of ballast-geogrid interaction using the discrete element method. *Geosynthetics International*, 19(6), 470-479.
- Forsman, J. and Slunga, E. (1994). The interface friction and anchor capacity of synthetic georeinforcement. *5th. International Conference on Geotextiles, Geomembranes and Related Products*, Singapore, 405-410.
- Frohling, R.D., Sheffel, H. and Ebersohn, W. (1995). The vertical dynamic response of a rail vehicle caused by track stiffness variations along the track. Proc., 14th IAVSD Symp., International Association for Vehicle System Dynamics, Praha, Czech Republic.
- Hoppe, E.J. (2001). The use, design, and control of bridge approach slabs. *Routes and Roads* No. 312, October, pp.24-33.
- Hunt, H. and Winkler, M. (1997). Settlement of Railway Track near Bridge Abutments. *Proceedings of the Institution of Civil Engineers, Transport*, 123(1), pp68-73.
- Harkness, J. (2009). Potential particles for the modelling of interlocking media in three dimensions. *International Journal For Numerical Methods In Engineering* 80, 1573-1594.
- Han, X. (1998). Evaluation of ballast materials based on ballast particle characteristics and functions. Ph.D. Thesis, University of Massachusetts Amherst.
- Hashash, Y. M. A., Nezami, E, Zhao, D. and Ghaboussi, J. (2005). DBLOCK3D: A 3-D discrete element analysis code for simulation of granular media and soil-machine interaction. NASA Workshop on Granular Materials in Lunar and

Martian Exploration, Kennedy Space Center, Florida.

- Hicks, R. G. (1970). Factors influencing resilient response of granular materials. Ph.D. Thesis, University of California, Berkeley, California.
- Hicks, R. G. and Monismith, C. L. (1971). Factors influencing the resilient properties of granular materials. Hwy. Res. Rec. 345, 15-31.
- Holubec, I. and D' Appolonia, E. (1973). Effect of particle shape on the engineering properties of granular soils. ASTM STD 523, American Society for Testing and Materials. pp. 304-318.
- Hossain, Z., Indraratna, B., Darve, F. and Thakur, P. K. (2007). DEM analysis of angular ballast breakage under cyclic loading. *Geomechanics and Geoengineering: An International Journal* 2, No. 3, 175-181.
- Huang, H. (2010). Discrete element modeling of railroad ballast using imaging based aggregated morphology characterization. Ph.D. thesis. University of Illinois at Urban-Champaign.
- Indraratna, B., Ionescu, D. and Christie, H. D. (1998). Shear behavior of railway ballast based on large-scale triaxial tests. *Journal of Geotechnical and Geoenvironmental Engineering* 124(5), 439-449.
- Itasca, (1999). Particle Flow Code in Three Dimensions. Itasca Consulting Group, Inc., Minnesota.
- Janardhanam, R. and Desai, C. S. (1983). Three-dimensional testing and modelling of ballast. *Journal of Geotechnical Engineering, ASCE* 109, No. 6, 783-796.
- Jewell, R. A., Milligan, G. W. E, Sarsby, R. W. and Dubois, D. (1984). Interaction between soil and geogrids. *Proceeding of Symposium on Polymer Grid Reinforcement*. London: Thomas Telford Ltd: 18-29.
- Jewell, R. A., (1990). Reinforcement bond capacity. *Géotechnique* 40(3), 513-518.
- Kerr A D. and Moroney, B.E. (1993). Track transition problems and remedies. Bulletin 742, American Railway Engineering Association, Landover, Md., 267-298.
- Kwan, C. C. (2006). Geogrid Reinforcement of railway ballast. Ph.D. dissertation, University of Nottingham.
- Knutson, R. M. (1976). Factors influencing the repeated load behaviour of railway ballast, Ph.D. dissertation, University of Illinois Urbana-Champaign.

- Koerber, R. M., Wayne, M. H. and Carroll, R. G., (1989). Analytic behaviour of geogrid anchorage. *Proc., Geosynthetics' 89 conf.*, IFAI, San Diego, 525-536.
- Kolisoja, P. (1997). Resilient behaviour of granular materials for analysis of highway pavements. Ph.D. Thesis, University of Nottingham, Nottingham, U.K.
- Konietzky, H., Te Kamp, L., Groeger, T. and Janner, C. (2004). Use of DEM to model the interlocking effect of geogrids under static and cyclic loading. *Numerical Modelling in Micromechanics via Particle Methods*, Tokyo, Japan: pp3-11.
- Konietzky, H., Te Kamp, L. and Hainbuchner, E. (2000). Tensar geogrid modeling part II: interaction of the geogrid with soil (pullout test). Progress Report, Prepared for Tensar International, ITASCA Consultants GmbH, Gelsenkirchen, Germany.
- Konietzky, H., Te Kamp, L. (2001). Tensar geogrid modelling. Internal report.
- Kwan, C.C. (2006). Geogrid reinforcement of railway ballast. Ph.D. Thesis, The University of Nottingham.
- Lei, X. and Zhang, B. (2010). Influence of Track Stiffness Distribution on Vehicle and Track Interactions in Track Transition. *Proceedings of the Institution of Mechanical Engineers, Part F: Journal of Rail and Rapid Transit* 224: 592-604.
- Lackenby, J., Indraratna, B., McDowell, R. G. and Christie, D. (2007). Effect of confining pressure on ballast degradation and deformation under cyclic triaxial loading. *Geotechnique* 57, No. 6, 527-536.
- Lekara, F. (1997). Permanent deformation behaviour of unbound granular materials. Licentiate Thesis, Royal Institute of Technology, Stockholm.
- Lekarp, F., Isacsson, U. and Dawson, A. (2000a). State of the art. I: Resilient response of unbound aggregates. *Journal of Transportation Engineering ASCE*, Vol. 126, 66-75.
- Lekarp, F., Isacsson, U. and Dawson, A. (2000b). State of the art. II: Permanent strain response of unbound aggregates. *Journal of Transportation Engineering ASCE*, Vol. 126, 76-83.
- Li, D., (2000). Deformations and remedies for soft railroad subgrade subjected to heavy axle loads. *Advances in transportation and Geoenvironmental systems using geosynthetics*, ASCE, Reston, Va., 307-321.

- Li, D., Davis, D. (2005). Transition of railroad bridge approaches. *Journal of Geotechnical and Geoenvironmental Engineering*, 131(11), 1392-1398.
- Lim, W. L. (2004). Mechanics of railway ballast behaviour. Ph.D. Thesis, The University of Nottingham.
- Lim, W. L. and McDowell, G. R. (2005). Discrete element modelling of railway ballast. *Granular Matter* 7(1): 19-29.
- Lobo-Guerrero, S. and Vallejo, L. E. (2005). Crushing a weak granular material: experimental numerical analyses. *Geotechnique* **55**, No. 3, 243-249.
- Lobo-Guerrero, S. and Vallejo, L. E. (2006). Discrete element method analysis of Railtrack ballast degradation during cyclic loading. *Granular Matter* **8**, No. 3-4, 195-204.
- Lu, M. and McDowell, G. R. (2006). Discrete element modelling of ballast abrasion. *Geotechnique* **56**, No. 9, 651-656.
- Lu, M. and McDowell, G. R. (2007). The importance of modelling ballast particle shape in DEM. *Granular Matter* **9**, No. 1, 69-80.
- Lu, M. and McDowell, G. R. (2008). Discrete element modelling of railway ballast under triaxial conditions. *Geomech. Geoengng:Int. J.* **3**, No. 4, 257-270.
- Lu, M. and McDowell, G. R. (2010). Discrete element modelling of railway ballast under monotonic and cyclic triaxial loading. *Geotechnique* **60**, No. 6, 459-467.
- Marketos, G. and Bolton, M. D. (2010). Flat boundaries and their effect on sand testing. *International Journal for Numerical and Analytical Methods in Geomechanics*, **34**. 821-837.
- Matsushima, T., Saomoto, H., Matsumoto, M., Toda, K. and Yamada, Y. (2003). Discrete element simulation of an assembly of irregularly --shaped grains: Quantitative comparison with experiments. In: 16th ASCE Engineering Mechanics Conference, July 16--18, University of Washington, Seattle.
- McDowell, G. R., W. L. Lim, et al. (2005). Laboratory simulation of train loading and tamping on ballast. *Proceedings of the Institution of Civil Engineers-Transport* 158(2): 89-95.
- McDowell, G. R., Harireche, O., Konietzky, H., Brown, S. F. and Thom, N. H. (2006). Discrete element modelling of geogrid-reinforced aggregates.

- Proceedings of the Institution of Civil Engineers: Geotechnical Engineering 159, No. GE1, 35-48.
- McDowell, G.R. and Stickley, P. (2006). Performance of geogrid-reinforced ballast. *Ground Engineering*, 39(1), 26-30.
- McDowell, G. R., de Bono, J., Chen, C., Cai, W. Ferrellec, J-F., Li, H. and Falagush, O., 2012. Recent applications of DEM in Geomechanics. *3rd international Workshop on Modern trends in Geomechanics*, Nottingham, UK.
- Milligan, C. L. and love, J. P. (1985). Model testing of geogrids under an aggregate layer on soft ground. Thomas Telford, London.
- Moghadas, N.F and Small, J. C. (2005). Pullout behaviour of geogrids. *Iranian Journal of Science & Technology*, Transaction B, Engineering. Vol.29, No. B3.
- Moraci, N. and Piergiorgio, R. (2006): Factors affecting the pull-out behaviour of extruded geogrids embedded in a compacted granular soil.- *Geotextiles and Geomembranes* 24, 220-242.
- Morgan, J. R. (1966). The response of granular materials to repeated loading. *Proceedings of the 3rd ARRB Conference*, 1178-1192.
- Moore, W. M., Britton, S. C. and Schrivner, F. H. (1970). A laboratory study of the relation of stress to strain for a crushed limestone base material. Res. Rep. 99-209 5F, Study 2-8-65-99, Texas Transp. Inst., Texas A&M University, College Station, Texas.
- Mulabdic, M. and Minazek, K. (2010). Effect of transverse ribs of geogrids of pullout resistance. *Geosynthetics: Advanced Solutions for a Challenging World*, 9th ICG, 23.-27. May, pp. 743-746, Palmeira, Vidal, Sayao & Ehrlich (eds.), Guarujá Brasilien.
- Nezami. E. G., Zhao, D. Hashash, Y. M. A. and Ghaboussi, J. (2004). A fast contact detection algorithm for 3-D discrete element method," *Computers and Geotechnics*, Vol 31, pp575-587.
- Nezami, E. G., Hashash, Y.M.A., Zhao, D. and Ghaboussi, J. (2007). Simulation of front end loader bucket-soil interaction using discrete element method. *International Journal for Numerical and Analytical Methods in Geomechanics*, 31(9), 1147 – 1162.

- Oostveen, J. P., Maas, K. C. and Hendrikse, C. S. H. (1994). The coefficient of interaction for geogrids in non-cohesive soil. *5th. International Conference on Geotextiles, Geomembranes and Related Products*, Singapore, 427- 432.
- O'Reilly, M. P. and Brown, S. F. (1991). *Cyclic loading of soils: from theory to design*, Glasgow: Blackie and Son Ltd.
- Oxford University., 1980. The use of mesh products to improve the performance of granular fill on soft ground. Reprot 1346/81 to Netlon.
- O'Sullivan, C. (2011). *Particulate Discrete Element Modelling: A Geomechanics Perspective*. Spon Press/Taylor & Francis.
- Poschel, T. and Schwager, T. (2005). *Computational Granular Dynamics: Models and Algorithms*. Springer, Berlin.
- Price, M., Murariu, V., and Morrison, G., 2007. Sphere clump generation and trajectory comparison for real particles. In: *Discrete Element Methods 2007 Conference*, 27--29 August, Brisbane, Australia.
- Palmeira, E. M. and Milligan, G. E. (1989). Large Scale Direct Shear Tests on Reinforced Soil. *Soils and Foundations, Japanese Society of Soil Mechanics and Foundation Engineering*, **29**(1), 18-30.
- Palmeira, E.M. (2009). Soil-geosynthetic interaction: Modelling and analysis. *Geotextiles and Geomembranes* 27, 368-390,
- Pettijohn, F. J. (1957). *Sedimentary Rocks*. 2nd Ed, Chap.2, Harper Bros., New york, pp718.
- Powire, W., Ni, Q., Harkness, R. M. and Zhang, X. (2005). Numerical modelling of pane strain tests on sands using a particulate approach. *Geotechnique*, 55, No. 4, 297-306.
- Qian, Y., Tutumluer, E. and Huang, H. (2011). A Validated Discrete Element Approach for Studying Geogrid-Aggregate Reinforcement Mechanisms.- *Proceedings of the ASCE Geo-Institute Geo-Frontiers Conference on Advances in Geotechnical Engineering*, 13.-16. März, Geotechnical Special Publication 211, Han & Alzamora (eds.), Dallas, Texas (USA).
- Rada, G. and Witczak, M. W. (1981). Comprehensive evaluation of laboratory resilient moduli results for granular material. *Transp. Res. Rec. 810*, Transportation Research Board, Washington, D.C., 23-33.

- Railtrack Line Specification, (2000). RT/CE/S/006 Issue 3: Track Ballast and Stoneblower Aggregate. Railtrack PLC.
- Raymond, G.P. (2002). Reinforced Ballast Behaviour Subjected to Repeated Loading. *Geotextiles and Geomembranes* 20, 39-61.
- Robinson, R. G. (1974). Measurement of the elastic properties of granular materials using a resonance method. TRRL Supplementary Rep. No. 111UC, TTRL.
- Roefeld, M. A. (1980). A study of mechanical degradation of a coarse aggregate subject to repeated loading. Master's thesis, University of Missouri, Rolla.
- Roner, C. J. (1985). Some effect of shape, gradation and size on the performance of railroad ballast. M.S. degree project report, Report No. AAR85-324P, Department of Civil Engineering, University of Massachusetts, Amherst, June.
- Rose J., Walker, L.A. and Li, D. (2002). Heavy haul asphalt underlayment trackbeds: pressure, deflection, materials, properties measurements. Proc. Railway engineering (CD-ROM), ECS Publications, Edinburgh, UK.
- Seed, H. B., Chan, C. K. and Lee, C. E. (1962). Resilience characteristics subgrade soils and their relation to fatigue failures. Proc. Int. Conf. Structural Design of Asphalt Pavements, Ann Arbor, Michigan, 611-636.
- Seed, H. B., Mitry, F. G., Monismith, C. L. and Chan, C. K. (1965). Predictions of Pavement Deflection from Laboratory Repeated Load Tests. Report No. TE-65-6, Soil Mechanics and Bituminous Material Research Laboratory, University of California, Berkeley, California.
- Selig, E. T. and Waters, J.W. (1994). Track Geotechnology and Substructure Management. Thomas Telford, London.
- Shenton, M. J. (1974). Deformation of railway ballast under repeated loading conditions. British Railways Research and Development Division.
- Shenton, M. J. (1985). Ballast Deformation and Track Deterioration. Proc. of a Conf. on Track Technology, University of Nottingham, 11-13 Jul 1984, Thomas Telford Limited, London.
- Stahl, M. and Konietzky, H. (2011). Discrete element simulation of ballast and gravel under special consideration of grain-shape, grain-size and relative density. *Granular Matter* 13: 417-428.
- Stewart, H. E. and Selig, E. T. (1984). Correlation of concrete tie track performance

in revenue service and at the facility for accelerated service testing, US Fed Railroad Adm. Off. Res. Dev. Rep. FRA ORD, 131.

- Tensar International., (2007). The properties and performance of tensar uniaxial geogrids. Tensar International Ltd, Blackburn, UK.
- Tensar International., (2009). Tensar Geosynthetics in Civil Engineering. *Tensar International Ltd*, Blackburn, UK.
- Tensar International., (2010). TriAx brochure. Tensar International Ltd, Blackburn, UK.
- Teixeira, S. H. C., Bueno, B. S. and Zornberg, J. G. (2007). Pullout resistance of individual longitudinal and transverse geogrid ribs, *Journal of Geotechnical and Geoenvironmental Engineering*, ASCE, Jan, 37-50.
- Thom, N. H. (1988). Design of road foundations. Ph.D. Thesis, University of Nottingham, Nottingham, U.K.
- Thom, N. H. and Brown, S. F. (1988). The effect of grading and density on the mechanical properties of a crushed dolomitic limestone. *Proceedings of the 14th ARRB Conference*, Vol. 14, Part 7, 94-100.
- Thom, N. H. and Brown, S. F. (1989). The mechanical properties of unbound aggregates from various sources. *Unbound Aggregates in Roads*, (eds. R. H. Jones, and A. R. Dawson), 130-142. London: Butterworth.
- Thornton, C. (2000). Numerical simulations of deviatoric shear deformation of granular media. *Geotechnique* **50**, No. 1, 43-53.
- Tomlinson, M.J. (1995). *Foundation design and construction*, 6th edition. Longman.
- Thompson, M. R. (1989). Factors affecting the resilient moduli of soil and granular materials, Rep. No. FHWA-TS-90-031, National Technical Information Service, Springfield, Va, pp. 15.
- TRI/Environmental (2001), IN-PLANE ROTATIONAL STIFFNESS (A.K.A. TORSIONAL RIGIDITY): Is this a relevant property for base reinforcement geosynthetics? TENAX Corporation, Baltimore, US.
- Varandas, J. N., Holscher, P. and Silva .M. A. G. (2011). Dynamic behaviour of railway tracks on transition zones. *Computers and structures* 89, 1468-1479.

- Wang, L., Park, J., and Fu, Y., 2007. Representation of real particles for DEM simulation using X-ray tomography. *Construction and Building Materials*, 21, 338--346.
- Wilson-Fahmy, R. F., Koerner, R. M. and Sansone, L. (1994). Experimental behavior of polymeric geogrids in Pullout. *Journal of Geotechnical Engineering, ASCE*, 120(4), pp661-677.
- Winkler, E. (1867). *Die Lehre Von Elasticitaet Und Festigkeit*. 1st Edn., H. Dominicus, Prague.
- Zhang, J., Yasufuku, N. and Ochiai, H., (2007). A few considerations of pullout test characteristics of geogrid reinforced sand using DEM analysis, *Geosynthetics Engineering Journal* 22: 103-110.
- Zhang, J., Yasufuku, N. and Ochiai, H. (2008). Discrete element modelling of geogrid pullout test. *Geosynthetics in Civil and Environmental Engineering*: 11-14.
- Zhao, D., Nezami, E. G., Hashash, Y. M. A. and Ghaboussi, J. (2006) Three-dimensional discrete element simulation for granular material. *Engineering Computations*, 23(7), 749-770.